Title
Data-Driven Characterization of Vertical Structural Response in Instrumented Buildings Using Dense Sensor Network

ISBN
9798247915751

Author
Bolourani, Anahita

Publication Date
2026-05-26

Peer reviewed|Thesis/dissertation

UNIVERSITY OF CALIFORNIA

Los Angeles

Data-Driven Characterization of Vertical Structural Response in Instrumented Buildings Using Dense Sensor Network

A dissertation submitted in partial satisfaction of the requirements for the degree Doctor of Philosophy in Civil Engineering

by

Anahita Bolourani

2026

ABSTRACT OF THE DISSERTATION

Data-Driven Characterization of Vertical Structural Response

in Instrumented Buildings Using Dense Sensor Network

by

Anahita Bolourani

Doctor of Philosophy in Civil Engineering

University of California, Los Angeles, 2026

Professor Yousef Bozorgnia, Co-Chair

Professor Henry V. Burton, Co-Chair

Earthquake engineering practice has traditionally focused on the horizontal components of ground motion, while the vertical component and its effects on building response have received less attention. This dissertation addresses this gap by developing a data-driven framework to characterize vertical structural response in instrumented buildings and to improve understanding of vertical dynamic properties, floor-level acceleration demands, and code-based vertical seismic load effects. Using sensor recordings from past earthquakes, complemented by numerical simulation and code-oriented evaluation, the research provides recommendations to inform future provisions of the United States building codes. The study uses dense triaxial acceleration recordings from the Community Seismic Network at the NASA Jet Propulsion Laboratory campus. Six mid-rise JPL buildings, ranging from four to nine stories, are analyzed using earthquake records that were consistently recorded across the selected buildings.

A Python-based data preparation and processing pipeline is developed to retrieve, verify, convert, filter, and align the recorded building response. The processed records are then used to identify vertical and horizontal structural response frequencies through Fourier amplitude spectra, power spectral density, transfer functions, and coherence functions. The results show that vertical response frequencies are generally higher than horizontal frequencies. Across the six buildings, dominant vertical frequency is typically concentrated in the approximately 5–10 Hz range, while dominant horizontal frequency occurs at the fundamental horizontal mode, approximately 0.7–1.8 Hz. To interpret the measured vertical frequency ranges captured using sensor recordings, a refined three-dimensional numerical model of JPL 183 is analyzed. The simulation results show that vertical modal mass is distributed across many modes, and that substantially more modes are required to capture vertical response than are required for horizontal modal response. Stiffness-perturbation studies are then used to distinguish global vertical response from slab-dominated vibration. A key finding is that the dominant vertical response is often not the lowest identified vertical frequency but instead occurs at higher frequency ranges associated with global vertical response, slab vibration, or coupled global-local behavior.

This dissertation also evaluates vertical and horizontal floor response spectra using 5%-damped pseudo-spectral acceleration computed from measured floor accelerations. The vertical floor response spectra show strong period dependence, with the largest vertical amplification generally concentrated in the short-period range of approximately 0.08–0.25 seconds. Vertical acceleration demand generally increases with height. Horizontal floor response spectra show a different pattern: short-period horizontal amplification is generally more modest, while stronger amplification occurs at intermediate-to-longer periods associated with horizontal modal response. Comparisons with ASCE/SEI 7-22 Chapter 13 show that current horizontal height-amplification assumptions capture the general concept of increasing acceleration demand with height but do not fully represent the measured period dependence. For vertical response, the results indicate that the current code framework does not provide an explicit vertical floor-response-spectrum or height-amplification model. Therefore, a separate vertical floor-amplification factor is strongly recommended for future consideration in nonstructural component design.

Finally, the dissertation evaluates two approaches in the current building codes (ASCE, 2022) for calculating vertical seismic load effect: the period-independent expression based on $0.2S_{DS}$ and the period-dependent expression based on $0.3S_{av}$. The two approaches are compared using NGA-West2 ground-motion models for more than 3,000 seismic scenarios and ASCE 7 Hazard Tool data for 19,316 California sites. The results show that the relationship between the two expressions depends strongly on the vertical period and seismic design category. The $0.2S_{DS}$ expression can underestimate vertical seismic demand for moderate vertical periods, especially around 0.05–0.20 seconds in higher seismic design categories, while it can be overly conservative for very short and long vertical periods compared to results derived from $0.3S_{av}$. Based on these findings, the dissertation provides period- and seismic-design-category-dependent recommendations for calculating vertical seismic load effects and proposes refinements to improve the long-period behavior of the vertical design spectrum.

Overall, this dissertation demonstrates that vertical structural response is an important structural dynamic phenomenon that should be characterized using measured data, physical interpretation, and period-dependent design considerations. The findings provide empirical evidence and building code-oriented recommendations for improving the treatment of vertical response in future building code provisions.

The dissertation of Anahita Bolourani is approved.

Jonathan P. Stewart

Monica D. Kohler

Yousef Bozorgnia, Committee Co-Chair

Henry V. Burton, Committee Co-Chair

University of California, Los Angeles

2026

To my beloved mother, Azita Salimitari, and father, Mahmoud Bolourani, whose endless love, sacrifices, and prayers made this journey possible.

To whom I owe everything …

CONTENTS

LIST OF FIGURES

LIST OF TABLES

Acknowledgement

Financial support for this dissertation, or portions of the research presented herein, was provided by the University of California, Los Angeles (UCLA) Graduate Fellowship and the National Science Foundation under Award No. 2025310. This support is gratefully acknowledged. Any opinions, findings, conclusions, or recommendations expressed in this dissertation are my own and do not necessarily reflect the views of the supporting agencies.

I am grateful to my advisors, Professor Yousef Bozorgnia and Professor Henry V. Burton, for their invaluable guidance and support throughout my doctoral studies. I also sincerely thank Professor Jonathan P. Stewart and Professor Monica D. Kohler for serving on my Ph.D. committee and for their thoughtful feedback and guidance. Their expertise and perspectives greatly strengthened the quality and direction of this work.

I gratefully acknowledge the Community Seismic Network (CSN), the Jet Propulsion Laboratory (JPL), and the California Institute of Technology (Caltech) for their collaboration and for providing access to the data and resources essential to this dissertation. I especially thank Dr. Richard Guy and Professor Monica D. Kohler for facilitating access to the CSN records and the JPL building. I also thank Dr. Tadahiro Kishida for their invaluable guidance on signal processing, Computers and Structures, Inc. (CSI) for providing a software license, and Prof. Grigorios Lavrentiadis, Dr. Silvia Mazzoni, Dr. Aidin Tamhidi, and Ala N. Tak for their guidance and helpful discussions during this research.

Finally, I express my deepest gratitude to my family: mother, father, and brother, whose love, sacrifices, and support made this achievement possible. This milestone would not have been possible without the people who stood beside me, encouraged me, and helped me continue forward.

VITA

2012-2016	B.Sc. in Civil Engineering, University of Tehran, Tehran, Iran
2016-2019	M.Sc. in Structural Engineering, University of Tehran, Tehran, Iran
2022-2026	Ph.D. Candidate in Structural and Earthquake Engineering, Civil and Environmental Engineering, University of California, Los Angeles

CHAPTER 1. Introduction

1.1 Motivation and Background

Earthquake engineering practice has historically emphasized the horizontal components of ground motion because lateral shaking produces the most visible global deformation demand in buildings. This emphasis is reflected in analysis procedures, design provisions, and the large body of research devoted to estimating lateral periods, lateral response spectra, and horizontal floor acceleration demands. The vertical component of ground motion, however, is also a fundamental part of earthquake excitation and has been recognized for more than a century. Early studies documented the existence and characteristics of vertical shaking and explored the relationship between vertical and horizontal components (Banerji, 1925; Blake, 1933; Gutenberg, 1931; Klotz, 1915; Wood, 1911).

For many years, a common design simplification assumed that vertical motion could be represented as approximately two-thirds of the horizontal motion. Subsequent studies showed that this approximation is not generally reliable. The vertical-to-horizontal ratio depends on oscillator period, source-to-site distance, magnitude, site conditions, and other ground-motion characteristics (Abrahamson & Litehiser, 1989; Bozorgnia et al., 1998; Bozorgnia et al., 1995; Niazi & Bozorgnia, 1991). These findings motivated the development of vertical spectra and ground-motion models, and they have influenced modern seismic design provisions (ASCE, 2016, 2022; Bozorgnia & Campbell, 2004, 2016; Gülerce & Abrahamson, 2011).

Although the building codes and guidelines have been modified based on researchers' findings, vertical ground motion remains represented more simply than horizontal motion in most structural design workflows. However, evidence from post-event field observations, such as the Northridge Earthquake in 1994, the Kobe Earthquake in 1995, and the L'Aquila Earthquake in 2009, underscores the potentially devastating impact of vertical ground motions (Bozorgnia et al., 1998; Di Sarno et al., 2011; Varevac et al., 2010). In the past, two important points were raised questioning the significance of vertical ground motion. Firstly, it was assumed that standard structures, designed based on building codes, already have enough safety measures against vertical forces. Second, vertical motions have low energy. However, studies and observations argue against these viewpoints, suggesting that the relationship between structural and excitation periods is more important than energy content; moreover, structural failure could still occur due to the combined effects of intense vertical and horizontal motions (Anderson & Bertero, 1973; Hamidia et al., 2022; Harrington & Liel, 2016; Lee & Mosalam, 2014; Liberatore et al., 2019; Papazoglou & Elnashai, 1996).

The first gap in current knowledge concerns the vertical dynamic characteristics of buildings. Horizontal fundamental frequencies are commonly estimated, measured, and used in seismic design and assessment through both analytical methods and recorded response data (Alonso-Rodríguez & Miranda, 2016; Biot, 1943; Ghahari et al., 2010). By comparison, vertical natural frequencies are much less routinely characterized. Vertical building response can involve several interacting mechanisms, including axial deformation of columns and walls, deformation of gravity framing, bending of beams and slabs, and coupled global-local vibration. Because these mechanisms can occur in overlapping frequency ranges, they are difficult to distinguish using sparse instrumentation. There are a few studies that have demonstrated that vertical response can be identified from measured building data. For example, Bozorgnia et al. estimated the vertical frequencies of twelve structures using recordings from the Northridge earthquake; they reported that the lowest identified vertical frequencies of structural members and systems ranged from 3.9 to 13.3 Hz, corresponding to periods of approximately 0.075 to 0.26 s (Bozorgnia et al., 1998). A recent study by Vera investigated vertical modal parameters using simplified two-dimensional structural models, with comparisons to recorded motions from three buildings instrumented at their base and roof during one seismic event (Vera, 2022). However, the number of buildings with dense floor-by-floor vertical recordings remains limited, and the physical interpretation of measured vertical frequency ranges, particularly the distinction between global vertical modes and slab-dominated vibration, remains underdeveloped.

The second gap concerns floor-level acceleration demand for nonstructural components. These systems are often acceleration-sensitive and may control post-earthquake functionality even when the primary structural system remains stable. Floor response spectra (FRS) provide a period-dependent representation of the acceleration demand that a component experiences at a given floor and have long been used to support the seismic design of nonstructural systems, particularly in essential facilities. An approximate method for generating floor response spectra for essential facilities was introduced by the U.S. Army and the Tri-Services Committee in 1986 and was later refined by other researchers (Departments of the Army, 1986; Kehoe & Hachem, 2003; Welch & Sullivan, 2017). Peak horizontal floor acceleration and horizontal floor response spectra have been studied extensively using analytical, numerical, and measured-response approaches (Anajafi & Medina, 2018, 2019; Chaudhuri & Hutchinson, 2004; Clayton & Medina, 2012; Fathali & Lizundia, 2011; Miranda & Taghavi, 2005; Sullivan et al., 2013; Wang et al., 2021). In contrast, the vertical floor response spectrum (VFRS) remains much less developed, particularly in measured-data studies. Although numerical investigations, such as the study by Lu et al. (2017) on the Shanghai Tower, have provided important insight into vertical floor demands, there is still a need for comprehensive studies based on earthquake recordings (Lu et al., 2017). This gap is important because vertical floor accelerations may affect the design of acceleration-sensitive nonstructural systems in buildings where post-earthquake functionality is critical. Moreover, the current nonstructural component design provisions in ASCE/SEI 7-22 Chapter 13 provide explicit height-amplification expressions for horizontal component design forces, but vertical nonstructural effects are not represented through an analogous VFRS-based height-amplification framework (ASCE, 2022). A measured-data evaluation is needed to determine whether vertical floor acceleration demand increases with elevation, over which component-period ranges it is most important, and how it compares with the horizontal height-amplification assumptions already present in design provisions.

The third gap concerns the vertical seismic load effect, E_v, used in building codes and guidelines. The equivalent static representation of vertical seismic loading traces back to early seismic provisions such as ATC 3-06 (Applied Technology Council, 1978). Modern provisions still permit a simplified expression based on the horizontal short-period design spectral acceleration, while also allowing a period-dependent expression based on the vertical design spectral acceleration at the vertical period of interest (ASCE, 2022; LATBSDC, 2023). These two approaches do not necessarily produce consistent results because one is independent of the vertical period and the other is explicitly period dependent. The implications of choosing one method over the other, therefore, need to be evaluated across vertical period ranges, seismic design categories, ground-motion models, and site-specific hazard conditions.

Recent advances in seismic monitoring have created new opportunities to address these challenges through measured building-response data. By recording structural motions during earthquakes, sensor networks provide direct evidence of how buildings respond to ground motions. Back in 1932, US Congress funding enabled the first record of ground motion in California, marking the beginning of using sensors in this field. The earliest recorded instance of strong ground motions was captured during the Long Beach, California earthquake on 10 March 1933 (Trifunac & Todorovska, 2001). Since then, seismic instrumentation has expanded substantially; today, approximately 2,000 ground-level recording devices are distributed across California, providing valuable information for earthquake characterization and infrastructure resilience (Tamhidi et al., 2023). As sensor technology becomes more affordable, the same monitoring concept is increasingly moving from sparse regional networks toward dense urban and building-level deployments, enabling cities and campuses to function as instrumented "smart-city" testbeds for seismic response studies (Tamhidi, 2022).

Today, networks such as the California Strong Motion Instrumentation Program (CSMIP) and the Community Seismic Network (CSN) provide valuable data to understand earthquake shaking and improve infrastructure resilience (Clayton et al., 2011; Haddadi et al., 2012). However, traditional building instrumentation is often sparse, with sensors placed only at selected levels such as the base, mid-height, and roof. While such configurations can capture important response features, they are generally insufficient to resolve how vertical motion develops floor by floor or to distinguish global building response from localized behavior. Dense triaxial instrumentation, especially when sensors are distributed across multiple floor levels and plan locations, provides the data needed to identify repeatable structural responses. CSN is especially well-suited for this purpose because it deploys low-cost triaxial accelerometers across communities and inside buildings, including many installations with sensors distributed along the height of structures (Clayton et al., 2011; Clayton et al., 2015; Kohler et al., 2022).

In summary, while several studies have made strides in understanding the characteristics of vertical ground motions, certain aspects in this area remain ambiguous. The motivation for this dissertation is not simply that vertical ground motion exists, but that structural responses remain insufficiently characterized in three areas: measured vertical dynamic properties, floor-level acceleration demand on nonstructural systems, and code-level representation of vertical seismic load effects. This dissertation addresses these issues through a unified framework that combines dense CSN recordings from the JPL campus, targeted numerical simulation, and probabilistic code evaluation. This research seeks to bridge the existing knowledge gaps and gain insights into vertical ground motions and their impact on structural responses.

1.2 Objectives and Contributions

The objective of this dissertation is to develop a data-driven characterization of structural seismic response in instrumented buildings, with particular emphasis on vertical response. The study uses measured floor-level accelerations to examine how earthquake excitation is transmitted and amplified within buildings and how those observations can inform structural analysis, nonstructural component demand assessment, and code-level evaluation of vertical seismic effects. The specific objectives and contributions are as follows:

1. Develop a data preparation and processing framework for dense CSN building records. The framework automates record retrieval, extraction, building-sensor availability checks,

format conversion, filtering, and alignment of multi-floor acceleration records. This contribution establishes the dataset used for all subsequent measured response analyses.

2. Introducing a framework to identify vertical and horizontal structural frequency ranges from the sensor recordings. The framework combines Fourier amplitude spectra, power spectral density, floor-to-reference transfer function, and coherence function to identify repeatable response frequencies and distinguish likely structural peaks from noise or input-motion artifacts.

3. Interpret measured vertical frequencies using numerical simulation. A refined three-dimensional numerical model of JPL 183 is used as a case study to relate the data-driven vertical frequency ranges to underlying structural mechanisms. The model incorporates vertical mass assignment, refined slab shell meshing, and sensor-to-model location mapping to support comparison between measured and simulated modal response. Stiffness-perturbation analyses, including slab-stiffened and vertical-element-stiffened cases, are used to classify the identified frequency ranges as global vertical response, slab-dominated vibration, or coupled global–local response.

4. Quantify vertical and horizontal floor response spectra and height amplification. The dissertation computes 5%-damped VFRS and HFRS from measured floor accelerations, evaluates short-period consistency with peak floor acceleration, and summarizes height amplification factors as functions of floor elevation, component period, building, and event.

5. Evaluate the relevance of ASCE/SEI 7-22 Chapter 13 height-amplification assumptions to measured floor response. The horizontal provisions are evaluated against measured HFRS, while the same functional forms are tested for transferability to vertical amplification. This contribution provides preliminary evidence for component-period-dependent horizontal refinement and a separate vertical floor-amplification factor.

6. Evaluate alternative code expressions for vertical seismic load effect, E_v. The dissertation compares the period-independent expression based on $0.2S_{DS}$ with the period-dependent expression based on $0.3S_{av}$ using NGA-West2 ground-motion models and California site-specific data. The analysis identifies vertical-period and seismic-design-category ranges where the simplified expression can either overestimate or underestimate the period-dependent vertical demand. This study provides a recommendation for future building codes provisions regarding the vertical seismic load effect.

Together, these contributions connect measured building response with physical interpretation and design practice. The dissertation provides empirical evidence that vertical response is not only a ground-motion characteristic but also an in-structure dynamic response phenomenon. It also shows that vertical floor demands and vertical seismic load effects should be interpreted with explicit attention to period range, building height, and structural response mechanism.

1.3 Organization and Outline

This dissertation is organized into seven chapters. The sequence of chapters progresses from the measurement platform and data preparation to frequency identification, physical interpretation, floor response spectra, code-level vertical seismic load evaluation, and overall conclusions.

Chapter 1, Introduction: This chapter motivates the study by reviewing the role of vertical ground motion in structural and nonstructural response, identifying gaps in measured vertical building-response characterization, and summarizing the objectives and contributions of the dissertation.

Chapter 2, Instrumented Building and Data Pipeline: This chapter introduces the Community Seismic Network and the JPL campus instrumentation that form the measured-data foundation of the dissertation. It describes the six case-study buildings, their sensor configurations, and the selected earthquake records. Furthermore, this chapter introduces a Python-based platform that was developed and used for data preparation, ensuring a simplified process for downloading, synthesizing essential data sets and signal processing, including noise removal, corner frequencies, and zero-padding.

Chapter 3, Identification of Structural Frequencies via Data-Driven Methods: This chapter presents the frequency-identification framework based on Fourier amplitude spectra, power spectral density, transfer functions, and coherence function. The framework is applied to six instrumented JPL buildings to identify vertical and horizontal response frequency ranges and to compare dominant vertical and horizontal dynamic behavior.

Chapter 4, Identification of Structural Vertical Frequencies via Simulation: This chapter develops and analyzes a refined three-dimensional numerical model of JPL 183 to provide a physical interpretation of the vertical frequency ranges identified from recorded earthquake responses. It evaluates the number of modes required to capture vertical modal mass participation, examines the computational challenges associated with vertical modal analysis, and uses stiffness-perturbation studies to distinguish global vertical modes from slab-dominated and coupled vibration modes. The chapter then compares the simulation-derived modal frequencies with the measured frequency bands, linking the observed vertical response to specific structural mechanisms.

Chapter 5, Floor Response Spectra: This chapter computes vertical and horizontal floor response spectra from the processed CSN records and evaluates height amplification factors. It examines the period ranges where vertical and horizontal amplification are most significant, summarizes between-event and within-event trends, and compares measured amplification with ASCE/SEI 7-22 Chapter 13 height-amplification assumptions.

Chapter 6, Vertical Seismic Load Effects on Building Code: This chapter evaluates two alternative code approaches for calculating Ev. It uses NGA-West2 scenario-based ground-motion models and ASCE 7 Hazard Tool data for California sites to quantify the ratio between period-dependent and period-independent expressions. The chapter provides period- and seismic-design-category-based recommendations for the calculation of vertical seismic load effects in United States building code.

Chapter 7, Summary, Conclusions, Limitations, and Future Work: This chapter summarizes the major findings of the dissertation, consolidates the conclusions from the measured-data, simulation, floor-response, and code-evaluation studies, and identifies limitations and future research needs.

CHAPTER 2. Instrumented Building and Data Pipeline

This chapter describes the framework that underpins the dataset and preparation pipeline used in this dissertation. It first provides an introduction for the Community Seismic Network (CSN) and CSN instrumentation of the NASA Jet Propulsion Laboratory (JPL) campus, explaining why this densely instrumented, prototype smart-city setting is well-suited for studying vertical structural response. The chapter then defines the scope of the case-study JPL buildings, summarizes their instrumentation, and presents the Python-based data preparation and processing pipeline used to retrieve, clean, and standardize the CSN records. Finally, it outlines the criteria used to select a consistent set of earthquake events for all buildings, providing a foundation for the investigations of structural vertical responses in the subsequent chapters.

2.1 The Community Seismic Network (CSN)

The CSN is an existing novel seismic monitoring system that leverages a dense network of low-cost sensors to capture earthquake ground shaking. CSN, originally established by Caltech, is currently a collaborative academic effort of Caltech[1] and UCLA. It is a community-driven, strong-motion network in the Los Angeles region that addresses the limitations of sparse traditional networks.

[1] The California Institute of Technology

In the CSN's original design, community volunteers host triaxial MEMS[2] accelerometers connected to local micro-computers, which stream data to cloud servers for real-time analysis (Clayton et al., 2011). This cloud computing architecture (using services like Amazon Web Services) enables the network to handle data surges during earthquakes and rapidly deliver useful shaking results. One of the network's products is an automatic map of peak ground acceleration delivered within seconds of an earthquake, providing first responders with block-by-block intensity insights (Abdelbarr et al., 2023; Clayton et al., 2011). A key motivation of CSN is to improve post-earthquake situational awareness by capturing localized effects and assessing building-specific responses (Clayton et al., 2015).

2.1.1 CSN's Sensors Architecture

Each CSN station consists of a low-cost, three-component MEMS accelerometer interfaced with a Linux-based computer (typically a Raspberry Pi or similar ARM processor unit) that continuously samples acceleration waveforms (Kohler et al., 2018). The sensor packages cost about \$500 (compared with several thousand dollars or more for other strong-motion accelerograph systems, for instance, the Etna-2 costs about \$5500 per unit (Lawrence Livermore National Laboratory, 2019)), yet can record strong motions up to about ±2g, making them effective for even intense shaking. A nominal sampling rate of approximately 50 samples per second is used, which is sufficient to capture building and ground motions in the frequency range of engineering interest (A higher sampling rate is also feasible). Each station analyzes data in real time; if a triggering earthquake motion is detected, the system automatically transmits shaking intensity and

[2] Micro-Electro-Mechanical Systems, for more details about this sensor, refer to (Evans et al., 2005) and (Clayton et al., 2011)

timing to cloud servers (Clayton et al., 2011; Clayton et al., 2015). The CSN website[3] provides access to recorded acceleration time-series in the standard Seismic Analysis Code (SAC) format[4] that is commonly employed for seismic waveform data.

2.1.2 CSN Evolution and Expansion

The CSN has grown dramatically from a small volunteer-based pilot in 2011 into a large regional array by the mid-2020s. By 2015, CSN consisted of several hundred stations across metropolitan Los Angeles, yielding much finer spatial coverage than conventional seismic networks (Clayton et al., 2015). A major expansion came in the late 2010s through a partnership with the Los Angeles Unified School District; by 2020, the CSN-LAUSD sub-network had deployed approximately 300 MEMS accelerometers in local school campuses (Clayton et al., 2020).

Ongoing growth and state partnerships have extended CSN's reach beyond schools and homes. By 2024, the network comprised over 1,200 three-component stations across Southern California, marking an unprecedented density of strong-motion instrumentation. Notably, a collaboration (financial support) with UCLA, the California Geological Survey, and other foundations, in this period, helped fill regional gaps by adding stations outside Los Angeles. Geographically, CSN's footprint now spans the greater Los Angeles area and its surrounding regions, making it one of the world's densest urban seismic arrays (Kohler et al., 2022; Mohammed et al., 2024).

[3] http://csn.caltech.edu/data/
[4] Seismic Analysis Code (Appendix A)

2.1.3 Key advantages of the CSN for this research

In the context of this research, the CSN database emerges as a critical resource for two primary reasons:

i) **Dense Instrumentation in Buildings and Support for Vertical Structural Response Studies:** A distinguishing feature of CSN is its unprecedented dense instrumentation of individual buildings, with floor-by-floor sensor coverage. Conventional strong-motion monitoring programs (e.g., the California Strong Motion Instrumentation Program, CSMIP) typically install only a few 3-axis accelerometers per building (often just at the base, mid-height, and roof). In contrast, CSN deployments strive to place at least one triaxial sensor on each floor of the structure of interest. This strategy yields a high-resolution vertical array of data over the height of the building. For example, a 52-story steel moment-frame high-rise in downtown Los Angeles has been instrumented with CSN accelerometers on nearly every floor, providing a detailed record of the building's full dynamic response during earthquake ground shaking (Kohler et al., 2016). Figure 2.1 shows this contrast in terms of sensor density. The CSN equipped every floor with a sensor in the vertical direction, whereas the sensors in CSMIP's deployment in the same building were limited to the base and top floors. This dense floor-by-floor coverage captures how motion amplifies and propagates upward, which cannot be adequately observed in a sparse two-sensor setup. As a result, CSN can measure subtle differences in shaking between floors and identify complex structural behaviors. Before CSN, such rich structural monitoring was rarely available outside of specialized research.

These vertically distributed sensors open new possibilities for this research to investigate vertical structural responses (e.g., quantifying the distribution of the vertical response over the height of a building, identifying a structure's natural frequencies, and floor-level response spectra from real earthquake recordings).

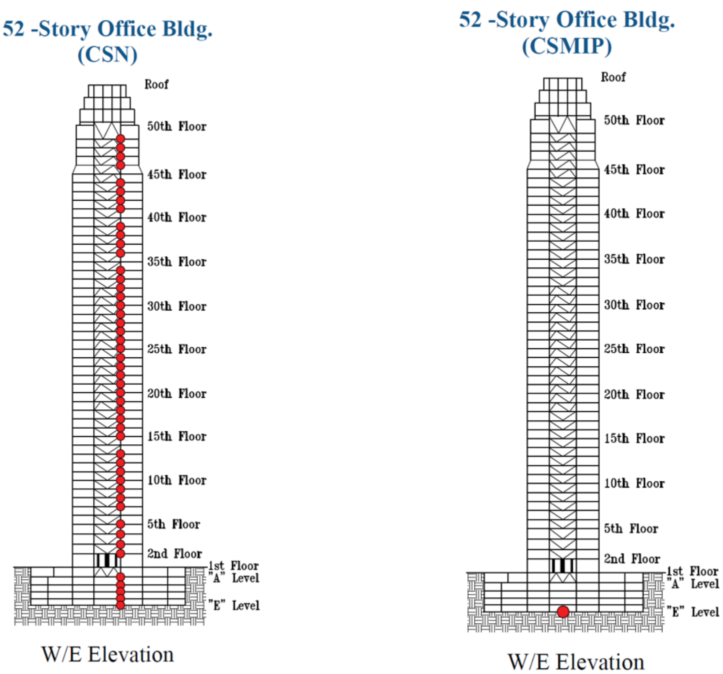

(a) (b)

Figure 2.1. Comparative distribution of vertical sensors in a 52-story building in downtown LA: a) CSN vs. b) CSMIP. Red dots represent the locations of the triaxial sensors.

ii) **Real-World Deployments and Case Studies:** CSN has also demonstrated its capabilities through large-scale deployments that turn entire communities into living laboratories. The most notable example is the NASA JPL campus in Pasadena. Numerous buildings at JPL are instrumented with CSN sensors, effectively transforming the campus into a prototype smart-city observatory for earthquakes. The JPL-CSN network, described further in Section 2.2, is especially well aligned with the objectives of this research, providing high-resolution building-specific data essential for investigating vertical structural response.

2.2 The Jet Propulsion Laboratory (JPL) Campus

The JPL campus in Pasadena, California, is NASA's primary center for robotic space and Earth science research in collaboration with Caltech. The campus spans approximately 1 km^2 in the southern foothills of the San Gabriel Mountains, near several active fault systems (Figure 2.2), and contains a diverse range of buildings, from small wood-frame structures and modular units to steel and reinforced-concrete buildings. This diversity of building typologies provides a rich set of different construction styles, making the JPL campus an ideal testbed for different types of seismic studies.

Through the JPL-CSN collaboration, this campus is instrumented with an exceptionally dense array of seismic sensors (Kohler et al., 2022). Approximately 220 triaxial accelerometers have been deployed across numerous buildings on the JPL grounds. About 100 of these sensors are located at ground level, spaced about 100 m apart on average, forming a tight grid of ground-motion stations across the campus. The remaining instruments are installed inside buildings, with many structures housing a sensor on every floor to capture the full-height response. This floor-by-floor deployment means that several buildings have one or more CSN accelerometers on upper stories in addition to the ground-level unit.

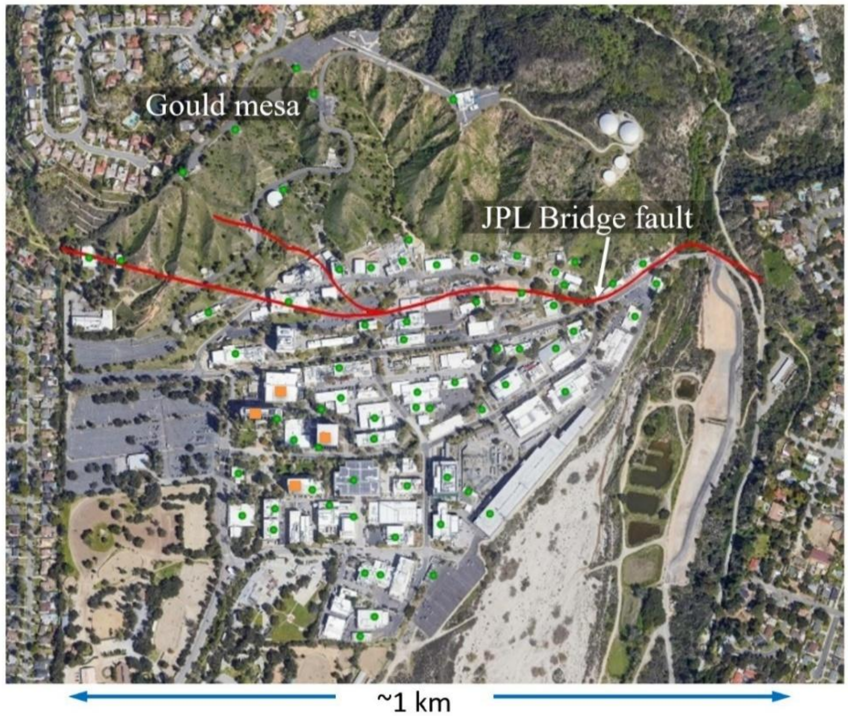

Figure 2.2. Satellite map illustrating the distribution of CSN accelerometer (green dot) installations across the NASA-JPL campus (source image: CSN website)

The JPL-CSN network enables advanced real-time tracking of seismic response. The 100 ground-level stations are used to contribute peak acceleration data to an experimental ShakeMap for the campus, and a custom ShakeCast setup utilizes those measurements to estimate potential building-specific damage in real-time. Each instrumented building is assigned fragility curves (e.g., from HAZUS models) so that when an earthquake occurs, the CSN's ShakeMap output can feed into a localized ShakeCast analysis for JPL, providing immediate structural performance assessments for the entire campus. This capability demonstrates how a dense network can support earthquake warning and situational awareness at the community scale (Kohler et al., 2018; Kohler et al., 2022). Moreover, because dozens of structures on campus experience the same seismic events, researchers can perform direct cross-building analyses of structural behavior under identical ground shaking. In other words, JPL's instrumentation enables a side-by-side comparison of how different buildings respond to the same earthquake, providing a unique opportunity to validate analytical models and understand the influence of structural design on seismic performance.

In summary, the dense sensor network on the JPL campus has enabled a detailed investigation of vertical structural response, which is a central focus of this dissertation, and can pave the way for creating more earthquake-resilient cities for the future.

2.3 Scope: Case study Buildings

This study focuses on the vertical structural response assessment of multiple mid-rise, instrumented buildings located on the JPL campus. Six buildings have been selected for investigation, all of which are equipped with at least one triaxial accelerometer per floor. These structures range from four to nine stories in height and are among the tallest buildings on the JPL campus. The list of buildings considered in this research is provided in Table 2.1.

Table 2.1. Overview of selected buildings from the JPL campus

	Building	**Number of Floors**	**Number of Sensors**	**Number of basement-level**
1	JPL 180	9	28	1
2	JPL 183	9	18	0
3	JPL 238	8	8	0
4	JPL 264	8	8	0
5	JPL 321	6	7	1
6	JPL 303	4	4	0

In the JPL-CSN metadata used in this study, Floor 1 corresponds to the ground floor/reference level. Therefore, floor numbers reported in this dissertation follow the CSN metadata convention unless otherwise noted. All six buildings are investigated through data-driven analysis, providing a view across different heights and ensuring that the conclusions are not drawn from a single structure alone. For the numerical simulation component of the research, the study focuses on a single representative building, JPL 183 (Figure 2.3), to develop and validate the simulation methodology. The insights and results from this case are then cross-checked against the empirical data to evaluate the generality and robustness of the findings.

Figure 2.3. JPL 183 Building (source image: Google Maps)

Numerical simulations are conducted in ETABS using three-dimensional models of selected buildings (Computers and Structures, 2023; Massari et al., 2018). In this simulation, specific complex effects (such as soil–structure interaction) are disregarded to maintain a narrow focus on the response of the building's primary structural system.

For the data-driven component, R and Python computer platforms are used to prepare, process, analyze, and visualize the datasets derived from the CSN sensors. All accelerograms are prepared using NGA (Next Generation Attenuation) -consistent strong-motion processing procedures (Goulet et al., 2021). Section 2.4 describes the data preparation- pipeline in detail.

2.4 Data Preparation Pipeline

2.4.1 Preparing Recorded Structural Response

Given the focus on structural seismic responses in a prototype smart city, implementing an automated data-preparation process is pivotal to efficient, consistent analysis. A Python-based data preparation pipeline is developed to acquire and preprocess acceleration records from CSN instrumented buildings. As shown in Figure 2.4, the data preparation pipeline consists of a sequence of steps: downloading raw data, extracting (unzipping), verifying that the target building's sensors captured the desired events, and converting the data into a format suitable for signal processing. Automating these steps not only saves time but also ensures that the data is prepared in a standardized way for the next phases of the research.

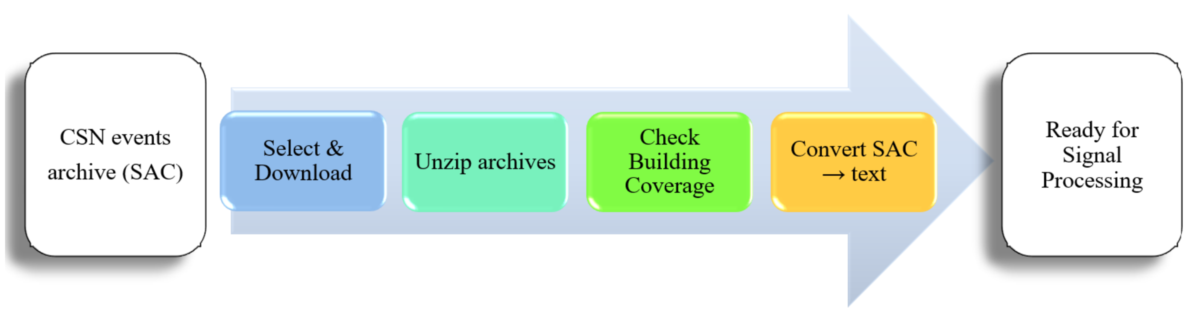

Figure 2.4. Automated data preparation pipeline for CSN building records

The pipeline's first task is to retrieve the relevant records by accessing the CSN website's HTML source and automatically downloading the specified motion files. The CSN website provides access to a comprehensive collection of ground-motion records (over 90 earthquakes). A selection interface is incorporated to filter the records of interest, since not every recorded motion is pertinent to this study's focus. Specifically, previous research indicates that the vertical component of ground motion can vary significantly with factors such as magnitude and source-to-site distance (Bozorgnia et al., 1995). To ensure we gather only the most relevant data, the procedure allows users to specify parameters like the earthquake name, magnitude range, and distance range. Based on these criteria, the *Download* function automatically fetches the corresponding acceleration of time-history files from the CSN database.

The *Unzip* function then extracts these files to facilitate easier access and handling of the data (Figure 2.5 shows the Download and Unzip process for JPL180). Together, the Download and Unzip steps provide a streamlined way to collect large volumes of raw sensor data and prepare them for analysis without manual intervention.

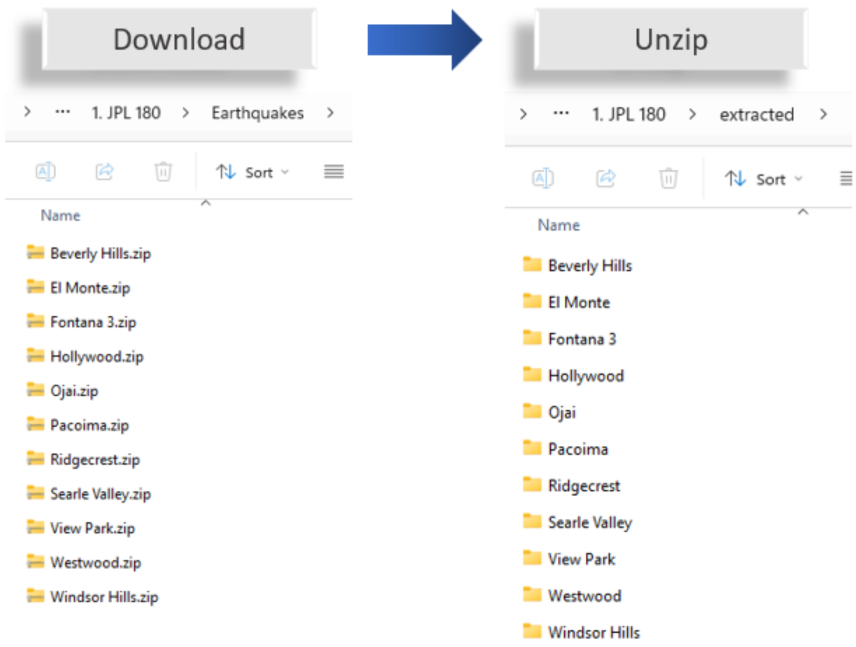

Figure 2.5. The “Download” and “Unzip” functions in the data preparation pipeline

In the next step, the *Check Record* function verifies whether the target building sensors recorded the chosen seismic events. The output of this function is a CSV summary file indicating whether the recorded motion is present or absent for the target building (Figure 2.6 shows an example of the Check Record output). If a target building does not record a given earthquake, the absence is flagged, and that event can be excluded from further analysis for that building.

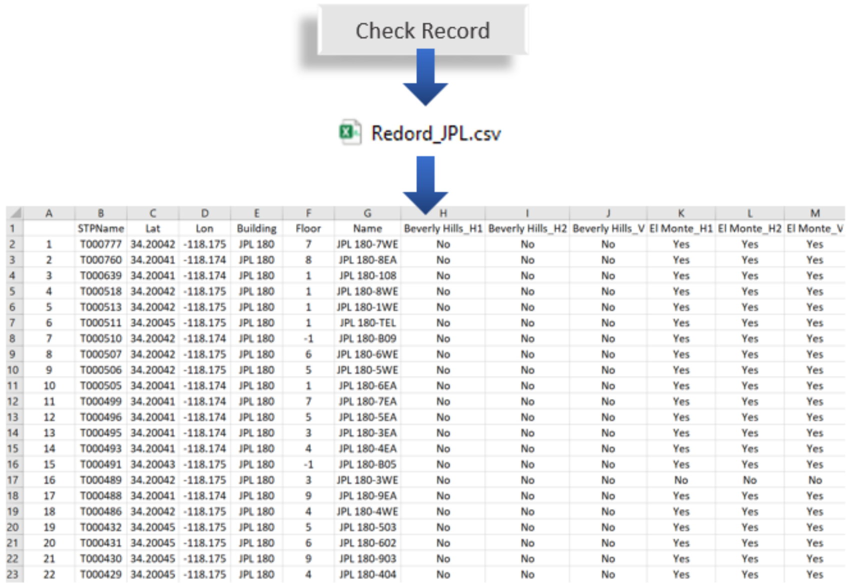

	A	B	C	D	E	F	G	H	I	J	K	L	M
1		STPName	Lat	Lon	Building	Floor	Name	Beverly Hills_H1	Beverly Hills_H2	Beverly Hills_V	El Monte_H1	El Monte_H2	El Monte_V
2	1	T000777	34.20042	-118.175	JPL 180	7	JPL 180-7WE	No	No	No	Yes	Yes	Yes
3	2	T000760	34.20041	-118.174	JPL 180	8	JPL 180-8EA	No	No	No	Yes	Yes	Yes
4	3	T000639	34.20041	-118.174	JPL 180	1	JPL 180-108	No	No	No	Yes	Yes	Yes
5	4	T000518	34.20042	-118.175	JPL 180	1	JPL 180-8WE	No	No	No	Yes	Yes	Yes
6	5	T000513	34.20042	-118.175	JPL 180	1	JPL 180-1WE	No	No	No	Yes	Yes	Yes
7	6	T000511	34.20045	-118.175	JPL 180	1	JPL 180-TEL	No	No	No	Yes	Yes	Yes
8	7	T000510	34.20042	-118.174	JPL 180	-1	JPL 180-B09	No	No	No	Yes	Yes	Yes
9	8	T000507	34.20042	-118.175	JPL 180	6	JPL 180-6WE	No	No	No	Yes	Yes	Yes
10	9	T000506	34.20042	-118.175	JPL 180	5	JPL 180-5WE	No	No	No	Yes	Yes	Yes
11	10	T000505	34.20041	-118.174	JPL 180	1	JPL 180-6EA	No	No	No	Yes	Yes	Yes
12	11	T000499	34.20041	-118.174	JPL 180	7	JPL 180-7EA	No	No	No	Yes	Yes	Yes
13	12	T000496	34.20041	-118.174	JPL 180	5	JPL 180-5EA	No	No	No	Yes	Yes	Yes
14	13	T000495	34.20041	-118.174	JPL 180	3	JPL 180-3EA	No	No	No	Yes	Yes	Yes
15	14	T000493	34.20041	-118.174	JPL 180	4	JPL 180-4EA	No	No	No	Yes	Yes	Yes
16	15	T000491	34.20043	-118.175	JPL 180	-1	JPL 180-B05	No	No	No	Yes	Yes	Yes
17	16	T000489	34.20042	-118.175	JPL 180	3	JPL 180-3WE	No	No	No	No	No	No
18	17	T000488	34.20041	-118.174	JPL 180	9	JPL 180-9EA	No	No	No	Yes	Yes	Yes
19	18	T000486	34.20042	-118.175	JPL 180	4	JPL 180-4WE	No	No	No	Yes	Yes	Yes
20	19	T000432	34.20045	-118.175	JPL 180	5	JPL 180-503	No	No	No	Yes	Yes	Yes
21	20	T000431	34.20045	-118.175	JPL 180	6	JPL 180-602	No	No	No	Yes	Yes	Yes
22	21	T000430	34.20045	-118.175	JPL 180	9	JPL 180-903	No	No	No	Yes	Yes	Yes
23	22	T000429	34.20045	-118.175	JPL 180	4	JPL 180-404	No	No	No	Yes	Yes	Yes

Figure 2.6. The “Check Record” function in the data preparation pipeline

The final function in the code is *Convert Format*, which converts the data files from their original format to the format required by this project’s processing tools. The acceleration records obtained from the CSN website are provided in the SAC[5] format, which contains raw (unfiltered) time-series data. While it is possible to handle SAC files directly using libraries such as ObsPy, this research adopts an NGA-based signal-processing approach that requires input in text format. Therefore, this function automatically converts each SAC file to a text file.

In summary, the developed pipeline integrates all four functions (Download, Unzip, Check Record, and Convert Format) to automate data preparation, filtering, and formatting of raw acceleration data for use in Signal Processing as the next step. The pipeline user interface is shown in Figure 2.7.

[5] Seismic Analysis Code

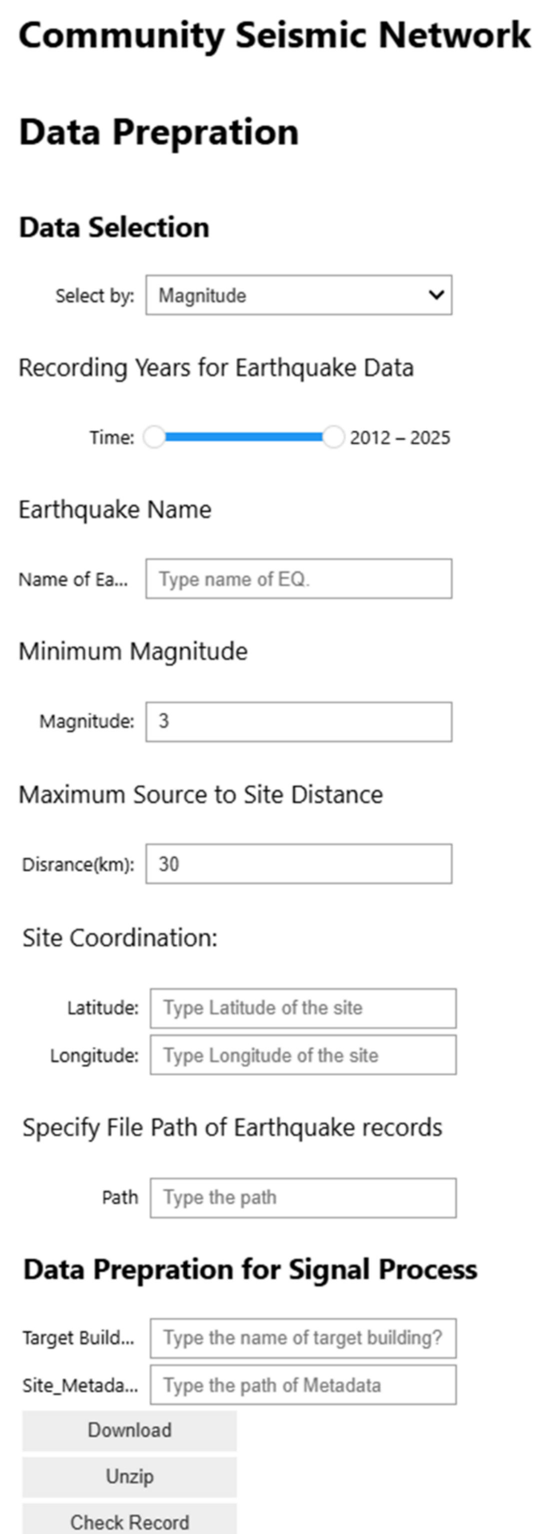

Figure 2.7. Python-based pipeline for CSN data preparation

2.4.2 Processing Recorded Structural Response

Signal processing is important for ensuring the reliability and precision of structural response analyses, particularly when examining vertical motions. The vertical component of ground motion is generally richer in high-frequency content and therefore contains more noise than the horizontal components. This difference is illustrated in Figure 2.8, which shows the recorded motion from a sensor on the sixth floor of the JPL 183 building during the Searle Valley earthquake.

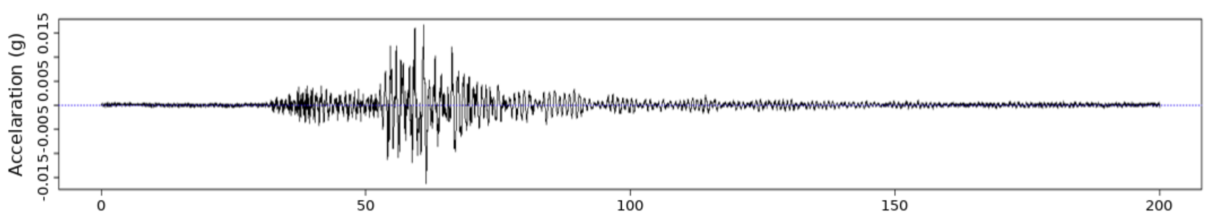

(a)

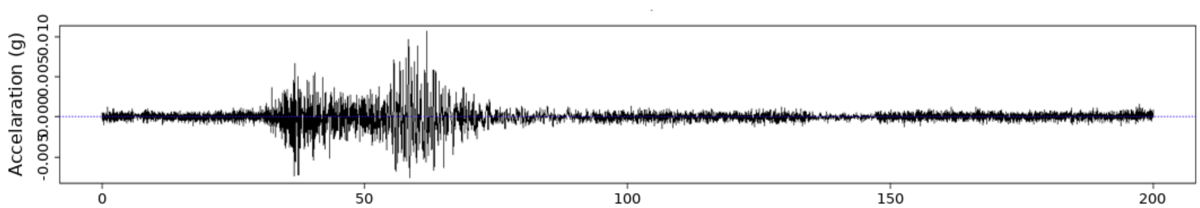

(b)

Figure 2.8. Recorded motion analysis for "Sensor-T000675" on the 6th floor of JPL 183 building during the Searle Valley earthquake for the a) horizontal and b) vertical directions

Acceleration data recorded by sensors inherently contain both low-frequency and high-frequency noises. This is the case for both ground motions and structural responses. Low-frequency noise in structures might result from broad, slow vibrations, whereas high-frequency noise can be introduced by small, rapid disturbances, such as footsteps or other minor impacts.

These vibrations can mask or distort the true structural response, making it challenging to isolate the actual behavior from the raw data. Therefore, an essential part of data processing is to apply filters that remove these unwanted frequencies at both ends of the spectrum while preserving the meaningful signal.

The filtering procedure involves two components: a low-pass filter and a high-pass filter. The low-pass filter (LPF) sets an upper corner frequency limit and removes most of the signals above that threshold, effectively removing high-frequency noise. Conversely, the high-pass filter (HPF) imposes a lower frequency cutoff to eliminate low-frequency noise. In other words, the LPF allows only the lower-frequency content of the signal to pass through the filter while blocking higher frequencies, and the HPF allows only the higher-frequency content to pass while blocking lower frequencies. Careful selection of these filter corner frequencies ensures that the retained portion of the signal covers the relevant frequency range needed for structural analysis (Boore, 2005; Douglas & Boore, 2011).

This study's processing methodology follows the NGA guidelines for strong-motion data (Ancheta et al., 2014; Goulet et al., 2021), which integrates effective processing techniques with well-established theoretical foundations.

The zero-padding technique is also applied to each time series to establish a common time frame across all sensors. Zero-padding involves adding zero-valued data points at the beginning and end of each record, ensuring that all sensor signals share the same start and end times. Aligning the records in this way guarantees consistency when comparing or combining their responses in the analysis (Goulet et al., 2021).

2.5 Data Set and Seismic Event Selection

As described in Section 2.4, a Python-based pipeline is utilized to retrieve and prepare building response data from the CSN. The CSN database provides online access to seismic events recorded between 2012 and 2025, encompassing over 90 earthquake records (*Community Seismic Network*). From this extensive dataset, a subset of 11 earthquakes is identified for detailed investigation. The selection focuses on events of at least moderate size and proximity, specifically, those with moment magnitude Mw > 3.0 and/or a site-to-source distance less than 30 km. This approach ensures that either the event's size or its proximity to the site would produce a meaningful response in the instrumented buildings. Recorded motions meeting these criteria are downloaded from the CSN repository. However, not every candidate event has usable recordings for the structures of interest. Sensors in the selected JPL buildings successfully recorded data for 6 of the 11 candidate events. For these six events, the raw acceleration time series is processed to remove noise and improve signal quality, following the methodology outlined in Section 2.4.2.

A consistency check is also performed across all six instrumented JPL buildings. To compare structural responses under the same ground shaking, we require that an earthquake be recorded by all six buildings with acceptable data quality. Applying this criterion reduced the set of usable events to four. In other words, some of the initially recorded events had to be excluded because at least one building did not capture the event, or the recorded signals were too noisy for the analysis of this structure. The final selection comprises four earthquakes that were commonly recorded across all six buildings and met the quality standards after processing. Table 2.2 summarizes the key characteristics of these four earthquakes.

Table 2.2. Characteristics of the Recorded Earthquakes

	Earthquake Name	Magnitude	Depth (km)	Epicentral Distance (Km)
1	El Monte	4.5	16.9	19.84
2	Pacoima	4.2	8.8	26.85
3	Searle Valley	6.4	10.7	178.16
4	Ridgecrest	7.1	8	182.27

Two of the selected ground motions (El Monte and Pacoima) are from moderate-magnitude events that occurred at relatively close distances (on the order of 20–30 km), whereas the other two events (the Searle Valley and Ridgecrest earthquakes in 2019) are large-magnitude earthquakes that occurred farther away (~180 km) but were still adequately recorded. By focusing on these four earthquakes, we ensure a consistent and comparable set of input ground motions for evaluating the dynamic response of the six JPL buildings in the subsequent analysis.

CHAPTER 3. Identification of Structural Frequencies via Data-Driven Methods

Identifying a building's modal frequencies from earthquake recordings requires a robust, data-driven framework that isolates repeatable structural vibration from event-specific input effects and measurement noise. In this chapter, triaxial acceleration response histories recorded at the base and multiple floors are transformed into the frequency domain to identify response peaks that persist across floors and earthquakes. Candidate modal frequencies are inferred by combining spectra (Fourier amplitude spectra and Welch power spectral density) with input–output measures (floor-to-base transfer and coherence functions), so that peaks are retained only when they exhibit both amplification relative to the reference level and strong coherence.

This chapter is organized as follows. Section 3.1 presents the identification framework and the signal-processing tools used to extract candidate frequencies. Sections 3.2 and 3.3 apply the framework to six instrumented JPL campus buildings, extracting vertical and horizontal frequencies, elevation-dependent amplification trends, and coherence-supported peak selection. Section 3.4 consolidates the results into the final set of candidate modal frequency bands for each building.

3.1 Identification framework

Acceleration time series from triaxial sensors (recorded at the base and various floor levels during seismic events) are analyzed to extract the structure's vertical vibration modes. The methodology integrates several complementary analyses: Fourier amplitude spectra (FAS) via the Fast Fourier Transform (FFT), power spectral density (PSD) estimation (using Welch's method), transfer function evaluation (floor response relative to the base input), and the coherence function, to identify candidate vertical frequencies. Each of these tools plays a specific role: the FAS and PSD reveal predominant frequency peaks in the signals, the transfer function highlights frequencies at which the building amplifies the input ground motion, and the coherence function verifies the consistency of input-output interaction at those frequencies. By combining these approaches, the framework distinguishes true structural frequencies from noise or site-specific effects. In general, system-identification methods may be grouped into parametric and non-parametric approaches. Parametric methods estimate modal properties by fitting an assumed mathematical model, such as an input–output model with specified parameters, to recorded motions, whereas non-parametric methods estimate frequency-domain relationships directly from the recorded data without imposing a specific structural model form (Stewart & Fenves, 1998). The present study follows a non-parametric, frequency-domain identification approach based on spectral amplitudes, power spectral densities, transfer functions, and coherence functions. In the recorded-data analyses of this section, the reference signal is the CSN Floor 1 record. Based on the CSN metadata interpretation adopted in this dissertation, Floor 1 corresponds to the ground-level record. Therefore, the terms "ground-level reference" and "Floor 1 reference" are used interchangeably in the data-driven transfer-function and coherence analyses.

3.1.1 Fourier Transform

The first step in characterizing the frequency content of a recorded acceleration signal is to transform it into the frequency domain using the Fourier transform. For continuous acceleration time series $x(t)$ of duration T_f, the Fourier transform is expressed as (Bozorgnia & Bertero, 2004; Bracewell, 1986):

$$F(\omega) = \int_0^{T_f} x(t)e^{-i\omega t}dt \qquad \text{Eq 3.1}$$

where $F(\omega)$ is the Fourier transform of $x(t)$, ω is the circular frequency (in radians per second), which is equal to $2\pi f$, T_f is the total signal duration, and $i = \sqrt{-1}$ is the imaginary unit. Using Euler's formula, the complex exponential kernel can be expanded as:

$$e^{-i\omega t} = cos(\omega t) - i. sin\,(\omega t) \qquad \text{Eq 3.2}$$

and by substituting the expression from Eq 3.2, Equation 3.1 can be reformulated as (Bozorgnia & Bertero, 2004):

$$F(\omega) = \int_0^{T_f} x(t)\,cos(\omega t)\,dt - i\int_0^{T_f} x(t) sin\,(\omega t)\,dt \qquad \text{Eq 3.3}$$

This can be reorganized as two separate integrals (Bozorgnia & Bertero, 2004):

$$F(\omega) = C(\omega) - i\,S(\omega) \qquad \text{Eq 3.4}$$

Where $C(\omega)$ and $S(\omega)$ represent the real and imaginary parts of the Fourier transform, respectively. From these, two fundamental spectra are obtained (Bozorgnia & Bertero, 2004; Clough & Penzien, 1993):

1. **Fourier Amplitude Spectrum (FAS)**: The FAS represents the magnitude of each frequency component present in the motion, essentially indicating how much each frequency contributes to the overall signal. It is defined as:

$$FAS(\omega) = \sqrt{C(\omega)^2 + S(\omega)^2} \qquad \text{Eq 3.5}$$

2. **Fourier Phase Spectrum**: The Fourier Phase Spectrum provides insights into the phase relationship between the cosine and sine components.

$$\Phi(\omega) = tan^{-1}(\frac{S(\omega)}{C(\omega)}) \qquad \text{Eq 3.6}$$

When dealing with a digitized recorded motion, the calculation of the Fourier spectrum is typically executed using the Discrete Fourier Transform (DFT) or the efficient FFT algorithm (Bozorgnia & Bertero, 2004; Brigham, 1988; Press et al., 1992). Further explanation of the distinctions between FFT and DFT, along with the reasoning behind the preference for FFT in this study, is provided in Appendix B.

Due to the discrete nature of recorded motions, there exists a constraint on the extraction of short- and long-period information. The highest frequency represented by the Fourier spectrum is the Nyquist frequency, $f_N = 1/(2\Delta t)$. In other words, the Nyquist period is the shortest period that can be accurately represented through sampling without introducing distortion (Bozorgnia & Bertero, 2004; Nyquist, 1924). Given the 0.02-second interval of digitization in CSN's acceleration record, the Fourier spectrum's minimum period is 0.04 seconds, and subsequently, the Nyquist frequency for CSN data is 25 Hz.

The FFT is applied to each vertical acceleration record to obtain its FAS using the NumPy library (Cooley & Tukey, 1965; Harris et al., 2020). Peaks in the FAS vs. frequency plot indicate the dominant frequency components of the building's response under the given earthquake excitation. In other words, a pronounced peak in the FAS signifies that the recorded motion contains a strong contribution at that frequency. These FAS-identified frequencies serve as initial candidates for the building's vertical natural frequencies. However, because earthquake signals can be noisy and non-stationary, further spectral analyses are employed to confirm and refine these candidates.

3.1.2 Power Spectral Density

FFT converts signals from the time domain to the frequency domain. However, challenges arise when dealing with inherently noisy signals, such as earthquake recordings. In such scenarios, the Power Spectral Density (PSD) emerges as an alternative method. The PSD offers an advantageous approach for extracting frequency content by analyzing the distribution of signal power across different frequency components. By emphasizing frequencies where the signal's power is high relative to the background noise, the PSD helps distinguish true structural frequencies from random noise fluctuations. In essence, broadband noise (which spans all frequencies) tends to average out, whereas persistent spectral peaks stand out more clearly in the PSD. This makes PSD estimation more resilient to noise interference, yielding more reliable frequency information for complex seismic acceleration data (Brigham, 1988; Mikami et al., 2008; Oppenheim et al., 1999).

Mathematically, the PSD $S_{xx}(\omega)$ of a signal $x(t)$ can be derived from its autocorrelation function via the Wiener–Khinchin theorem. The autocorrelation function $R_{xx}(\tau)$ measures how the signal correlates with a time-shifted version of itself. For an acceleration signal $x(t)$, it can be expressed as a function of time lag τ (Bendat & Piersol, 1993; Bendat & Piersol, 2011):

$$R_{XX}(\tau) = \lim_{T \to \infty} \int_0^T x(t)x(t+\tau)dt \quad \text{Eq 3.7}$$

where τ is the time delay. The PSD is then given by the Fourier transform of the autocorrelation (Bendat & Piersol, 1993):

$$S_{xx}(f) = \int_{-\infty}^{+\infty} R_{XX}(\tau)e^{-i\omega\tau}d\tau \quad \text{Eq 3.8}$$

In practice, PSD is estimated using averaging techniques to obtain a smooth spectrum. In this study, Welch's method (Welch, 1967), an improved averaged periodogram technique, is employed to compute the PSD of each acceleration record. Welch's method partitions the time series into overlapping segments, computing the FFT-based periodogram (power spectrum) for each segment, and then averaging these periodograms. This averaging results in a smoother and more stable PSD curve (For additional details, refer to Appendix C). We utilize the implementation of Welch's method via the "*matplotlib.mlab*" library in Python (Hunter, 2007) to analyze the vertical acceleration data.

The resulting PSD plots highlight the predominant frequency components of the signal: frequencies corresponding to prominent PSD peaks are those with the highest signal power and are interpreted as dominant frequencies of the building's vertical response. These peak frequencies, especially if they consistently appear across multiple earthquake events, are strong candidates for the structure's natural vertical modes.

3.1.3 Transfer Function Analysis

To confirm that a candidate frequency indeed corresponds to a structural vibration (and not merely a frequency present in the input motion), we next examine the transfer function between the building's base motion and its response at upper levels. A transfer function characterizes the relationship between the input and output of a linear system in the frequency domain, showing how the system amplifies or de-amplifies the input at each frequency. In the context of building seismic response, the floor-to-base transfer function $H(f)$ is defined as the ratio of the output motion (at a given floor) to the input motion (at the base) in the frequency domain. We can estimate this as the ratio of the cross-power spectral density between the floor and base signals to the auto-spectral density of the base signal (Bendat & Piersol, 1993):

$$H(f) = \frac{S_{xy}(f)}{S_{xx}(f)} \qquad \text{Eq 3.9}$$

where $x(t)$ is the vertical acceleration at the base level (input) and $y(t)$ is the vertical acceleration at an upper floor (output). Here, $S_{xx}(f)$ is the PSD of the base acceleration (as defined in Equation 3.8), and $S_{xy}(f)$ is the cross-PSD between the base and floor signals. The $S_{xy}(f)$ can be obtained from the cross-correlation function $R_{xy}(\tau)$ of the two signals, which are derived from the following equations (Bendat & Piersol, 1993):

$$R_{XY}(\tau) = \lim_{T\to\infty} \int_0^T x(t)y(t+\tau)dt \qquad \text{Eq 3.10}$$

$$S_{xy}(f) = \int_{-\infty}^{+\infty} R_{XY}(\tau)e^{-i\omega\tau}d\tau \qquad \text{Eq 3.11}$$

where $R_{XY}(\tau)$ represents the Cross-Correlation Function of signals at the Base and Upper Levels. The autocorrelation function ($R_{XX}(\tau)$) quantifies the similarity between a signal and its delayed version, while the Cross-Correlation Function ($R_{XY}(\tau)$) measures the degree of correspondence between two different signals.

By taking the ratio S_{xy}/S_{xx}, the transfer function normalizes the floor's response by the input spectrum. This normalization isolates the building's amplification characteristics: it highlights frequencies at which the structure responds strongly relative to the input, regardless of the specific spectral shape of the ground motion. A peak in $H(f)$ indicates that at frequency f, the floor motion is significantly larger than what the base input would suggest, implying a resonant amplification due to the structure's dynamics, so that we can confirm whether the frequency peaks observed in the FAS/PSD indeed correspond to the building's own resonant behavior or it is related to the input motion. Moreover, since spectral amplitudes and transfer-function ordinates can be sensitive to smoothing, in this study, Konno–Ohmachi smoothing with bandwidth parameter $b = 40$ was applied to the spectral estimates used for visual interpretation and peak identification (Konno & Ohmachi, 1998). This bandwidth was selected to reduce narrow-band fluctuations while preserving the main frequency-dependent features of the spectra. The same smoothing choice was used consistently for all records so that comparisons across floors, events, and buildings were not affected by record-specific smoothing decisions (Mikami et al., 2008; Stewart & Fenves, 1998).

3.1.4 Coherence Function

To statistically validate the consistency of the input-output relationship at the identified frequencies, we employ the coherence function. The coherence between two signals $x(t)$ and $y(t)$ (in our case, the base and floor vertical accelerations) is a frequency-dependent measure ranging from 0 to 1; where a coherence value of 1 at a particular frequency means the signals are perfectly linearly related at that frequency, whereas a value of 0 means there is no linear relationship at that frequency. Mathematically, coherence is defined as the normalized magnitude-squared cross-spectrum between the two signals (Bendat & Piersol, 1993; Bendat & Piersol, 2011).

$$\gamma^2{}_{xy}\,(f) = \frac{|S_{xy}(f)|^2}{S_{yy}(f).S_{xx}(f)} \qquad \text{Eq 3.12}$$

where $\gamma_{xy}\,(f)$ is the coherence between signals x and y at frequency f. The $S_{xy}(f)$ represents the cross-PSD between the two signals, while $S_{xx}(f)$ and $S_{yy}(f)$ denote their individual PSD at the frequency f (Equations 3.8 and 3.11).

Evaluating the coherence function $\gamma_{xy}(f)$ between the base and floor motions provides a statistical check for each candidate frequency. Thus, the coherence function serves as a critical validation metric to distinguish genuine building response frequencies. Throughout this section and Section 3.3, the "dominant frequency" is defined as the frequency corresponding to the maximum amplification observed in the transfer-function magnitude.

3.2 Vertical Frequency Results from Recordings

In this section, the identification framework developed in Section 3.1 is applied to earthquake recordings from four events to estimate the vertical natural frequencies of six instrumented buildings on the JPL campus (Buildings 180, 183, 238, 264, 321, and 303). Building characteristics, instrumentation layouts, and earthquake metadata are documented in Chapter 2. For each building, candidate frequency peaks are identified using a consistent set of complementary indicators: recurring spectral peaks in the frequency-domain measures (FAS/PSD), amplification in the floor-to-base transfer functions, and coherence between the reference level and upper floors.

The following subsections present the building-by-building vertical frequency identification results for the six case-study structures. For each building, paired plots of the vertical floor-to-base transfer function and the corresponding magnitude-squared coherence are provided.

To maintain clarity and comparability across the six buildings, the plots presented in this chapter focus on the El Monte event, with supporting plots for the other earthquakes reported in Appendix D.

3.2.1 Vertical Frequency Identification for Building JPL 183

JPL 183 is a nine-story building with no basement, instrumented with two vertical sensor lines: one along the east side and one along the west side of the building (one triaxial sensor per floor in each line, for a total of 18 sensors). This configuration provides redundancy for frequency identification: response features that appear at consistent frequencies across all lines (with acceptable coherence) are more likely to represent global building response, whereas features that occur inconsistently across lines are more likely attributable to local effects or measurement noise.

Following the identification framework described in Section 3.1, vertical transfer functions and coherence were computed separately for the east and west sides, using the Floor 1 sensor in the same line as the reference input. Peak frequencies were then selected for each floor, earthquake, and sensor line combination. The east- and west-vertical line peaks were paired and averaged (frequency and coherence) to obtain a single representative set of peak frequencies for each floor and event. This averaging approach reduces sensitivity to plan-wise differences and yields a building-level estimate of vertical frequencies.

Figure 3.1 presents the vertical transfer function and corresponding magnitude-squared coherence for JPL 183 during the El Monte earthquake. The vertical dashed red line denotes the lower usable frequency; frequency content below this boundary is not interpreted because it is more strongly affected by limited low-frequency excitation and increased sensor-noise contamination. Above this cutoff, the amplification peaks occur at nearly the same frequencies across all floors. The usable bandwidth for all earthquakes is determined through the signal-processing procedures described in Chapter 2.

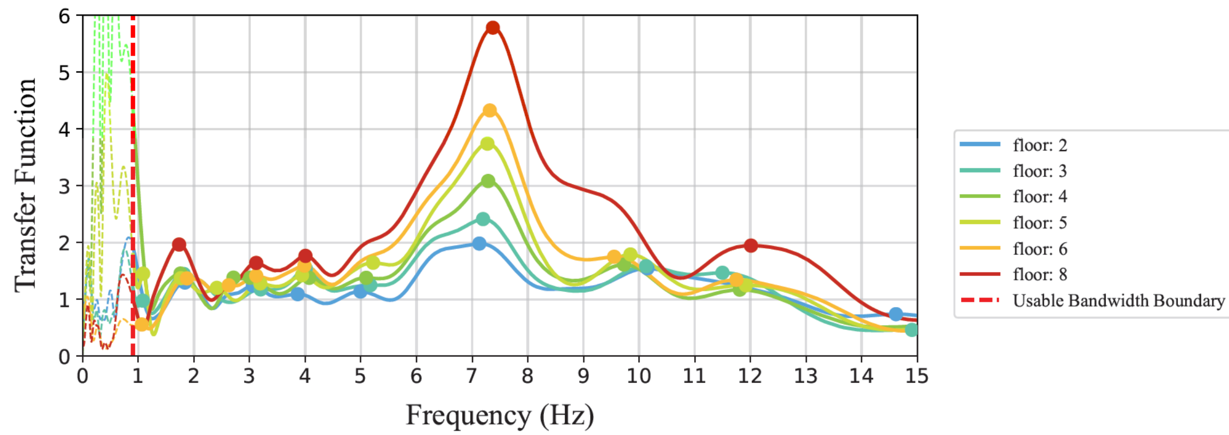

(a)

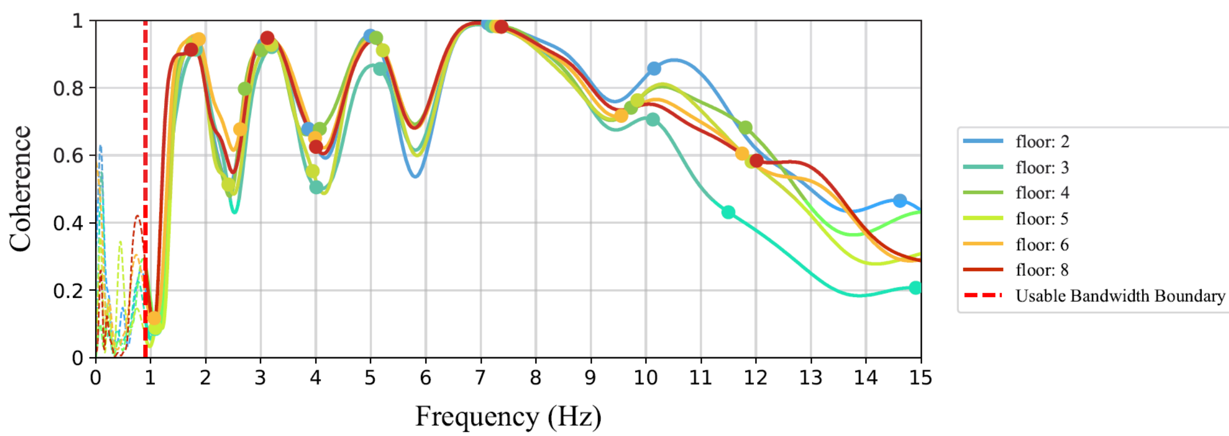

(b)

Figure 3.1. a) Vertical floor-to-base transfer function and b) magnitude-squared coherence for JPL 183 during the El Monte earthquake. The dashed red line marks the lower usable bandwidth

As shown in Figure 3.1a, the transfer functions exhibit multiple distinct peaks within the usable band. The most significant and clearly defined amplification occurs in the ~7–8 Hz range, where the upper floors show pronounced amplification relative to the base. In the corresponding coherence curves (Figure 3.1b), the same band is associated with high coherence (often approaching unity), indicating a strong, consistent linear relationship between the base input and the floor response at these frequencies. In addition to this dominant band, recurring peaks are observed in the ~1.6–2 Hz, ~2.9–3.3, ~4–4.5 Hz, and ~5–6 Hz ranges. These lower-to-moderate-frequency peaks generally coincide with moderate-to-high coherence in the El Monte record, supporting an interpretation as building-governed response components rather than incidental peaks in the input spectrum.

Two systematic response characteristics are also evident. First, amplification generally increases with elevation, most notably near the dominant frequency ~7–8 Hz peak. This height-dependent growth is consistent with a predominantly global, near-in-phase vertical response, in which floor motions remain synchronized while relative response amplitudes increase toward the upper stories. Second, coherence tends to decrease at higher frequencies (~10–12 Hz), and any high-frequency peaks in this range are therefore treated more cautiously unless they are repeatable across events and floors and maintain sufficiently high coherence.

The El Monte results suggest a set of candidate vertical frequencies; however, distinguishing true structural modes from event-specific or noise-related peaks requires comparison across multiple earthquakes. To assess event-to-event repeatability and isolate the most persistent response features, peak frequencies were extracted for each seismic event and summarized by averaging across the instrumented floors. Table 3.1 reports the resulting floor-averaged peak frequencies and corresponding coherence values (mean ± standard deviation across floors) for the four earthquakes considered in this study.

Table 3.1. Floor-Averaged Vertical Peak Frequencies and Coherence by Event for JPL 183

	Frequency /Coherence	Peak 1	Peak 2	Peak 3	Peak 4	Peak 5
El Monte	$f \pm \sigma\ (Hz)$	1.66±0.13	3.11±0.07	4.00±0.12	5.21±0.08	7.21±0.41
	$\gamma^2\ \pm \sigma$	0.89±0.06	0.94±0.02	0.80±0.10	0.95±0.02	0.99±0.01
Pacoima	$f \pm \sigma\ (Hz)$	1.88±0.08	3.26±0.13	4.27±0.07	5.52±0.13	7.59±0.18
	$\gamma^2\ \pm \sigma$	0.52±0.10	0.72±0.11	0.55±0.04	0.73±0.10	0.76±0.10
Ridgecrest	$f \pm \sigma\ (Hz)$	1.72±0.11	3.31±0.04	4.06±0.11	5.86±0.62	8.15±0.22
	$\gamma^2\ \pm \sigma$	0.88±0.05	0.99±0.00	0.97±0.01	0.95±0.01	0.88±0.06
Searle Valley	$f \pm \sigma\ (Hz)$	1.61±0.13	3.35±0.10	4.24±0.14	6.38±0.1	8.04±0.1
	$\gamma^2\ \pm \sigma$	0.92±0.03	0.95±0.02	0.89±0.04	0.78±0.08	0.77±0.09

Several observations follow from Table 3.1 and the underlying floor-level peaks:

- **~1.6–1.9 Hz (low-frequency range):** This peak range appears in all four events with relatively small floor-to-floor scatter. Coherence is high in El Monte, Ridgecrest, and Searle Valley, but noticeably lower in Pacoima. Because this band lies closer to the lower usable bandwidth than the higher peaks, its strength and coherence can be more sensitive to record-specific low-frequency energy and signal-to-noise conditions. It is therefore considered a plausible low-frequency vertical response component but interpreted with appropriate caution when coherence drops.

- **~3.1–3.4 Hz (moderate-frequency range):** A clear and repeatable peak near ~3 Hz is observed in most events, typically with very high coherence. Pacoima again exhibits reduced coherence, but the peak remains identifiable and stable in frequency. The combination of persistence and strong coherence in the larger events supports that this band can be considered as a candidate for the vertical response frequency.

- **~4.0–4.4 Hz (moderate-frequency range):** This frequency range is highly repeatable across events and floors, with particularly strong coherence in Ridgecrest and generally moderate-to-high coherence in El Monte and Searle Valley. Pacoima again shows reduced coherence in this band; however, the peak frequency remains stable, suggesting the feature is still structurally relevant even if the input–output consistency is weaker for that record.

- **~5.4–5.6 Hz (moderate-frequency range):** This feature is also repeatable across the dataset and is strongly supported by high coherence in El Monte and Ridgecrest. The larger inter-floor scatter reported for El Monte reflects that, on some upper floors, nearby peaks (especially the dominant ~7–8 Hz resonance) can overshadow or partially merge with the ~5–6 Hz feature, complicating peak separation in that event.

- **~7.0–7.6 Hz (dominant vertical-response range):** This is the most prominent and dominant peak range in the transfer functions, most clearly expressed in the El Monte record, where both amplification and coherence are very high. The band is detected in all events and shows the strongest height-dependent amplification, supporting interpretation as the dominant vertical natural frequency range of JPL 183.

In contrast, higher-frequency peaks (e.g., near 9–12 Hz and above) were observed only occasionally across the full event–floor dataset and, when present, were often accompanied by more variable or reduced coherence; therefore, these features are treated as secondary/conditional rather than primary vertical-mode candidates.

Overall, after evaluating the transfer-function amplifications, coherence, and repeatability across floors and earthquakes, JPL 183 is found to exhibit a stable set of candidate vertical response frequencies clustered around ~1.7 Hz, ~3.3 Hz, ~4.2 Hz, ~5.5 Hz, and ~7.2 Hz. Among these, the ~7–8 Hz range is identified as the dominant vertical frequency band of the building based on its consistently largest amplification and strong coherence in the best-excited records

3.2.2 Vertical Frequency Identification for Building JPL 180

Building JPL 180 is a nine-story structure with one basement level. For vertical-frequency identification, Floor 1 is used as the reference level for all earthquakes. JPL 180 is instrumented with three vertical sensor lines (east, middle, and west), with one triaxial accelerometer per floor in each line (27 floor sensors total), plus one additional sensor in the basement. The vertical frequency identification follows the same data-driven framework described in Section 3.1 and the same multi-line consistency/averaging strategy used for JPL 183 in Section 3.2.1. Figure 3.2 presents the vertical transfer function and the corresponding coherence for JPL 180 during the El Monte earthquake.

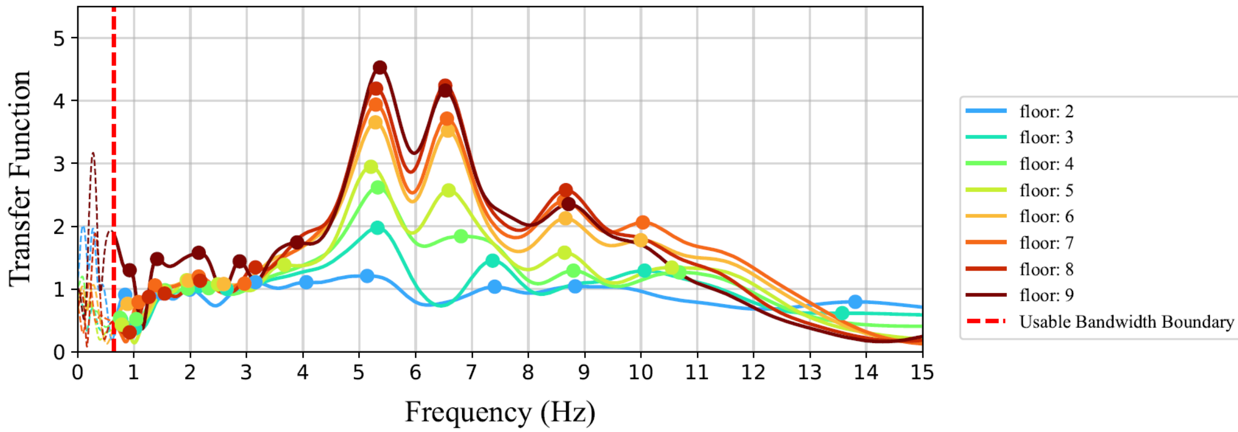

(a)

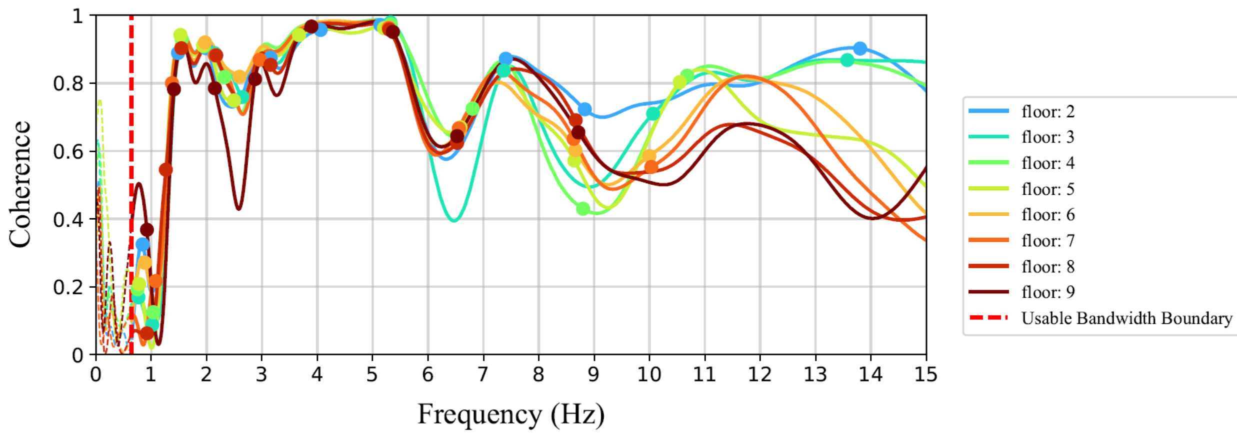

(b)

Figure 3.2. a) Vertical floor-to-base transfer function and b) magnitude-squared coherence for JPL 180 during the El Monte earthquake. The dashed red line marks the lower usable bandwidth

As shown in Figure 3.2a, the transfer functions exhibit several distinct amplification peaks within the usable band. The strongest and most repeatable amplification occurs in the ~5–7 Hz range, where transfer-function amplitudes increase systematically with elevation. This height-dependent growth is consistent with a predominantly global vertical response component.

Additional peaks are evident in the ~8–10 Hz range, where the transfer function shows moderate-to-strong amplification across multiple floors. A higher-frequency feature is also occasionally visible near the upper end of the plotted range (~13–15 Hz), but its strength and reliability depend on the event and floor. The corresponding coherence functions (Figure 3.2b) provide an important validation check: coherence is generally high through the dominant response bands (often ≳0.8 over the principal peaks). Coherence becomes more variable and tends to decrease toward higher frequencies (particularly beyond ~10–12 Hz).

To distinguish persistent structural response features from record-specific artifacts, peak frequencies were extracted for each event (after averaging across the three sensor lines) and then summarized by averaging across Floors 2–9. Table 3.2 reports the resulting floor-averaged peak frequencies and coherence for the four earthquakes.

Table 3.2. Floor-Averaged Vertical Peak Frequencies and Coherence by Event for JPL 180

	Frequency /Coherence	**Peak 1**	**Peak 2**	**Peak 3**	**Peak 4**	**Peak 5**
El Monte	$f \pm \sigma\ (Hz)$	5.27 ± 0.12	6.75 ± 0.21	8.65 ± 0.10	10.24 ± 0.33	15.31 ± 0.71
	$\gamma^2\ \pm \sigma$	0.96 ± 0.04	0.81 ± 0.07	0.62 ± 0.11	0.85 ± 0.11	0.80 ± 0.11
Pacoima	$f \pm \sigma\ (Hz)$	5.48 ± 0.10	6.18 ± 0.10	8.21 ± 0.08	10.48 ± 0.52	15.56 ± 0.78
	$\gamma^2\ \pm \sigma$	0.93 ± 0.02	0.89 ± 0.00	0.90 ± 0.06	0.90 ± 0.04	0.75 ± 0.08
Ridgecrest	$f \pm \sigma\ (Hz)$	5.49 ± 0.04	7.55 ± 0.15	8.32 ± 0.12	9.37 ± 0.13	13.86 ± 0.70
	$\gamma^2\ \pm \sigma$	0.91 ± 0.02	0.77 ± 0.08	0.62 ± 0.19	0.72 ± 0.05	0.26 ± 0.07
Searle Valley	$f \pm \sigma\ (Hz)$	5.42 ± 0.11	7.43 ± 0.60		9.52 ± 0.19	13.57 ± 0.19
	$\gamma^2\ \pm \sigma$	0.86 ± 0.04	0.70 ± 0.04		0.59 ± 0.07	0.25 ± 0.12

Several consistent observations follow from Table 3.2 and the underlying floor-level peaks:

- **~5.3–5.6 Hz (Dominant vertical-response range):** This band is present in all four events and consistently high coherence (event-averaged $\gamma^2 \approx 0.86$–0.96). It is also one of the most significant amplification features in the El Monte transfer functions and shows clear elevation-dependent growth. Collectively, these observations support interpreting the ~5.4 Hz band as a robust, building-governed vertical response frequency range.
- **~6.1–7.9 Hz (secondary range adjacent to the dominant 5–8 Hz region):** A second repeatable range is observed in the ~6–8 Hz neighborhood, but with appreciable event-to-event variability (overall mean 7.13 ± 0.59 Hz). In El Monte and parts of Pacoima, this range tends to appear closer to ~6.2–6.8 Hz, whereas Ridgecrest and Searle Valley emphasize a higher cluster near ~7.4–7.9 Hz. Coherence remains moderate-to-high overall ($\gamma^2 = 0.77 \pm 0.08$), indicating a structurally relevant feature, but the broader scatter suggests sensitivity to excitation characteristics and/or peak-separation effects between closely spaced resonances in the 5–8 Hz region.
- **~8.1–8.9 Hz (mid–high-frequency range; conditionally observed):** A peak range in the ~8–9 Hz band is repeatedly detected in El Monte, Pacoima, and (less consistently) Ridgecrest, with moderate-to-high coherence ($\gamma^2 = 0.73 \pm 0.18$). The band is not recovered in Searle Valley in the summarized peak set, indicating that its observability is more event-dependent than the ~5.4 Hz range.
- **~9.0–11.5 Hz (repeatable mid–high-frequency range, with event-dependent center frequency):** A higher-frequency range is consistently identified near ~9–11 Hz (overall mean 9.88 ± 0.56 Hz), with coherence that is moderate on average ($\gamma^2 = 0.76 \pm 0.14$).

- **~13–15 Hz (high-frequency range; conditional/secondary):** A high-frequency peak is identified in multiple events, but its coherence is strongly inconsistent across the dataset. El Monte and Pacoima show comparatively high coherence at this peak ($\gamma^2 \approx$ 0.75–0.80 on average), while Ridgecrest and Searle Valley show low coherence ($\gamma^2 \approx$ 0.25–0.26 on average). Given the reduced and highly variable coherence, this band is treated as a secondary/conditional feature (i.e., not a primary vertical-mode candidate) unless additional records beyond the current dataset demonstrate repeatability with consistently strong coherence.

Averaged across all events, floors, and sensor-line locations, the representative peak centers are approximately 5.4 Hz, 7.1 Hz, 8.4 Hz, 9.9 Hz, and 14.4 Hz, with the ~5.4 Hz range identified as the dominant vertical frequency band of JPL 180 based on its persistence, consistently high coherence, and strong amplification growth with elevation.

3.2.3 Vertical Frequency Identification for Building JPL 238

JPL 238 is an eight-story building with no basement, instrumented with one sensor on each floor. For the vertical transfer-function analysis, Floor 1 is used as the reference level for the El Monte and Pacoima events, while Floor 2 is used as the reference for Ridgecrest and Searle Valley. Figure 3.3 presents the floor-to-base transfer function and corresponding coherence for all instrumented floors of JPL 238 during the El Monte earthquake.

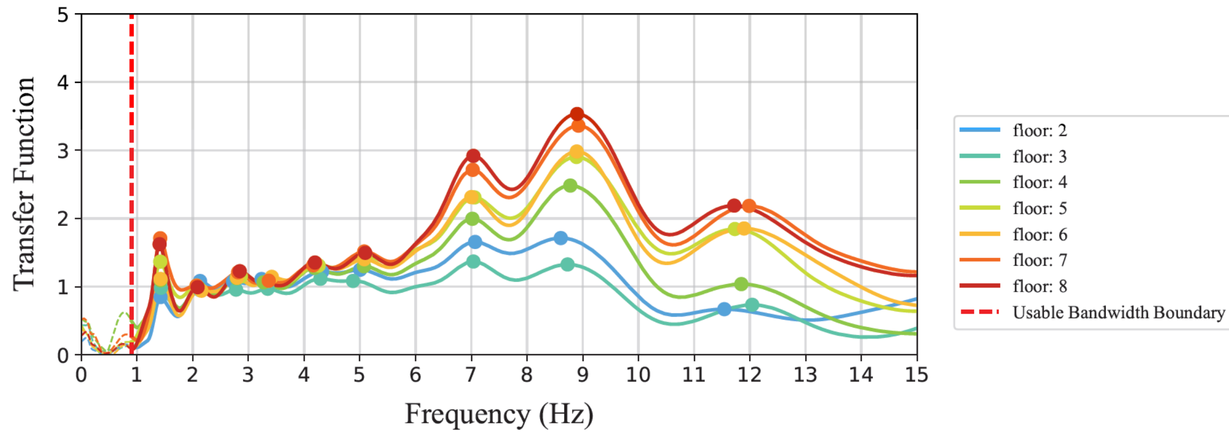

(a)

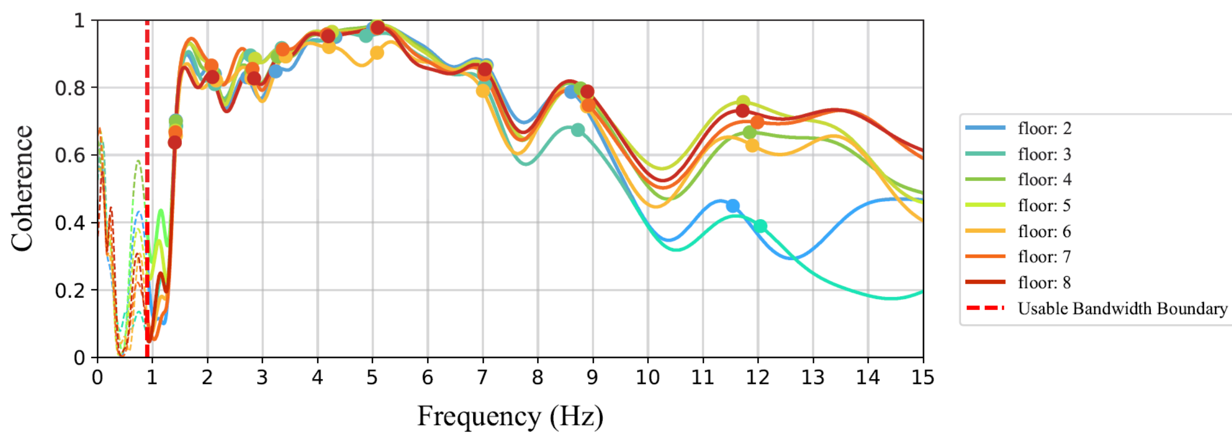

(b)

Figure 3.3. a) Vertical floor-to-base transfer function and b) magnitude-squared coherence for JPL 238 during the El Monte earthquake. The dashed red line marks the lower usable bandwidth

As shown in Figure 3.3a, the vertical floor-to-base transfer functions exhibit multiple well-defined amplification peaks within the 1–15 Hz band, indicating several candidate vertical-response frequencies. The corresponding coherence functions (Figure 3.3b) show that these peaks generally coincide with moderate-to-high coherence (typically $\gamma_{xy}^2 \gtrsim 0.8$, and often higher over the dominant bands), indicating that the floor responses are strongly and consistently related to the base input at those frequencies. Moreover, resonance amplitudes increase with elevation, most notably on the upper floors (e.g., Floor 8), while lower floors exhibit reduced amplification. This systematic increase with height is consistent with a predominantly global, in-phase vertical response.

Several resonance features are evident in the El Monte spectra for this building. A low-frequency feature near $f \approx 1.4$–1.5 Hz is visible; however, it is only modestly amplified and is accompanied by moderate coherence (approximately $\gamma_{xy}^2 \sim 0.60$–0.70). Importantly, this peak is not persistent across the full dataset for JPL 238 (≈28–30% occurrence across all event–floor recordings); it might have been caused by the influence of lower-bound filtering/usable-bandwidth limitations in other records. Additional peaks are present in the 2–3 Hz range, but their amplification is comparatively smaller. In contrast, the most pronounced resonant features occur near $f \approx 7$ Hz and $f \approx 8.5$–9 Hz, where amplification is strong across all floors (especially the upper floors), and coherence remains relatively high, supporting interpretation as well-defined vertical response frequencies for this event. A broader high-frequency feature is also evident around $f \approx 10$–12 Hz; While it appears consistently in the transfer functions, the coherence in this band is generally lower and more variable, particularly for the lower floors, so it is treated with greater caution. Minor peaks around $f \approx 4$–5 Hz are also present and show comparatively strong coherence in this record.

To robustly identify JPL 238's vertical modes, the spectral peaks were extracted for each earthquake and cross-verified among all instrumented floors. Table 3.3 summarizes the floor-averaged peak frequencies and their mean coherence for each event (with the inter-floor standard deviation noted for frequency and coherence). For each earthquake, the same set of prominent frequencies emerges, within a narrow variation range, underscoring the consistency of the building's vertical dynamic properties.

Table 3.3. Floor-Averaged Vertical Peak Frequencies and Coherence by Event for JPL 238

	Frequency /Coherence	Peak 1	Peak 2	Peak 3	Peak 4	Peak 5	Peak 6	Peak 7
El Monte	$f \pm \sigma\ (Hz)$	2.11±0.03	2.80±0.04	4.23±0.05	5.04±0.07	7.04±0.02	8.82±0.11	11.82±0.16
	$\gamma^2\ \pm \sigma$	0.85±0.02	0.88±0.02	0.94±0.02	0.97±0.03	0.92±0.02	0.78±0.06	0.62±0.14
Pacoima	$f \pm \sigma\ (Hz)$			4.12±0.05	5.51±0.14	7.52±0.06	9.33±0.13	
	$\gamma^2\ \pm \sigma$			0.80±0.03	0.85±0.01	0.93±0.02	0.90±0.03	
Ridgecrest	$f \pm \sigma\ (Hz)$	2.12±0.03	2.94±0.07	4.06±0.11	5.86±0.62	8.15±0.22	9.85±0.05	
	$\gamma^2\ \pm \sigma$	0.97±0.01	0.94±0.00	0.96±0.01	0.92±0.03	0.82±0.00	0.54±0.02	
Searle Valley	$f \pm \sigma\ (Hz)$	2.22±0.02		4.24±0.14	6.38±0.1	8.04±0.1		
	$\gamma^2\ \pm \sigma$	0.98±0.00		0.94±0.01	0.93±0.01	0.85±0.03		

As summarized in Table 3.3, the floor-averaged peaks (reported as $f \pm \sigma$across floors, with corresponding $\gamma^2 \pm \sigma$) cluster into a small number of recurring frequency ranges. The most consistent bands are:

- **~2–3 Hz (low-frequency range):** The very small inter-floor scatter and high coherence in Ridgecrest and Searle Valley indicate a stable, building-governed response feature; its absence in Pacoima likely reflects record-dependent bandwidth/energy limitations rather than a change in structural properties. However, it is noteworthy that these peaks exhibit very low amplitudes across all events and should therefore be interpreted with caution.

- **~4–6.5 Hz (moderate-frequency range):** A peak in this range is present in all four earthquakes. Coherence remains consistently high, but the larger frequency scatter in Ridgecrest ($\sigma = 0.62$ Hz) and the event-to-event shift in the mean frequency suggest this feature behaves as a broader response band that is more sensitive to excitation characteristics and measurement variability than the other peaks.
- **~7.0–8.2 Hz (mid-high-frequency range):** This response range appears in every event, though with an event-dependent center frequency. The repeated detection across events indicates a consistent structural contribution, while the upward shift in Ridgecrest/Searle Valley suggests this range may be more sensitive to record-specific bandwidth and excitation.
- **~9–10 Hz (the dominant vertical range):** A peak in this band is identified in El Monte (8.82 ± 0.11 Hz, $\gamma^2 = 0.78 \pm 0.06$), Pacoima (9.33 ± 0.13 Hz, $\gamma^2 = 0.90 \pm 0.03$), and Ridgecrest (9.85 ± 0.05 Hz, $\gamma^2 = 0.54 \pm 0.02$), but it is not observed in Searle Valley. Although the transfer functions exhibit recognizable amplification when present, coherence is more variable (dropping to moderate levels in Ridgecrest), indicating that we should exercise greater caution in this band.

Finally, Table 3.3 shows a higher-frequency peak near 11.82 ± 0.16 Hz in El Monte with lower coherence (0.62 ± 0.14); because it is not reproduced in the other events summarized in the table and exhibits reduced coherence, it is best interpreted as a secondary feature rather than a primary vertical-mode candidate.

3.2.4 Vertical Frequency Identification for Building JPL 264

JPL 264 is an eight-story building with no basement, instrumented with one sensor per floor. The first floor is treated as the reference for vertical motion. Figure 3.4 presents the floor-to-base vertical transfer function (amplitude spectrum) and corresponding coherence for all instrumented floors of JPL 264 during the El Monte earthquake.

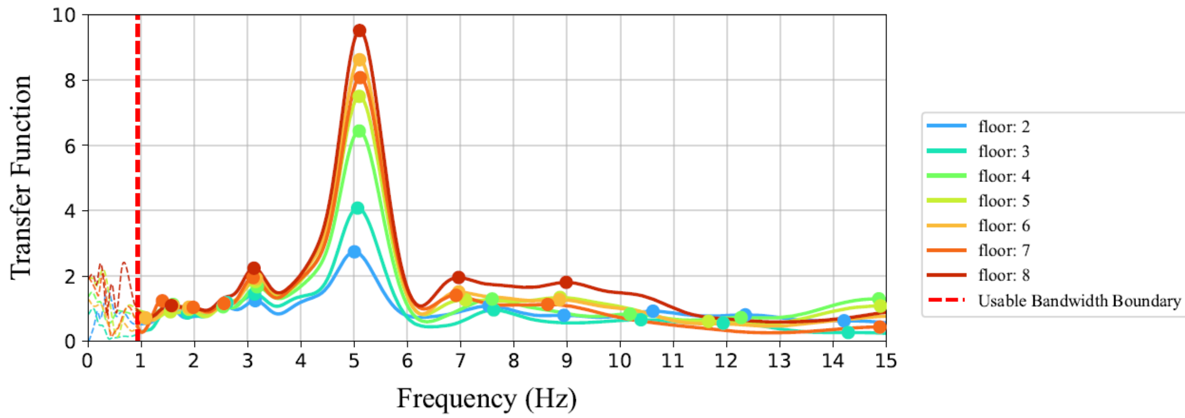

(a)

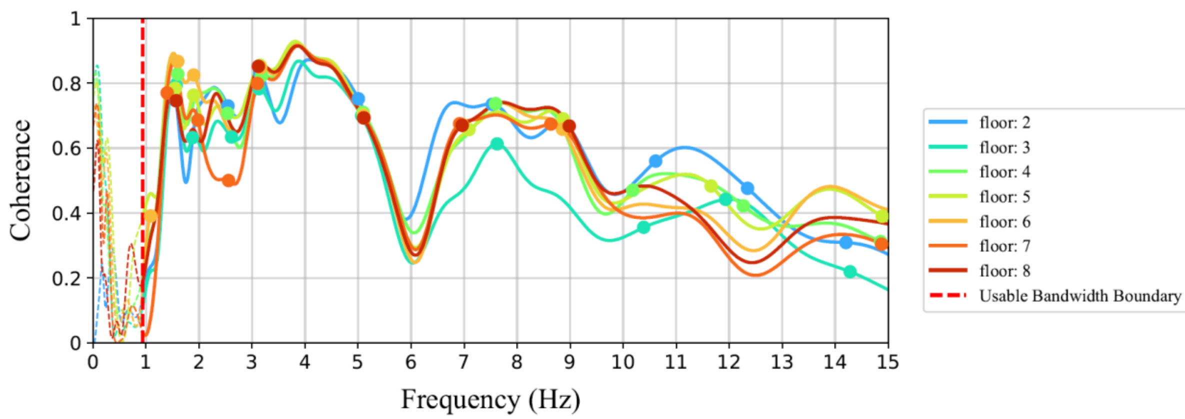

(b)

Figure 3.4. a) Vertical floor-to-base transfer function and b) magnitude-squared coherence for JPL 264 during the El Monte earthquake. The dashed red line marks the lower usable bandwidth

As shown in Figure 3.4a, several distinct resonant features are apparent in the El Monte spectra for JPL 264. A low-frequency peak appears around $f \approx 1.6$–2 Hz, although it is only modestly amplified. Slightly higher in frequency, additional small peaks can be observed in the 2–3 Hz range (e.g., near 2.5–3.1 Hz), but their amplification in the transfer function is comparatively minor. In contrast, more pronounced resonant peaks occur at $f \approx 5.1$ Hz and in the $f \approx 7$–9 Hz band. The ~5 Hz peak is clearly visible across all floors (with a pronounced increase in transfer function amplitude) and exhibits consistently high coherence, indicating that it is a significant contributor to the vertical response. The most prominent features of this event lie in the mid-to-high-frequency range around 7–9 Hz: for example, a strong peak emerges near 7.5 Hz and another near 9 Hz. A broader high-frequency feature is also evident around $f \approx 10$–12 Hz. While this high-frequency band appears as a weak peak in the transfer functions of several floors, the coherence in this range is generally lower and more variable (especially for the lower floors), so it must be treated with caution. As with JPL 238, any peak identified near this upper frequency band is scrutinized to ensure it is not an artifact of noise or input spectra.

To robustly identify JPL 264's vertical modal frequencies, the spectral peaks were systematically extracted from each earthquake record and cross-verified across all instrumented floors. Table 3.4 summarizes the floor-averaged peak frequencies and their mean coherence values for each of the four events (mean ± standard deviation across floors).

Table 3.4. Floor-Averaged Vertical Peak Frequencies and Coherence by Event for JPL 264

	Frequency /Coherence	Peak 1	Peak 2	Peak 3	Peak 4	Peak 5	Peak 6
El Monte	$f \pm \sigma\ (Hz)$	1.68±0.17	2.56±0.03	3.14±0.02	5.09±0.04	7.24±0.3	10.71±0.57
	$\gamma^2\ \pm \sigma$	0.79±0.05	0.66±0.09	0.88±0.02	0.70±0.02	0.77±0.12	0.54±0.12
Pacoima	$f \pm \sigma\ (Hz)$	1.98±0.1	2.23±0.00	3.14±0.05	5.07±0.05	7.71±0.54	10.08±0.27
	$\gamma^2\ \pm \sigma$	0.74±0.06	0.83±0.00	0.80±0.04	0.93±0.02	0.83±0.02	0.94±0.01
Ridgecrest	$f \pm \sigma\ (Hz)$	1.87±0.15	2.69±0.00	2.96±0.00	4.97±0.08	7.84±0.4	
	$\gamma^2\ \pm \sigma$	0.99±0.00	0.95±0.00	0.97±0.00	0.90±0.04	0.44±0.14	
Searle Valley	$f \pm \sigma\ (Hz)$	1.69±0.05	2.55±0.03	3.24±0.03	5.07±0.08		
	$\gamma^2\ \pm \sigma$	0.98±0.01	0.90±0.03	0.95±0.01	0.83±0.02		

Despite some record-to-record and event-to-event variability, a consistent set of prominent frequencies emerges for JPL 264, with only narrow variation around their mean values. In other words, the building exhibits a stable vertical frequency signature that is largely repeatable across different earthquakes. The most recurrent frequency bands, inferred from Table 3.4 and the full suite of recordings, can be grouped as follows:

- **~1.6–2.7 Hz (low-frequency range):** One or two low-frequency peaks in this range appear in almost all the recordings. In the larger events, these frequencies show high coherence (in some cases $\gamma^2 \approx 0.98$), indicating a genuine structural response component. However, their amplification levels are generally low, and in a few records, they can be obscured by noise or filtering limits. Thus, while this band likely contains the building's fundamental vertical mode, the response at these frequencies is subtle, and careful interpretation is required (particularly for events with limited energy below ~2 Hz).

- **~3–5 Hz (moderate-frequency range):** A distinct response feature in the 3 to 5 Hz range is observed in all events. The peak frequency within this band tends to cluster around 5.0 Hz and 3.0 Hz. Coherence values for this band remain high throughout (often 0.8–0.9 or above), underscoring that it is a reliable structural characteristic rather than an incidental noise peak.
- **~7–8 Hz (mid-high frequency range):** This frequency range is evident in most of the earthquake records for JPL 264. Across the dataset, peaks in the upper-7 to low-8 Hz range are identified repeatedly (average ~7.6 Hz), albeit with slight event-to-event shifts. The coherence associated with these peaks is generally very high. The absence or weakening of the ~7–8 Hz features in the Searle Valley record (which lacked significant content above ~6 Hz) likely reflects the limitations of that particular input rather than any change in the building's properties.
- **~9–10 Hz (high-frequency range):** A high-frequency resonant peak around 9–10 Hz was excited in the Pacoima and El Monte events. This mode is not observed universally across all records; it is largely absent in more distant events (due to their usable bandwidth).

Finally, in one instance (the El Monte earthquake), a small peak was detected around $f \approx$ 14–15 Hz in the floors' spectra; however, this high-frequency feature was accompanied by low coherence ($\gamma^2 < 0.4$ on most floors) and did not recur in the other events. Therefore, it is regarded as a secondary artifact rather than a fundamental vertical mode of the building. Applying the combined criteria of peak recurrence, transfer-function amplification, and high coherence, the analysis of JPL 264 identifies a set of candidate vertical natural frequencies at approximately 1.8, 2.5, 3.2, 5.1, 7.6, and 10.3 Hz, with the 5.1 Hz mode emerging as the dominant vertical frequency.

3.2.5 Vertical Frequency Identification for Building JPL 321

JPL 321 is a six-story structure with a single basement level. One vertical accelerometer is installed per floor. For all earthquake records except one, the first floor is used as the reference level in computing transfer functions. In the case of the Pacoima event, data from the Floor 1 sensor is unavailable, so Floor 2 is used as the reference level for that event. Figure 3.5 shows the vertical transfer function amplitudes and corresponding coherence for floors above the base in the El Monte event.

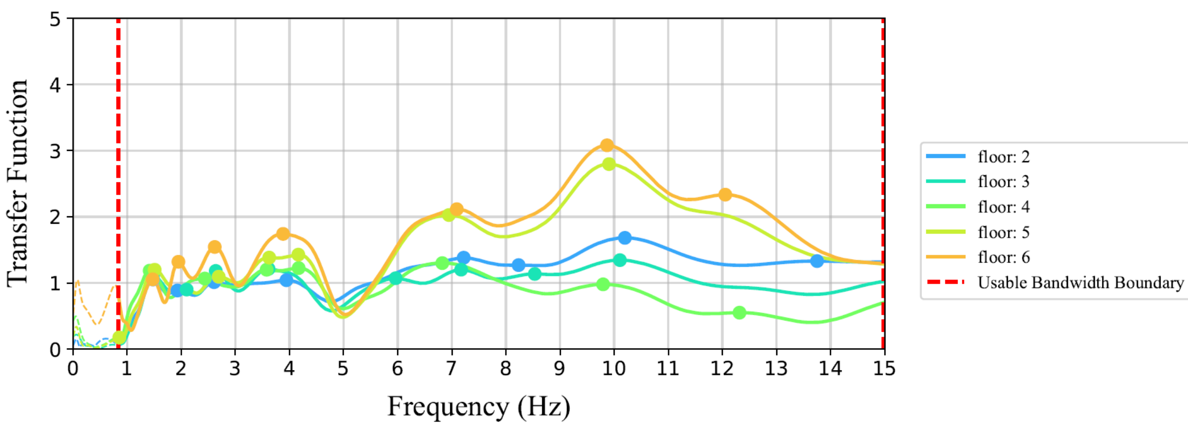

(a)

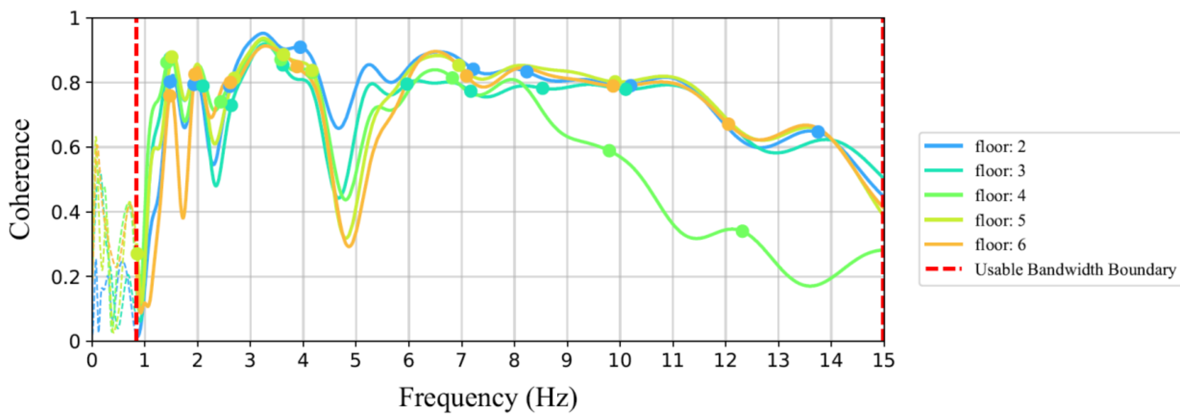

(b)

Figure 3.5. a) Vertical floor-to-base transfer function and b) magnitude-squared coherence for JPL 321 during the El Monte earthquake. The dashed red line marks the lower usable bandwidth

As shown in Figure 3.5a, the transfer functions for the instrumented floors exhibit several clear amplification peaks within the usable frequency band (≈1–15 Hz). The corresponding coherence curves in Figure 3.5b generally show high values over the principal peaks (typically $\gamma_{xy}^2 \gtrsim 0.8$), indicating that the observed resonant features primarily reflect a consistent input–output relationship between the reference level and upper floors.

For the El Monte event, the most persistent amplification features occur near ~1.4 Hz, ~2.0 Hz, ~2.6 Hz, ~4.0 Hz, ~7.1 Hz, ~10.0 Hz, and ~12.5 Hz, consistent across floors. The strongest amplification in Figure 3.5a is observed in the upper levels (e.g., Floors 5–6), particularly in the higher-frequency bands (~10 Hz and above), whereas lower floors generally exhibit reduced amplification. This elevation-dependent increase in response is consistent with a predominantly global vertical mode shape, in which relative motion tends to grow with height.

To assess repeatability beyond a single record, peak frequencies were extracted from each event and summarized in Table 3.5 by averaging across the available floors in JPL 321 (with the inter-floor standard deviation reported for both frequency and coherence).

Table 3.5. Floor-Averaged Vertical Peak Frequencies and Coherence by Event for JPL 321

	Frequency /Coherence	**Peak 1**	**Peak 2**	**Peak 3**	**Peak 4**	**Peak 5**	**Peak 6**	**Peak 7**
El Monte	$f \pm \sigma\ (Hz)$	1.47±0.03	1.99±0.08	2.6±0.08	4.04±0.13	7.05±0.15	9.98±0.15	12.51±0.54
	$\gamma^2 \pm \sigma$	0.84±0.04	0.84±0.02	0.78±0.03	0.88±0.02	0.85±0.04	0.65±0.15	0.59±0.08
Pacoima	$f \pm \sigma\ (Hz)$		2.09±0.00	2.87±0.13	4.28±0.06	7.61±0.17	9.18±0.13	12.03±0.11
	$\gamma^2 \pm \sigma$		0.91±0.00	0.86±0.05	0.83±0.06	0.96±0.02	0.98±0.01	0.94±0.02
Ridgecrest	$f \pm \sigma\ (Hz)$	1.11±0.10	1.77±0.11	2.59±0.12	4.19±0.04	6.74±0.57	8.86±0.00	12.25±0.00
	$\gamma^2 \pm \sigma$	0.97±0.01	0.99±0.01	0.97±0.01	0.97±0.01	0.88±0.02	0.75±0.00	0.58±0.00
Searle Valley	$f \pm \sigma\ (Hz)$	1.29±0.00	1.92±0.05	2.61±0.09	4.5±0.05	5.87±0.05	8.83±0.10	
	$\gamma^2 \pm \sigma$	0.86±0.03	0.98±0.00	0.96±0.00	0.88±0.03	0.69±0.08	0.66±0.06	

Across the four events, the peaks cluster into a small set of recurring frequency ranges:

- **~1.1–1.5 Hz (low-frequency range):** Identified in El Monte, Ridgecrest, and Searle Valley with high coherence (≈0.84–0.99), but it lies relatively close to the lower usable bandwidth and is not captured in the Pacoima summary.
- **~1.8–2.1 Hz:** Appears in multiple events with consistently high coherence (≈0.84–0.99), indicating a stable low-frequency vertical response component when sufficiently excited.

- **~2.6–2.9 Hz:** Present in all four events with high coherence (≈0.78–0.97) and relatively small inter-floor scatter, supporting interpretation as a robust structural response frequency band.
- **~4.0–4.5 Hz:** Also present across events with generally high coherence (≈0.83–0.97), indicating another repeatable response band.
- **~5.9–7.6 Hz:** This range appears in all events, but with a noticeable event-to-event shift in its center frequency (El Monte: 7.05 ± 0.15Hz; Pacoima: 7.61 ± 0.17Hz; Ridgecrest: 6.74 ± 0.57Hz; Searle Valley: 5.874 ± 0.055Hz). Coherence is generally strong ($\gamma_{xy}^2 \approx 0.84$–0.96 in El Monte and Pacoima) but drops in Searle Valley (≈ 0.69), suggesting stronger sensitivity to excitation characteristics and/or reduced signal-to-noise at these frequencies.
- **~8.8–10.0 Hz:** Recurrent across events; coherence ranges from moderate to very high depending on the record (notably high during Pacoima), indicating a consistent higher-frequency response that can be strongly excited in some events. Importantly, this frequency band also exhibits the largest transfer-function amplification across recorded events, indicating that it is the most strongly excited and most energetically dominant vertical response feature.
- **~12.0–12.7 Hz:** Identified in El Monte, Pacoima, and Ridgecrest but not in Searle Valley; coherence is moderate and, for El Monte, the inter-floor scatter is comparatively larger ($\sigma \approx 0.74$ Hz), so this feature is best interpreted as a higher-mode response that is conditionally observable (i.e., more dependent on event bandwidth and record quality).

Consistent with the combined selection criteria (recurrence across floors/events, transfer-function amplification, and elevated coherence), JPL 321 exhibits a repeatable set of candidate vertical natural frequencies at approximately ~1.4, ~1.9, ~2.7, ~4.2, ~6.8, ~9.4, and ~12.4 Hz. Among these frequencies, the f~9.4 Hz is interpreted as the dominant vertical natural frequency of JPL 321.

3.2.6 Vertical Frequency Identification for Building JPL 303

JPL 303 is a four-story structure with no basement, instrumented with one sensor per floor. The first floor is treated as the reference level for all earthquake events, and vertical transfer functions are computed for Floors 2–4 relative to the reference level. The available dataset for this building is more limited (fewer instrumented levels and fewer high-quality records), and the recordings were noisier than the other buildings; therefore, the identified peaks should be interpreted more cautiously. Figure 3.6 presents the vertical floor-to-base transfer function and the corresponding coherence for JPL 303 during the El Monte earthquake.

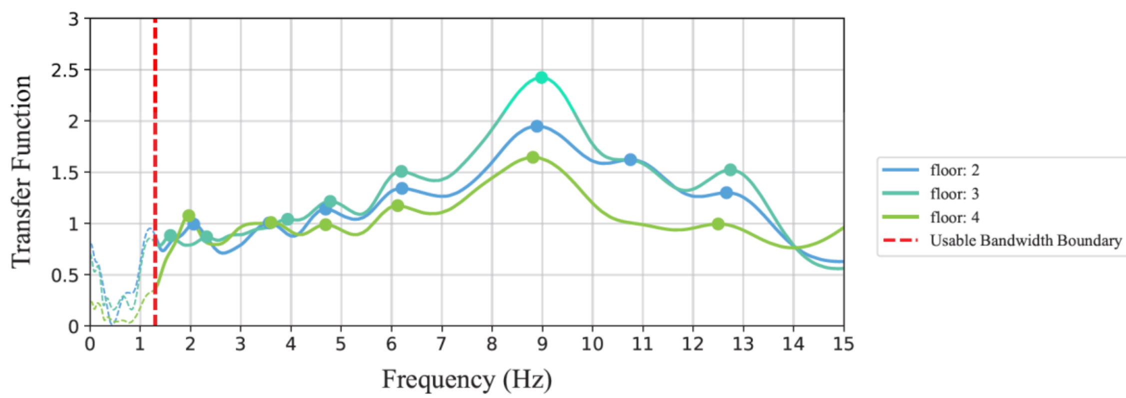

(a)

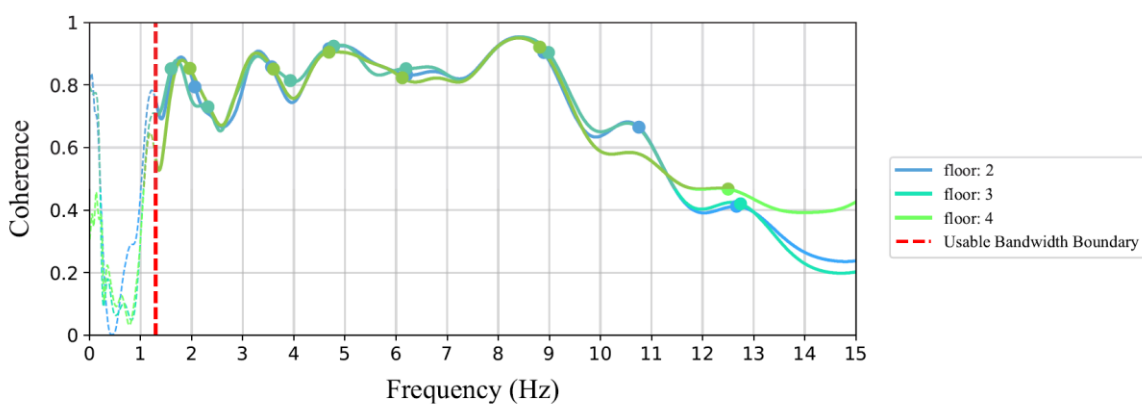

(b)

Figure 3.6. a) Vertical floor-to-base transfer function and b) magnitude-squared coherence for JPL 303 during the El Monte earthquake. The dashed red line marks the lower usable bandwidth

As shown in Figure 3.6a, multiple amplification peaks are observed within the usable band. The coherence curves in Figure 3.6b indicate moderate-to-high coherence. In the El Monte record, clear response peaks are visible near ~1.9 Hz, ~3.7 Hz, ~4.7 Hz, ~6.2 Hz, and a strong dominant peak near ~8.9 Hz. A higher-frequency feature near at ~10 Hz and ~12–13 Hz is also visible but is accompanied by reduced coherence and greater variability, consistent with the higher-modes contribution.

To evaluate repeatability across events, peak frequencies were extracted for each earthquake and then averaged across floors. Because this building is low-rise and the data are noisier, the peaks were consolidated into a smaller set of six robust frequency clusters, which are reported in Table 3.6.

Table 3.6. Floor-Averaged Vertical Peak Frequencies and Coherence by Event for JPL 303

	Frequency /Coherence	**Peak 1**	**Peak 2**	**Peak 3**	**Peak 4**	**Peak 5**	**Peak 6**
El Monte	$f \pm \sigma\ (Hz)$	1.88±0.20	3.70±0.16	4.72±0.04	6.17±0.04	8.90±0.07	12.64±0.10
	$\gamma^2\ \pm \sigma$	0.84±0.03	0.84±0.03	0.93±0.00	0.78±0.03	0.94±0.01	0.64±0.15
Pacoima	$f \pm \sigma\ (Hz)$	1.81±0.00	3.99±0.02	4.61±0.06	5.75±0.14	8.76±0.11	11.23±0.00
	$\gamma^2\ \pm \sigma$	0.89±0.00	0.85±0.00	0.88±0.03	0.79±0.06	0.95±0.00	0.95±0.00
Ridgecrest	$f \pm \sigma\ (Hz)$	2.05±0.09	3.88±0.00	4.80±0.03	6.19±0.14	8.30±0.10	
	$\gamma^2\ \pm \sigma$	1±0.00	0.99±0.00	0.99±0.00	0.93±0.01	0.91±0.03	

	Frequency /Coherence	Peak 1	Peak 2	Peak 3	Peak 4	Peak 5	Peak 6
Searle Valley	$f \pm \sigma\ (Hz)$	1.46±0.04			6.34±0.00	8.13±0.00	
	$\gamma^2\ \pm \sigma$	0.94±0.00			0.80±0.00	0.76±0.00	

Across all events, the most reliable peaks cluster into the following six recurring frequency ranges:

- **~1.5–2.1 Hz:** This band is observed in all events, with frequencies ranging from ~1.45 Hz (Searle Valley) to ~2.05 Hz (Ridgecrest), and coherence is consistently high. The event-to-event shift in the center frequency suggests sensitivity to excitation bandwidth and record quality, as expected for a short building with limited data.
- **~3.7–4.0 Hz:** A repeatable peak in the upper-3 to ~4 Hz range appears in El Monte, Pacoima, and Ridgecrest with strong coherence ($\gamma^2 \approx 0.84$–0.99). It is not clearly observed in Searle Valley.
- **~4.6–4.8 Hz:** This band is also consistently detected in El Monte, Pacoima, and Ridgecrest, and it exhibits very high coherence ($\gamma^2 \approx 0.88$–0.99). In the El Monte plot, this peak is distinct and well-supported by the coherence plateau, suggesting a repeatable structural contribution in this frequency neighborhood.
- **~5.7–6.3 Hz:** Peaks in this band are observed in all four events, with modest event-to-event shifts (≈5.75–6.34 Hz). Coherence remains moderate-to-high, supporting interpretation as a recurring response feature; however, its variability indicates that it may be more sensitive to record bandwidth and signal-to-noise conditions.

- **~8.1–8.9 Hz:** This is the most persistent and strongest range across all events. It also shows high coherence across most records (El Monte, Pacoima, Ridgecrest: $\gamma^2 \approx 0.91$–0.96) and corresponds to the largest transfer-function amplification in all events, with the peak near ~8.9 Hz dominating the response and increasing with height. Given its consistent appearance and strong amplification, this band is interpreted as the dominant vertical frequency range of JPL 303.
- **~11–13 Hz:** This band is detected primarily in El Monte (~12.6 Hz) and Pacoima (~11.2 Hz). Its coherence is more variable, and it is not observed in Ridgecrest or Searle Valley. Given the building's noisier dataset and the small number of instrumented floors, this cluster should be treated as less robust than the dominant ~8–9 Hz band.

Overall, JPL 303 exhibits a repeatable set of candidate vertical response frequencies at ~1.9, 3.8, 4.7, 6.1, 8.6, and 12.3 Hz. Among these, the ~8.1–8.9 Hz band is interpreted as the dominant vertical frequency range of the building. Because JPL 303 has a low-rise (4-story) structure and the available records are fewer and noisier than for the other buildings, these estimates should be regarded as preliminary/less certain.

3.3 Horizontal Frequency Results from Recordings

The horizontal frequency identification for each building was carried out using the methodology described in Section 3.1. The procedure is analogous to the vertical frequency analysis. For each instrumented building and seismic event, the two orthogonal horizontal acceleration components (denoted HNE and HNN, representing nominal east–west and north–south orientations) were processed independently to obtain their individual transfer function and coherence spectra. These component-specific results were then combined to produce a representative overall horizontal transfer function and coherence by taking the geometric mean of the two horizontal components. In mathematical terms, if $H_1(f)$ and $H_2(f)$ denote the amplitude of transfer functions derived from the HNE and HNN components, respectively, the combined horizontal transfer function is defined as:

$$H_{\text{geo}}(f) = \sqrt{H_1(f)\ \cdot\ H_2(f)} \qquad \text{Eq 3.13}$$

Likewise, given the coherence spectra $\gamma_1^2(f)$ and $\gamma_2^2(f)$ for the two horizontal directions, the combined coherence is defined as:

$$\gamma_{\text{geo}}^2(f) = \sqrt{\gamma_1^2(f)\ \cdot\ \gamma_2^2(f)} \qquad \text{Eq 3.14}$$

This spectrum provides a single intensity measure of the building's horizontal frequency response. Figure 3.7 presents the horizontal transfer function results for the two orthogonal components, (a) HNE and (b) HNN, as well as (c) their geometric-mean combination for JPL 180 during the El Monte earthquake. For completeness, all individual HNE and HNN component plots are provided in Appendix D. In this section, the geometric-mean transfer function and coherence are used as the primary reference for identifying resonant frequencies in each building's horizontal response.

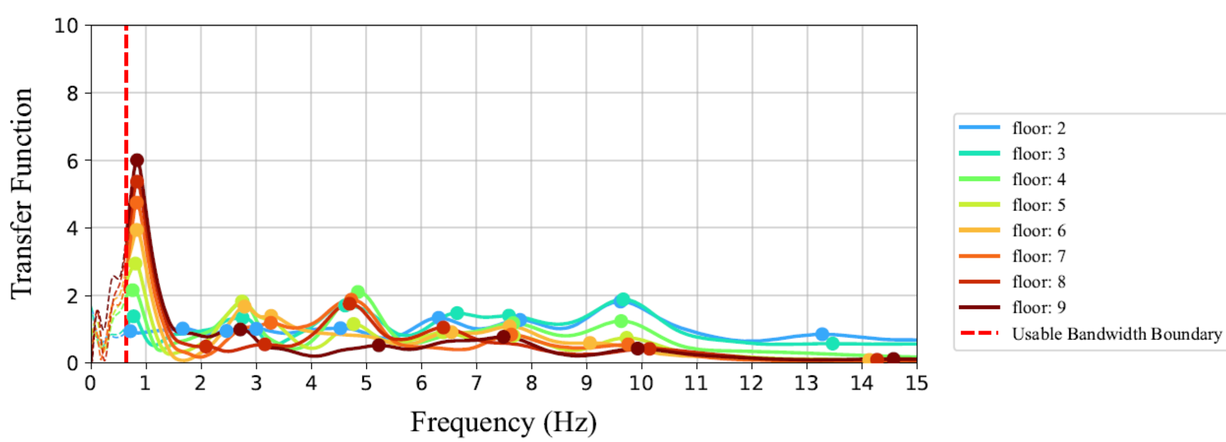

(a)

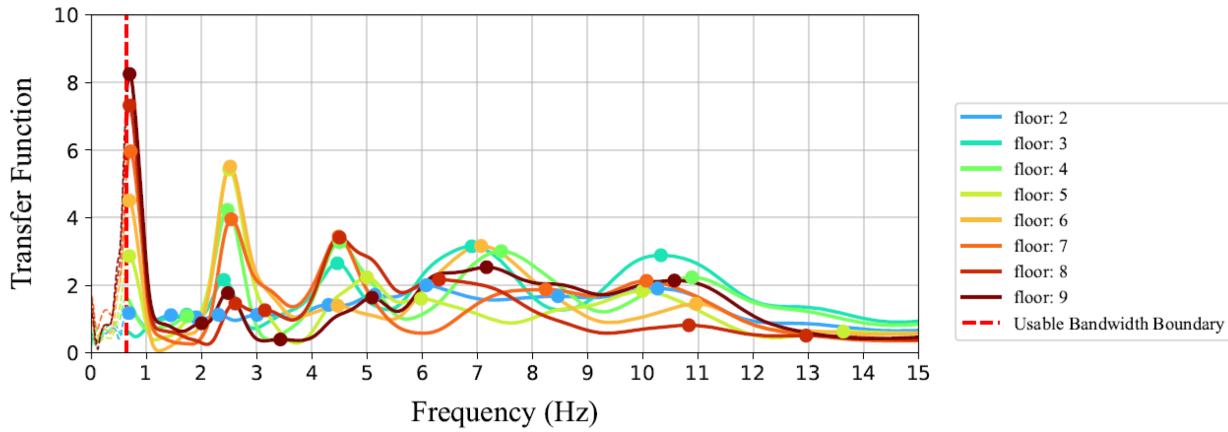

(b)

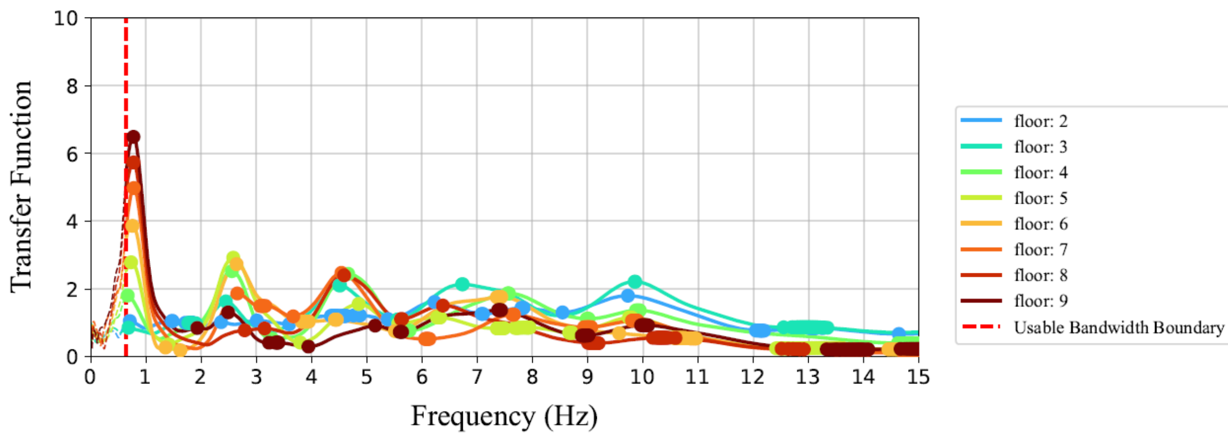

(c)

Figure 3.7. Horizontal transfer function of Building JPL 180 at the middle sensor line during the El Monte earthquake for the component of a) HNE, b) HNN, c) geometric-mean of horizontal components

As shown in Figure 3.7, for building JPL 180, the horizontal transfer and coherence functions reveal a fundamental resonance around 1.5 Hz across floors 2 through 9. This dominant mode appears in the geometric-mean spectrum as well as in the individual spectra for the HNE and HNN components. While the fundamental frequency remains the same in all cases, the HNE and HNN spectra show minor differences at higher frequencies, particularly in some peak amplitudes, indicating slight direction-specific influences on the building's response. By "averaging" the two horizontal components, these orientation-specific variations are smoothed out, yielding a more robust overall characterization of the structure's horizontal frequency. In all cases, smaller peaks at higher frequencies (with lower coherence) correspond to higher-order vibration modes. A vertical red dashed line at approximately 0.8–1 Hz marks the lower bound of the analysis's usable frequency range, below which the results become less reliable due to limited data fidelity. The following subsections present the building-by-building horizontal frequency identification results for the six case-study structures.

3.3.1 Horizontal Frequency Identification for Building JPL 183

For building JPL 183, horizontal frequency identification follows the same data-driven procedure described in Section 3.3 for combining orthogonal components. Additionally, the analysis is performed separately for the east and west sensor lines; peak frequencies are first identified per floor and per line, and then the corresponding east- and west-line peaks are paired and averaged consistent with the averaging strategy described for the vertical response in Section 3.2.1. Figure 3.8 presents the resulting geometric-mean horizontal transfer functions and their corresponding coherence for the El Monte earthquake.

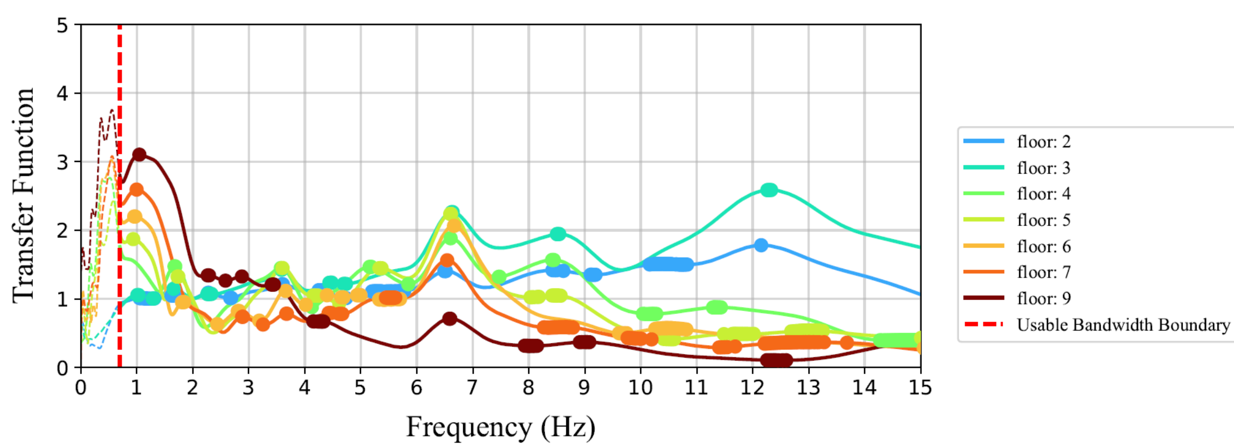

(a)

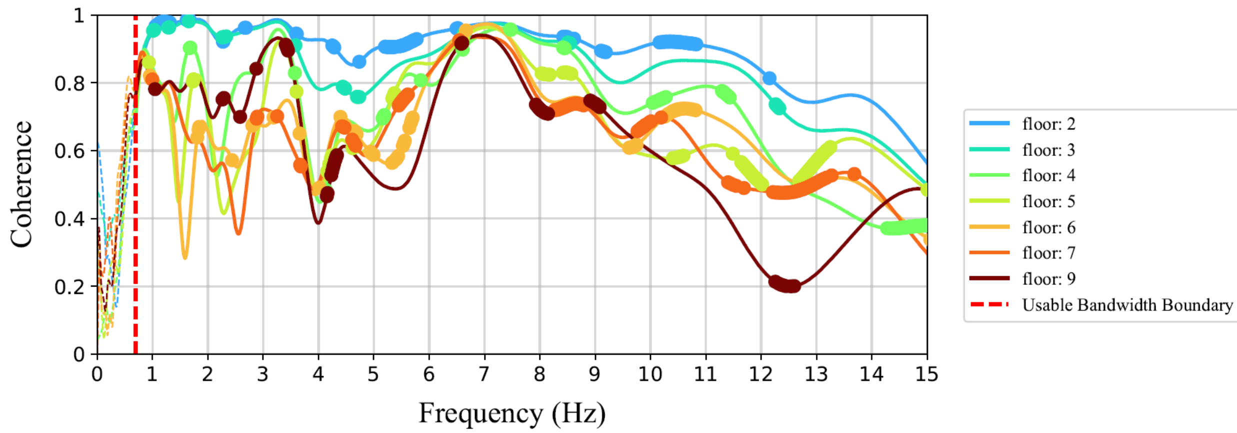

(b)

Figure 3.8. a) Horizontal floor-to-base transfer function and b) magnitude-squared coherence for JPL 183 during the El Monte earthquake. The dashed red line marks the lower usable bandwidth

As shown in Figure 3.8a, several resonant features are evident above the usable bandwidth. The lowest-frequency resonance occurs just above the cutoff, at ~1 Hz, and it exhibits the expected first-mode trend: amplification generally increases with elevation, with the upper floors (e.g., Floor 9) reaching substantially larger transfer-function amplitudes than the lower floors. The coherence curves (Figure 3.8b) indicate that this low-frequency band is accompanied by high coherence on most floors, supporting the interpretation that it is a genuine horizontal building response despite its proximity to the usable-bandwidth boundary.

Beyond the fundamental frequency band, additional peaks are visible at higher frequencies. A repeatable mid-frequency feature appears in the ~3.6–3.7 Hz range (modest amplification but generally coherent), followed by another response feature around ~5 Hz. A broader, more pronounced higher-frequency band is also present in the ~6.5–7.2 Hz range and shows consistently high coherence in the El Monte record (often near $\gamma^2 \approx 0.9$). At frequencies above ~10–12 Hz, coherence decreases and becomes more variable, particularly for upper floors, so any features in that band are treated cautiously unless they recur consistently across events and floors.

To evaluate repeatability beyond a single earthquake, peak frequencies were extracted for each event and then summarized by averaging across the available floors (Table 3.7). Reported values are the mean ± standard deviation across floors for each event, along with the corresponding mean ± standard deviation of coherence at the selected peaks.

Table 3.7. Floor-Averaged Horizontal Peak Frequencies and Coherence by Event for JPL 183

	Frequency /Coherence	Peak 1	Peak 2	Peak 3	Peak 4
El Monte	$f \pm \sigma\ (Hz)$	1.08 ± 0.18	3.68 ± 0.03	5.25 ± 0.10	6.97 ± 0.24
	$\gamma^2 \pm \sigma$	0.83 ± 0.09	0.75 ± 0.12	0.73 ± 0.03	0.91 ± 0.03
Pacoima	$f \pm \sigma\ (Hz)$	1.14 ± 0.16		5.16 ± 0.19	7.91 ± 0.21
	$\gamma^2 \pm \sigma$	0.80 ± 0.05		0.68 ± 0.08	0.59 ± 0.08
Ridgecrest	$f \pm \sigma\ (Hz)$	0.88 ± 0.05	3.20 ± 0.14	4.69 ± 0.20	7.00 ± 0.10
	$\gamma^2 \pm \sigma$	0.83 ± 0.09	0.71 ± 0.17	0.64 ± 0.10	0.61 ± 0.09
Searle Valley	$f \pm \sigma\ (Hz)$	0.91 ± 0.04	3.61 ± 0.21	4.77 ± 0.15	6.62 ± 0.09
	$\gamma^2 \pm \sigma$	0.87 ± 0.09	0.56 ± 0.14	0.65 ± 0.06	0.58 ± 0.09

Several observations follow from Table 3.7 and the underlying floor-level peaks:

- **~ 1.0–1.7 Hz (lowest-frequency range; candidate fundamental horizontal mode):** This range is present in all four events at the event-averaged level, with moderate inter-floor scatter and generally moderate-to-high coherence. Because portions of this band can lie near the lower usable-bandwidth boundary (especially when the peak occurs near ~1 Hz on some floors), its clarity can be record- and event-dependent;

nevertheless, its repeatability and its height-dependent amplification trend support interpretation as the fundamental horizontal-response frequency range of JPL 183.

- **~ 3.2–3.7 Hz (mid-frequency range):** A peak in the ~3–4 Hz range appears in El Monte, Ridgecrest, and Searle Valley, with coherence that is moderate to high when the peak is present. This feature is not consistently determined in the Pacoima record, suggesting greater sensitivity to event bandwidth and/or signal-to-noise conditions. Across the full event–floor dataset, this range is observed less frequently than the primary ranges, consistent with a higher-mode feature that is conditionally excited.

- **~ 4.6–5.3 Hz (mid-frequency range):** This response range is repeatable across events, although its center frequency shifts modestly from event to event (e.g., ~5.25 Hz in El Monte versus ~4.7–4.8 Hz in Ridgecrest/Searle Valley). Coherence is typically moderate (event means around $\gamma^2 \approx 0.64$–0.73), indicating a structurally relevant band that is somewhat more sensitive to record characteristics than the fundamental resonance.

- **~ 6.6–7.9 Hz (higher-frequency range):** A consistent higher-frequency range is present in all events, centered near ~7 Hz for El Monte and Ridgecrest, shifting downward in Searle Valley (~6.6 Hz) and upward in Pacoima (~7.9 Hz). Its recurrence across the dataset supports interpretation as a repeatable higher-horizontal-mode range, albeit with greater event-to-event variability than the lower-frequency peak.

Higher-frequency peaks near ~10 Hz and above are observed only rarely (and in a small fraction of event–floor cases) and tend to coincide with reduced and/or more variable coherence;

therefore, they are treated as secondary/conditional features rather than robust horizontal-mode candidates.

Finally, averaging across all events, all floors, and both sensor-line locations yields representative horizontal response frequencies of approximately 1.4 Hz, 3.5 Hz, 4.9 Hz, and 7.1 Hz, with corresponding mean coherence levels of approximately 0.79, 0.68, 0.66, and 0.70, respectively. Based on its position as the lowest repeatable frequency band and its characteristic height-dependent amplification behavior, the ~1.1–1.6 Hz band is interpreted as the fundamental horizontal natural frequency range of JPL 183, while the ~3.5 Hz, ~4.9 Hz, and ~7.1 Hz ranges are interpreted as repeatable higher-mode horizontal response features of the structure.

3.3.2 Horizontal Frequency Identification for Building JPL 180

In JPL 180, peak frequencies are identified for each line and then averaged across the three lines to obtain a single representative set of frequencies (and coherence) for each floor and event, consistent with the line-averaging strategy used for vertical frequency of JPL 180 (Section 3.2.2). Figure 3.9 presents the horizontal floor-to-base transfer-function amplitudes and coherence for the El Monte earthquake.

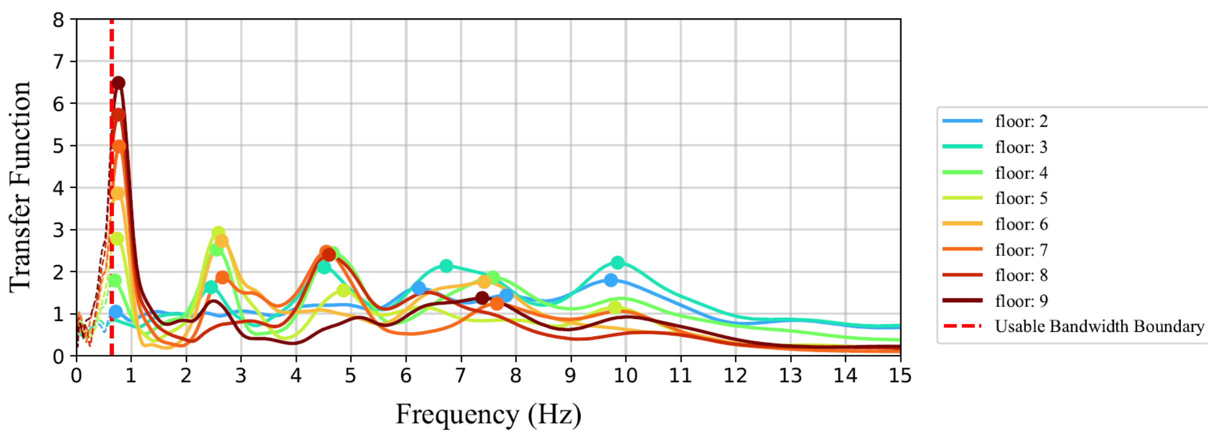

(a)

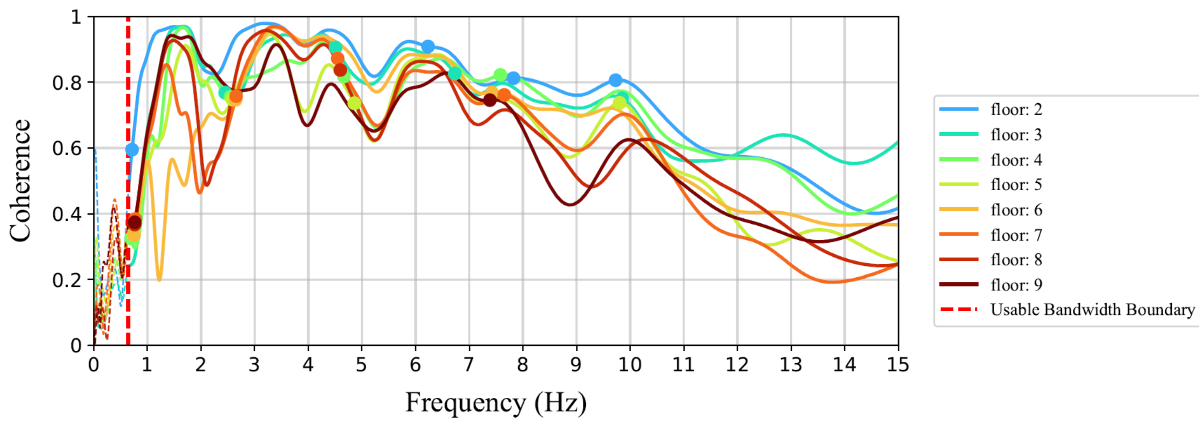

(b)

Figure 3.9. a) Horizontal floor-to-base transfer function and b) magnitude-squared coherence for JPL 180 during the El Monte earthquake. The dashed red line marks the lower usable bandwidth

Several repeatable resonant features are evident above the usable bandwidth. A pronounced low-frequency amplification band occurs just above the cutoff (≈0.7–0.9 Hz), and it exhibits a clear first-mode signature: transfer-function amplitudes increase systematically with elevation, with the upper floors showing the largest amplification. However, coherence in this lowest-frequency band is only moderate (and notably lower than in the mid-frequency peaks), which is consistent with the known sensitivity of coherence estimates near the lower usable-bandwidth limit. Beyond the lowest-frequency band, the El Monte transfer functions show distinct amplification peaks near ~2.6 Hz, ~4.7 Hz, ~6.7 Hz, and ~9.7–10 Hz. These peaks generally coincide with moderate-to-high coherence, particularly in the ~2–8 Hz range, where coherence commonly remains elevated across floors. At higher frequencies (approximately above 10–12 Hz), coherence decreases and becomes more variable; therefore, features in that band are treated as secondary unless they recur consistently across events and floors. To evaluate event-to-event repeatability, peak frequencies were extracted for each floor and then averaged across the instrumented floors (Table 3.8).

Table 3.8. Floor-Averaged Horizontal Peak Frequencies and Coherence by Event for JPL 180

	Frequency /Coherence	Peak 1	Peak 2	Peak 3	Peak 4	Peak 5
El Monte	$f \pm \sigma\ (Hz)$	0.75 ± 0.04	2.58 ± 0.12	4.73 ± 0.20	6.70 ± 0.55	9.74 ± 0.21
	$\gamma^2 \pm \sigma$	0.40 ± 0.08	0.73 ± 0.06	0.83 ± 0.09	0.79 ± 0.04	0.65 ± 0.04
Pacoima	$f \pm \sigma\ (Hz)$	0.99 ± 0.08	2.55 ± 0.31	5.22 ± 0.11	7.63 ± 0.32	9.99 ± 0.26
	$\gamma^2 \pm \sigma$	0.25 ± 0.19	0.70 ± 0.07	0.63 ± 0.04	0.89 ± 0.05	0.59 ± 0.04
Ridgecrest	$f \pm \sigma\ (Hz)$	0.70 ± 0.05	2.52 ± 0.04	4.43 ± 0.19	6.54 ± 0.24	10.11 ± 0.13
	$\gamma^2 \pm \sigma$	0.49 ± 0.24	0.83 ± 0.04	0.72 ± 0.12	0.67 ± 0.12	0.41 ± 0.10
Searle Valley	$f \pm \sigma\ (Hz)$	0.74 ± 0.04	2.51 ± 0.09	4.53 ± 0.14	6.95 ± 0.14	
	$\gamma^2 \pm \sigma$	0.63 ± 0.16	0.80 ± 0.09	0.66 ± 0.12	0.59 ± 0.17	

Across the four earthquakes, the identified horizontal peaks cluster into a small set of recurring frequency ranges, indicating a stable horizontal frequency signature for JPL 180:

- **~0.7–0.9 Hz (lowest-frequency range; candidate fundamental horizontal mode):** In all events, this band is observed and shows the most characteristic first-mode behavior (systematic amplification growth with height). Coherence in this band is more variable and tends to be lower than for the mid-frequency peaks, most notably in Pacoima, consistent with the band's proximity to the lower usable-bandwidth boundary and the sensitivity of low-frequency estimates to event-specific excitation and signal-to-noise conditions.

- **~2.4–2.7 Hz (low-to-mid-frequency range):** This peak is one of the most stable across the dataset and is consistently supported by high coherence. This combination of persistence and coherence indicates a reliable higher-mode horizontal response feature.

- **~4.4–5.1 Hz (mid-frequency range):** A repeatable peak occurs in all events, with modest event-to-event shifts in its center frequency (e.g., slightly higher in Pacoima). Coherence is generally moderate to high, supporting interpretation as a structurally governed response band.

- **~6.4–7.4 Hz (higher-frequency range):** This range is present in all events where it could be resolved, with noticeable event-to-event variation. Coherence is often strong, but the larger scatter suggests that this band may include closely spaced higher-mode contributions whose apparent peak locations can shift with excitation characteristics and peak-separation difficulties.

- **~9.7–10.1 Hz (high-frequency range; conditionally observable):** This peak is evident in El Monte, Pacoima, and Ridgecrest but is not consistently recovered in Searle Valley, consistent with reduced usable high-frequency content and/or weaker excitation in that record. Coherence in this band is moderate and more variable, so it can be treated as a higher-mode feature that is less robust than the lower-frequency response.

Synthesizing the transfer-function amplification behavior, coherence support, and repeatability across floors, sensor lines, and earthquakes, JPL 180 exhibits that the ~0.7–0.9 Hz band can be interpreted as the fundamental horizontal natural frequency range of JPL 180, while the higher-frequency bands (2.5 Hz, 4.7 Hz, 6.9 Hz, and ~10 Hz) are interpreted as higher-mode horizontal responses.

3.3.3 Horizontal Frequency Identification for Building JPL 238

For JPL 238, transfer functions and coherence were computed using the lowest instrumented floor as the reference. The reference level varied by event due to data availability: Floor 1 for El Monte, Floor 3 for Pacoima, and Floor 2 for Ridgecrest and Searle Valley. Floor 6 had no recordings in all events except El Monte; therefore, the transfer functions for those events exclude Floor 6. In Figure 3.10, the horizontal transfer function and corresponding coherence for floors 2 through 8 are plotted.

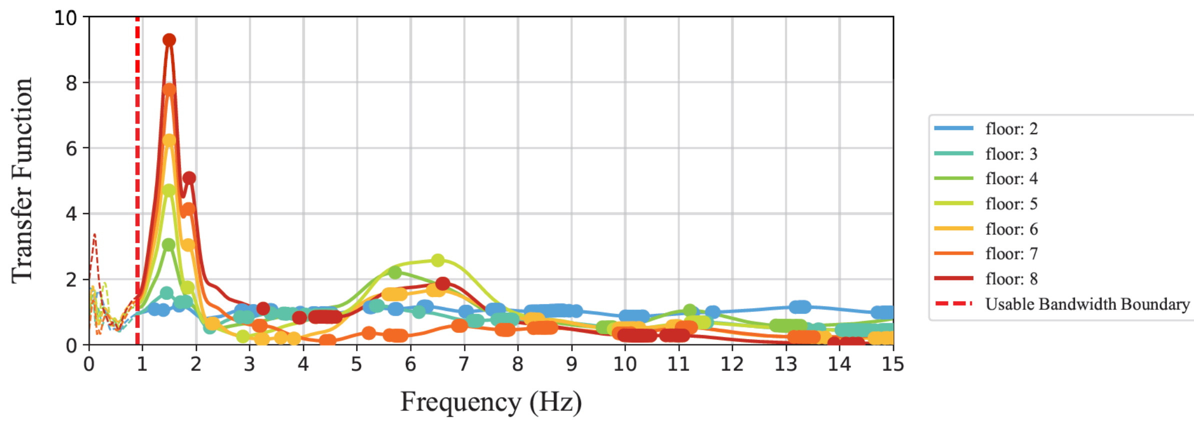

(a)

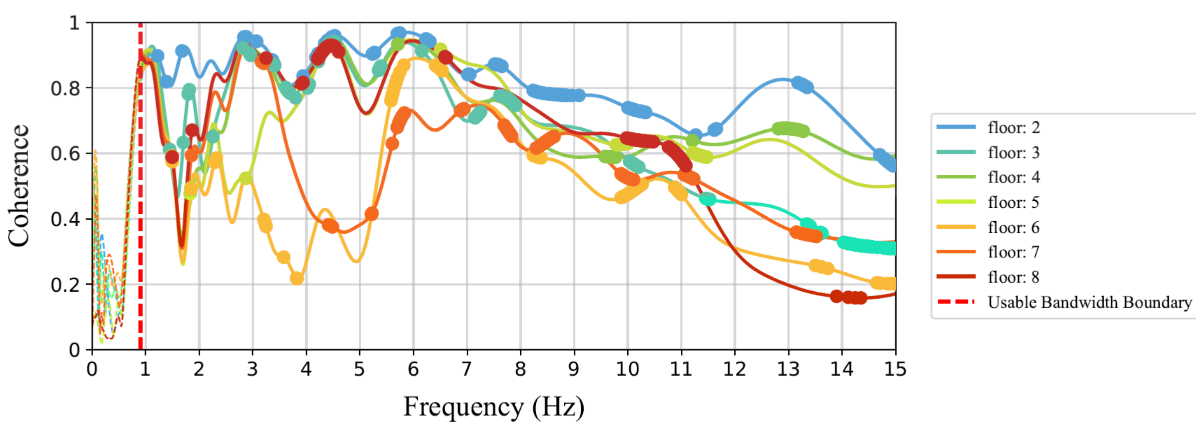

(b)

Figure 3.10. a) Horizontal floor-to-base transfer function and b) magnitude-squared coherence for JPL 238 during the El Monte earthquake. The dashed red line marks the lower usable bandwidth

As shown in Figure 3.10, two prominent resonant peaks are evident in the horizontal direction: the first peak occurs at approximately 1.5 Hz, and the second peak is observed around 6 Hz for this event. The fundamental horizontal mode (Peak 1 ~1.5 Hz) shows increasing amplification with height, for instance, the top floor (8th) reaches a transfer function amplitude of about 10.0 at this frequency, whereas the second floor's amplification is closer to ~1.0. This trend is consistent with a first-mode shape in which deformations (and therefore relative motion with respect to the base) grow toward the top of the building. The second, higher-frequency peak (~6 Hz) is also apparent across all floors, though its amplitude distribution is somewhat different. The coherence values confirm the reliability of these identified frequencies. At the fundamental ~1.5 Hz peak, coherence between the reference and each floor is moderate (around 0.6–0.7 for the El Monte event), indicating a reasonably consistent phase relationship despite some possible complexity in the response. In contrast, at the ~6 Hz peak, the coherence is high (often on the order of 0.8–0.9, reaching ~0.90 for the top floor in El Monte), which implies a very clear, in-phase response of the floors with respect to the reference at this higher mode.

Table 3.9 summarizes the dominant horizontal frequencies identified for JPL 238 in each event, along with the coherence at those peaks. The fundamental horizontal frequency (1.55 ± 0.12 Hz) was clearly identified in nearly all records, while a higher-mode frequency in the ~5.5–6.1 Hz range was also observed in most cases.

Table 3.9. Floor-Averaged Horizontal Peak Frequencies and Coherence by Event for JPL 238

	Frequency /Coherence	Peak 1	Peak 2
El Monte	$f \pm \sigma\ (Hz)$	1.51±0.07	6.14±0.44
	$\gamma^2\ \pm \sigma$	0.64±0.11	0.90±0.03
Pacoima	$f \pm \sigma\ (Hz)$	1.81±0.00	5.52±0.09
	$\gamma^2\ \pm \sigma$	0.63±0.01	0.89±0.03
Ridgecrest	$f \pm \sigma\ (Hz)$	1.50±0.02	5.69±0.10
	$\gamma^2\ \pm \sigma$	0.61±0.03	0.89±0.02
Searle Valley	$f \pm \sigma\ (Hz)$	1.56±0.14	5.75±0.12
	$\gamma^2\ \pm \sigma$	0.69±0.06	0.85±0.02

Despite some event-to-event variability, the fundamental horizontal mode of the building is consistent. Averaging across all floors and all events yields a first-mode frequency of ≈1.55 Hz (with a standard deviation of ~0.12 Hz) and an average coherence of 0.64 ± 0.09 at that frequency. This ~1.5 Hz frequency can be identified as the fundamental lateral (horizontal) mode of this 8-story structure. The higher-frequency peak (~5.85 Hz) shows more variability between events and may represent a higher-order horizontal mode of JPL 238.

3.3.4 Horizontal Frequency Identification for Building JPL 264

For JPL 264, Floor 1 is used as the reference level for all events. Using horizontal floor-to-base transfer function analysis, up to five distinct resonant frequency peaks are identified for each seismic event in this building. Figure 3.11 shows these peaks clearly for the El Monte earthquake.

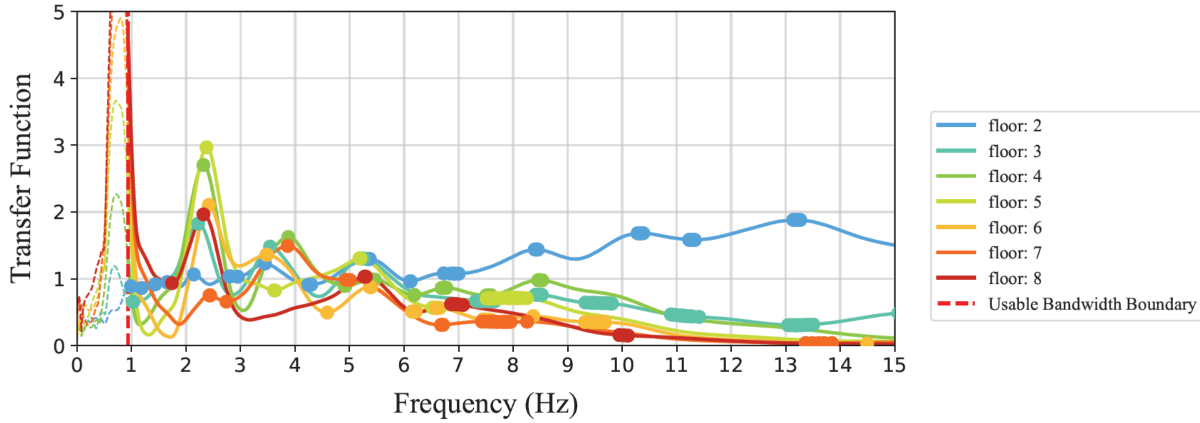

(a)

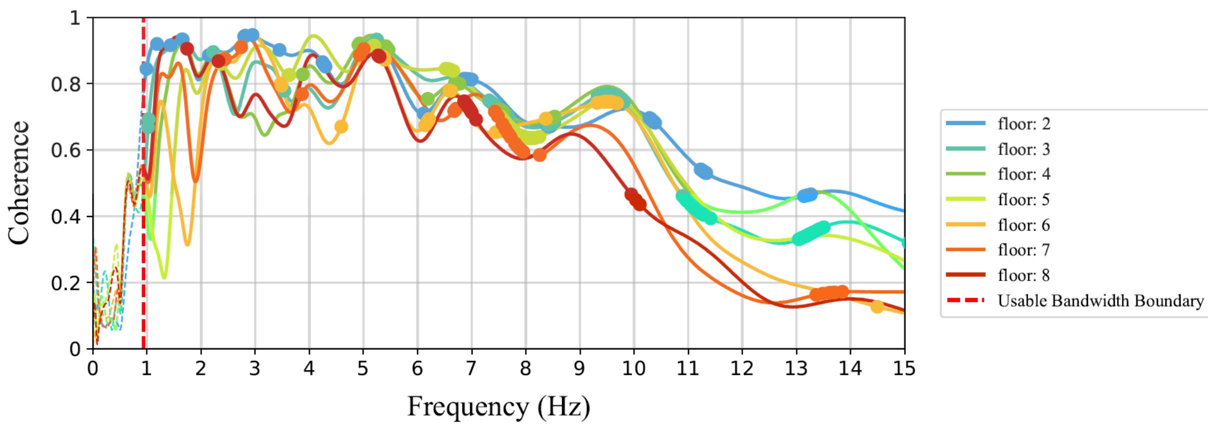

(b)

Figure 3.11. a) Horizontal floor-to-base transfer function and b) magnitude-squared coherence for JPL 264 during the El Monte earthquake. The dashed red line marks the lower usable bandwidth

As shown in Figure 3.11a, the El Monte transfer functions exhibit several clear amplification peaks within the usable bandwidth. A strong spike occurs just below ~1 Hz; however, because it lies at/just below the usable-bandwidth boundary, it is not treated as a reliable structural resonance. Within the interpretable frequency range, the most repeatable resonant features occur near ~2.3 Hz, ~3.6–3.9 Hz, ~5.2 Hz, and ~8.3 Hz, which are evident across multiple floors.

The corresponding coherence curves in Figure 3.11b provide strong validation of these peaks. Coherence is generally high ($\gamma^2 \gtrsim 0.8$) throughout the primary resonance band from roughly ~0.7 to ~6 Hz, indicating a consistent linear input–output relationship between the base and upper floors at the dominant peaks. However, coherence is moderate near the ~8 Hz peak (typically ~0.6–0.7), and it drops progressively at frequencies higher than ~10 Hz.

To evaluate repeatability beyond a single record, this procedure is applied to this building for all events, and Table 3.10 summarizes the event-wise results for the combined horizontal response of JPL 264.

Table 3.10. Floor-Averaged Horizontal Peak Frequencies and Coherence by Event for JPL 264

	Frequency /Coherence	Peak 1	Peak 2	Peak 3	Peak 4	Peak 5
El Monte	$f \pm \sigma\ (Hz)$		2.32±0.10	3.63±0.18	5.19±0.15	8.35±0.16
	$\gamma^2\ \pm \sigma$		0.88±0.01	0.82±0.04	0.91±0.02	0.66±0.04
Pacoima	$f \pm \sigma\ (Hz)$		2.58±0.08	3.92±0.15	5.76±0.13	8.01±0.15
	$\gamma^2\ \pm \sigma$		0.70±0.08	0.84±0.05	0.66±0.04	0.67±0.04
Ridgecrest	$f \pm \sigma\ (Hz)$	0.68±0.01	2.18±0.16	3.58±0.18	4.87±0.30	7.65±0.11
	$\gamma^2\ \pm \sigma$	0.25±0.04	0.84±0.05	0.83±0.05	0.81±0.06	0.63±0.04
Searle Valley	$f \pm \sigma\ (Hz)$	0.78±0.02	2.35±0.16	3.40±0.06	4.69±0.28	
	$\gamma^2\ \pm \sigma$	0.35±0.04	0.82±0.11	0.84±0.08	0.71±0.09	

Across the four earthquakes, the identified horizontal peaks organize into a small set of repeatable frequency ranges. Importantly, the lowest-frequency range (sub-1 Hz) is interpreted as the fundamental horizontal mode of JPL 264 based on its transfer-function behavior and height-dependent amplification pattern:

- **~ 0.68–0.78 Hz** (**fundamental horizontal mode**): A pronounced low-frequency resonance is clearly observed in the Ridgecrest and Searle Valley records (event-averaged peaks of 0.68 Hz and 0.78 Hz, respectively). In these events, this peak exhibits the most consistent first-mode signature: amplification increases systematically with elevation (i.e., the transfer-function magnitude increases as the response is tracked to higher floors without exception). The absence of this peak in El Monte and Pacoima is attributed to record-dependent usable-bandwidth (i.e., low-frequency content below ~1 Hz is filtered out), rather than a change in the building's dynamic properties. Taken together, the strong amplification and consistent height trend support classifying ~0.74±0.05Hz as the fundamental horizontal natural frequency of the structure.

- **~2.2–2.6 Hz**: This range is present in all events where frequencies above ~1 Hz are interpretable, and it generally exhibits high coherence (often $\gamma^2 \approx 0.8$–0.9). Given its repeatability but higher frequency than the ~0.7–0.8 Hz mode, it is interpreted as a higher (secondary) horizontal mode range.

- **~3.4–3.9 Hz**: A stable mid-frequency range that repeats across the events with consistently high coherence (typically $\gamma^2 \approx 0.82$–0.84 on average).

- **~4.7–5.8 Hz**: A persistent band observed in each event, with modest event-to-event shifts in its center frequency (e.g., ~5.2 Hz in El Monte versus ~5.8 Hz in Pacoima) and high coherence.

- **~7.6–8.4 Hz**: A higher-frequency range observed in El Monte, Pacoima, and Ridgecrest with moderate coherence (typically $\gamma^2 \approx 0.63$–0.67). Its absence in the Searle Valley is most consistent with reduced high-frequency usable content in that record rather than a structural change.

Overall, JPL 264 exhibits a repeatable horizontal frequency signature with a fundamental mode at ~0.7 Hz, followed by higher-mode ranges centered near ~2.4 Hz, ~3.6 Hz, ~5.2 Hz, and ~8.0 Hz.

3.3.5 Horizontal Frequency Identification for Building JPL 321

In JPL 321, for the horizontal-response evaluation, the first floor is treated as the reference level for all earthquakes except Pacoima, for which the Floor 1 record was unavailable, and Floor 2 was used as the reference. In addition, for the Ridgecrest and Searle Valley events, recordings from Floors 5 and 6 were not available, so those event-wise statistics are computed using Floors 2–4 only. Figure 3.12 presents the geometric-mean horizontal transfer functions and the corresponding coherence for the El Monte earthquake.

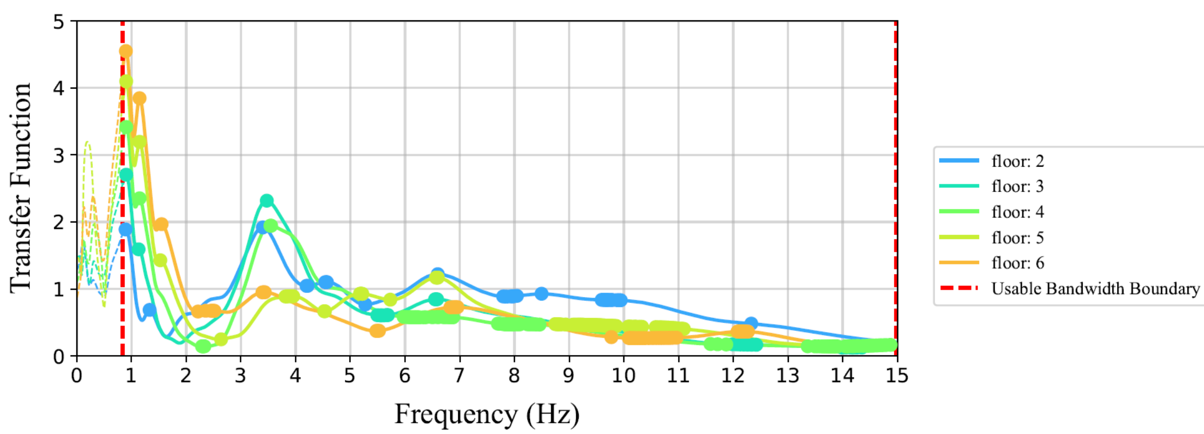

(a)

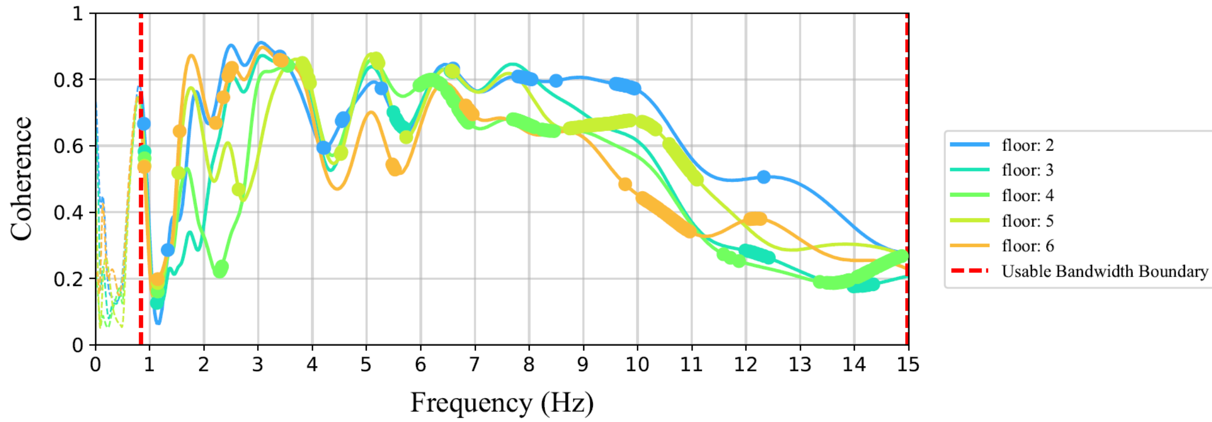

(b)

Figure 3.12. a) Horizontal floor-to-base transfer function and b) magnitude-squared coherence for JPL 321 during the El Monte earthquake. The dashed red line marks the lower usable bandwidth

Above the lower usable bandwidth (vertical dashed line near ~0.8 Hz), two response bands are clear: (i) a mid-frequency peak near ~3.4–3.6 Hz, and (ii) a higher-frequency peak near ~6.5–6.8 Hz. These peaks are observed across multiple floors, and their coherence values are generally high, indicating a consistent and reliable input–output relationship between the reference level and upper floors at these resonances. A lower-frequency feature near ~0.9 Hz is also visible in the transfer functions and exhibits the expected qualitative first-mode signature; however, because it lies very close to the usable-bandwidth boundary, it should be interpreted with caution. Coherence systematically decreases above roughly ~10–12 Hz, and no additional high-frequency peaks are treated as robust horizontal modes in this building based on the available records. To identify frequency beyond a single record, the resulting event-wise peak statistics for JPL 321 are summarized in Table 3.11.

Table 3.11. Floor-Averaged Horizontal Peak Frequencies and Coherence by Event for JPL 321

	Frequency /Coherence	Peak 1	Peak 2	Peak 3
El Monte	$f \pm \sigma\ (Hz)$	0.90±0.00	3.56±0.19	6.64±0.11
	$\gamma^2\ \pm \sigma$	0.55±0.19	0.84±0.02	0.80±0.05
Pacoima	$f \pm \sigma\ (Hz)$		4.06±0.06	7.14±0.24
	$\gamma^2\ \pm$		0.66±0.03	0.86±0.03
Ridgecrest	$f \pm \sigma\ (Hz)$	1.00±0.01	3.28±0.17	6.45±0.08
	$\gamma^2\ \pm \sigma$	0.75±0.04	0.74±0.04	0.79±0.05
Searle Valley	$f \pm \sigma\ (Hz)$	1.25±0.00	3.31±0.07	6.60±0.26
	$\gamma^2\ \pm \sigma$	0.62±0.03	0.75±0.05	0.70±0.04

Across the four earthquakes, the identified horizontal peaks cluster into three recurring frequency ranges, indicating a stable horizontal frequency signature for JPL 321:

- **~0.9–1.2 Hz (lowest-frequency range; candidate fundamental horizontal mode):** This band is clearly observed in El Monte, Ridgecrest, and Searle Valley, with moderate-to-high coherence. The absence of Peak 1 in Pacoima is most consistent with record-dependent low-frequency limitations, rather than a change in structural properties.

- **~3.3–4.1 Hz (mid-frequency range):** This band is observed in all events and is generally supported by moderate-to-high coherence ($\gamma^2 \approx 0.66$–0.84). The upward shift in Pacoima (≈4.06 Hz) relative to the other events (≈3.28–3.56 Hz) is attributed to a combination of record-specific excitation/bandwidth and the alternative reference level, but the repeated appearance confirms that this is a robust higher-mode horizontal response feature.

- **~6.4–7.3 Hz (higher-frequency range):** This peak is also repeatable across events and exhibits consistently strong coherence ($\gamma^2 \approx 0.70$–0.86). Similar to the mid-frequency band, Pacoima shows a modest upward shift (≈7.14 Hz) compared to El Monte/Ridgecrest/Searle Valley (≈6.45–6.64 Hz), but the persistence across the dataset supports interpretation as a stable higher-mode range.

Averaged across all events and floors, the representative horizontal peak frequencies for JPL 321 are approximately 1.02 Hz, 3.55 Hz, and 6.75 Hz, with corresponding mean coherence values of approximately 0.63, 0.76, and 0.80, respectively. Based on its position as the lowest repeatable frequency band and its first-mode amplification characteristics, the ~1.0 Hz band is interpreted as the fundamental horizontal natural frequency of JPL 321, while the ~3.6 Hz and ~6.7 Hz bands are interpreted as higher horizontal mode ranges.

3.3.6 Horizontal Frequency Identification for Building JPL 303

For the horizontal-response evaluation in JPL 303, Floor 1 is treated as the reference level for all events. In El Monte, recordings are available on Floors 1–4 (allowing three output transfer functions relative to Floor 1). In Pacoima, Ridgecrest, and Searle Valley, the Floor 4 recordings are unavailable; consequently, the horizontal transfer function and coherence estimates for those events are based on Floors 2 and 3. However, identifiable peaks for these three events are observed only on Floor 3; Floor 2 (immediately above the reference) generally exhibits weak or ambiguous peaks because in a short and large plan structure such as JPL 303, the relative motion between Floors 1 and 2 is small and the transfer function often remains close to unity. Figure 3.13 presents the horizontal transfer functions and the corresponding coherence for the El Monte earthquake.

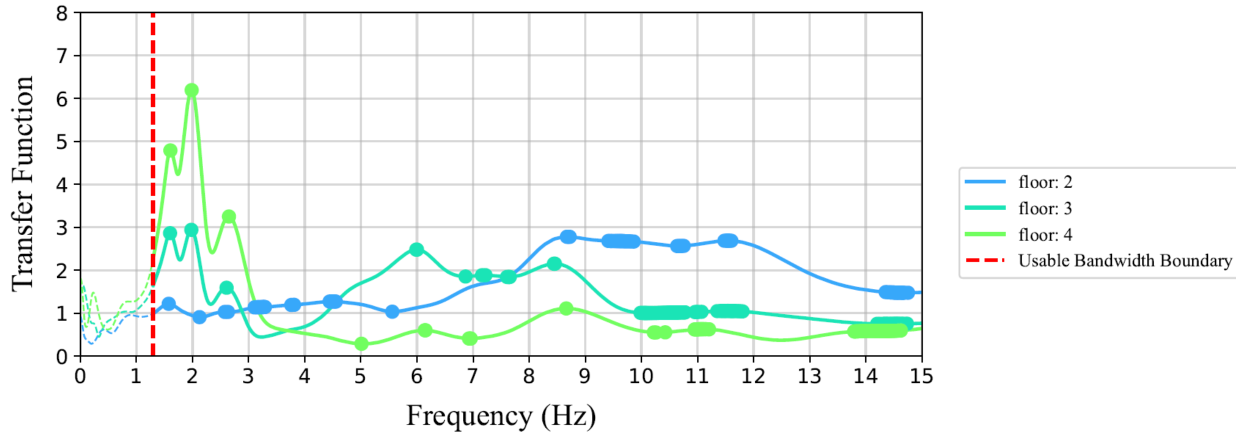

(a)

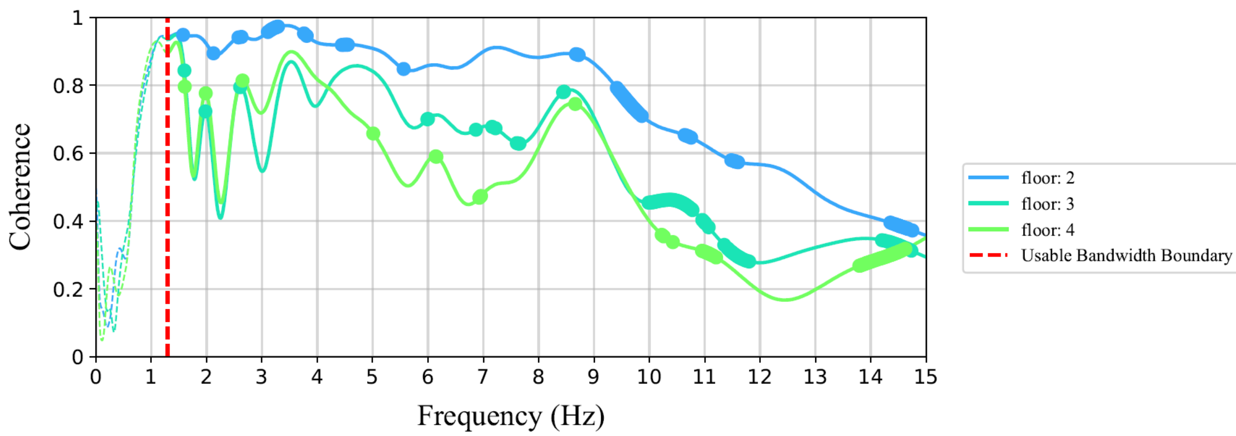

(b)

Figure 3.13. a) Horizontal floor-to-base transfer function and b) magnitude-squared coherence for JPL 303 during the El Monte earthquake. The dashed red line marks the lower usable bandwidth

As shown in Figure 3.13a, three response bands are apparent above the usable-bandwidth boundary. One clear resonant feature is present in ~1.6–2.0 Hz, most strongly expressed at the upper levels in El Monte (particularly Floor 4, which exhibits the largest amplification). The coherence in Figure 3.13b is generally moderate-to-high over this band. This range can be treated as the candidate fundamental horizontal mode. A secondary resonance is visible near ~6 Hz in El Monte, most clearly on Floors 4. Coherence at this peak is moderate. Finally, a distinct peak is observed near ~8–9 Hz across Floors 2–4 in

El Monte, with moderate-to-high coherence. At frequencies above ~10–12 Hz, coherence decreases progressively; therefore, features in this range are not considered robust horizontal modes for JPL 303 based on the current dataset. To assess event-to-event repeatability, peak frequencies were extracted for each earthquake and summarized by averaging across the available floors (Table 3.12).

Table 3.12. Floor-Averaged Horizontal Peak Frequencies and Coherence by Event for JPL 303

	Frequency /Coherence	**Peak 1**	**Peak 2**	**Peak 3**
El Monte	$f \pm \sigma\ (Hz)$	1.85±0.19	6.07±0.07	8.60±0.10
	$\gamma^2\ \pm \sigma$	0.82±0.10	0.65±0.06	0.81±0.06
Pacoima	$f \pm \sigma\ (Hz)$		5.82±0.00	7.99±0.2
	$\gamma^2\ \pm \sigma$		0.75±0.00	0.84±0.06
Ridgecrest	$f \pm \sigma\ (Hz)$	1.67±0.00	5.18±0.00	6.45±0.08
	$\gamma^2\ \pm \sigma$	0.77±0.00	0.70±0.00	0.60±0.00
Searle Valley	$f \pm \sigma\ (Hz)$	1.78±0.00	5.90±0.00	6.60±0.26
	$\gamma^2\ \pm \sigma$	0.72±0.00	0.47±0.00	0.71±0.02

Across the four earthquakes, the identified horizontal peaks cluster into three recurring frequency ranges:

- **~1.65–2 Hz (lowest-frequency range; candidate fundamental horizontal mode):** Detected in El Monte, Ridgecrest, and Searle Valley with moderate-to-high coherence. Its absence in Pacoima is most consistent with event-dependent usable bandwidth.
- **~5.5–6 Hz (mid-frequency range):** Present whenever a stable mid-frequency peak could be resolved, but with more variable coherence (from ~0.55 to ~0.75). This band is interpreted as a higher horizontal mode range with greater sensitivity to record quality and excitation characteristics.

- **~6.5–8.5 Hz (higher-frequency range; most repeatable across events):** Appears in all four events, with coherence typically in the moderate-to-high range (~0.65–0.85). This persistence across the dataset indicates a stable higher-mode horizontal-response feature of JPL 303.

Finally, averaging across all events and all available floors indicates that the ~1.8 Hz frequency is identified as the candidate fundamental horizontal natural frequency of JPL 303, followed by ~5.8 Hz and ~8.2 Hz, which are interpreted as repeatable higher-mode horizontal response ranges.

3.4 Summary of data-driven frequencies

In this chapter, a data-driven methodology is introduced to identify the natural frequencies of six instrumented buildings in both vertical and horizontal directions, where the horizontal response is defined by the geometric mean of the two orthogonal horizontal components. A frequency is considered a candidate modal frequency of the building if it satisfies three key criteria within the usable bandwidth of the recording: (1) it corresponds to a pronounced peak in the transfer-function magnitude, indicating significant amplification of the base input at that frequency, (2) it appears as a recurring prominent peak in the transfer function spectra across multiple recordings (across multiple floors and earthquakes), and (3) it exhibits a relatively high coherence value between the reference level and floor signals. Frequencies meeting these criteria are flagged as likely structural vertical natural frequencies, since the concurrence of these features strongly suggests a true structural resonance rather than a noise artifact or a site-specific input characteristic.

In Table 3.13, two terms are used to summarize the identified frequency contents in each direction: i) the fundamental frequency, which is taken as the lowest frequency among selected peaks in transfer function spectra, and ii) the dominant frequency, which is defined as the frequency corresponding to the maximum amplification observed in the transfer-function magnitude. These values represent the central frequency of the principal low-frequency mode and the strongest response mode in each orientation, respectively.

Table 3.13. Fundamental vs. dominant frequencies (Hz) identified for each instrumented JPL building.

Building	Vertical Frequency (Hz)		Horizontal Frequency (Hz)	
	Fundamental	**Dominant**	**Fundamental**	**Dominant**
JPL 183	~1.7 Hz	~7.2 Hz	~1.1 Hz	~1.1 Hz
JPL 180	~5.4 Hz	~5.4 Hz	~0.8 Hz	~0.8 Hz
JPL 238	~2.1 Hz	~8.8 Hz	~1.6 Hz	~1.6 Hz
JPL 264	~1.8 Hz	~5.1 Hz	~0.7Hz	~0.7 Hz
JPL 321	~1.4 Hz	~9.4 Hz	~1.0 Hz	~1.0 Hz
JPL 303	~1.9 Hz	~8.5 Hz	~1.8 Hz	~1.8 Hz

Several key trends emerge from the results in this chapter:

1. **Horizontal dominant response is the fundamental mode, while vertical dominant response often is not:** In the horizontal direction, the lowest-frequency (fundamental) resonance is consistently the primary signature used to define the building's horizontal behavior, and it aligns with the dominant transfer-function peak (Table 3.13). In contrast, in the vertical direction, the dominant peak is often located at a higher frequency than the lowest detected vertical range. This observation can be explained by the fact that the vertical floor-to-reference response is influenced not only by global axial deformation of the primary vertical system (columns/walls), but also by higher-frequency vertical mechanisms, such as floor-system bending, local slab/beam

participation, and higher-order axial modes, which can collectively produce larger relative floor accelerations (and therefore larger transfer-function amplification) than the first vertical mode range.

2. **Vertical modal frequencies are higher than horizontal modal frequencies for the same structure, especially for dominant modes:** Table 3.13 shows that dominant vertical frequencies fall in the ~5–10 Hz range, whereas dominant/fundamental horizontal frequencies are ~0.7–1.8 Hz for these buildings. This happens because vertical vibration is primarily governed by the combination of the vertical system's axial stiffness and the bending stiffness of floor systems, both of which are typically much larger than the lateral stiffness of building frames/walls. Higher stiffness generally leads to higher natural frequencies, so vertical resonances commonly occur at shorter periods than horizontal modes.
3. **At dominant frequencies, transfer-function amplification increases with elevation in both vertical and horizontal directions:** Across the case-study buildings, the dominant frequency bands are repeatedly associated with an amplification pattern that grows with floor level, as visible in the multi-floor transfer-function plots (Figures 3.1-3.13). This behavior can be an indication of a global mode shape that is consistent with the identification logic described in the framework. For global modes, the mode shape magnitude generally increases toward upper stories (whether in lateral displacement/acceleration for sway or in relative vertical floor motion for vertical modes that are observable in the instrumented layout). This observation in the vertical direction will be re-examined in Chapter 4.

4. **Coherence decreases near the edges of the usable bandwidth:** Across multiple buildings, low-frequency peaks that lie close to the lower usable bandwidth boundary show reduced and/or more variable coherence, and in some cases are not observed in a given event (e.g., fundamental peaks missing in some Pacoima summaries). Similarly, coherence tends to drop at higher frequencies. This behavior is expected since filtering, limited record energy, and reduced signal-to-noise ratio weaken the linear input–output relationship (or make it harder to estimate reliably), causing the coherence to decrease.

Overall, the data-driven frequency identification has yielded a set of reliable modal frequency bands for each building, highlighting the distinctions between vertical and horizontal dynamic behavior. These empirical findings provide a baseline for comparison with analytical results. Chapter 4 will present a simulation-based modal analysis for a selected building (JPL183) as a case study, allowing direct comparison between the data-derived frequencies from Chapter 3 and those predicted by a detailed numerical model.

CHAPTER 4. Identification of Structural Vertical Frequencies via Simulation

This chapter focuses on identifying the natural vertical vibration characteristics of an instrumented mid-rise building through numerical simulation. An initial ETABS model developed by collaborators at Caltech (Massari et al., 2017) is refined and analyzed. The objectives of this chapter are:

1. Investigate how many modes are required to achieve high cumulative vertical modal mass participation and quantify the computational implications.
2. Extract the building's vertical modal properties (natural frequencies and vertical modal mass participation factors) using the numerical model.
3. Differentiate global vertical modes from slab-dominated vibrations using a stiffness-perturbation strategy.
4. Cross-check simulation results against data-driven frequency bands identified from the CSN sensor recordings in Chapter 3.

To achieve these goals, the chapter is organized as follows: Section 4.1 describes the case-study building (JPL 183) and the development of its numerical model. Section 4.2 evaluates the number of modes required for reliable vertical modal analysis and the associated computational cost. Section 4.3 reports the baseline and stiffness-perturbed modal results to distinguish global vertical modes from slab-dominated modes. Section 4.4 compares the simulation-derived frequencies with the data-driven frequency bands identified from earthquake recordings in Chapter 3

4.1. Numerical Model for Case Study (JPL 183)

The case study for the simulation approach is the JPL 183 building, a nine-story structure located at NASA's JPL campus. This building is instrumented with a dense array of CSN sensors, enabling a rich comparison between simulation and real seismic response data. The building has two vertical columns of triaxial accelerometers on its west and east sides, with two sensors per floor, for a total of 18 sensors covering all floors (Figure 4.1). These sensors provided the data used in Chapter 3 to identify candidate vertical frequencies.

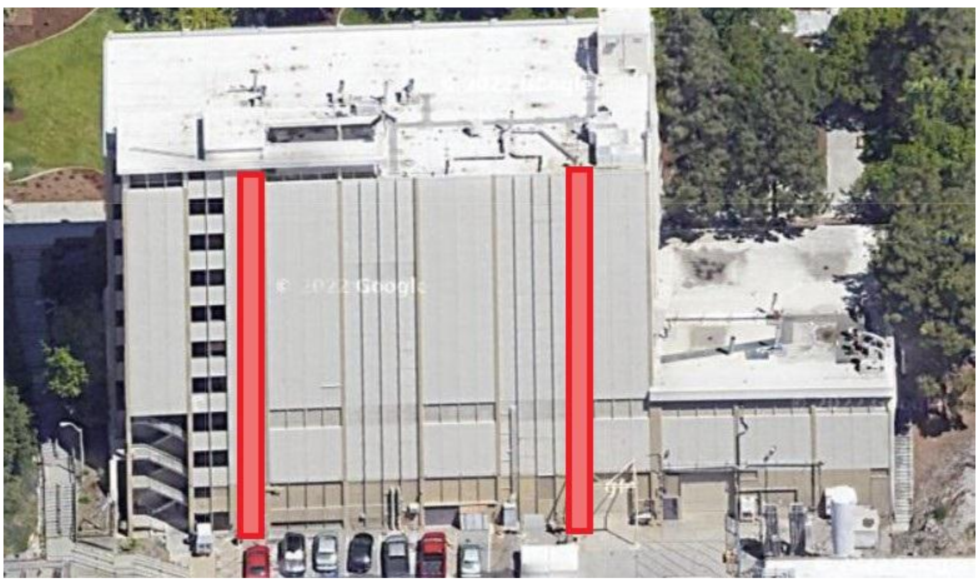

Figure 4.1. Sensor placement on the JPL 183 building (south elevation view), with two vertical arrays of sensors indicated by red markers on the western and eastern facades. (image source: Google Maps)

To correlate the simulation results with the data-driven findings, the sensor locations are explicitly mapped to the corresponding nodes of the finite element model. A Python script was developed to retrieve precise sensor position coordinates from the CSN metadata and to ensure that the ETABS model contains node points at those same locations (Figure 4.2).

```
For JPL 183, Sensors are not vertically alignment

 9 sensors has the Latitude: 34.19933, we named them "type 1"
 9 sensors has the Latitude: 34.19932, we named them "type 2"
 the distance between sensors type 1 and type 2 : 30.37 m

Please select based on which coordinate analyzed should be done
```

Figure 4.2. Output of a Python script identifying the floor plan coordinates of the CSN sensors in JPL 183, used to map sensor locations to the ETABS model nodes.

An architectural drawing of the building's floor plan (Figure 4.3, showing the 7th floor as an example) further illustrates the floor layout and the sensor positions on each level, which helped in aligning the model nodes with sensor coordinates.

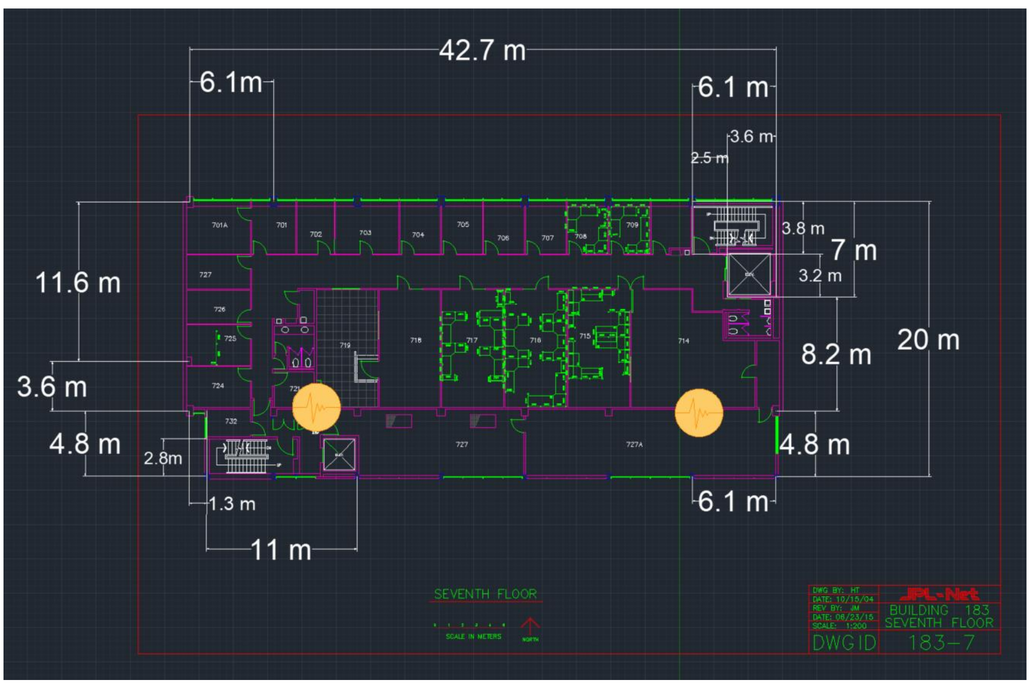

Figure 4.3. AutoCAD depiction of JPL building 183's 7th Floor Plan, including dimensions (Excerpt from the building's blueprints), with sensor locations indicated by orange circles.

JPL 183 is a steel moment-resisting frame structure with reinforced concrete floor slabs, and it is braced by masonry infill/shear walls at its east and west sides (two tall shear-wall piers extending the full height of the building). To investigate its vertical dynamic characteristics, a detailed 3D numerical model was developed in ETABS (Computers and Structures, 2023). The initial ETABS model was created from the original design drawings by Caltech researchers (Massari et al., 2017). In this study, the model has been refined and expanded for the specific purpose of vertical frequency analysis. Figure 4.4 shows a three-dimensional view of the ETABS model. In Figure 4.4, floor slabs are modeled with shell elements (depicted as horizontal plate elements). The model explicitly captures the full geometry and material properties of JPL 183, including all beams, columns, walls, and floor diaphragms.

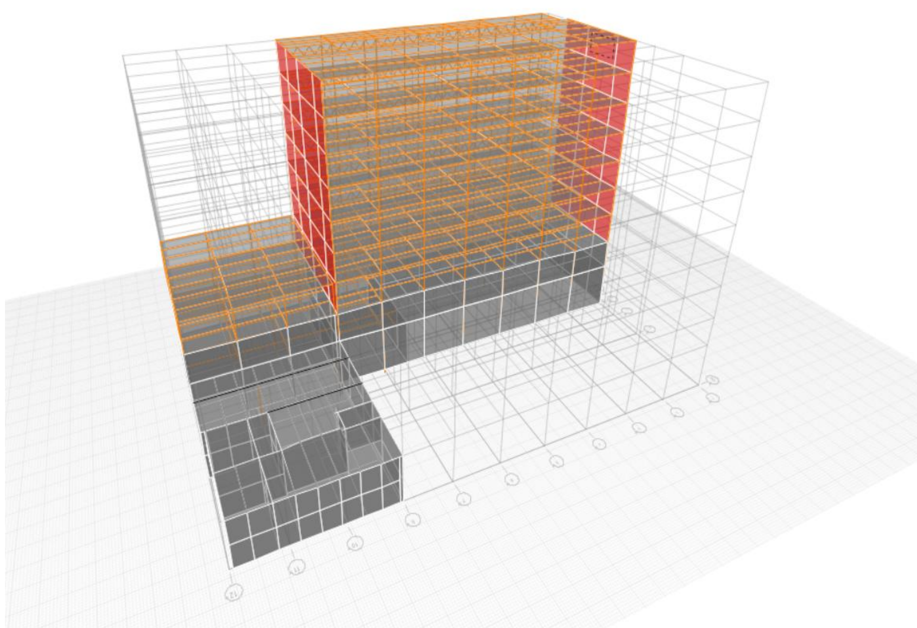

Figure 4.4. Three-dimensional ETABS model of the JPL 183 building, showing the steel frame (moment-resisting beams and columns) as line elements and the two primary shear-wall piers (in red) on the east and west sides that provide significant vertical and lateral stiffness to the structure

Every floor level was modeled with its actual plan shape and dimensions. The first through fourth floors have unique layouts due to geometry and other architectural features, while the fifth through ninth floors share a common "typical" plan. Figure 4.5 presents an overview of the floor plan geometry for selected levels. The model explicitly represents all floor diaphragms and their extents at each level, which is important for capturing distributed vertical mass and stiffness.

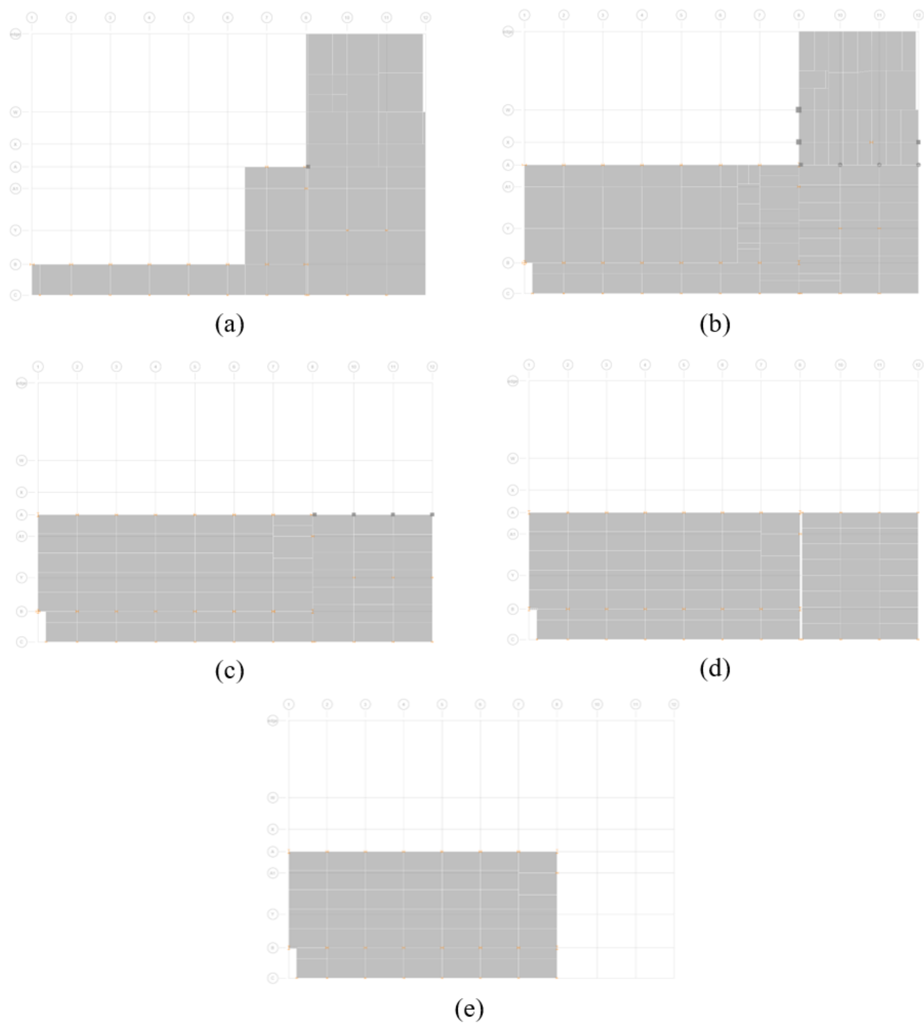

Figure 4.5. Floor plans of JPL 183 at various levels included in the ETABS model: (a) 1st floor corresponding to the ground-level reference in the CSN metadata (base), (b) 2nd floor, (c) 3rd floor, (d) 4th floor, and (e) 5th–9th floors (typical). These plans were used to assign the floor slab geometry and mass distribution in the model for each story.

The floor slabs are modeled as concrete shell elements (assuming uncracked concrete properties for stiffness). Four distinct slab thicknesses were assigned in accordance with the original design: 7.5 in, 6 in, 4.5 in, and 3.5 in at various levels. Figure 4.6 illustrates this variation in slab thickness across the height of the building, with different colors indicating the slab thickness assigned to each floor in the model. The lower floors use thicker slabs for higher capacity (e.g., 7.5″ on parts of the 1st floor, highlighted in purple in the model), whereas the typical upper floors have thinner slabs (4.5″ or 3.5″, shown in green and orange).

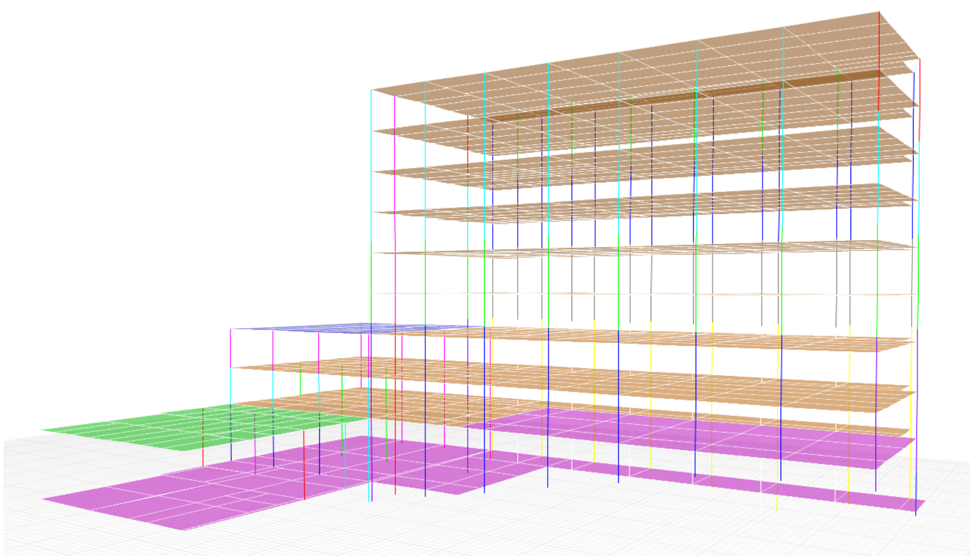

Figure 4.6. Variation of floor slab thickness across different stories in the JPL 183 model.

The structural wall elements in the initial model are of two types: (1) unreinforced masonry infill walls, which are modeled with an equivalent elastic stiffness (approximately 9″ thick masonry), and (2) reinforced concrete shear walls, with thicknesses varying up to 48″–72″ at the base. Figure 4.7 shows the wall elements in the ETABS model color-coded by thickness: the teal-colored walls indicate masonry panels above the base level (~9″ thick), while the red, yellow, and other warm colors correspond to concrete shear wall segments of various thicknesses (10″ up to

72″) as per the original design. All steel columns and beams in the model use their as-built cross-sectional properties. Each floor's beams and girders connect to the columns and support the shell slab elements, ensuring the composite action of the frame and slab is represented.

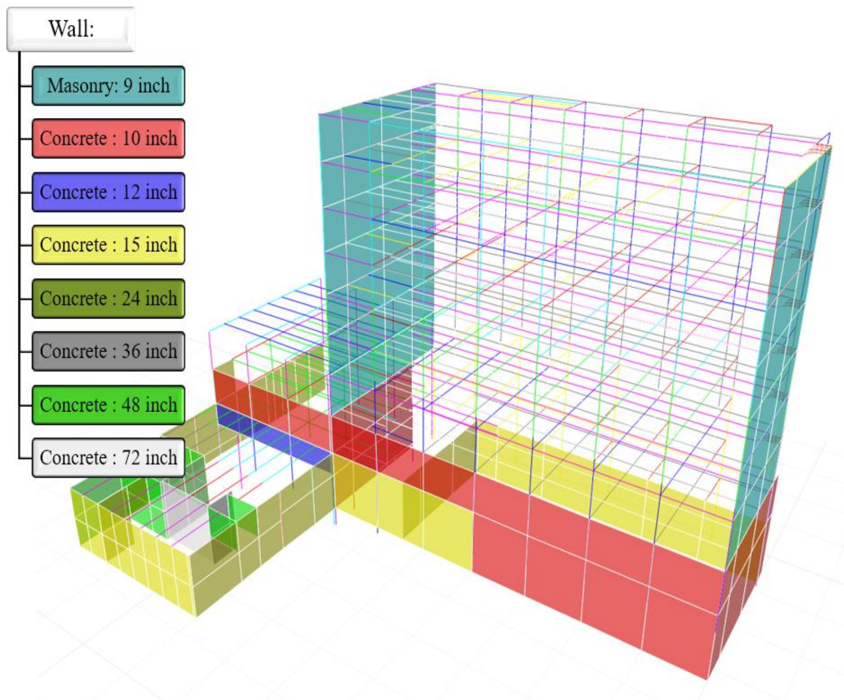

Figure 4.7. Masonry walls and reinforced concrete shear walls as modeled in JPL 183, color-coded by thickness.

At the base of the structure, all columns and wall supports are modeled as pinned. Gravity loads, including the building's self-weight (dead load), live loads, superimposed dead loads, and façade loads, were applied to the model in accordance with the design gravity load criteria. These gravity loads contribute to the total mass of the structure and thus influence its dynamic behavior in the vertical direction.

Several important modifications were made to the initial Caltech-provided model to tailor it for vertical analysis:

- **Vertical mass inclusion**: The original model did not include lumped vertical masses at all nodes. In the revised model, mass in the vertical direction was assigned at every node of the finite element mesh. This ensures that the modal analysis captures the vertical inertia of floor slabs and other components, which is critical for extracting vertical modes.

- **Refined slab meshing:** The finite-element mesh for the floor slabs was refined to better capture higher vertical frequency local modes (such as slab bending and floor panel vibrations). The initial model meshed each floor with roughly one shell element per bay (~ 6.1 m by 3.6 m elements); this coarse mesh could underrepresent the vertical behavior of the slabs at higher modes. The mesh was refined so that the largest element dimension is about 1.5 m (resulting in roughly 8× more elements per floor compared to the original mesh). Figure 4.8 visualizes the effect of slab meshing on mode shape: Figure 4.8.a shows the original coarse mesh, and Figure 4.8.b shows the refined mesh. The refined mesh increases the model's degrees of freedom, enabling it to capture intricate vertical mode shapes (e.g., higher-order slab flexure) that were previously unaccounted for.

- **Adding structural elements**: A careful review of the building drawings was conducted to identify any structural elements that were missing in the initial ETABS model. Minor omissions were corrected; for example, a floor beam on the 1st level that was absent in the original model was added to ensure that all load paths and stiffness contributions are present in the numerical model.

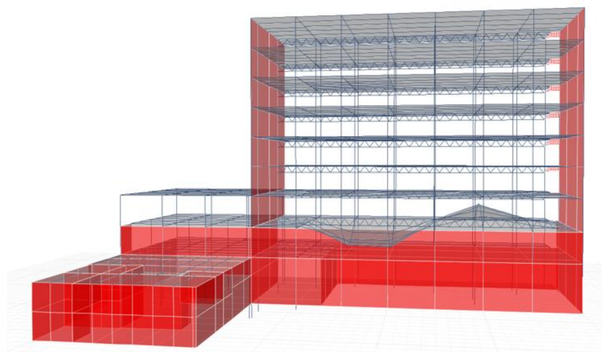

(a)

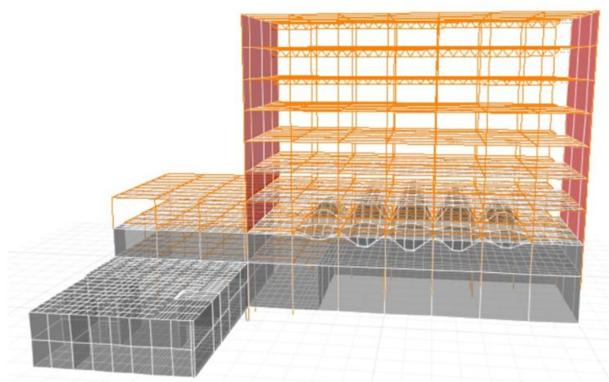

(b)

Figure 4.8. Effect of slab mesh refinement on the simulated vertical mode shape of the JPL 183 ETABS model. a) Mode shape obtained using the original coarse slab mesh, b) Mode shape obtained using the refined slab mesh

With the enhanced model in place, we performed modal analyses to extract the building's natural vibration modes in the vertical direction. Key dynamic properties obtained include natural frequencies and modal mass participation ratios. Before focusing on the frequencies themselves, an important practical question is how many modes are required to adequately represent vertical motion. Since vertical vibrations involve many local slab modes, a large number of modes may be needed to accumulate a significant total mass participation in the vertical direction.

4.2. Required Number of Modes for Vertical Modal Analysis

To assess the structural behavior of the JPL 183 building in the vertical direction, it is important to determine an appropriate number of modes to include in the modal analysis. This involves balancing computational efficiency with analytical precision. Selecting too few modes may result in an incomplete or even misleading characterization of the building's vertical dynamics (missing important modes), whereas extracting too many modes can introduce significantly increased computational time without much improving results. Deciding on the "optimal" number of modes requires consideration of the complexity of the structure (number of degrees of freedom), the frequency range of interest, and the available computational resources.

In standard practice, seismic design codes such as ASCE 7 suggest using enough modes to achieve a high cumulative modal mass participation (typically >90%) in each principal direction (ASCE, 2022). However, such guidance primarily targets horizontal (lateral) modal analysis, in which 90% modal mass participation can be achieved with a few first modes, and these standards do not explicitly address vertical modal analysis. For a complex floor system such as JPL 183, it was not immediately clear how many modes would be needed to reach 90% mass participation in the vertical direction, which motivated a series of trial analyses.

Several modal analysis scenarios were conducted, extracting progressively larger numbers of modes, to evaluate the cumulative vertical modal mass participation (MMP) achieved and the computation time required in each case. The scenarios and the corresponding results are summarized in Table 4.1.

Table 4.1. Results for Different Scenarios and the Number of Modes for Vertical Modal Analysis

Number of Modes	Analysis Runtime on CPU[6]	Relative Runtime	Cumulative Vertical MMP* (%)
50	~5 minutes	100%	0.1%
400	~2 hours	240%	12%
2,000	~7 hours	840%	44%
4,000	~18 hours	2160%	75%
10,000	>50 hours	>6000%	96.4%

* MMP = Modal Mass Participation in the vertical (U_Z) direction

Based on the results in Table 4.1, thousands of modes are required to capture a high percentage of the total mass in the vertical direction for this building. Even with 4,000 modes, the cumulative vertical modal mass participation was only about 75%, and it required approximately 18 hours of computation to reach that point. In fact, nearly 10,000 modes had to be extracted to exceed 90% of vertical mass participation (at the cost of more than 50 hours of runtime). By contrast, horizontal modal analyses for the same structure converge to 90% mass with far fewer modes; only 3 to 10 modes are needed if one ignores vertical mass participation. This stark difference highlights that the vertical response of JPL 183 is distributed across a large number of modes. The reason is that there are many floor slab vibration modes (local vertical modes) each contributing a small fraction of the total mass, so thousands of these modes must be summed to reach a substantial cumulative mass.

[6] CPU runtime was measured on a local Windows PC equipped with an 11th Gen Intel(R) Core(TM) i7-1185G7 processor @ 3.00 GHz and 16.0 GB RAM.
Reported runtimes are approximate wall-clock times for the ETABS modal analyses and may vary depending on solver settings, model configuration, the number of nodes, and background processes. These values are provided primarily to illustrate the relative computational cost of the different modal-analysis scenarios, rather than to serve as machine-independent benchmark runtimes.

To visualize how vertical modal mass participation is distributed across the extracted modes, Figure 4.9 presents a bar chart of individual-mode MMP values, indicating each mode's contribution to the total vertical mass.

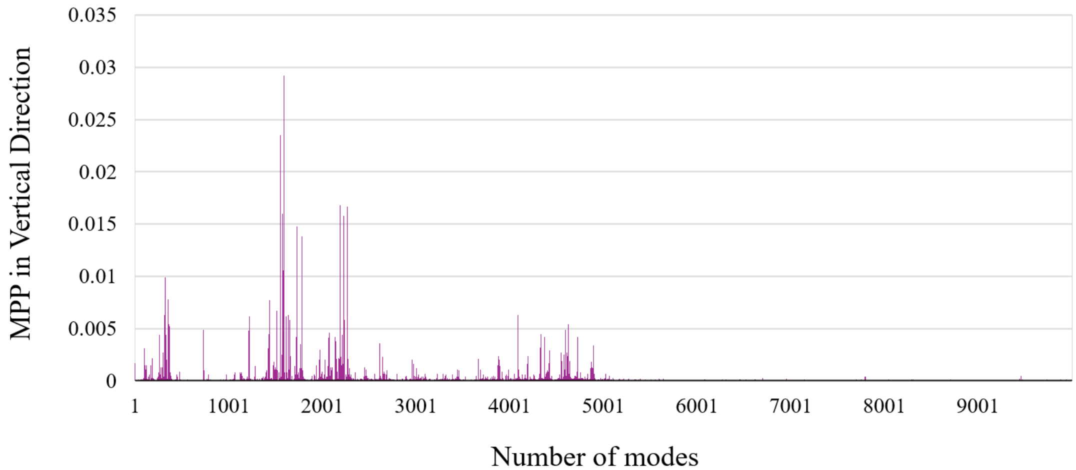

Figure 4.9. MMP distribution in different vertical modes

As shown in Figure 4.9, the vast majority of modes contribute negligible vertical MMP (typically well below ~0.5%), whereas only a limited number of modes reach participation on the order of 1–3%. As a result, the building's vertical inertia is not dominated by a small subset of low-order modes. Consistent with this observation, Figure 4.10 (a) shows the cumulative vertical MMP increasing gradually as additional modes are included. It reaches high participation levels (e.g., ~90%) only after several thousand modes and then gradually plateaus, indicating diminishing gains from including additional higher-order modes. Figures 4.10 (b) and 4.10 (c) present the cumulative modal mass participation in the two orthogonal horizontal directions (HNE and HNN).

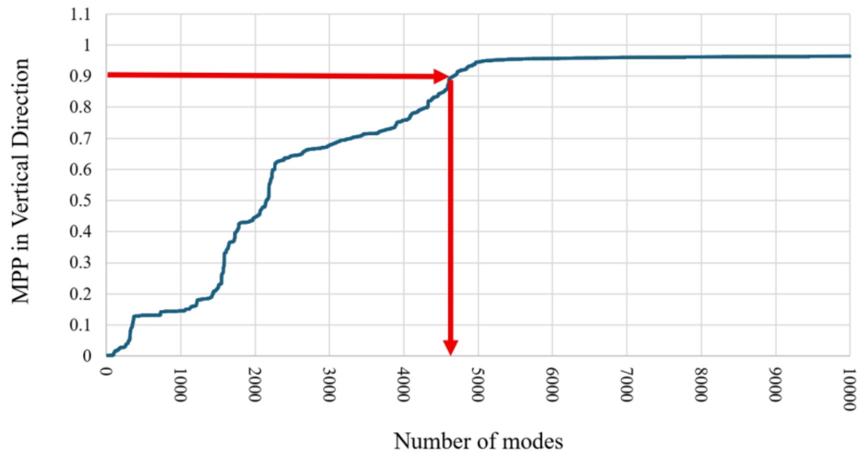

(a)

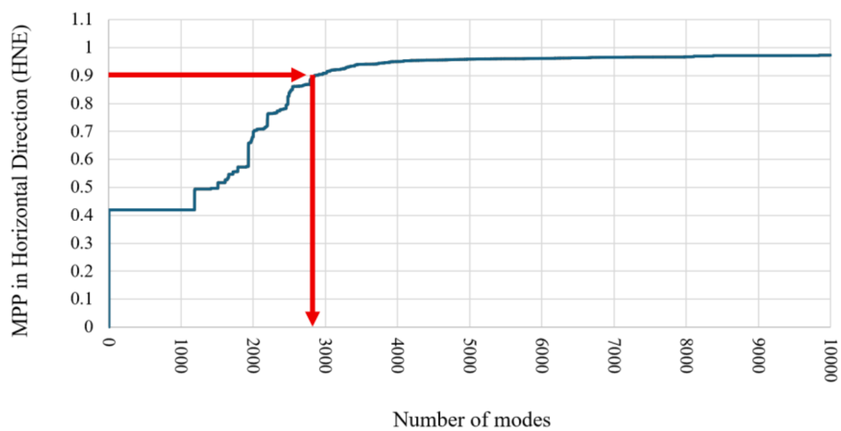

(b)

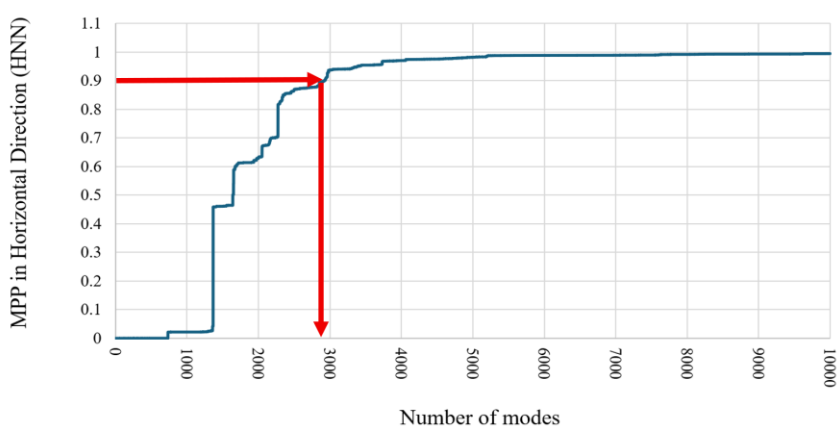

Figure 4.10. Cumulative MMP in a) vertical direction b) horizontal (HNE), and c) horizontal (HNN)

In both horizontal directions, a substantial portion of the participating mass is captured by a relatively limited subset of modes, and the cumulative participation rises to ~90% by approximately 3,000 modes, after which the curves plateau. It should be emphasized that this does not imply the existence of 3,000 predominantly horizontal modes. Rather, this count corresponds to the first approximately 3,000 eigenmodes of the same finely discretized three-dimensional model also used for vertical modal analysis. In that model, translational mass is retained at the slab-shell joints in all directions, and the floor system is represented with a dense slab mesh and additional nodes introduced to resolve vertical slab response. By contrast, in a conventional lateral seismic idealization that does not retain the vertically enriched slab discretization, 90% cumulative mass participation in each horizontal direction is achieved within the first few global lateral modes, specifically fewer than 30 modes in the simplified comparison model. Therefore, by comparison, the vertical cumulative MMP (Figure 4.10) accumulates more gradually and requires several thousand additional modes to reach similar participation levels.

It is evident from these results that with the current level of discretization (mesh density) and structural complexity, obtaining >90% vertical mass participation requires extracting near 5,000 modes, which dramatically increases computation time. Furthermore, we observed that a model including full vertical mass yields a much slower accumulation of modal mass than a model focusing on horizontal modes only. For instance, if distributed vertical mass is excluded (i.e., only lateral inertia considered), 90% cumulative mass in each horizontal direction was achieved with fewer than 30 modes in this building. With distributed vertical mass included, that number jumps to a few thousand (for horizontal) and many thousands (for vertical).

In summary, the JPL 183 Building study demonstrates that the number of modes required for a reliable vertical modal analysis depends on several factors, including the structure's geometry, material stiffness, support conditions, finite element mesh resolution, and available computational resources. Notably, achieving the traditional 90% cumulative MMP in the vertical direction demands analysis of substantially more modes than needed for horizontal analysis. If localized slab modes are of limited significance to global structural behavior, 90% vertical MMP may be unnecessary. In other words, the 90% MMP target widely used in horizontal seismic analysis (as suggested by ASCE 7 for principal horizontal directions) may not be a good benchmark for vertical analysis. This observation reveals a gap in standard practice and underlines the need for building codes and researchers to revisit and clarify guidance on the appropriate number of modes needed for vertical structural analysis and adopt more efficient and insightful criteria. A future study is needed to analyze multiple buildings and conclude a minimum MMP in the vertical direction for the investigation of global building response, rather than slab vibrations.

4.3. Identifying Global vs. Slab Vertical Modes via Stiffness Perturbation

Through the baseline modal analysis of JPL 183 (with the full model and unmodified properties), we first identified the dominant vertical frequencies of the building by selecting the modes with the highest participation in the vertical direction. These modes represent the strongest contributors to vertical motion. Table 4.2 summarizes ten representative modes with notable MMP in the vertical direction, spanning frequencies from ~1 Hz to ~20 Hz.

Table 4.2. Baseline Modal Analysis Results for Vertical Frequencies of the JPL 183 Building

	Mode	Period	Frequency	Vertical MMP (U_Z)	Sum U_Z
1	318	1.004	0.996	0.010	0.070
2	1548	0.272	3.676	0.024	0.257
3	1572	0.245	4.082	0.016	0.285
4	1582	0.236	4.237	0.011	0.300
5	1586	0.228	4.386	0.029	0.330
6	1728	0.124	8.065	0.015	0.394
7	1780	0.113	8.850	0.014	0.425
8	2185	0.056	17.857	0.017	0.529
9	2186	0.056	17.857	0.014	0.543
10	2227	0.051	19.608	0.016	0.589

The strongest contributors in this set are concentrated in the 3.68–4.39 Hz band ($U_Z \approx 0.011 - 0.029$), with the largest single-mode vertical participation occurring at 4.386 Hz. Additional modes with meaningful vertical participation occur near 8.065 Hz and 8.850 Hz. The lowest-frequency mode among those listed is 0.996 Hz, which is consistent with a global "breathing" response involving axial deformation of columns and walls; however, its vertical participation is relatively small compared with other modes.

It is important to distinguish between global vertical modes and slab-dominated local modes because each represents a fundamentally different deformation mechanism. Therefore, they influence the structure's vertical response in different ways. Based on the baseline results alone, it is not straightforward to determine which frequency bands correspond primarily to global vertical modes (dominated by the vertical elements, such as columns and shear walls) versus slab-dominated local modes, because modes in the 3–5 Hz and 8–9 Hz ranges can involve varying combinations of slab flexure and frame/wall axial deformation.

To distinguish these mechanisms, two stiffness-perturbation studies are performed. We created two variant models with altered stiffness properties, in order to suppress one type of behavior at a time and observe the effect on the modal frequencies: 1) Slab-stiffened model and 2) Vertical-element-stiffened model.

4.3.1. Identifying Global Vertical Modes via Slab-stiffened case

In this case, the stiffness (Young's modulus, E) of all floor slab elements was artificially increased by a large factor (while keeping all columns and walls at their baseline stiffness). By making the slabs much stiffer, we effectively suppress modes that involve significant slab deformation, allowing the global vertical modes (where columns and walls deform axially) to stand out more clearly. A modal analysis was performed on this slab-stiffened model, and the prominent vertical modes were identified as before. The results (Table 4.3) show a markedly different set of dominant frequencies compared to the baseline.

Table 4.3. Modal Analysis Results for Vertical Frequencies in the Slab-stiffened model

	Mode	Period	Frequency	Vertical MMP (U_Z)	Sum U_Z
1	76	0.13	7.692	0.057	0.353
2	23	0.271	3.69	0.038	0.21
3	18	0.291	3.436	0.029	0.154
4	10	0.323	3.096	0.028	0.082
5	11	0.312	3.205	0.024	0.106
6	5	0.356	2.809	0.023	0.035
7	71	0.139	7.194	0.019	0.291
8	6	0.349	2.865	0.017	0.052
9	597	0.048	20.833	0.016	0.598
10	14	0.301	3.322	0.015	0.121

In the stiffened-slab scenario, the highest-participation vertical mode occurs at approximately $7.44 \pm 0.25\ Hz$, and other strong modes occur around $3.20\ \pm 0.29\ Hz$. The key observation is that these frequency bands did not shift much when the slabs were stiffened. These frequencies, therefore, appear to be associated with the vertical frame elements, i.e., they are likely the global vertical modes of JPL 183.

4.3.2. Identifying Global Vertical Modes via Vertical-element-stiffened model

In the second variant, the stiffness of the vertical elements, including all columns and walls, was substantially increased, while slab properties were kept at their baseline values. This modification reduces global vertical deformation by making the vertical load-resisting system comparatively rigid, such that the remaining prominent modes are governed primarily by the floor slabs, which become the more flexible components. Modal analysis of this vertical-stiffened model yielded the dominant frequencies listed in Table 4.4.

Table 4.4. Modal Analysis Results for Vertical Frequencies in the Vertical-element-stiffened model

	Mode	**Period**	**Frequency**	**Vertical MMP (U_Z)**	**Sum U_Z**
1	1598	0.183	5.464	0.032	0.285
2	1597	0.183	5.464	0.021	0.253
3	1592	0.184	5.435	0.013	0.225
4	353	0.992	1.008	0.011	0.111
5	1600	0.182	5.495	0.011	0.296
6	2478	0.026	38.462	0.010	0.408
7	340	0.996	1.004	0.010	0.085
8	1428	0.337	2.967	0.008	0.184
9	1622	0.159	6.289	0.007	0.317
10	2542	0.025	40.000	0.007	0.417

In this scenario, the most significant vertical modes occur at roughly 5.4–5.5 Hz, with the largest single-mode vertical MMP occurring at 5.464 Hz. A mode near 1.0 Hz also appears with moderate participation. Therefore, frequency ranges of 5.63±0.33 Hz and 1 Hz appear more likely to correspond to the frequencies of the slabs in JPL 183.

In summary, the stiffness-perturbation simulations allow us to classify the key vertical modal frequency bands of the JPL 183 building by their origin:

- Frequencies in the **3–4 Hz range** and a higher band around **7–8 Hz** represent **global vertical modes** of the building, where the vertical frame elements, including columns and walls, deform in phase through the building's height (the whole building "bouncing" as a unit). These frequency bands remained largely unchanged when the slabs were stiffened.

- Frequencies in the **~5 Hz to 6 Hz range** are predominantly associated with **floor slab vibration modes**, where the floor slabs bounce between the column supports. These frequencies became the dominant modes when the frame was made rigid, indicating their slab-dominated character.
- An intermediate frequency around **~4 Hz** appears to involve a coupled mode where both the slabs and the vertical frame participate in the motion (in the baseline model). In the stiffening studies, the ~4 Hz mode changed behavior when either component (slab/frame) was stiffened, suggesting it is not a purely global or slab mode but a mixed one.
- A low-frequency mode near **~1 Hz** is present in the modal results but is not classified as a global vertical-element mode, because it does not shift when columns and walls are stiffened. Also, this mode had relatively low participation. Since JPL 183 is very stiff vertically, such a low frequency of 1 Hz may involve some foundation flexibility.

By performing these comparative simulations, we have effectively differentiated the global vs. local (slab) vertical modes in the structure and identified their respective frequency bands. The next section examines how well the simulation results match the data and discusses any discrepancies.

4.4. Data-Driven vs. Simulation Vertical Frequencies

Having identified the key vertical frequencies of the JPL 183 Building through simulation, we now compare these findings with the data-driven results obtained from actual earthquake recordings (Chapter 3). In Chapter 3, a systematic analysis of the recordings, using floor Fourier spectra, PSDs, transfer functions, and coherence, revealed consistent frequency peaks that we interpret as the building's vertical natural frequencies.

Across the four earthquakes analyzed (El Monte, Pacoima, Ridgecrest, and Searle Valley), the recordings in JPL 183 consistently exhibit five repeatable peak families centered near 1.6–1.9 Hz, 3.1–3.4 Hz, 4.0–4.4 Hz, 5.4–5.6 Hz, and 7.2–7.6 Hz (Table 3.1). The persistence of these spectral peaks across different earthquakes and across different floors strongly suggests that they correspond to the building's intrinsic vertical vibration modes, rather than artifacts of any specific input motion. Among these, the 7–8 Hz family produces the most pronounced amplification and the strongest elevation-dependent growth in the transfer functions and is therefore interpreted as the dominant vertical response band of JPL 183. The ~3.2 Hz and ~4.2 Hz families are also highly repeatable and generally supported by moderate-to-high coherence, whereas the lowest-frequency family (1.6–1.9 Hz) lies closest to the lower usable bandwidth and is more sensitive to record-specific signal-to-noise conditions (as reflected by reduced coherence in the Pacoima record).

The simulation results show remarkable agreement with the measured data on these frequency bands. From the baseline modal analysis and stiffness-perturbation studies (Section 4.3), we determined that the JPL 183 Building exhibits prominent vertical modes at approximately 3–4 Hz and 7–8 Hz (global modes), as well as slab-dominated modes at approximately 5–6 Hz. This aligns almost one-to-one with the frequencies identified in the CSN data: ~3.2 Hz, ~4.0 Hz, ~5.5 Hz, and ~7.4 Hz.

Specifically, both approaches converge on the conclusion that the building's fundamental global vertical mode is the one producing the ~3–4 Hz peak in the recordings. The simulation indicates that this mode is primarily axial deformation of the vertical elements (columns and walls). The secondary global mode appears in the ~7–8 Hz range and is consistently observed in the data (the dominant peak in the recordings). On the other hand, the simulation reveals a slab-flexure mode in the ~5–6 Hz.

One important interpretation issue is that the measured dominant frequency is also influenced by the locations at which the response is recorded. For JPL 183, the available CSN sensors are installed along the east and west sensor lines and are located closer to the perimeter framing and vertical support lines than to the mid-panel regions of the floor slabs. Therefore, the strong measured amplification in the 7–8 Hz range is consistent with the simulation-based interpretation of this band as a global vertical response involving the vertical framing system. However, this observation should not be interpreted as implying that slab-dominated modes are unimportant. Because the ~5–6 Hz band is associated with slab-flexural vibration in the simulation, sensors installed closer to the middle of slab panels could potentially record stronger slab-dominated response and, in some cases, may identify the slab-frequency band as the locally dominant response. Thus, the dominant vertical frequency identified from measured data should be understood as a response feature that depends not only on the structural modal properties and earthquake excitation, but also on sensor location within the floor plan.

There are a few noteworthy differences between the simulation and the recorded-data results that merit discussion. First, the baseline FE model contains a mode near 1.0 Hz with non-negligible vertical participation, whereas the data-driven analysis in Chapter 3 does not show a stable, repeatable peak at ~1 Hz. This is consistent with the Chapter 3 interpretation strategy, which excludes frequencies below the lower usable bandwidth because low-frequency content is more sensitive to limited excitation and elevated noise. In the recordings, the lowest repeatable response range instead appears in the ~1.6–1.9 Hz range.

Second, the modal analyses predict several higher-frequency modes (e.g., ~18–20 Hz and above), but comparable peaks are not consistently apparent in the earthquake recordings. At higher frequencies, the transfer functions typically exhibit lower coherence and increased noise measurement. Additionally, due to constraints on usable bandwidth in signal processing, we can not see these modes clearly in the results of Chapter 3.

Overall, the simulation and data-driven results are consistent at the level of the primary frequency bands. Both approaches identify repeatable vertical response ranges near ~3.1–3.4 Hz and ~7–8 Hz (global vertical modes) and near ~5–6 Hz (slab-dominated modes), with the remaining differences attributable to modeling idealizations and bandwidth/signal-to-noise limitations in the recordings. Figure 4.11 provides an annotated example transfer function illustrating the alignment between the measured peak families and the simulation-derived modal bands.

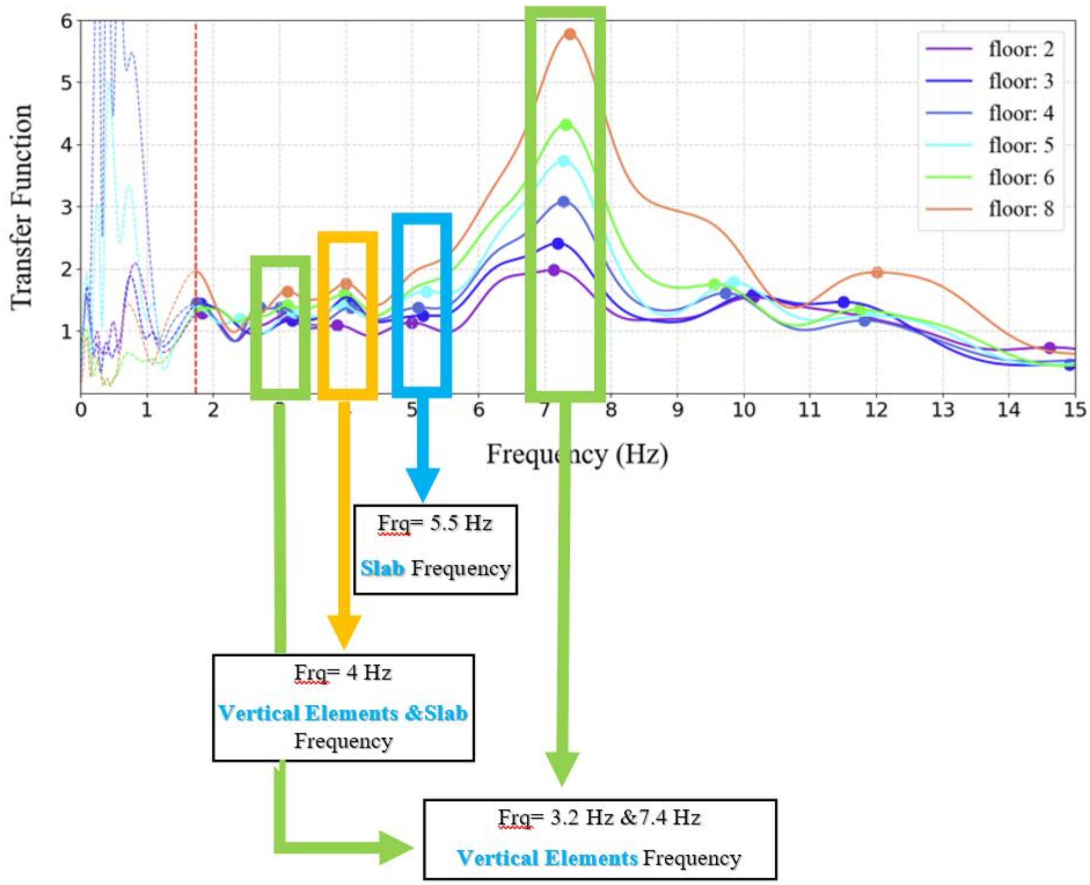

Figure 4.11. Comparison of data-driven and simulation-derived vertical frequencies for JPL 183. The plot shows a representative floor-to-base transfer function (PSD ratio) from the El Monte earthquake, with peaks near 3.2 Hz, 4.0 Hz, 5.5 Hz, and 7.4 Hz. Colored annotations indicate the interpretation of each peak: green for global vertical modes (vertical frames), blue for slab-dominated modes, and orange for a coupled mode involving both slab and frame.

CHAPTER 5. Floor Response Spectra

Floor response spectra (FRS) describe the intensity measure demand experienced by nonstructural components, equipment, and building contents. They are obtained from the responses of a single-degree-of-freedom (SDOF) system subjected to an input motion. The input motion to the SDOF has been filtered and amplified by the supporting structure. Unlike ground response spectra, FRS represent motion at a specific floor level and therefore depend on the dynamic properties of the building, the vibration period of the component, the floor elevation, and the frequency content of the earthquake record. This distinction is especially important for acceleration-sensitive nonstructural components, whose seismic demand can differ substantially from that of the ground motion alone.

This chapter evaluates vertical and horizontal FRS using the processed CSN recordings from six instrumented mid-rise buildings subjected to four earthquake events. For each building, event, floor, and sensor line, the 5%-damped pseudo-spectral acceleration is computed and used to evaluate the vertical floor response spectra (VFRS), horizontal floor response spectra (HFRS), and height amplification factors (HAF). The measured amplification trends are then summarized statistically and compared with the height-amplification assumptions in ASCE/SEI 7-22 Chapter 13. In the CSN metadata used in this study, Floor 1 corresponds to the ground-level record. Therefore, the measured HAF values are computed relative to the ground-level record. This convention is consistent with the reference condition used in the ASCE/SEI 7-22 Chapter 13 height-amplification framework, in which floor acceleration demand is expressed relative to the ground-level or base demand.

The chapter is organized as follows. Section 5.1 presents the background and motivation. Section 5.2 describes the data, FRS computation, HAF definitions, and ASCE/SEI 7-22 benchmarking approach. Sections 5.3 and 5.4 present the VFRS and HFRS results, respectively. Section 5.5 summarizes the key findings and recommendations.

5.1 Introduction and Background

Earthquake experience has repeatedly shown that a building may remain structurally stable yet lose critical functionality because of damage to nonstructural components (NSCs), including mechanical/electrical equipment, piping and sprinkler systems, ceilings, facades, and architectural attachments. NSC failures can create life-safety hazards (e.g., falling components), drive repair costs, and prolong downtime, directly affecting resilience goals that extend beyond collapse prevention (Bruneau et al., 2003). In performance-based earthquake engineering, this reality has elevated the importance of acceleration demand as a primary input for designing the seismic force resisting system for acceleration-sensitive NSCs, whose seismic response is driven predominantly by inertia forces rather than story drift (Filiatrault et al., 2021; Wang et al., 2021). A central challenge, however, is that the acceleration experienced by NSCs is not the ground motion itself, but the in-structure motion which has been filtered and amplified by the building.

Floor acceleration demands are commonly represented using floor response spectra (FRS). The FRS at a given floor is obtained by treating the recorded (or computed) absolute floor acceleration as the support excitation to a set of linear single-degree-of-freedom (SDOF) oscillators and extracting the peak response across a range of periods at a specified damping ratio. In this way, FRS captures not only the magnitude of floor accelerations, but also their frequency content, which is critical because floor motions are dynamically filtered by the building and can become resonant excitations for components whose vibration periods align with modal periods of the supporting structure (Merino et al., 2020; Miranda & Taghavi, 2005; Wang et al., 2021). This filtering is precisely why peak floor acceleration alone is often insufficient: a modest change in structural dynamic properties or component period can produce large changes in the spectral ordinates that control component demands.

Within this chapter, two directional variants of floor spectra are considered. HFRS describe period-dependent acceleration demands derived from horizontal floor motions, while VFRS describes analogous demands derived from vertical floor motions. This distinction between VFRS and HFRS matters because the mechanisms that shape amplification with height can differ markedly between horizontal and vertical responses (Acosta et al., 2023; Wang et al., 2021).

In practice, a commonly used spectral ordinate for nonstructural component qualification is the 5%-damped pseudo-spectral acceleration (PSA). Within this framework, peak floor acceleration may be viewed as the short-period limit of the same spectrum, representing the response of a very stiff oscillator and therefore providing a complementary measure for rigid-component demand. Because floor motion also varies systematically with elevation, both FRS and peak measures are naturally interpreted as a function of the normalized height, z/h, where z is the floor elevation above the base and h is the total building height. This enables consistent comparisons across floors and across buildings and makes height-wise amplification a central measure of floor acceleration demand.

The central focus of this chapter is the height amplification factor (HAF), which is a dimensionless measure describing how floor acceleration demands at a given elevation compare to input ground demand. Several parameters influence floor response, including the structural period, mode shapes, damping, structural inelasticity (if any), and record characteristics. However, the height-wise amplification is widely used in design because it is based on where the components are installed in the building. This amplification is represented in design standards using a simple function with floor height as the key input. With these issues in mind, the primary focus of this chapter is on the amplification of floor acceleration over the building height, the consistency of this variation across buildings and events, and whether the simplified assumptions made for current design capture the observed trends.

Building codes often try to strike a balance between accuracy and usability by using simplified procedures rather than requiring explicit spectra at every floor. In the United States, the primary framework for most projects remains the equivalent-static nonstructural component (NSC) force equation in ASCE/SEI 7-22 (ASCE, 2022), which incorporates a simplified height-amplification term. In this formulation, the code effectively assumes that the floor acceleration increases linearly with elevation, reaching approximately 3.5 times the base value at the roof. This approach is widely used because it reduces a complex, floor-dependent dynamic response to a single dimensionless factor. Its adequacy, however, depends on whether it reflects both the central tendency of this amplification and the variability across buildings in both horizontal and vertical directions.

Prior research has devoted considerable attention to the amplification of horizontal floor accelerations over the height of a building. Miranda and Taghavi developed a practical approximate method for estimating horizontal floor acceleration demands in multistory buildings that respond elastically or nearly elastically, showing that the variation with height depends on the structural dynamic properties and higher-mode contributions (Miranda & Taghavi, 2005). Subsequent research, particularly studies using instrumented buildings to assess horizontal floor demands, has demonstrated that the relationship between floor spectra and height depends on the structural characteristics of the building which are not fully captured by simplified representations (Anajafi & Medina, 2018; Fathali & Lizundia, 2011; Reinoso & Miranda, 2005).

The importance of focusing on height amplification is even greater in the vertical direction, where design practice has often relied on simplified proxies for estimating the demand (e.g., vertical design spectra derived by scaling horizontal spectra or constant vertical design effects) rather than explicit, height-dependent characterization based on the VFRS. Yet both field observations and analytical studies have shown that vertical response can be amplified over the height of a building. This issue was studied using twelve instrumented buildings affected by the Northridge earthquake, which documented peak vertical structural accelerations exceeding the base values by factors ranging from approximately 1.1 to 6.4 (Bozorgnia et al., 1998). This evidence based on recorded responses complements more recent analytical and simulation-based studies showing that vertical floor acceleration demand can increase with elevation, challenging the traditional assumption that buildings behave as vertically rigid systems for design purposes (Acosta et al., 2023; Moschen et al., 2015). Researchers further reported that vertical peak floor accelerations in elastic steel moment-resisting frames can reach up to five times the vertical peak ground acceleration and that the largest amplifications may occur at girder midspans, indicating that vertical demand can vary not only with height but also with location within a floor (Gremer et al., 2019). Comparable findings in terms of vertical spectral amplification over the building height have also been reported for reinforced concrete buildings (Francis et al., 2017; Mazloom & Assi, 2023).

Taken together, the studies on horizontal and vertical floor acceleration responses suggest that height amplification is real, often substantial, and not always consistent with simplified universal profiles; however, an important gap remains between mechanism-focused research and design-oriented empirical characterization. Many studies rely on analytical and idealized models or limited sensor configurations, which are necessary for identifying drivers but may not fully establish which HAF trends are robust across multiple buildings and events, nor quantify the associated dispersion. This gap is especially consequential for the vertical direction, where empirical data is very limited. This chapter addresses these gaps by developing empirical FRS in both the horizontal and vertical directions from dense, floor-by-floor triaxial recordings collected on the JPL campus using the CSN instrumentation framework.

5.2 Methodology

This section describes the workflow used to transform the processed CSN floor-acceleration recordings into directional FRS, height-wise amplification metrics, and code-comparison diagnostics. The methodology includes: (1) assembly of the processed absolute floor-acceleration data set, (2) computation and validation of the 5%-damped FRS, (3) derivation of period-dependent height-amplification metrics, (4) quantification of mean profiles and confidence intervals, and (5) benchmarking of the measured amplification profiles against the simplified and period-dependent formulations used in ASCE/SEI 7-22 Chapter 13.

5.2.1 Data and Processing Summary

The FRS analyses are carried out for the following six buildings located on the JPL campus: JPL 180, 183, 238, 264, 321, and 303. Each building is instrumented with at least one triaxial CSN accelerometer on each floor, enabling floor-by-floor measurement of two orthogonal horizontal components and one vertical component of motion. The recordings are obtained from the CSN database and prepared using the automated data pipeline described in Chapter 2.

To ensure a consistent basis for between-building comparisons, the analysis is restricted to the four earthquakes recorded in acceptable quality across all six buildings. These events include two moderate, nearby events (the M4.5 *El Monte* and M4.2 *Pacoima* earthquakes) and two larger but more distant events from the 2019 Ridgecrest sequence (the M6.4 *Searle Valley* foreshock and M7.1 *Ridgecrest* mainshock). During each of these earthquakes, CSN sensors captured the floor accelerations at a sampling rate of ~50 Hz, yielding a Nyquist frequency of ~25 Hz.

Let $c = (b, l, e)$ denote a unique building–sensor-line–earthquake combination, where b indexes the building, l the sensor-line, and e the earthquake. The absolute (or total) floor acceleration time series for a given floor j in component q is then denoted by

$$a_{cj}^{(q)}(t), \qquad q \in (V, H_1, H_2) \qquad \text{Eq 5.1}$$

where V denotes the vertical component and H_1 and H_2 denote the two orthogonal horizontal components.

All acceleration records are processed using the NGA-consistent strong-motion workflow adopted in Chapter 2, including high-pass and low-pass filtering, and zero-padding to align all channels associated with a given earthquake on a common time axis. The lower and upper filter frequency limits are respectively denoted by $f_{L,c}$ and $f_{U,c}$. The corresponding usable period interval is defined as

$$\mathcal{T}_c^{use} = \left[\frac{1.25}{f_{U,c}}, \frac{0.8}{f_{L,c}}\right] \qquad \text{Eq 5.2}$$

Periods outside $\mathcal{T}_c^{\mathrm{use}}$ are retained in spectral results for transparency but are not used as the basis for interpreting spectral peaks.

Some JPL buildings contain multiple vertical lines of triaxial sensors located at different plan positions. Accordingly, the FRS and height-amplification ratios are evaluated separately for each sensor line. This approach avoids mixing motions recorded at different plan locations, which may reflect torsional response, diaphragm effects, or other spatial variations within the building.

5.2.2 Computation and Validation of FRS

At each floor, the processed absolute floor acceleration is treated as the support excitation to a linear single-degree-of-freedom (SDOF) system. For a system with a natural period T, circular frequency $\omega_n = \frac{2\pi}{T}$ and damping ratio ξ, the equation of motion in terms of the relative to the floor motion displacement response $u_{cj}^{(q)}(t;T,\xi)$ is (Chopra, 2000):

$$\ddot{u}_{cj}^{(q)}(t;T,\xi) + 2\xi\omega_n\dot{u}_{cj}^{(q)}(t;T,\xi) + \omega_n^2 u_{cj}^{(q)}(t;T,\xi) = -\,a_{cj}^{(q)}(t) \qquad \text{Eq 5.3}$$

where c and j are defined in section 5.2.1. From this response, the spectral displacement is defined as

$$S_{d,cj}^{(q)}(T,\xi) = \max_t \left| u_{cj}^{(q)}(t;T,\xi) \right| \qquad \text{Eq 5.4}$$

The corresponding pseudo-spectral acceleration is

$$PSA_{cj}^{(q)}(T,\xi) = \frac{\omega_n^2}{g}\, S_{d,cj}^{(q)}(T,\xi) \qquad \text{Eq 5.5}$$

where g is the gravitational acceleration, so that the result is expressed in units of g.

This study adopts the 5% damped PSA at a given floor as the FRS measure. The floor spectra are generated in **R** computer package using the *PS_cal_cpp* routine from the "RCTC package" (Wang et al., 2017), with the processed acceleration time series, oscillator period, damping ratio, and time step $\Delta t = 0.02$s as inputs. This function returns a two-row output, with spectral acceleration in the first row and PSA in the second row. PSA is calculated at periods up to 10 s with a period increment of $\Delta T = 0.001$s.

The vertical floor response spectrum at the floor j is defined as

$$VFRS_{cj}(T) = PSA_{cj}^{(V)}(T, 0.05) \qquad \text{Eq 5.6}$$

For the horizontal direction, spectra are first computed separately for the two orthogonal horizontal components and then combined for a given period using the geometric mean. Thus, the horizontal floor response spectrum is defined as

$$HFRS_{cj}(T) = \sqrt{PSA_{cj}^{(H_1)}(T, 0.05)\, PSA_{cj}^{(H_2)}(T, 0.05)} \qquad \text{Eq 5.7}$$

The geometric-mean combination in Eq. (5.7) is adopted consistently with the horizontal-response convention used in Chapter 3 and is performed before the height-amplification ratios are evaluated.

A short-period consistency check is used to validate the computed spectra. For each processed component record, the peak absolute floor acceleration (PFA) is computed directly from the time series as

$$PFA_{cj}^{(q)} = \max_{t} \left| a_{cj}^{(q)}(t) \right| \qquad \text{Eq 5.8}$$

For the horizontal direction, the direction-specific PFA used in amplification calculations is defined by the geometric mean of $PFA_{cj}^{(H_1)}$ and $PFA_{cj}^{(H_2)}$.

At very short periods, the SDOF response approaches the rigid-component limit, so the short-period PSA should approach the corresponding PFA. In this study, the practical short-period proxy is taken as $T_s = 0.01\ s$; therefore, the validation check is

$$PSA_{cj}^{(q)}(0.01\ s, 0.05) \approx PFA_{cj}^{(q)} \qquad \text{Eq 5.9}$$

5.2.3 Height-wise Amplification Metrics

To compute the HAF, the reference level, denoted by r_c, is defined as the ground instrumented level for each building-event-sensor-line combination (c). This choice preserves consistency across buildings with and without basement levels.

The general height amplification factor is defined as:

$$HAF_{cj}^{(d)}(T) = \frac{FRS_{cj}^{(d)}(T)}{FRS_{c,r_c}^{(d)}(T)}\ , \qquad d \in (V, H) \qquad \text{Eq 5.10}$$

Because the supporting structure does not amplify all periods equally, the height-amplification factor varies with period. For this reason, HAF is examined at several period ranges, each serving a different interpretive purpose:

- **Short-period evaluation:** HAF is evaluated at $T = 0.01$ s to represent the short-period amplification. This value is used in the validation step and is expected to approximately match the corresponding PFA ratio.
- **Full period-dependent evaluation:** HAF is examined over the full analyzed period range, $0.01 \leq T \leq 10$ s, to characterize the overall spectral amplification trend with height.
- **Selected-period evaluation:** For concise reporting and comparison, HAF is evaluated at a discrete set of representative periods, $T_{sel} =$ (0.01, 0.025, 0.05, 0.075, 0.1, 0.15, 0.2, 0.25, 0.3, 0.4, 0.5, 0.75, 1, 1.5, 2, 3, 4, 5, 7.5, 10), which span the short-, intermediate-, and long-period ranges of practical interest.

- **Structural-period evaluation:** HAF is also evaluated at the building's structural period, which is inferred from the frequency-identification results in Chapter 3 to assess the behavior of amplification near the dominant measured structural frequencies.

5.2.4 Within-Event and Between-Event Statistical Summaries

Two complementary statistical summaries are used in this chapter. The first is an *between-event summary*, in which the common earthquake set is treated as repeated observations for a fixed building, sensor line, floor, direction, and period. The second is an *within-event summary*, in which all valid height profiles for a given event are combined to obtain an earthquake-specific mean amplification trend and its uncertainty bounds. Together, these two summary levels provide both a building-centered view of repeatability and an earthquake-centered view of common height-dependent amplification behavior.

Let $X^{(d)}_{(b,e,l)j}(T)$ denote a generic response quantity for building b, earthquake e, sensor line l, floor j, direction d, and oscillator period T. Note that X may represent $FRS^{(d)}_{(b,e,l)j}(T)$, or $HAF^{(d)}_{(b,e,l)j}(T)$.

For the between-event summary, let $\mathcal{E}^{(d)}_{(b,l)j}$ denote the set of earthquakes contributing valid observations after application of the record-acceptance and usable-band criteria, and let $n^{(d)}_{(b,l)j}$ denote the number of such contributing earthquakes. The between-event mean is then defined as

$$\bar{X}^{(d)}_{(b,l)j}(T) = \frac{1}{n^{(d)}_{(b,l)j}} \sum_{e\in\mathcal{E}^{(d)}_{(b,l)j}} X^{(d)}_{(b,e,l)j}(T) \qquad \text{Eq 5.11}$$

and the corresponding sample standard deviation is

$$s_{(b,l)j}^{(d)}(T) = \sqrt{\frac{1}{n_{(b,l)j}^{(d)}-1}\sum_{e\in\mathcal{E}_{(b,l)j}^{(d)}}\left[X_{(b,e,l)j}^{(d)}(T) - \bar{X}_{(b,l)j}^{(d)}(T)\right]^2} \qquad \text{Eq 5.12}$$

A 90% confidence interval for the between-event mean is estimated using the Student-t distribution:

$$\bar{X}_{(b,l)j}^{(d)}(T) \pm t_{0.95,\, n_{(b,l)j}^{(d)}-1}\frac{s_{(b,l)j}^{(d)}(T)}{\sqrt{n_{(b,l)j}^{(d)}}} \qquad \text{Eq 5.13}$$

These between-event summaries are used to report mean HAF values for individual buildings and sensor lines. Because the number of common earthquakes is small, these intervals are interpreted mainly as descriptive bounds on the mean.

A second and complementary summary is constructed at the earthquake level. For each earthquake, all valid building-line HAF profiles are combined to obtain a single mean amplification trend over the building height. Because the buildings do not all have the same height or the same number of instrumented floors, the profiles cannot be averaged based on the floor number. To make them comparable, each profile is first written in terms of normalized height, $\eta = z/h$, and then interpolated to a common height grid, η_g. For a fixed earthquake, direction, and selected period, let $Y_{(b,l)e}^{(d)}(\mathrm{T}, \eta_g)$ denote the interpolated amplification profile for a given building-line. If $N_e^{(d)}(T, \eta_g)$ is the number of such profiles, the within-event mean amplification profile is:

$$\bar{Y}_e^{(d)}(T, \eta_g) = \frac{1}{N_e^{(d)}(T,\eta_g)}\sum_{(b,l)} Y_{(b,l)e}^{(d)}(T, \eta_g) \qquad \text{Eq 5.14}$$

Each building-line profile contributes equally to this average, regardless of how many floors it contains. Uncertainty in the within-event mean profile is quantified using nonparametric cluster bootstrap resampling[7] at the building-line level. For each bootstrap, the valid building-line profiles for an earthquake are resampled with replacement, the mean profile is recomputed, and the 5th and 95th percentiles of the bootstrap means define the 90% confidence interval:

$$CI_{90,e}^{(d)}\ (T,\eta_g) = \left[Q_{0.05}\ (\bar{Y}_e^{*(d)}(T,\eta_g)),\ Q_{0.95}(\bar{Y}_e^{*(d)}(T,\eta_g))\right] \qquad \text{Eq 5.15}$$

where $\bar{Y}_e^{*(d)}$ denotes the bootstrap mean profile.

Because floor responses within the same building-line profile are not independent, the bootstrap is applied at the profile level so that this within-profile dependence is preserved, yielding a more realistic estimate of uncertainty.

5.2.5 Benchmarking Against ASCE/SEI 7-22

The final step in the methodology is to benchmark the measured and empirically modeled amplification trends against the two height-amplification formulations used in ASCE/SEI 7-22 Chapter 13 for nonstructural component design (ASCE, 2022).

The simplified height-amplification form is written as

$$H_{f,simp}(\eta) = 1 + 2.5\eta \qquad \text{Eq 5.16}$$

and the period-dependent form is written as

$$H_{f,pd}(\eta) = 1 + a_1\eta + a_2\eta^{10} \qquad \text{Eq 5.17}$$

---

[7] Cluster bootstrap resampling is a bootstrap procedure for clustered or grouped data in which the resampling is performed at the cluster level rather than at the individual-observation level. In each bootstrap replicate, whole clusters are sampled with replacement, and all observations within each selected cluster are retained together. This preserves the within-cluster dependence structure and is therefore more appropriate than ordinary observation-level bootstrap resampling when data are correlated within buildings, subjects, classes, or other groups.(Field & Welsh, 2007)

where the coefficient of a_1 and a_2 is determined as:

$$a_1 = min\left(\frac{1}{T_a}, 2.5\right), a_2 = max\left[1 - \left(\frac{0.4}{T_a}\right)^2, 0\right] \quad \text{Eq 5.18}$$

where T_a is the structural period used in the ASCE/SEI 7-22 Chapter 13. In this study, T_a is taken as the dominant period identified for the given building from the frequency-analysis results (Chapter 3).

Because CSN metadata Floor 1 corresponds to the ground-level record, the measured HAF values in this study are directly ground-referenced when an accepted CSN Floor 1 record is available. This reference condition is consistent with the ASCE/SEI 7-22 Chapter 13 height-amplification framework. Therefore, the ASCE benchmark curves are evaluated directly at the same normalized elevation coordinate z/h.

For the horizontal direction, Eqs. (5.16) and (5.17) are treated as direct benchmarks against the current ASCE/SEI 7-22 Chapter 13 framework. For vertical direction, however, the same equations are used only as transferability tests. In other words, the vertical comparison is not interpreted as a check against an existing vertical code provision, but rather as an assessment of whether the Chapter 13 horizontal functional forms are also capable of representing measured vertical amplification behavior.

Agreement between the measured data and each ASCE benchmark is quantified through the logarithmic code residual:

$$r_{i,m}^{ASCE} = ln\left(\frac{HAF_i}{HAF_{i,m}^{ASCE}}\right), \quad m \in (simp, pd) \quad \text{Eq 5.19}$$

from which the mean log-bias, weighted root-mean-square error, and median absolute relative error are computed. A positive mean residual indicates that the measured amplification tends to exceed the code benchmark, whereas a negative mean residual indicates that the benchmark is generally conservative.

In addition, a coverage metric is computed to quantify the extent to which the reference-adjusted ASCE curve lies within the empirical 90% confidence interval obtained from the within-event summaries. For a fixed direction d, selected period T_k, and earthquake e, this coverage is defined:

$$Cov_{e,m}^{(d)}(T_k) = \frac{1}{G}\sum_{g=1}^{G} \mathbf{1}\left[HAF_{ASCE,m}^{(d)}(T_k, \eta_g) \in CI_{90,e}^{(d)}(T_k, \eta_g)\right] \qquad \text{Eq 5.20}$$

where G is the number of points on the common normalized-height grid, m identifies the simplified or period-dependent benchmark, and $\mathbf{1}[\cdot]$ is the indicator function. This metric complements the residual-based statistics by showing how much of the observed amplification profile is captured by the code equation within the empirical uncertainty band.

Through this benchmarking step, the methodology addresses three questions: whether the current Chapter 13 assumptions are consistent with the measured horizontal amplification data, whether the period-dependent Chapter 13 form performs better than the simplified form, and whether the same code-shaped functions can be transferred to vertical amplification behavior.

5.3 Vertical Floor Response Spectra (VFRS) Results

This section presents the measured VFRS, the associated vertical height-amplification results, the statistical evidence for a height effect, the regression-based summaries, and the comparison of the measured vertical behavior with the Chapter 13 benchmark shapes. The results show that the vertical problem is not broadband and not weak. Instead, it concentrates in a relatively narrow short-period range, varies systematically with height, and aligns more closely with higher global vertical mode ranges than with the first vertical mode alone.

5.3.1 Validation of the Short-Period Vertical Metric

Before interpreting the vertical height-amplification results, this section verifies that the short-period metric is numerically consistent with the directly measured PFA. As summarized in Table 5.1, the agreement between PFA and $PSA(0.01\,\mathrm{s}, 5\%)$ in the vertical direction is remarkable. The mean ratio $PSA(0.01\,\mathrm{s}, 5\%)/PFA$ is 0.998, and the median ratio is 0.997, the root-mean-square error is $5.6 \times 10^{-5}\ g$, and all observations fall within $\pm 5\%$ of unity. Moreover, the correlation statistics support the same conclusion. The Pearson correlation coefficient and the Spearman correlation coefficient are almost 1. The building-level statistics, reported in detail in Appendix E, support the same conclusion across all six buildings.

Table 5.1. Summary of short-period validation statistics for the vertical direction (HNZ)

Statistic	Overall HNZ	Range across buildings (HNZ)
Number of datapoints (n)	245	13-93
Pearson (r)	≈ 1	≈ 1
Spearman (ρ)	≈ 1	0.994–1.000
Slope of (PSA) on (PFA)	0.996	0.995–0.998
Intercept (g)	1.8×10^{-5}	$2.2 \times 10^{-6} - 2.89 \times 10^{-5}$
R^2	≈ 1	≈ 1
Mean ratio (PSA/PFA)	0.998	0.997–0.998
Median ratio (PSA/PFA)	0.997	0.996–0.998

The regression of $PSA(0.01\,\mathrm{s}, 5\%)$ on PFA gives a slope of 0.996, an intercept of $1.8 \times 10^{-5}\ g$, and $R^2 \approx 1$. The slope remains very close to unity, the intercept remains negligibly small, and the scatter plot lies almost exactly on the 1:1 line (Figure 5.1). In other words, the validation shows not only that the two measures vary together, but also that they agree quantitatively to a remarkably high degree.

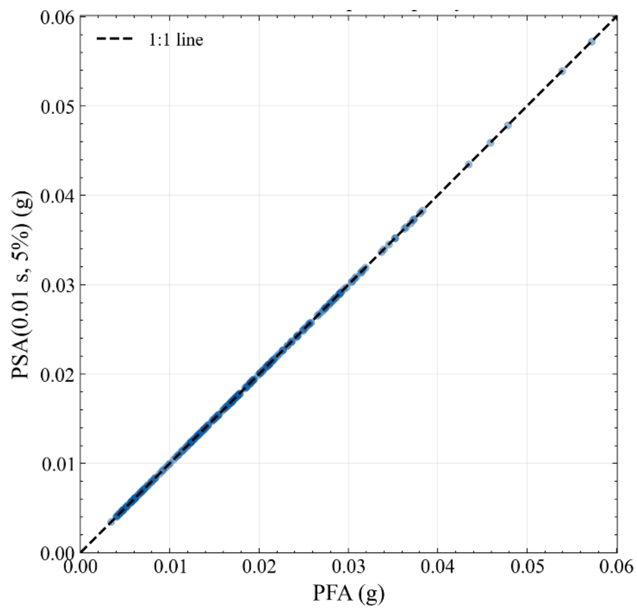

Figure 5.1. Scatter plot comparing vertical peak floor acceleration, PFA, with vertical pseudo-spectral acceleration, PSA, at T = 0.01 s and 5% damping.

5.3.2 Floor-by-Floor VFRS

The floor-by-floor VFRS plots show a clear and consistent directional character that is distinct from the horizontal response. Across the six buildings, the dominant vertical spectral demand is concentrated in a short-period band, generally between about 0.08 s and 0.25 s, with building-specific peaks most often occurring near 0.10–0.20 s. In contrast to the horizontal response, which tends to peak at intermediate periods, the measured vertical spectra are short period dominated. As illustrated in Figure 5.2, the vertical spectral ordinates are large and increase substantially toward the upper floors. To maintain consistency, Figure 5.2 presents the results for the El Monte earthquake, while the corresponding floor-by-floor VFRS plots for Pacoima, Ridgecrest, and Searle Valley are provided in Appendix F.

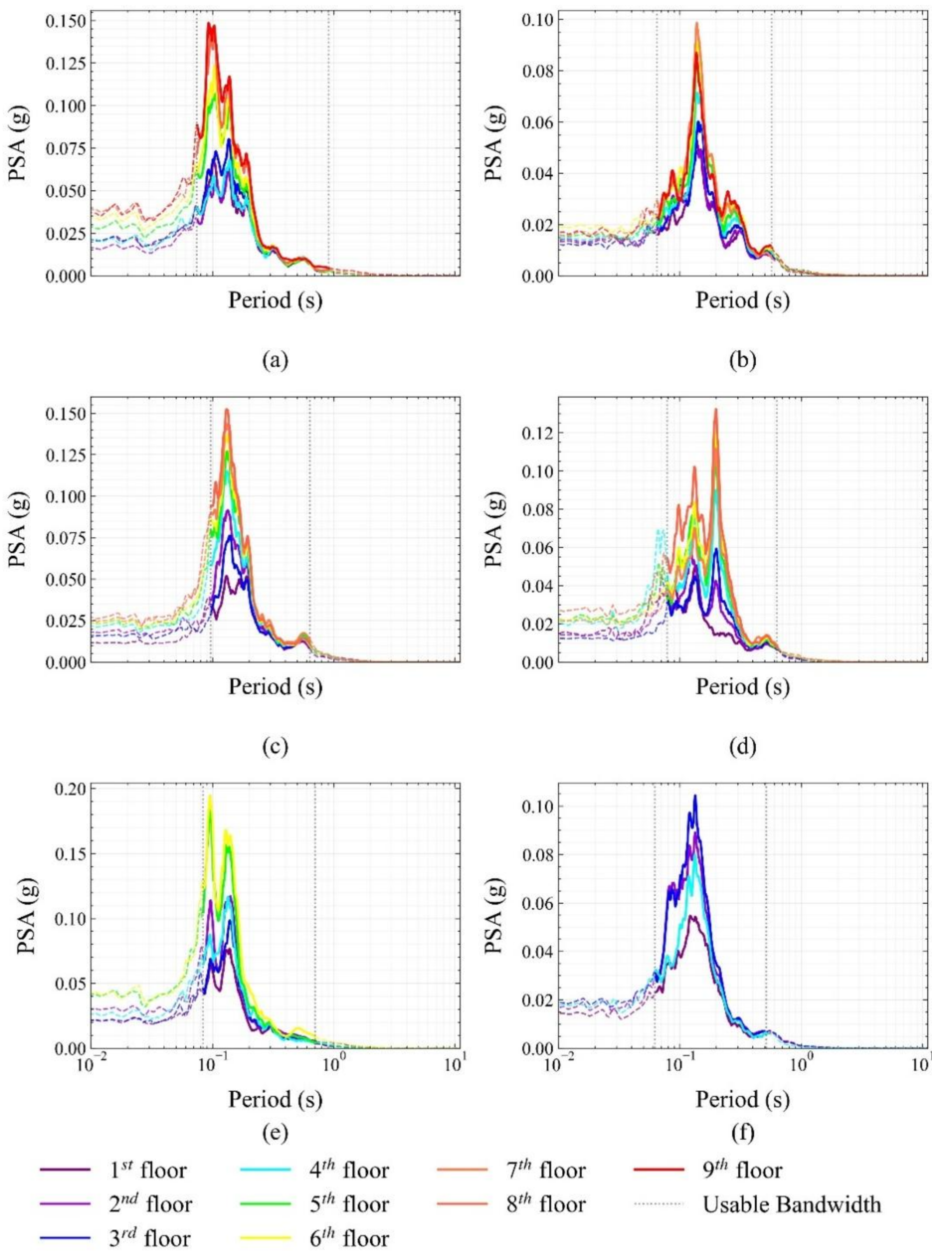

Figure 5.2. Floor-by-floor VFRS plots for the El Monte earthquake for a) JPL 180, b) JPL 183, c) JPL 238, d) JPL 264, e) JPL 321, and f) JPL 303

As shown in Figure 5.2, in JPL 180, the vertical response is strongly concentrated in the short-period range, with a dominant peak at approximately 0.09–0.16 s and a clear increase in spectral ordinates with height. The largest responses occur at the upper floors, particularly floors

8 and 9, indicating pronounced vertical amplification toward the roof. JPL 183 shows the same overall short-period concentration, but the response is more sharply focused, with a very pronounced dominant peak near about 0.13–0.16 s. The upper floors govern the response, with Floor 8 exhibiting the largest ordinate. Although JPL 183 is a nine-story building, the Floor 9 sensor on the west-side instrument line did not provide a usable record for this earthquake; accordingly, the highest floor included in the plotted spectra is Floor 8. JPL 238 is also dominated by short-period vertical response, and the principal response is distributed over roughly 0.10–0.16 s. A clear height-wise amplification trend is present, and the largest amplitudes occur at the upper floors, especially Floors 7 and 8. In JPL 264, the spectra are again concentrated in a short-period band, but the response is more irregular, with several peaks between about 0.10 and 0.20 s, and the strongest in-band peak occurring near 0.17–0.19 s. JPL 321 exhibits another very strong short-period case, characterized by two sharp upper-floor peaks near about 0.10 s and 0.13–0.15 s; Floors 5 and 6 produce the largest amplitude, approaching about 0.19–0.20 g. By contrast, JPL 303 gives the weakest response among the six buildings, a broader peak band around 0.09–0.15 s, maximum amplitudes of about 0.10–0.11 g, Floor 3 rather than the top available floor produces the largest peak, which indicates that the overall VFRS increases with height; however, it might be affected by the floor plan or other specific building features.

The floor-by-floor spectra also reveal an important event effect. For many buildings, the smaller nearby events produce narrower and sharper short-period peaks, whereas the larger Ridgecrest-sequence events broaden the vertical spectral shape and sometimes introduce secondary peaks at longer periods, shown in Figure 5.3. However, even when the spectrum broadens, the dominant vertical character remains concentrated in the short-period range.

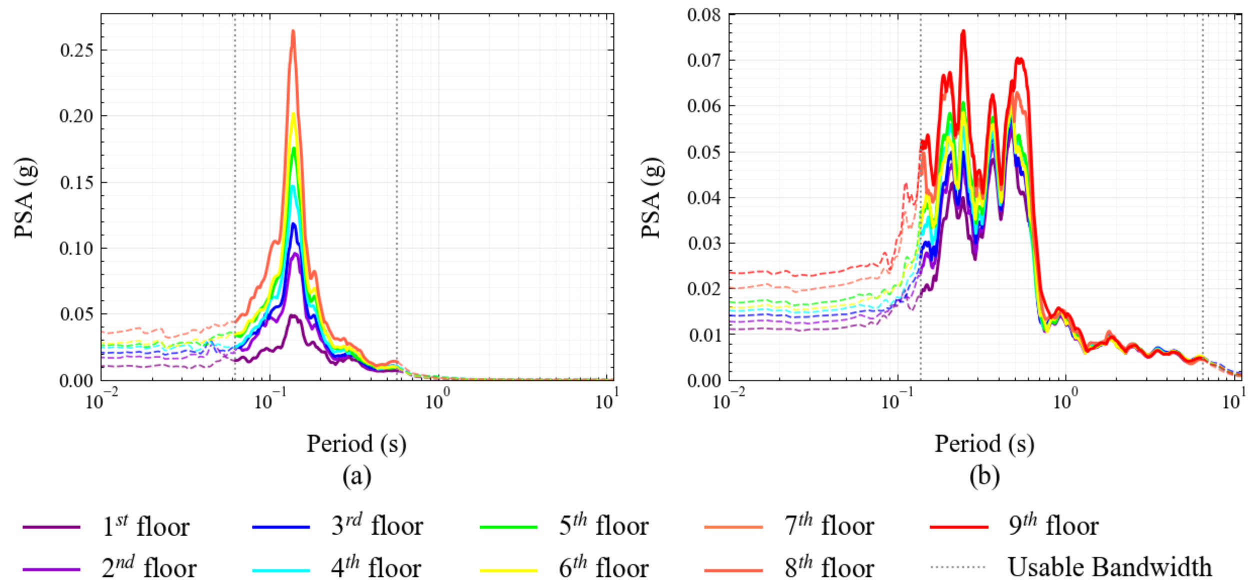

Figure 5.3. VFRS of JPL 183 at east-sensor line for earthquakes: a) El Monte, b) Ridgecrest

5.3.3 Height-wise Amplification of VFRS

The HAF results in the vertical direction show that the measured floor response is not only period dependent, but also strongly height dependent over a relatively narrow short-period band. Figure 5.4 presents the HAF profile over the full period range for the El Monte record in JPL 183 and shows that the demands in the upper floors are generally higher than the lower floors over the usable period range. The clearest separation of floors occurs between about 0.10 s and 0.25 s, which is consistent with the dominant short-period range in the VFRS plots. Outside this band, the vertical amplification weakens and becomes less orderly, but the overall tendency for larger upper-floor demand remains.

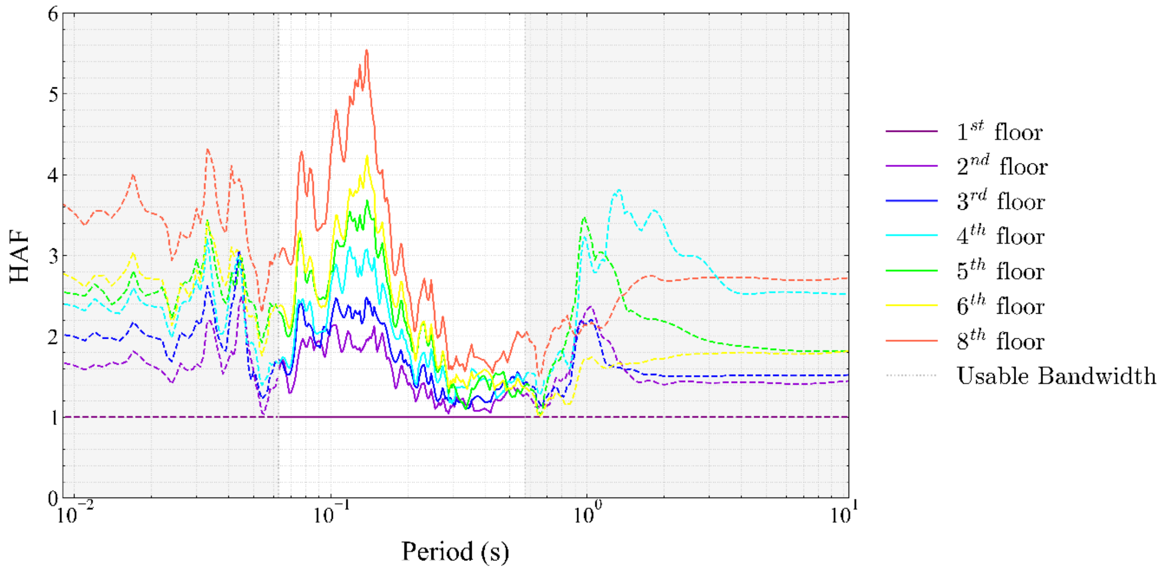

Figure 5.4. HAF profiles over the full period range for the vertical direction at the west-side line of JPL 183 during the El Monte earthquake.

The HAF results at $T = 0.01\ s$ are summarized by the between-event profiles in Figure 5.5. For the six buildings, the mean profile remains at unity at the reference level and generally increases toward the upper level. However, the strength of that increase varies substantially from one building to another. The strongest cases appear in JPL 321, JPL 180 middle-sensor line, JPL 264, and JPL 183 east-sensor line, where the mean profiles rise clearly above the lower-floor values and remain elevated toward the roof. JPL 238 shows the same overall trend but with a more moderate gradient, whereas JPL 303 stays close to unity over most of its height, indicating only weak sensitivity to elevation. This contrast shows that overall height alone does not explain the observed response; building-specific dynamic characteristics also play an important role.

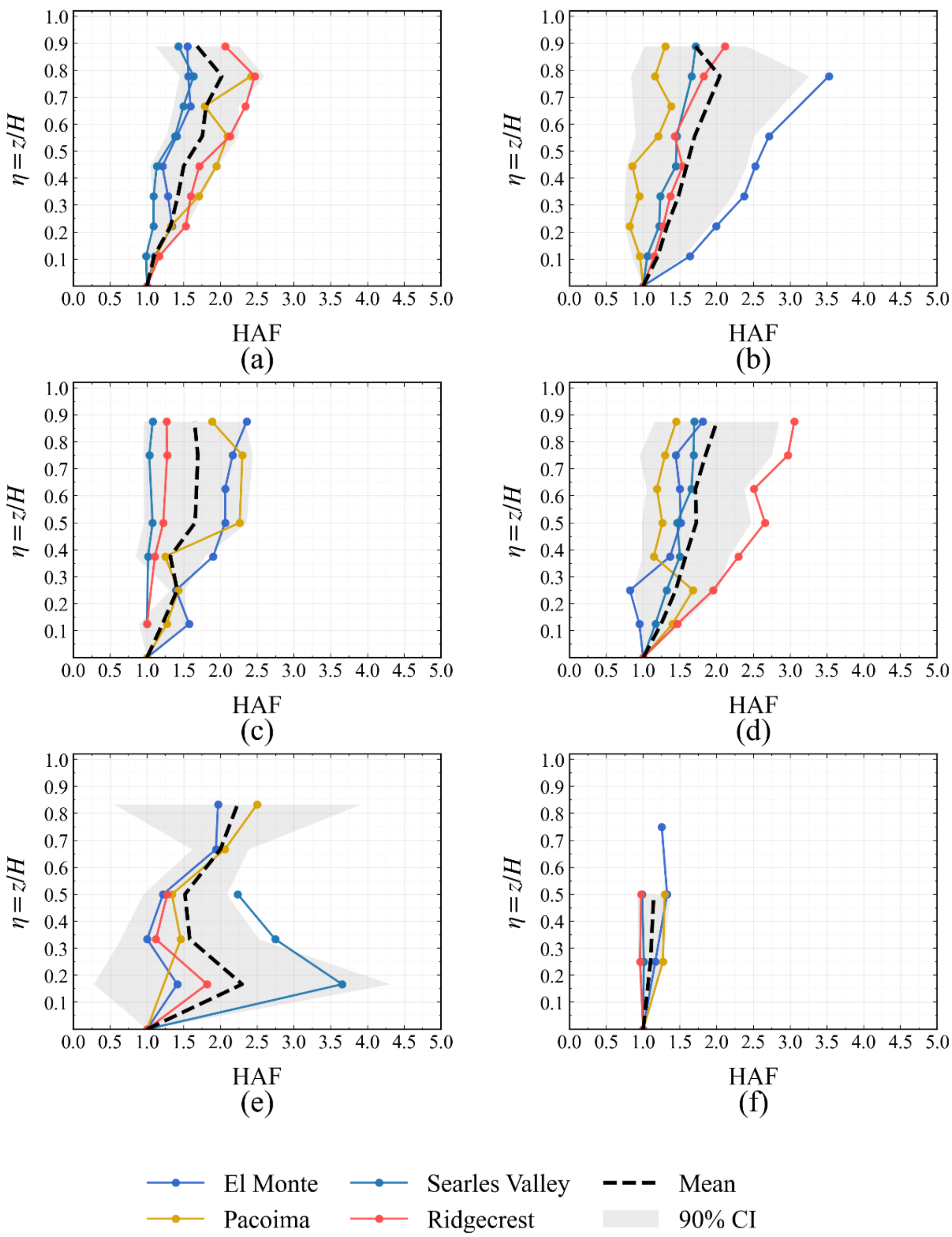

Figure 5.5. Between-event vertical HAF profiles at T=0.01 s for: (a) JPL 180 (middle-sensor line); (b) JPL 183 (east-sensor line); (c) JPL 238; (d) JPL 264; (e) JPL 321; and (f) JPL 303. Colored curves show the earthquake-specific profiles, the dashed black curve shows the between-event mean profile, and the shaded band shows the 90% confidence interval.

Table 5.2 summarizes the HAF at the highest accepted instrumented floor of each building line. The mean short-period amplification at the top floor reaches 2.23 in JPL 321, 2.13 in the west sensor line of JPL 180, and 2.00 in JPL 264, whereas JPL 303 remains much lower at about 1.25. Overall, the table shows that even the near-rigid, short-period portion of the vertical spectrum can be amplified substantially above the reference-floor response.

Table 5.2. Highest instrumented level HAF at 0.01s summary for vertical building-line profiles

Building		Highest instrumented level*	Mean HAF	Median HAF
JPL180	West	8	2.13	2.13
	Middle	9	1.68	1.55
	East	9	1.38	1.27
JPL183	West	9	1.67	1.62
	East	9	1.71	1.72
JPL 238		8	1.65	1.58
JPL 264		8	2.00	1.75
JPL 321		6	2.23	2.23
JPL 303		4	1.25	1.25

* CSN metadata Floor 1 corresponds to the ground-level record. The highest accepted floor is the highest instrumented level retained after record-quality screening. It is not interpreted as a roof-level sensor.

A more focused view is provided by the between-event profiles evaluated at the period of maximum vertical amplification for each building, shown in Figure 5.6. These results indicate that the dominant amplification for all buildings is concentrated mainly in the 0.10–0.25 s range, which is consistent with the period band already highlighted by the VFRS plots. They also show that the largest mean amplification does not always occur on the roof. In several buildings, especially JPL 183 and JPL 238, the maximum profile occurs at an upper-middle floor rather than at the highest floor. For this reason, the vertical response is more accurately described as upper-floor dominated than strictly roof dominated.

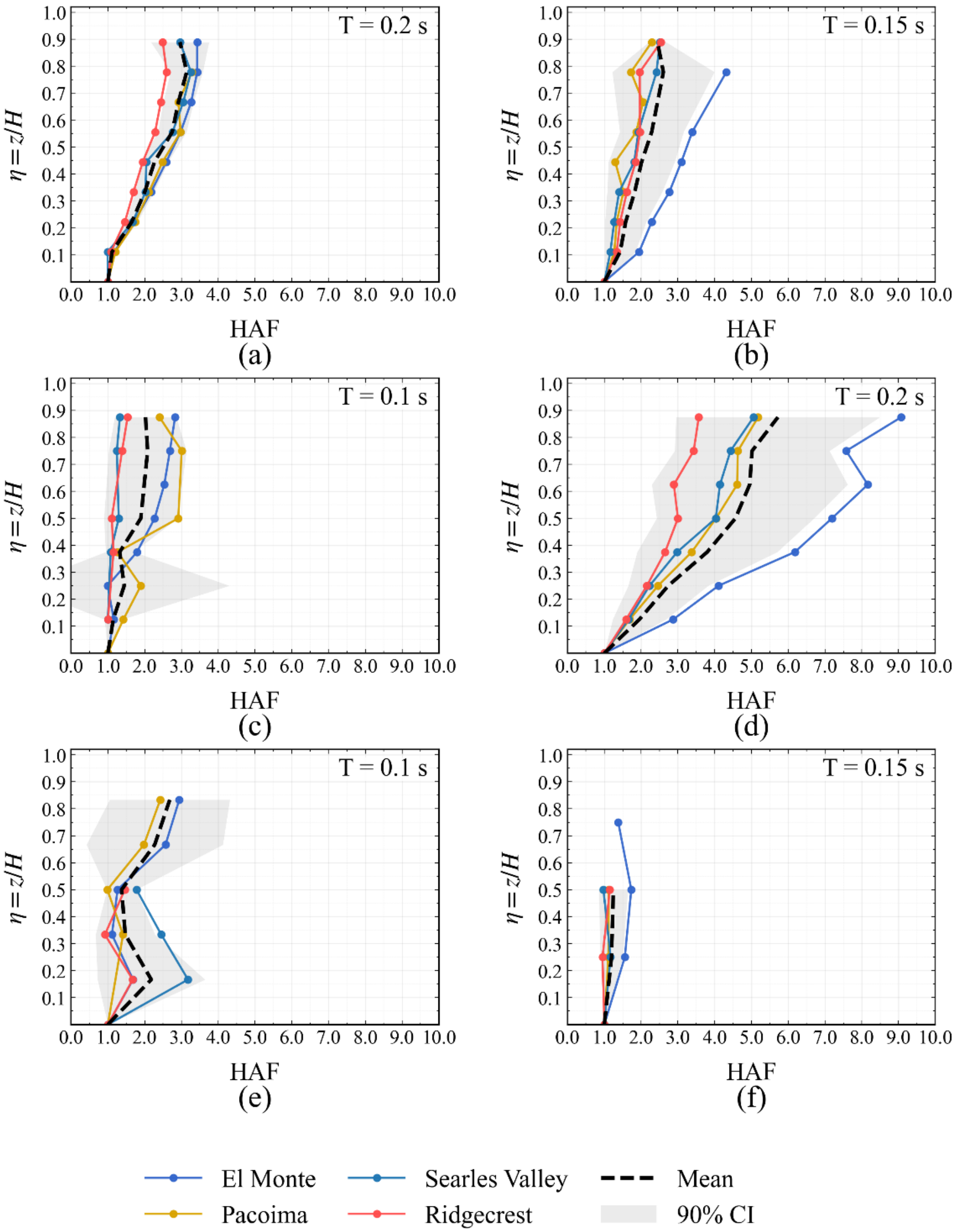

Figure 5.6. Between-event profiles corresponding to the period of maximum mean HAF in the vertical direction for each building: (a) JPL 180 (middle-sensor line) at T=0.2s; (b) JPL 183 (east-sensor line) at T=0.15s; (c) JPL 238 at T=0.1s; (d) JPL 264 at T=0.2s; (e) JPL 321 at T=0.1s; and (f) JPL 303 at T=0.15 s. Colored curves show the earthquake-specific profiles, the dashed black curve shows the between-event mean profile, and the gray area shows the 90% confidence interval.

As shown in Figure 5.6, the strongest amplification occurs in JPL 264 at 0.20 s, where the mean profile rises to about 5.72 in the upper floors and the 90% confidence band is very broad. This unusually large response appears to be driven mainly by the El Monte earthquake record and may reflect especially efficient excitation of a short-period vertical mode near 0.20 s, although a record-specific anomaly in that event cannot be ruled out. Other strong cases include JPL 180 middle-sensor line at 0.20 s, which shows a clear and relatively orderly increase with height to nearly 3.0 at the upper floors; JPL 183 east-sensor line at 0.15 s, which shows a pronounced upper-floor increase but also substantial event-to-event variability; JPL 238 at 0.10 s, which shows a more moderate yet still consistent upper-floor amplification trend; and JPL 321 at 0.10 s, which remains less monotonic than the other strong cases but still exhibits clear upper-level amplification. By contrast, JPL 303 at 0.025 s remains close to unity and shows only weak period-specific amplification. The HAF peak values at the top floor and their corresponding periods are summarized in Table 5.3.

Table 5.3. Maximum highest instrumented level HAF values summary for vertical building-line profiles

Building		**Highest instrumented level***	**Peak period (s)**	**Peak mean HAF**
JPL180	West	8	0.1	3.566
	Middle	9	0.2	2.961
	East	9	0.1	1.683
JPL183	West	9	0.25	2.501
	East	9	0.15	2.445
JPL 238		8	0.1	2.203
JPL 264		8	0.2	5.720
JPL 321		6	0.1	2.682
JPL 303		4	0.15	1.378

* CSN metadata Floor 1 corresponds to the ground-level record. The highest accepted floor is the highest instrumented level retained after record-quality screening. It is not interpreted as a roof-level sensor.

The within-event profiles in Figure 5.7 provide the complementary earthquake-centered perspective. This figure focuses on the period of 0.20 s because, for most cases, the strongest vertical amplification profiles occur at or near this period. All four earthquakes produce pooled upper-floor amplification clearly above unity at 0.20 s, although the strength of the effect varies from one event to another.

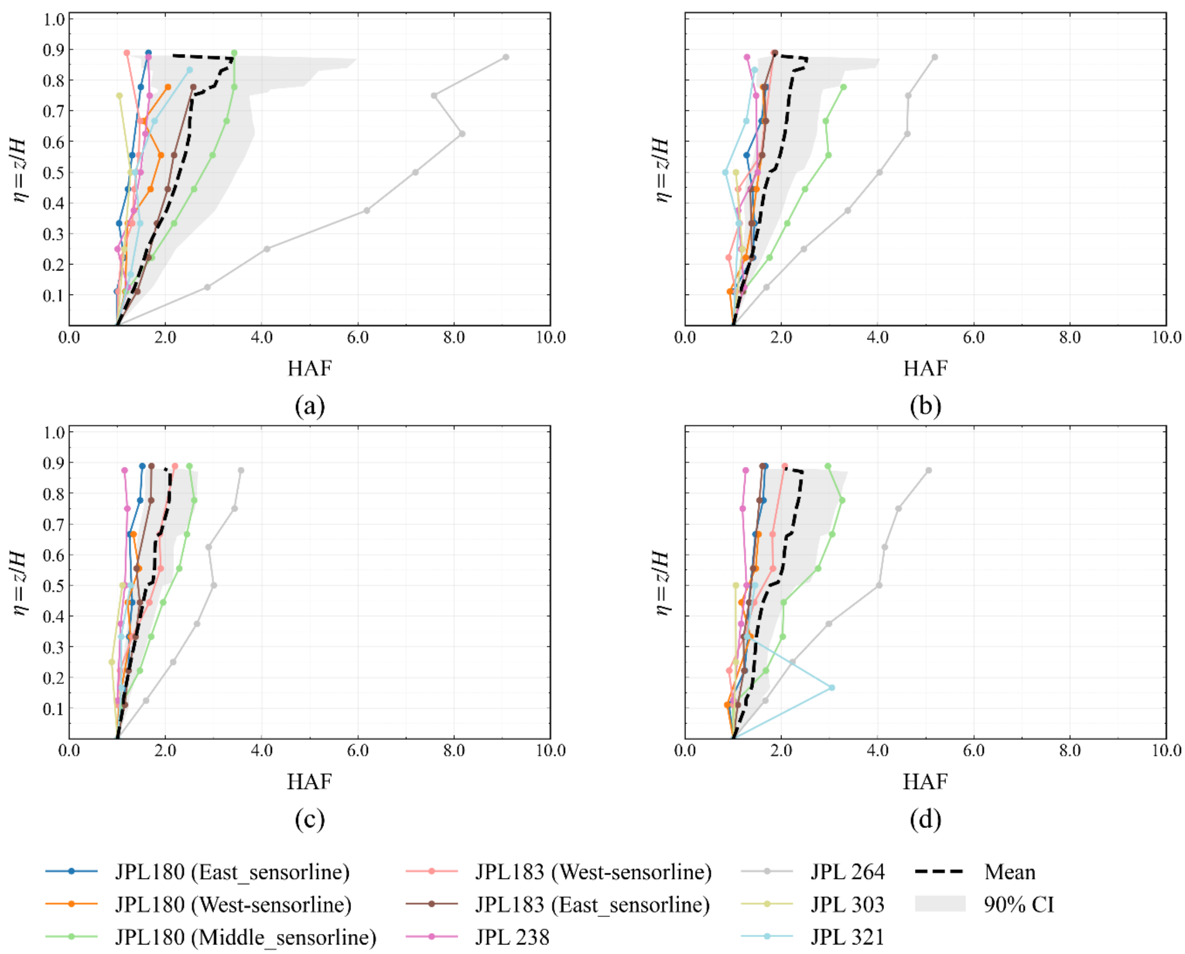

Figure 5.7. Within-event profiles for vertical HAF at T=0.2s for each earthquake: (a) El Monte; (b) Pacoima; (c) Searle Valley; (d) Ridgecrest. Colored curves show the building-specific profiles, the dashed black curve shows the within-event mean profile, and the gray area shows the corresponding 90% confidence interval.

The mean top-floor amplification is 2.931 for El Monte, 2.321 for Pacoima, 2.104 for Ridgecrest, and 2.434 for Searle Valley. The most visible irregularity in the within-event plots occurs for El Monte and is driven primarily by JPL 264. Because 0.20 s lies very close to one of JPL 264's dominant short-period vertical mode ranges, even a moderate nearby event can produce a very large upper-floor-to-reference-floor ratio when the reference-floor response remains comparatively small. This feature is therefore best interpreted as a building-specific resonance effect rather than evidence of a separate amplification range shared by the full dataset. Table 5.4 shows the within-event mean amplification of the top-level at the selected period and numerically quantifies the results from Figure 5.7.

Table 5.4. Within-event pooled vertical HAF summary at selected periods

Period (s)	El Monte	Pacoima	Ridgecrest	Searle Valley	Average
0.01	1.708	1.722	1.99	1.468	1.722
0.025	1.624	1.691	1.923	1.452	1.6725
0.05	1.647	1.758	2.029	1.481	1.72875
0.075	1.758	1.658	1.977	1.544	1.73425
0.10	2.376	1.639	2.1	1.621	1.934
0.15	2.119	1.95	2.409	2.023	2.12525
0.20	2.931	2.321	2.104	2.434	2.4475
0.25	2.037	2.032	2.043	1.838	1.9875
0.30	1.541	1.701	1.475	1.496	1.55325
0.40	1.463	1.323	1.225	1.204	1.30375
0.50	1.407	1.443	1.185	1.233	1.317
0.75	1.625	1.537	1.112	1.193	1.36675
1.00	1.317	1.683	1.044	1.082	1.2815
1.50	1.77	1.87	1.029	1.003	1.418
2.00	2.14	1.871	1.048	0.871	1.4825
3.00	1.964	1.803	1.101	0.858	1.4315
4.00	1.892	1.794	1.131	0.856	1.41825
5.00	1.86	1.819	1.142	0.857	1.4195
7.50	1.826	1.787	1.229	0.851	1.42325
10.00	1.82	1.772	1.352	0.851	1.44875

The amplification profiles are also evaluated at the dominant structural periods in the vertical direction. The strongest top-floor amplification values occur most often in higher vertical modes, especially V4, V5, and V6, rather than in the first vertical mode alone. This conclusion is further illustrated by the building-level comparisons in Table 5.5. For example, the largest amplification in JPL 264 is associated with V4 at about 5.1 Hz, while the first vertical mode at about 1.8 Hz produces a much smaller value. A similar pattern is observed in JPL 238, where the strongest amplification is associated with V6 rather than V1. Taken together, these results indicate that the vertical height effect observed in this chapter is governed by dynamic filtering within the building and is strongly tied to higher global vertical modes within the short-period band.

Table 5.5. Highest instrumented level vertical HAF summary at the first identified vertical mode and the vertical mode producing the maximum mean amplification for each building–sensor-line profile.

Building		Response	Mode	Period (s)	Frequency (Hz)	Mean HAF
JPL 180	West	max	V4	0.10	9.9	3.67
		1st mode	V1	0.19	5.4	1.73
	Middle	max	V1	0.19	5.4	3.73
		1st mode	V1	0.19	5.4	3.73
	East	max	V3	0.12	8.4	1.80
		1st mode	V1	0.19	5.4	1.65
JPL 183	West	max	V3	0.24	4.2	2.5
		1st mode	V1	0.59	1.7	1.33
	East	max	V5	0.14	7.2	2.63
		1st mode	V1	0.59	1.7	1.91
JPL 238		max	V6	0.11	9.4	2.33
		1st mode	V1	0.47	2.1	1.11
JPL 264		max	V4	0.20	5.1	5.74
		1st mode	V1	0.56	1.8	1.35
JPL 321		max	V6	0.11	9.4	2.42
		1st mode	V1	0.71	1.4	1.83
JPL 303		max	V5	0.12	8.5	1.46
		1st mode	V1	0.53	1.9	1.01

5.3.4 Comparison with ASCE/SEI 7-22 Chapter 13 Surrogate Models

ASCE/SEI 7-22 Chapter 13 provides an explicit height-amplification framework for nonstructural component design in horizontal direction, but it does not provide an analogous vertical floor-response-spectrum or vertical height-amplification model. The vertical seismic force requirement in Chapter 13 is instead treated through the vertical seismic load effect, E_v, without an explicit dependence on floor elevation, component period, or the vertical dynamic properties of the supporting structure. Therefore, the comparison in this section should not be interpreted as a direct evaluation of an existing vertical Chapter 13 HAF equation; rather, it is a transferability test. The purpose of the present section is to determine whether the functional forms used by Chapter 13 for horizontal height amplification can reasonably reproduce the measured vertical HAF trends, and at the end, a practical code-oriented recommendation is developed. The procedure follows the direct ground-referenced benchmarking framework introduced in Section 5.2.5.

The measured vertical HAF profiles are compared with the two Chapter 13 height-amplification forms: the simplified form and the period-dependent form. For the six buildings considered in this study, these two Chapter 13 surrogate models collapse to the same vertical benchmark profile. This occurs because the dominant vertical structural periods are sufficiently short (~0.1-0.2 s) that the period-dependent coefficients reduce to the simplified height-amplification form. Consequently, the simplified and period-dependent Chapter 13 surrogates produce identical values of mean log-bias, weighted RMSE, median absolute relative error, exceedance fraction, and within-event coverage at all analyzed oscillator periods. This overlap is an important result. It shows that, for the present dataset, the Chapter 13 period-dependent expression does not add useful vertical period sensitivity beyond the simplified linear height-amplification assumption. Thus, the main question becomes whether this common Chapter 13 linear shape can reproduce the measured vertical amplification trends.

Figure 5.8 compares the empirical highest-instrumented-level HAF with the Chapter 13 surrogate curves as a function of oscillator period. Because the measured HAF values are computed relative to CSN metadata Floor 1, which corresponds to the ground-level record, the ASCE height-amplification functions are evaluated directly. However, because the highest accepted instrumented level is not always located at $z/h = 1.0$, the ASCE surrogate values are evaluated at the building-specific highest measured normalized heights and then averaged across the six buildings. As a result, the simplified and period-dependent Chapter 13 surrogate lines nearly overlap at an average HAF value of approximately 3.1, rather than the roof-level value of 3.5 that would be obtained at $z/h = 1.0$. In contrast, the empirical vertical HAF varies substantially with oscillator period. The empirical HAF is approximately 1.9 at $T = 0.01$ s, increases to about 2.1 at $T = 0.10$ s, and reaches its maximum value of approximately 2.25 near $T = 0.15$–0.20 s. It then decreases rapidly to approximately 1.6 at $T = 0.30$ s, and remains close to about 1.25–1.40 for periods greater than 1.0 s.

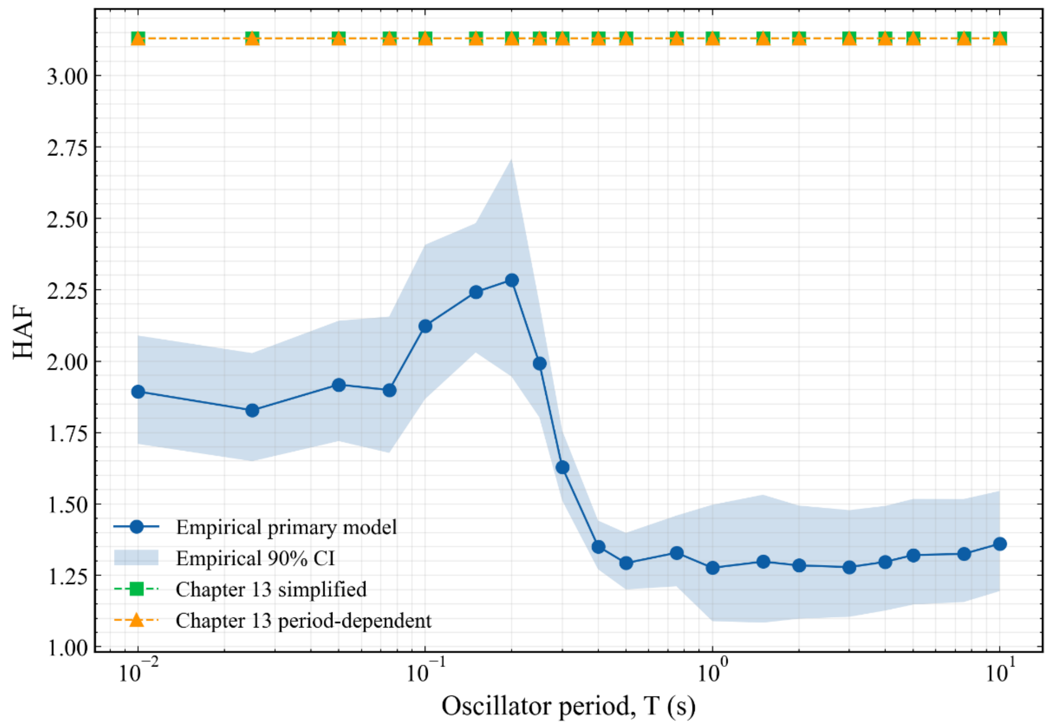

Figure 5.8. Highest level HAF versus oscillator period for the vertical direction.

Therefore, the measured vertical amplification is not consistent with a period-independent height-amplification factor. Instead, it is concentrated in a short-period band. The ASCE surrogate lines remain constant with oscillator period because the Chapter 13 height-amplification functions depend on normalized height and the supporting-structure period, but not explicitly on the nonstructural component oscillator period shown on the horizontal axis. The overlap between the simplified and period-dependent ASCE lines indicates that, for the vertical periods considered here, the period-dependent Chapter 13 form effectively reduces to the simplified linear height-amplification profile. This leads both ASCE surrogate models to overestimate the empirical central trend over most of the oscillator-period range, especially outside the short-period amplification band.

As summarized in Table 5.6, the mean log-bias is negative at all periods, indicating that the Chapter 13 surrogate is conservative on average for the pooled vertical dataset. However, conservatism alone does not imply that the model is a good representation of the measured response. At longer periods, the negative bias becomes large, the median absolute relative error increases, and the within-event coverage decreases. This indicates that the Chapter 13 surrogate is not tracking the measured period dependence; it is simply remaining high while the empirical vertical amplification decreases.

Table 5.6. Summary of vertical ASCE transferability metrics at representative oscillator periods.

period (s)	Empirical HAF	ASCE HAF	Mean log-bias	Weighted RMSE	Median Absolute Relative Error	Mean within-event coverage	Interpretation
0.01	1.78	3.13	-0.332	0.385	0.295	0.166	Conservative; weak coverage
0.05	1.81	3.13	-0.315	0.375	0.295	0.211	Conservative; weak coverage
0.1	1.98	3.13	-0.261	0.321	0.248	0.301	Partial agreement
0.15	2.09	3.13	-0.226	0.263	0.233	0.258	Lowest overall error
0.2	2.13	3.13	-0.155	0.203	0.168	0.671	Best overall coverage
0.25	1.87	3.13	-0.297	0.323	0.284	0.011	Rapid loss of agreement
0.5	1.26	3.13	-0.541	0.604	0.437	0.059	Strong overprediction
1	1.24	3.13	-0.515	0.603	0.381	0.18	Strong overprediction
5	1.28	3.13	-0.511	0.588	0.393	0.135	Strong overprediction
10	1.31	3.13	-0.507	0.587	0.389	0.16	Strong overprediction

The within-event coverage maps in Figure 5.9 provide a complementary view. The highest coverage occurs near $T = 0.20$s. However, the coverage drops sharply outside the short-period vertical amplification band, particularly for $T > 0.25$s. This behavior indicates that the ASCE surrogate does not provide a uniformly reliable vertical model across the oscillator-period range. Instead, it agrees with the empirical trend only near the period range where vertical floor amplification is strongest.

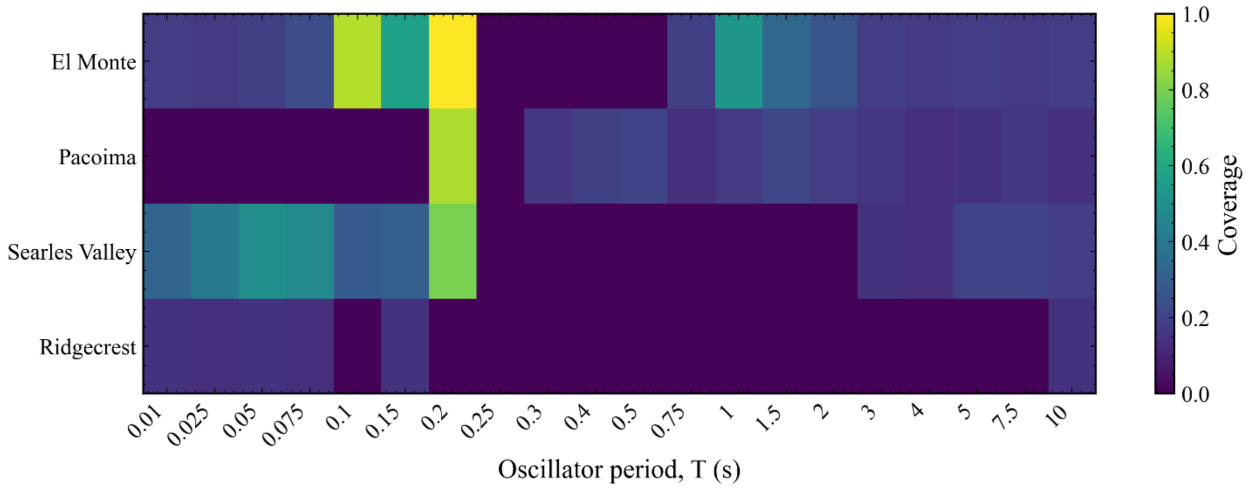

Figure 5.9. Within-event agreement coverage of transferred ASCE height-amplification surrogate models against measured vertical HAF.

The results of this study indicate that direct transfer of the ASCE/SEI 7-22 Chapter 13 horizontal HAF forms to nonstructural design in the vertical direction should be approached cautiously. For the dataset considered here, this transferred form generally appears to be conservative for the measured vertical HAF, especially outside the dominant short-period vertical amplification range. However, because the study is limited to six instrumented buildings and four earthquake events, broader datasets are needed before drawing general code-level conclusions. Therefore, the findings should be interpreted as preliminary evidence that vertical nonstructural design may benefit from a separate, period-dependent height-amplification framework, rather than either a direct adoption of the current horizontal formulation or the implicit assumption of no vertical height amplification ($HAF = 1$) through the current use of E_v in ASCE/SEI 7-22.

5.4 Horizontal Floor Response Spectra (HFRS) Results

5.4.1 Validation of the Short-Period Horizontal metric

Before interpreting the HFRS and the corresponding HAF results, the short-period consistency check introduced in Section 5.2.2 is repeated for the horizontal geometric-mean (HGM) direction. In this validation, both the PFA and the short-period spectral acceleration (at $T = 0.01s$) are evaluated using the same HGM definition. As summarized in Table 5.7, the agreement between $\mathrm{PSA_{HGM}}(0.01\ \mathrm{s})$ and PFA_{HGM} is extremely strong. Across all buildings and events, the mean and median ratio $\mathrm{PSA_{HGM}}(0.01\ \mathrm{s}, 5\%)/\mathrm{PFA_{HGM}}$ is 0.998, and all observations fall within ±5% of the 1:1 relationship. The correlation statistics also support the same conclusion. These values indicate not only strong rank and linear association, but also near-perfect quantitative agreement between the two measures.

Table 5.7. Summary of short-period validation statistics for the horizontal direction (HGM)

Statistic	Overall HGM	Range across buildings (HGM)
Number of datapoints (n)	241	13-93
Pearson (r)	≈ 1	≈ 1
Spearman (ρ)	≈ 1	≈ 1
Slope of (PSA) on (PFA)	0.999	0.998–0.999
Intercept (g)	-1.3×10^{-5}	-1.69×10^{-5} – -2.48×10^{-7}
R^2	≈ 1	≈ 1
Mean ratio (PSA/PFA)	0.998	≈ 0.998
Median ratio (PSA/PFA)	0.998	0.997–0.999

The regression of $PSA(0.01\ \mathrm{s}, 5\%)$ on PFAgives a slope of 0.999, an intercept of $-1.3 \times 10^{-5}g$, and $R^2 \approx 1$. The slope is nearly unity, the intercept is negligible, and the scatter plot lies almost exactly on the 1:1 line (Figure 5.10). This confirms that the computed HFRS satisfy the expected short-period limit.

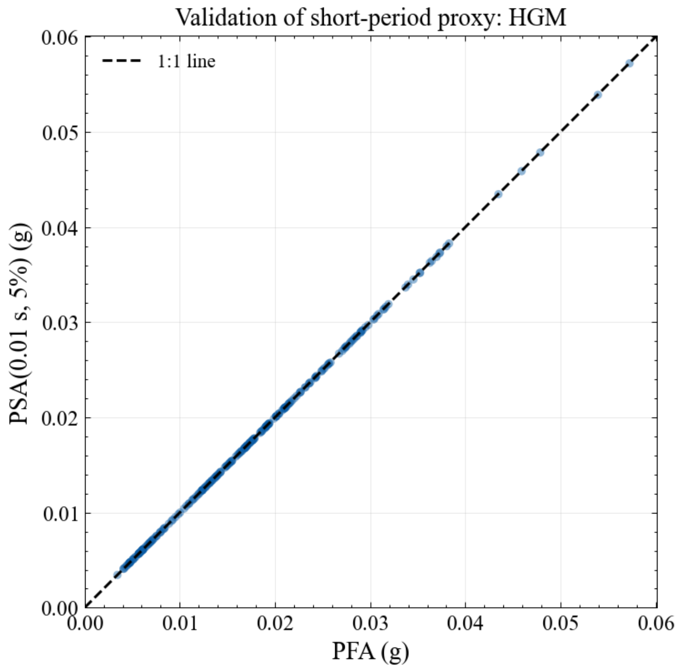

Figure 5.10. Scatter plot comparing horizontal peak floor acceleration, PFA, with horizontal pseudo-spectral acceleration, PSA, at T = 0.01 s and 5% damping.

5.4.2 Floor-by-floor HFRS

The floor-by-floor HFRS are computed using the HGM following the same 5%-damped PSA procedure described in Section 5.2.2. Figure 5.11 presents the HFRS for the El Monte earthquake for the six instrumented JPL buildings. For consistency with the VFRS presentation, the El Monte event is shown in this section, while the corresponding HFRS plots for other earthquakes are provided in Appendix F. In each panel, spectra are shown for the instrumented floors of the building, and the vertical dotted lines indicate the usable period range.

The HFRS results show that horizontal floor motions are strongly period-dependent. Across the six buildings, the spectra are not uniformly amplified over the full period range. Instead, each building filters the input motion and produces narrowband peaks that depend on the earthquake, the building, the sensor line, and the floor level. This behavior is important for acceleration-sensitive nonstructural components because components with periods near these amplified bands may experience demands much larger than those implied by the short-period or rigid-component response alone. Thus, while PFA_{HGM} represents the rigid-limit demand, the full HFRS are required to identify the component-period ranges where horizontal acceleration demand is largest.

The dominant HGM spectral peaks are generally concentrated in a short-to-intermediate period range, approximately 0.08–0.20 s. This period range concentration is observed in all six buildings, although the peak amplitudes and floor ordering vary substantially. JPL 238 and JPL 264 show some of the largest El Monte spectral ordinates, with peaks on the order of 0.12–0.14 g. JPL 183 and JPL 303 also show distinct short-period peaks, while JPL 180 and JPL 321 exhibit broader floor-to-floor variability. In several buildings, the largest response does not occur at the roof. In some cases, lower or intermediate floors can control the HFRS over the dominant period band. This floor-to-floor variation shows that HFRS are influenced by building-specific dynamic amplification, not simply by floor elevation.

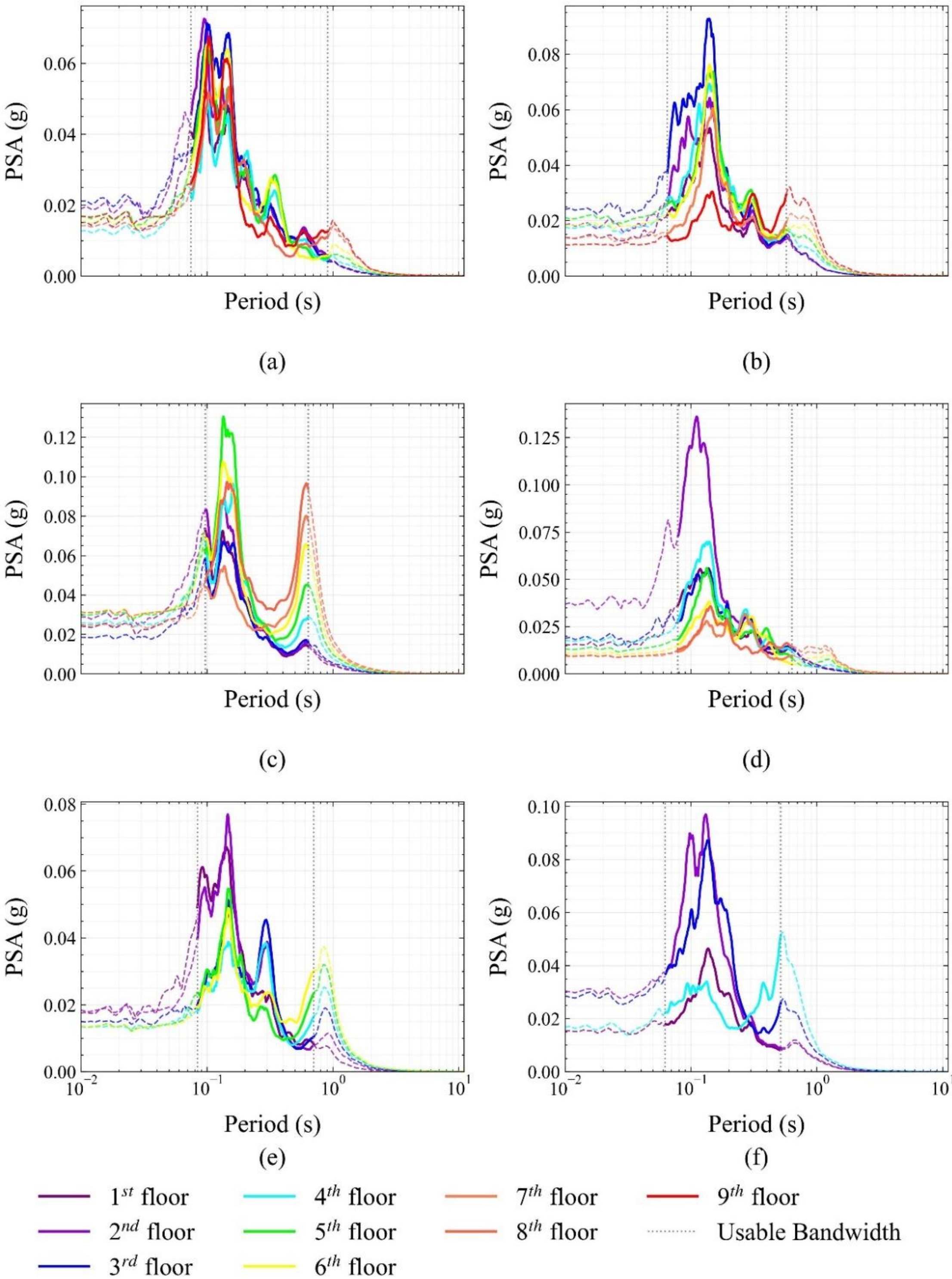

Figure 5.11. Floor-by-floor HFRS plots for the El Monte earthquake for a) JPL 180, b) JPL 183, c) JPL 238, d) JPL 264, e) JPL 321, and f) JPL 303

The results for the other earthquakes show that the same buildings can respond very differently depending on the input motion. Pacoima generally produces smaller HGM spectral ordinates than El Monte, but its dominant peaks remain concentrated mainly in the short-period range. In contrast, the Searle Valley and Ridgecrest records shift the controlling HFRS response toward longer periods in the range of ~0.4s and ~1.3s. The Ridgecrest spectra are often larger than the Searle Valley spectra, but the dominant period bands are similar for several buildings. This pattern suggests that the larger, more distant events excite the building-level horizontal dynamic response more strongly at intermediate-to-longer periods, whereas the moderate, nearby events emphasize shorter-period response.

Figure 5.12 highlights an event-dependent shift in the dominant horizontal response band of JPL 180 at the middle sensor line. In the present dataset, the smaller, closer earthquakes, El Monte and Pacoima, produce dominant HFRS peaks near $T \approx 0.09 - 0.1s$, which is consistent with excitation of the highest measured horizontal mode band of the building (the 5th mode with frequency $\approx 9.7 - 10.1\, Hz$). In contrast, the larger, farther earthquakes, Searle Valley and Ridgecrest, shift the controlling response toward longer periods, with strong peaks near $T \approx 0.4\, s$ and $T \approx 1.3\, s$, which are consistent with the second and first horizontal modes of JPL 180 which is provided in Chapter 3 ($f_2 = 2.4 - 2.7\, Hz$ and $f_1 = 0.7 - 0.9\, Hz$). This behavior is best interpreted as a spectral-compatibility effect between the input motion and the modal response bands of the supporting building. Smaller nearby events tend to preserve stronger short-period energy because smaller sources have higher corner frequencies and high-frequency wave components attenuate rapidly with distance, whereas larger and more distant events arrive at the site relatively richer in intermediate- and long-period content (Trifunac & Lee, 1990). The observed HFRS shift in JPL 180 is therefore consistent with prior studies showing that nonstructural acceleration demands depend on the supporting building's modal periods, the component-to-building tuning ratio, the component location, and the frequency content of the excitation (Anajafi & Medina, 2018, 2019)

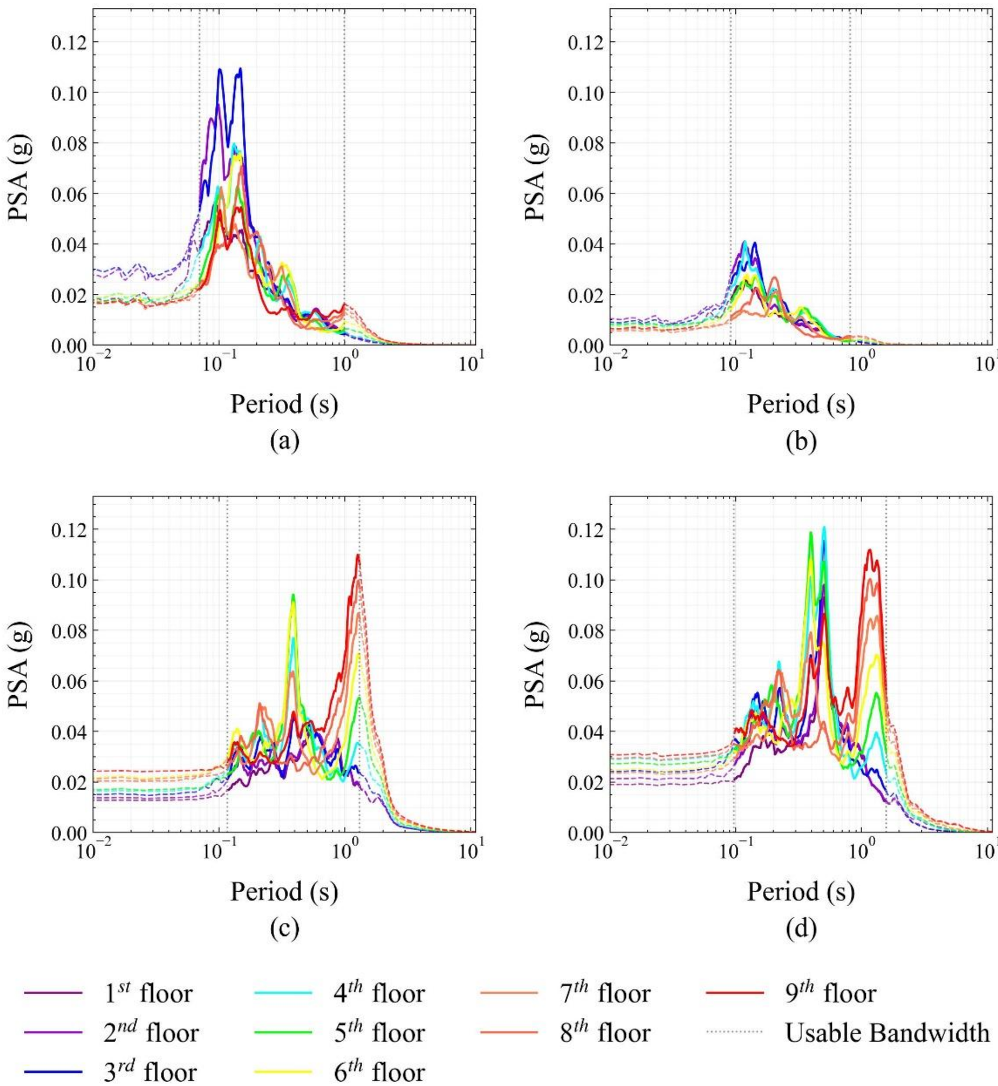

Figure 5.12. Floor-by-floor HFRS plots for JPL 180 at the middle sensor line for a) El Monte earthquake, b) Pacoima, c) Searle Valley, d) Ridgecrest

Between-building differences are noticeable and indicate that height-wise amplification in the horizontal direction is strongly period dependent. In general, when the response is associated with the fundamental horizontal mode, the larger HFRS amplitudes tend to occur at the upper floors, consistent with the larger first-mode displacement/acceleration participation near the top of the building. However, the El Monte spectra are dominated mainly by short-to-intermediate period peaks, which correspond more closely to higher-mode response bands. In these higher-mode ranges, the floor ordering is not monotonic with height. Instead, the controlling HFRS ordinate may occur at lower or intermediate floors, and the floor with the maximum response can change with period. This behavior is visible across several buildings: JPL 183 and JPL 303 show strong peaks at intermediate floors, JPL 238 and JPL 264 exhibit large responses that are not controlled by the roof, and JPL 180 and JPL 321 show multiple local peaks with changing floor dominance.

Overall, the floor-by-floor HFRS demonstrates that horizontal floor acceleration demands are governed by building-specific spectral amplification rather than by a uniform height-only trend. The dominant period band changes with earthquake characteristics, and the controlling floor can change with period, event, and sensor line. These observations motivate the period-by-period HAF analyses in the following sections, where the height dependence of $PSA_{\mathrm{HGM}}$is evaluated statistically across buildings and earthquakes rather than inferred from individual spectra alone.

5.4.3 Height-wise Amplification of HFRS

The horizontal HAF results show that the measured HFRS are strongly period dependent and that the degree of height-wise amplification changes substantially between the short-period and intermediate-to-long-period ranges. Unlike the vertical direction, where the strongest amplification is concentrated mainly in a narrow short-period band, the horizontal geometric-mean response, denoted here as HGM, exhibits relatively modest short-period amplification but much larger amplification near the dominant horizontal modal periods of the buildings.

Figure 5.13 presents a representative full-period HAF profile for the middle sensor line of JPL 180 during the Searle Valley earthquake. The figure shows that the horizontal amplification is not uniform over the range of considered periods. At very short periods, the HAF values are generally close to unity or only moderately above unity, indicating that the near-rigid horizontal floor acceleration is not strongly amplified relative to the reference floor. In contrast, a pronounced amplification band develops near the intermediate-period range, with the largest separation among floors occurring around $T \approx 1.0$–1.5 s. In this range, the upper floors exhibit substantially larger HAF values than the lower floors. This full-period view demonstrates that the strongest horizontal height effect is associated with dynamic amplification near modal response bands rather than with the short-period limit alone.

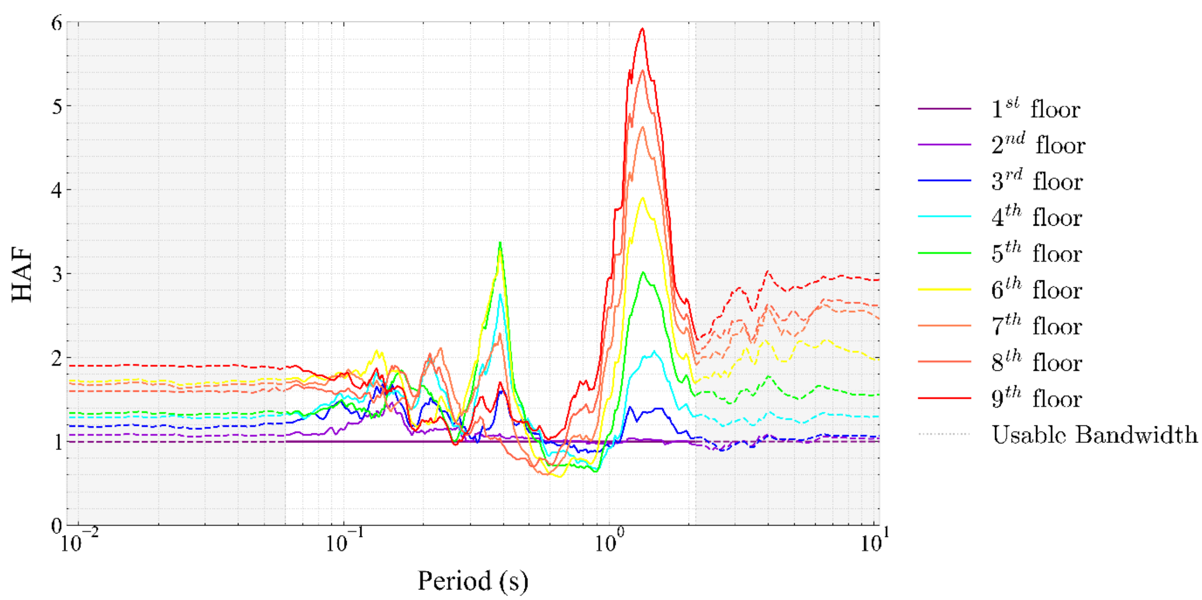

Figure 5.13. HAF profiles over the full period range for the horizontal geometric-mean direction at the middle-sensor line of JPL 180 during the Searle Valley earthquake.

The short-period horizontal HAF profiles are shown in Figure 5.14 for $T = 0.01$s. This period corresponds to the near-rigid oscillator limit and is expected to be closely related to the horizontal PFA ratio. Across all cases, the mean short-period profiles generally remain much closer to unity. Some buildings show moderate upper-floor amplification, but the profiles are not uniformly monotonic, and the magnitude of amplification varies considerably by building and sensor line. JPL 183 east sensor line and JPL 238 show the clearest short-period upper-floor amplification, while JPL 264 and JPL 180 middle sensor line show more moderate increases. JPL 303 remains close to unity over most of its height, and JPL 321 shows a mean top-floor value below unity, indicating that the highest accepted floor did not amplify the short-period HGM demand relative to the reference floor for the selected earthquake set.

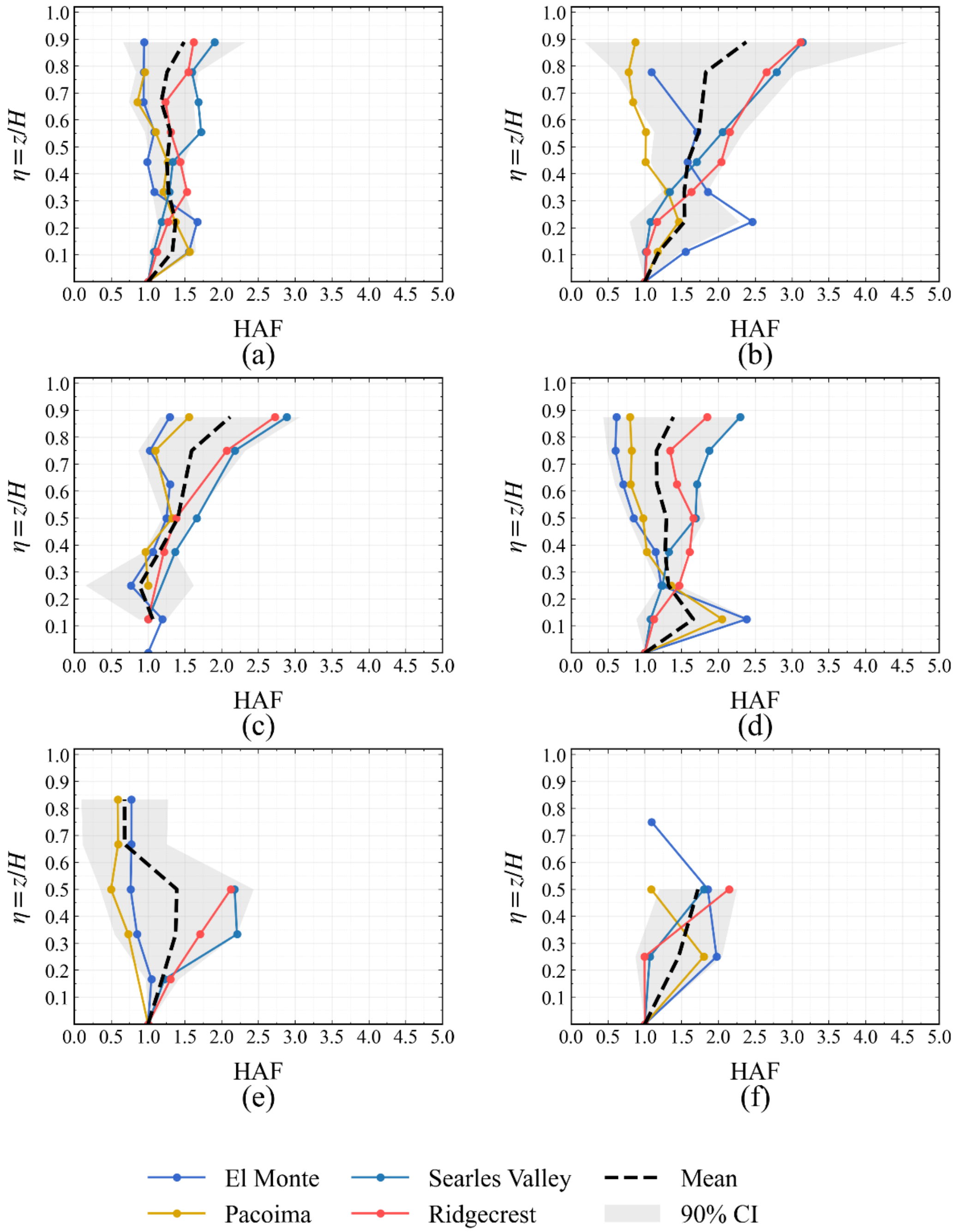

Figure 5.14. Between-event horizontal HAF profiles at T=0.01 s for: (a) JPL 180 (middle-sensor line); (b) JPL 183 (east-sensor line); (c) JPL 238; (d) JPL 264; (e) JPL 321; and (f) JPL 303. Colored curves show the earthquake-specific profiles, the dashed black curve shows the between-event mean profile, and the shaded band shows the 90% confidence interval.

The same short-period behavior is quantified in Table 5.8. For most building-line profiles, the mean top-floor HAF ranges from approximately 1.0 to 2.4. The smallest value occurs for JPL 321, with a mean HAF of 0.68, while the largest mean value occurs for the east sensor line of JPL 183, with a mean HAF of 2.38. By contrast, the west sensor line of JPL 180 and JPL 303 remain close to unity. These results show that short-period horizontal amplification exists in some buildings, but it is not the controlling horizontal amplification mechanism for the overall dataset.

Table 5.8. Highest instrumented level HAF at 0.01 s summary for horizontal building-line profiles

Building		**Highest instrumented level**	**Mean HAF**	**Median HAF**
JPL180	West	8*	1.04	1.04
	Middle	9	1.49	1.62
	East	9	1.40	1.27
JPL183	West	9	1.73	1.74
	East	9	2.38	3.12
JPL 238		8	2.12	2.14
JPL 264		8	1.39	1.32
JPL 321		6	0.68	0.68
JPL 303		4	1.09	1.09

* CSN metadata Floor 1 corresponds to the ground-level record. The highest accepted floor is the highest instrumented level retained after record-quality screening. It is not interpreted as a roof-level sensor.

A different pattern emerges when the HAF profiles are evaluated at the period of maximum mean horizontal amplification for each building, as shown in Figure 5.15. These periods are much longer compared to vertical direction: $T = 1.5$s for JPL 180 middle, $T = 0.75$s for JPL 183 east, $T = 0.75$s for JPL 238, $T = 1.5$s for JPL 264, $T = 1.0$s for JPL 321, and $T = 0.5$s for JPL 303. At these periods, the mean profiles show a much stronger and more systematic increase with height. In most cases, the upper floors clearly dominate the response, and the between-event mean profile rises from approximately unity at the reference floor to values between about 3 and 6 at the highest accepted floor.

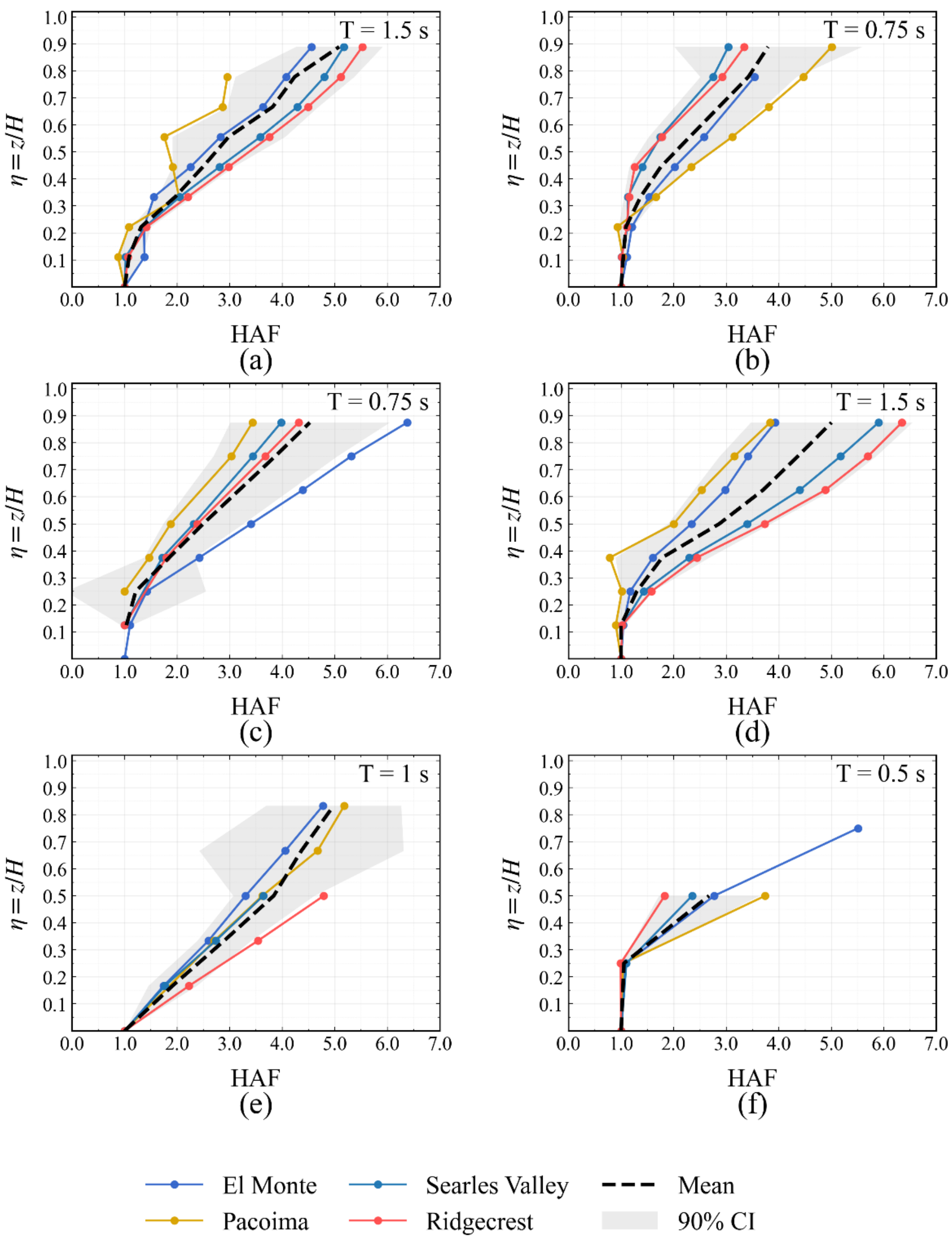

Figure 5.15. Between-event profiles corresponding to the period of maximum mean HAF in horizontal direction for each building: (a) JPL 180 (middle-sensor line) at T=1.5s; (b) JPL 183 (east-sensor line) at T=0.75 s; (c) JPL 238 at T=0.75 s; (d) JPL 264 at T=1.5 s; (e) JPL 321 at T=1.0 s; and (f) JPL 303 at T=0.5 s. Colored curves show the earthquake-specific profiles, the dashed black curve shows the Between-event mean profile, and the gray area shows the 90% confidence interval.

Table 5.9 summarizes the maximum top-floor mean HAF values and their corresponding periods for all building-line profiles. The peak periods fall between $T = 0.5$s and $T = 1.5$s for all cases, confirming that the dominant horizontal height amplification occurs in the intermediate-to-long-period range. The largest value in the dataset occurs for the west sensor line of JPL 180, where the mean top-floor HAF reaches 10.35 at $T = 1.5$s. The other JPL 180 sensor lines also peak at $T = 1.5$s, with mean top-floor HAF values of 5.08 for the middle line and 4.88 for the east line. JPL 264, JPL 321, and JPL 303 show similarly strong amplification, with peak mean HAF values of 5.00, 4.98, and 5.51, respectively. While JPL 183 and JPL 238 reach peak values between approximately 3.6 and 4.5.

Table 5.9. Maximum highest instrumented level HAF values for horizontal building-line profiles

Building		**Highest instrumented level**	**Peak period (s)**	**Peak mean HAF**
JPL180	West	8*	1.5	10.35
	Middle	9	1.5	5.08
	East	9	1.5	4.88
JPL183	West	9	0.75	3.63
	East	9	0.75	3.80
JPL 238		8	0.75	4.53
JPL 264		8	1.5	5.00
JPL 321		6	1	4.98
JPL 303		4	0.5	5.51

* CSN metadata Floor 1 corresponds to the ground-level record. The highest accepted floor is the highest instrumented level retained after record-quality screening. It is not interpreted as a roof-level sensor.

Because $T = 1.0$s falls within the dominant horizontal response range for most of the buildings considered in this study, the within-event profiles at this period, shown in Figure 5.16, provide a complementary view of the horizontal HAF behavior. At this period, the pooled mean profiles for all four earthquakes increase with height, indicating that the horizontal height effect is not caused by a single earthquake. However, the magnitude and dispersion differ among events. The El Monte panel shows the largest spread, mainly because one JPL 180 west-sensor line profile produces an unusually large upper-floor amplification relative to the rest of the dataset. This response should be interpreted cautiously because it is event- and sensor-line-specific and is not repeated with the same magnitude in the other earthquake records. The large value may reflect a combination of localized dynamic response along the west sensor line, possible torsional or plan-location effects, and the sensitivity of HAF ratios when the reference-floor spectral ordinate at $T = 1.0$s is relatively small. Record-specific effects, including local measurement noise or reduced signal-to-noise ratio at that sensor location, may also have contributed. Therefore, this profile is retained in the within-event comparison but is treated as an isolated high-amplification case rather than as representative of the overall horizontal HAF trend. Pacoima also shows a clear increasing trend with height. The Searle Valley and Ridgecrest panels show more moderate amplification and narrower clustering for most building lines, although upper-floor amplification remains evident. These within-event results confirm that the period-specific horizontal height effect is systematic, but also strongly affected by earthquake-to-earthquake variability.

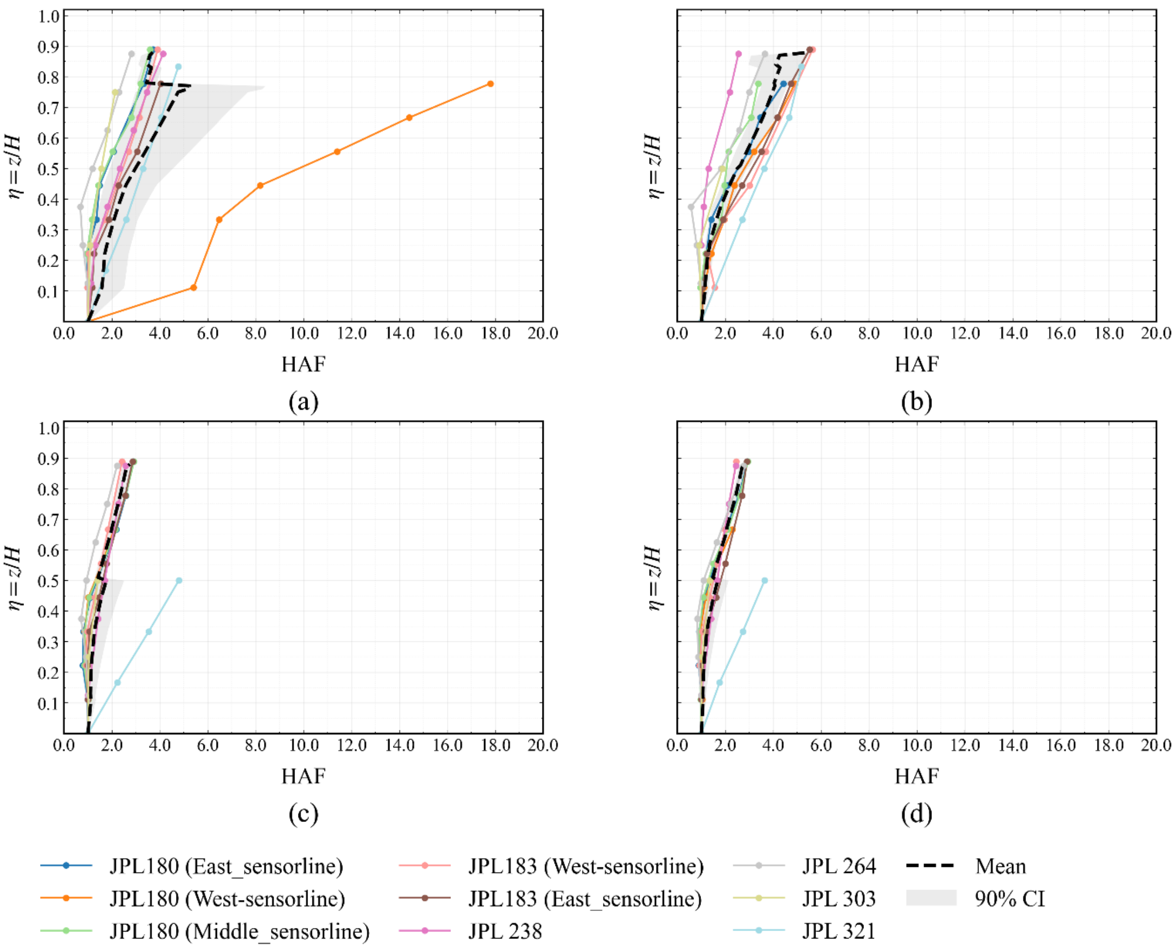

Figure 5.16. Within-event profiles corresponding to HAF in horizontal direction at T=1s for each earthquake: (a) El Monte; (b) Pacoima; (c) Searle Valley; (d) Ridgecrest. Colored curves show the building-specific profiles, the dashed black curve shows the within-event mean profile, and the gray area shows the corresponding 90% confidence interval.

Overall, the horizontal HAF results show two distinct regimes. First, at very short periods, the HGM response behaves similarly to a rigid-component or PFA-based measure, and the associated height amplification is generally modest and not consistently monotonic. Second, at intermediate-to-long periods, especially between approximately $T = 0.5$ s and $T = 1.5$ s, the HGM amplification becomes much stronger and more systematically height dependent. This period range corresponds to the range where the floor-by-floor HFRS in Section 5.4.2 showed pronounced modal amplification. Therefore, the horizontal response is better described as period-dependent and modal-band-sensitive, rather than as a simple height-only amplification trend.

5.4.4 Evaluation of Measured HFRS against ASCE Assumptions

Chapter 13 of ASCE 7-22 provides an explicit height-amplification framework for the horizontal seismic design force of nonstructural components. In the equivalent-static procedure, the horizontal component force is amplified through the height factor (H_f). As described in Section 5.2.5, ASCE generally permits using a simplified height factor ($H_f = 1 + 2.5\left(\frac{z}{h}\right)$) and when the approximate fundamental period of the supporting structure is available, the period-dependent form ($H_f = 1 + a_1\left(\frac{z}{h}\right) + a_2\left(\frac{z}{h}\right)^{10}$) should be implemented, where a_1 and a_2 are determined based on the fundamental period of the supporting structure. The comparison in this section is therefore a direct evaluation of the current ASCE horizontal height-amplification framework against the measured HFRS amplification obtained from the JPL-CSN dataset.

The measured HFRS amplification trends show that the current equations in the building code for height factor are incomplete in one important respect: neither the simplified nor the period-dependent equations depend on the period of the nonstructural component (T). The measured HFRS amplification, by contrast, varies strongly with T. This distinction is important because the horizontal floor response spectra are not governed only by elevation; they are also shaped by dynamic filtering of the supporting structure and by the degree of tuning between the component period and the dominant horizontal response periods of the building.

Figure 5.17 compares the empirical HAF at the highest sensor accepted level in the horizontal direction with the corresponding HAF values derived from the simplified and period-dependent models in ASCE Chapter 13. Because the measured HAF values are computed relative to CSN metadata Floor 1, which corresponds to the ground-level record, the ASCE height-amplification functions are evaluated directly. In this comparison, the ASCE benchmark is not evaluated at $z/h = 1.0$ for all buildings. Instead, the ASCE value is evaluated at the highest measured normalized elevation for each building. This gives an average simplified Chapter 13 value of approximately 3.0 and an average period-dependent Chapter 13 value of approximately 2.1.

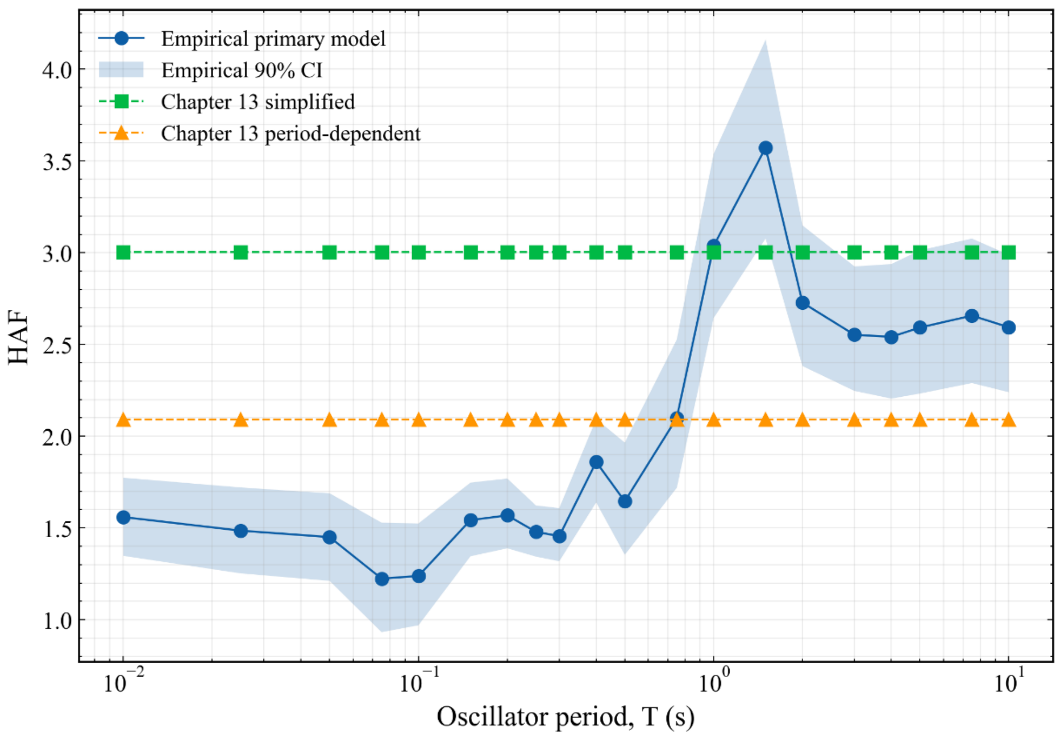

Figure 5.17. Highest level HAF versus oscillator period for the horizontal direction.

The ASCE values are constant with T because the Chapter 13 height-factor equations do not explicitly include the component oscillator period. In contrast, the empirical horizontal HAF varies substantially with oscillator period. At short periods, the empirical HAF is approximately 1.4–1.65 and is therefore well below both ASCE benchmarks, especially the simplified benchmark. The empirical curve decreases slightly around T~0.075–0.10 s, then increases rapidly through the intermediate-period range, reaching approximately 3.0 at $T = 1.0$ s and a maximum of approximately 3.6 at $T = 1.5$ s. Although many conventional anchored nonstructural components are expected to be stiffer than this range, these periods are still useful for interpreting flexible, suspended, isolated, or otherwise period-sensitive components and for identifying the modal amplification band of the supporting building. At longer periods, the empirical HAF decreases from the peak but remains near approximately 2.5–2.7 for periods greater than about 2 s. This period-dependent trend is the main reason a height-only model is insufficient for representing measured HFRS amplification.

Table 5.10 summarizes the ASCE comparison over representative oscillator periods. The mean log-bias is defined as $\overline{\ln\left(\frac{HAF_{\text{emp}}}{HAF_{\text{model}}}\right)}$, so that negative values indicate that the model overpredicts the measured HAF, while positive values indicate that the measured HAF exceeds the model. The table confirms the behavior observed in Figure 5.17. At short periods, both ASCE models overpredict the measured HAF, with the simplified model being more conservative. Near the modal amplification range around T=1.0–1.5 s, the measured amplification becomes comparable to the simplified ASCE benchmark and exceeds the period-dependent benchmark. At longer periods, the simplified benchmark remains moderately conservative, whereas the period-dependent benchmark tends to fall below the measured empirical HAF.

Table 5.10. Summary of horizontal ASCE comparison metrics at representative oscillator periods.

Period (s)	ASCE model	Empirical HAF	ASCE HAF	Mean log-bias	$RMSE_w$	MDARE	Coverage	Interpretation
0.01	simplified	1.49	3.13	-0.385	0.526	0.263	0.096	Strong overprediction
	period-dependent	1.49	2.1	-0.107	0.304	0.093	0.494	Improved but conservative
0.05	simplified	1.4	3.13	-0.416	0.574	0.262	0.104	Strong overprediction
	period-dependent	1.4	2.1	-0.138	0.351	0.095	0.497	Moderate overprediction
0.1	simplified	1.21	3.13	-0.458	0.676	0.288	0.149	Strong overprediction
	period-dependent	1.21	2.1	-0.179	0.46	0.082	0.621	Better coverage; still conservative
0.25	simplified	1.43	3.13	-0.398	0.501	0.319	0.104	Strong overprediction
	period-dependent	1.43	2.1	-0.12	0.242	0.11	0.424	Improved error but limited coverage
0.5	simplified	1.58	3.13	-0.316	0.39	0.256	0.272	Conservative
	period-dependent	1.58	2.1	-0.038	0.168	0.093	0.725	Best within-event coverage
1	simplified	2.83	3.13	-0.016	0.26	0.218	0.455	Measured demand begins to exceed code
	period-dependent	2.83	2.1	0.263	0.398	0.193	0.489	Underprediction in modal range
1.5	simplified	3.31	3.13	0.122	0.245	0.166	0.545	Underprediction near peak amplification
	period-dependent	3.31	2.1	0.4	0.496	0.567	0.236	Significant underprediction
2	simplified	2.54	3.13	-0.088	0.258	0.244	0.239	Good average bias
	period-dependent	2.54	2.1	0.191	0.327	0.078	0.469	Partial agreement
5	simplified	2.42	3.13	-0.094	0.199	0.168	0.511	Moderate agreement
	period-dependent	2.42	2.1	0.184	0.278	0.142	0.573	Moderate agreement
10	simplified	2.42	3.13	-0.1	0.187	0.162	0.517	Moderate agreement
	period-dependent	2.42	2.1	0.178	0.263	0.181	0.612	Moderate agreement

The within-event coverage maps in Figure 5.18 provide a complementary way to evaluate the ASCE models. These maps show the fraction of the empirical height grid for which the ASCE profile falls within the empirical confidence interval for each earthquake and oscillator period.

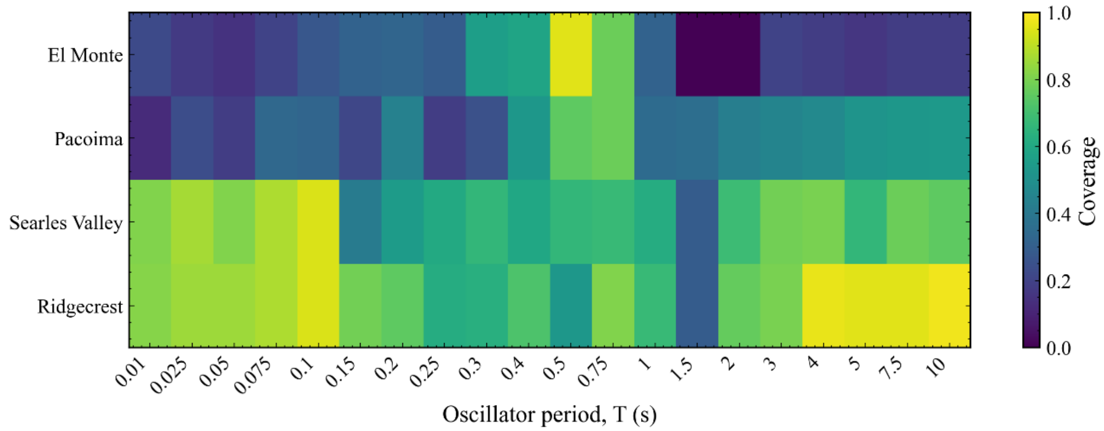

(a)

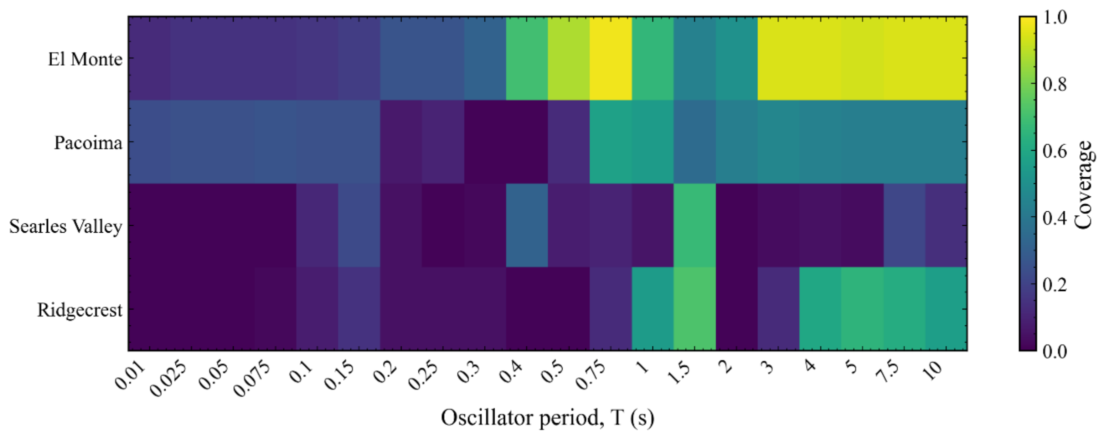

(b)

Figure 5.18. Within-event agreement coverage of the ASCE horizontal height amplification models against measured HAF: a) period-dependent model, b) simplified model

The period-dependent model, shown in Figure 5.18(a), generally provides better coverage than the simplified model over a broader portion of the period range, especially in the intermediate-period range where the measured horizontal amplification becomes more comparable to the code-implied profile. However, its coverage remains uneven across earthquakes and oscillator periods. The simplified model, shown in Figure 5.18(b), performs poorly at short periods for all events because it substantially overpredicts the measured horizontal HAF. At longer periods, the simplified model has better coverage for some event-period combinations, especially where the measured HAF approaches the code-implied value, but its behavior still remains inconsistent.

These results indicate that the current treatment of horizontal floor accelerations in ASCE Chapter 13 is useful but incomplete. The simplified model is attractive because of its simplicity, but it is too conservative for short-period demands and not sufficiently period sensitive for modal-band demands. The period-dependent model improves the comparison in some period ranges because it includes the supporting-structure period, but it still does not explicitly account for the component oscillator period T. Since the measured HFRS amplification varies strongly with T, a more complete code-oriented model should include both height and oscillator-period dependence.

5.5 Chapter Summary, Key Findings, and Recommendations

This chapter evaluated vertical and horizontal floor response spectra for six densely instrumented JPL buildings subjected to four common earthquake events. The analysis used 5%-damped PSA computed from processed floor acceleration records and expressed the results through height amplification factors. The short-period validation showed that $PSA(0.01\ \mathrm{s})$ closely reproduces PFA, supporting its use as a rigid-component demand metric.

The results demonstrate that floor acceleration demand is both height dependent and period dependent. In the vertical direction, the strongest amplification occurred over short periods, especially near the dominant vertical response bands, and decreased at longer periods. This indicates that vertical nonstructural component demand should not be represented as height independent. In the horizontal direction, amplification was generally modest over the short period ranges but increased significantly near intermediate periods associated with fundamental building modal response, showing that component-period effects are also important for HFRS.

Comparison with ASCE/SEI 7-22 Chapter 13 shows that the current horizontal height-amplification framework captures the general increase of demand with elevation, but it does not fully represent the period-dependent amplification observed in the measured spectra. More importantly, ASCE 7-22 Chapter 13 does not provide an explicit VFRS-based or height-dependent amplification model; vertical effects in nonstructural component design are addressed only through the concurrent vertical seismic force, E_v.

The results support two preliminary code-oriented recommendations. First, the horizontal height-amplification framework in ASCE/SEI 7 Chapter 13 should retain the concept of increasing demand with elevation but should be refined to include component-period dependence. Second, Chapter 13 should consider introducing a separate vertical floor-amplification factor, $H_{f,v}$, to account for the measured increase of vertical floor demand with height. This factor should not replace the code-level vertical seismic load effect, E_v; rather, it should complement E_v by representing the additional amplification that occurs within the building.

The results should be considered as data-driven recommendations based on the available JPL-CSN records. Additional validations using other buildings, stronger shaking records, different structural systems, and nonlinear response-history analyses are needed before broader code adoption. The findings of this chapter motivate Chapter 6, which shifts from measured in-building amplification to the vertical seismic load effect, E_v, and evaluates the efficacy of two different methods in current provisions for calculating the vertical design.

CHAPTER 6. Vertical Seismic Load Effects on Building Code

This study evaluates the efficacy of two alternative methods for estimating vertical seismic load effects (E_v), which are specified in United States building codes (i.e., ASCE 7-22) and guidelines (i.e., LATBSDC) and employed in the seismic design of structural and non-structural systems. In both approaches, the vertical seismic load is computed as a percentage of the nominal dead load. One method uses 20% of the horizontal short-period design spectral acceleration ($\mathrm{S_{DS}}$) as the dead load factor, while the other computes the dead load factor as 30% of the vertical spectral acceleration value at the vertical period of the structure ($\mathrm{S_{av}}$). The two approaches are evaluated and compared using (i) the results of probabilistic seismic hazard analysis carried out by USGS (which is the backbone data for ASCE 7-22) for 19,316 sites in California, and (ii) the NGA-West2 ground motion models for over 3,000 seismic scenarios. The results are presented in terms of the probability distribution of the ratio of the E_v values obtained from the two approaches $\left(\frac{0.3S_{av}}{0.2S_{DS}}\right)$ as a function of the vertical period of the structure. The evaluation reveals that the outcomes of applying the two methods are generally not consistent and depend significantly on the vertical period range of the structure. The study pinpoints period ranges where the results of one method substantially diverge from the other and provides recommendations for E_v calculations across various seismic design categories.

This chapter is organized as follows. Section 6.1 introduces the current code expressions for E_v, defines R_{E_v}, and the evaluation framework. Section 6.2 presents the scenario-based GMM evaluation using NGA-West2 model pairs. Section 6.3 presents the site-specific California evaluation using the ASCE 7 Hazard Tool. Section 6.4 synthesizes the findings and presents code-oriented recommendations.

The work presented in this chapter has been published as a peer-reviewed journal article in the ASCE Journal of Structural Engineering: Bolourani, Burton, and Bozorgnia, "Evaluation of Vertical Seismic Load Effects Specified in the United States Building Code," *Journal of Structural Engineering*, ASCE, 151(12), 04025224. The dissertation author was the primary author of this work and was responsible for the data generation, analysis, interpretation of results, and preparation of the manuscript. Professor Henry V. Burton and Professor Yousef Bozorgnia supervised the research, contributed to the interpretation of the results, and reviewed and edited the manuscript (Bolourani et al., 2025).

6.1 Introduction, background, and scope

According to the current US building code, there are different procedures to quantify the vertical seismic load effect (E_v) (i.e., the force used to design for the vertical ground motion component) (ASCE, 2016, 2022; LATBSDC, 2023). Early approaches to computing E_v in a design context were based on an equivalent static load coefficient that traces back to ATC 3-06 (1978) (ASCE, 2016; Chen, 2023). Initially defined as $0.2D$, where D represents the dead load of the structure; this coefficient was introduced without any clear explanation of its origin. Neither the initial ATC 3-06 guidelines nor the later NEHRP provisions offered a precise explanation of how the "0.2" factor was derived, which suggests that it arose from consensus-based judgments (Applied Technology Council, 1978; Federal Emergency Management Agency, 2009). A value of $0.2S_{DS} \times D$ is used in the most recent version of ASCE 7 (ASCE, 2016, 2022) and similar guidelines (LATBSDC, 2023) to compute the vertical seismic load effect, where S_{DS} represents the design horizontal spectral acceleration at a short period (0.2 seconds). The tentative rationale provided in ASCE 7 is that $0.2S_{DS}$ is reflected in the formula $0.3 \times \frac{2}{3}S_{DS}$. In this context, the 0.3 factor represents the 30% in the 100-30 orthogonal load combination rule, and the $\frac{2}{3}$ is the traditionally assumed ratio between the vertical and horizontal acceleration components (ASCE, 2016, 2022). However, prior studies have shown that the assumed $\frac{2}{3}$ ratio for $\frac{V}{H}$ is questionable at best and therefore unsuitable for justifying the use of $0.2S_{DS}$ as the basis for E_v (Bozorgnia & Campbell, 2016; Bozorgnia et al., 1995; Gülerce & Abrahamson, 2011; Niazi & Bozorgnia, 1991).

Furthermore, S_{DS} represents the horizontal spectral acceleration at a single horizontal period (0.2 seconds), which means the specified vertical load on a structure using $0.2S_{DS}$ is independent of the vertical period and vertical response spectra. Currently, when the vertical response spectrum is explicitly considered in the design, ASCE7-22 provides an alternative approach using $E_v = 0.3\mathrm{S_{av}} \times \mathrm{D}$, where S_{av} is the vertical spectral acceleration at the vertical period of interest. However, it still generally permits the use of either $0.2S_{DS}$ or $0.3S_{av}$ for calculating E_v (ASCE, 2016, 2022).

It is difficult to isolate the effect of the vertical ground motion component on structural damage that has been observed in the field, e.g., during post-earthquake reconnaissance. There have been field-based studies that have identified the vertical component as a serious contributor to observed earthquake damage (Di Sarno et al., 2011; Varevac et al., 2010). The vertical periods of structural and non-structural components and systems vary depending on the specific component. For example, Bozorgnia et al analyzed the vertical response of 12 instrumented structures recorded in the 1994 Northridge earthquake and identified a vertical period range of

0.075 to 0.26 seconds, underscoring the need for a period-dependent comparison of these two methods (Bozorgnia et al., 1998).

Recent research has investigated the effectiveness of using $0.2S_{DS} \times D$ for estimating E_v. Some studies suggest that using $0.2S_{DS} \times D$ is conservative, while others argue that this equation can be unconservative and poorly represents E_v (Keskin, 2020; Nielsen et al., 2020). This highlights a significant gap in literature and a need for a more comprehensive evaluation.

This study aims to evaluate the efficacy of two alternative methods for calculating E_v (i.e., $0.2S_{DS} \times D$ and $0.3S_{av} \times D$), over a range of vertical periods. Taking $0.3S_{DS} \times D$ to be the benchmark value, the degree of conservatism in $0.2S_{av} \times D$ expression is quantified based on the ratio $\frac{0.3S_{av}}{0.2S_{DS}}$, which we denote throughout the paper as R_{E_v}. A large data set of period-dependent R_{E_v} values is obtained from two sources: (i) NGA-West2 Ground Motion Models (GMMs) for over 3,000 seismic scenarios and (ii) the results from Probabilistic Seismic Hazard Analysis (PSHA) carried out by USGS for 19,316 sites in California. These sites span the entire state of California with a grid resolution of 0.05 by 0.05 degrees in latitude and longitude. Based on the probability distribution of R_{E_v} as a function of the vertical period of the structure, this research provides recommendations for building codes to adopt the most appropriate alternative for calculating E_v, considering the full range of overestimation and underestimation of the benchmark value.

6.2 Scenario-Based GMM Evaluation of E_v

6.2.1 Data generation using NGA-West2 model

In this section, for various earthquake scenarios, three sets of GMMs are utilized to generate datasets of R_{E_v} values, with each set requiring models for both the horizontal (to compute $0.2S_{DS}$) and vertical (to compute $0.3S_{av}$) components. To maintain consistency, vertical and horizontal models from the same modelers are used to compute R_{E_v}. The first R_{E_v} dataset is generated using the horizontal ground motion model developed by Abrahamson, Silva, and Kamai (abbreviated as ASK) (Abrahamson et al., 2014) and the vertical model developed by Gülerce and Abrahamson (abbreviated as GA), which provides a period-dependent vertical-to-horizontal ratio $\left(\frac{V}{H}\right)$ (Gülerce & Abrahamson, 2011). For this dataset, the median S_{DS} is computed using the ASK model, and S_{av} values are calculated by multiplying the $\frac{V}{H}$ from the GA model by the horizontal component from the ASK model. Given these two values, the ratio denoted as $R_{E_v,A} = \frac{0.3S_{av\_GA}}{0.2S_{DS\_ASK}}$ is computed.

The second dataset is generated using the horizontal GMM developed by Boore, Stewart, Seyhan, and Atkinson (abbreviated as BSSA) and the vertical GMM developed by Stewart, Boore, Seyhan, and Atkinson (SBSA) (Boore et al., 2014; Stewart et al., 2016). The BSSA model is used to compute the S_{DS}, and the SBSA model is used to compute period-dependent vertical acceleration S_{av}. The ratio for this dataset is denoted as $R_{E_v,B} = \frac{0.3S_{av\_SBSA}}{0.2S_{DS\_BSSA}}$.

The third dataset is developed using Campbell and Bozorgnia (abbreviated as CB) horizontal GMM and the Bozorgnia and Campbell (abbreviated as BC) vertical GMM is used to create the third and final dataset (Bozorgnia & Campbell, 2016; Campbell & Bozorgnia, 2014). Similar to SBSA, the BC model directly computes the period-dependent vertical acceleration, which along with the horizontal spectral acceleration at the 0.2s period computed using the CB model, is used to determine the ratio denoted as $R_{E_v,C} = \frac{0.3S_{av\_BC}}{0.2S_{DS\_CB}}$.

The three sets of R_{E_v} based on the different GMM pairs are combined by taking the equally weighted average of the individual values. The combined dataset, denoted as $R_{E_v,GMM}$, is generated for different scenarios that are characterized by all possible combinations (i) earthquake magnitudes ranging from $M = 4$ to $M = 8$ at intervals of 0.25, (ii) rupture distances ranging from $R_{rup} = 0\ km$ to $R_{rup} = 5\ km$ at $1\ km$ increments as well as $R_{rup} = 10\ km$ to $R_{rup} = 50\ km$ at $5\ km$ increments, and (iii) shear wave velocity time-averaged over the top 30 m of soil ranging from $V_{S30} = 200\ m/s$ to $V_{S30} = 700\ m/s$ at $50\ m/s$ intervals with an additional consideration of $V_{S30} = 760\ m/s$, and (iv) for the following periods (seconds):

$$T_v = \{0.01, 0.02, 0.03, 0.05, 0.075, 0.1, 0.15, 0.20, 0.25, 0.30,$$

$$0.40, 0.50, 0.75, 1.0, 1.5, 2.0, 3.0, 4.0, 5.0, 7.5, 10\}$$

The combinations of magnitudes, rupture distances, shear-wave velocities, and periods produce a total of 64,260 data points.

In this section, even though we use scenarios and GMMs to estimate $R_{E_v,GMM}$, we would like to stay close to the spirit of ASCE 7 to categorize the scenario results. For the seismic design of structures using ASCE 7-22 , the Seismic Design Category (SDC) is determined from an S_{DS} value (ASCE 7-22 Table 11.6-1) that is based on the PSHA results from USGS. However, as indicated above, the response spectra used in this section are scenario-based and derived from

GMMs. Therefore, a modified seismic design category (SDC*) is defined based on $S_{DS}{}^{*}$ which is the pseudo-spectral acceleration (PSA) at a short period (0.2 seconds) acquired from the GMMs. Table 6.1 presents the definition and number of seismic scenarios corresponding to each SDC*.

Table 6.1. Modified Seismic Design Category (SDC*)

SDC*	**Definition**	**Number of Seismic Scenarios**
A*	$S_{Ds}{}^{*} \leq 0.167$	989
B*	$0.167 < S_{Ds}{}^{*} \leq 0.33$	639
C*	$0.33 \leq S_{Ds}{}^{*} < 0.5$	407
D*	$0.5 \leq S_{Ds}{}^{*}$	1025
		Total: 3060

The dataset generated in this section enables the evaluation of $R_{E_v,GMM}$ across a diverse set of seismic hazard parameters. The data is divided into four subsets, each corresponding to one of the SDC*'s described in Table 6.1.

6.2.2 Probabilistic methodology

A probabilistic approach is used to examine the $R_{E_v,GMM}$ distribution that is used as the basis for evaluating the vertical seismic load effect. Figure 6.1(a) shows the $R_{E_v,GMM}$ distribution across the full range of vertical periods (T_v) and all scenarios with an SDC* of D*. The dashed yellow line indicates the threshold where $R_{E_v,GMM}$ is equal to 1.0, serving as a reference to assess the degree of conservatism in using $0.2S_{DS}$ versus $0.3S_{av}$ to calculate E_v. Each blue line represents a unique seismic scenario that plots $R_{E_v,GMM}$ as a function of T_v. For example, the green curve corresponds to the seismic scenario with $M = 6.5$, $R_{rup} = 10\ km$ and $V_{S30} = 760\ \mathrm{m/s}$. A histogram is generated at each period based on the data points of a given SDC*, resulting in 21 histograms for 21 discrete periods for each SDC*. As an example, Figure 6.1(b) shows the histogram and probability density function (PDF) generated based on 1025 $R_{E_v,GMM}$ values corresponding to $T_v = 0.1\ s$.

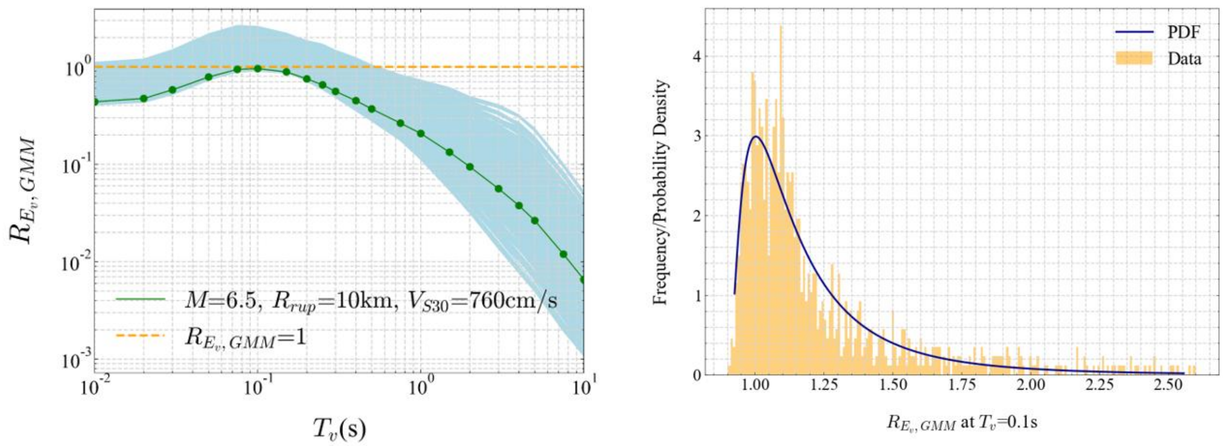

(a) (b)

Figure 6.1. (a) $R_{E_v,GMM}$ for all seismic scenarios where the SDC* is D* and (b) histogram and the best fitted distribution (lognormal) corresponding to $T_v = 0.1\ s$.

The data is further characterized by evaluating the goodness-of-fit of the period-dependent $R_{E_v,GMM}$ values against six commonly used probability distributions. Specifically, Lognormal, Normal, Exponential, Gamma, Beta, and Rayleigh distributions are considered. The goodness-of-fit for each distribution is assessed using three statistical measures: the Residual Sum of Squares (RSS), the Akaike Information Criterion (AIC), and the Bayesian Information Criterion (BIC). These metrics serve to evaluate the goodness-of-fit, the complexity of the model, and the likelihood of generating the observed data using the model, respectively. The distribution that yields the lowest RSS, AIC, and a more favorable BIC, is selected as the best representation of the data. These metrics are calculated as follows (Akaike, 1974; James et al., 2013; Schwarz, 1978):

$$RSS = \sum (y_i - \hat{y}_i)^2 \qquad \text{Eq 6.1}$$

$$AIC = 2k - 2\,ln(L) \qquad \text{Eq 6.2}$$

$$BIC = ln(n)\,k - 2\,ln(L) \qquad \text{Eq 6.3}$$

where y_i is the observed value, $\hat{y}_i$ is the value estimated from the distribution, k is the number of parameters in the statistical model, n is the sample size, and L is the maximum likelihood function of the model.

Once the best-fit model for the dataset is established, the PDFs are determined and used to compute the probability that R_{E_v} falls within specific ranges at a given T_v. For instance, at $T_v = 0.01\ s$, the probability of $R_{E_v,GMM} < 0.5$ can be computed, and a higher probability in this range would suggest that using $0.2S_{DS}$ is excessively conservative to represent E_v compared to $0.3S_{av}$. Similarly, to assess the interchangeability of the two methods with an acceptable error (e.g., 20%), the probability that $R_{E_v,GMM}$ falls between 0.8 and 1.2 can be computed.

While the probability distribution of $R_{E_v,GMM}$ can be computed for any discrete vertical period, such an approach is impractical for engineering applications. To address this issue, discrete vertical period ranges are defined based on those specified in Section 11.9.2 of ASCE 7-22, with a minor modification for improved accuracy. The considered ranges are as follows: $T_v \leq 0.025\ s$, $0.025\ s < T_v \leq 0.05\ s$, $0.05\ s < T_v \leq 0.1\ s$, $0.1\ s < T_v \leq 0.2\ s$, $0.2\ s < T_v \leq 0.5\ s$, $0.5\ s < T_v \leq 1.0\ s$, $1.0\ s < T_v \leq 2.0\ s$ and $2.0\ s < T_v$.

To improve the interpretability of the results, different R_{E_v} categories are defined, as described in Table 6.2. Note that these categories are based on engineering judgment and can be adjusted accordingly depending on how the findings of this study are being used (e.g., in a code development context).

Table 6.2. Categorizing the implications of $R_{E_v,GMM}$ falling into predefined intervals

Interval	Implication
$1.5 < R_{E_v}$	Using $0.2S_{DS}$ underestimates E_v by more than 50% compared to $0.3S_{av}$.
$1.2 < R_{E_v} \leq 1.5$	Using $0.2S_{DS}$ underestimates E_v.
$0.8 < R_{E_v} \leq 1.2$	Negligible difference between the two methods, allowing for flexibility in the approach used to calculate E_v.
$0.5 < R_{E_v} \leq 0.8$	Using $0.2S_{DS}$ provides a slightly more conservative estimation of E_v.
$R_{E_v} \leq 0.5$	Using $0.2S_{DS}$ significantly overestimates E_v by more than 50% compared to $0.3S_{av}$.

For better clarity, Figure 6.2 summarizes the data generation process, and the methodology used to evaluate E_v based on the GMMs.

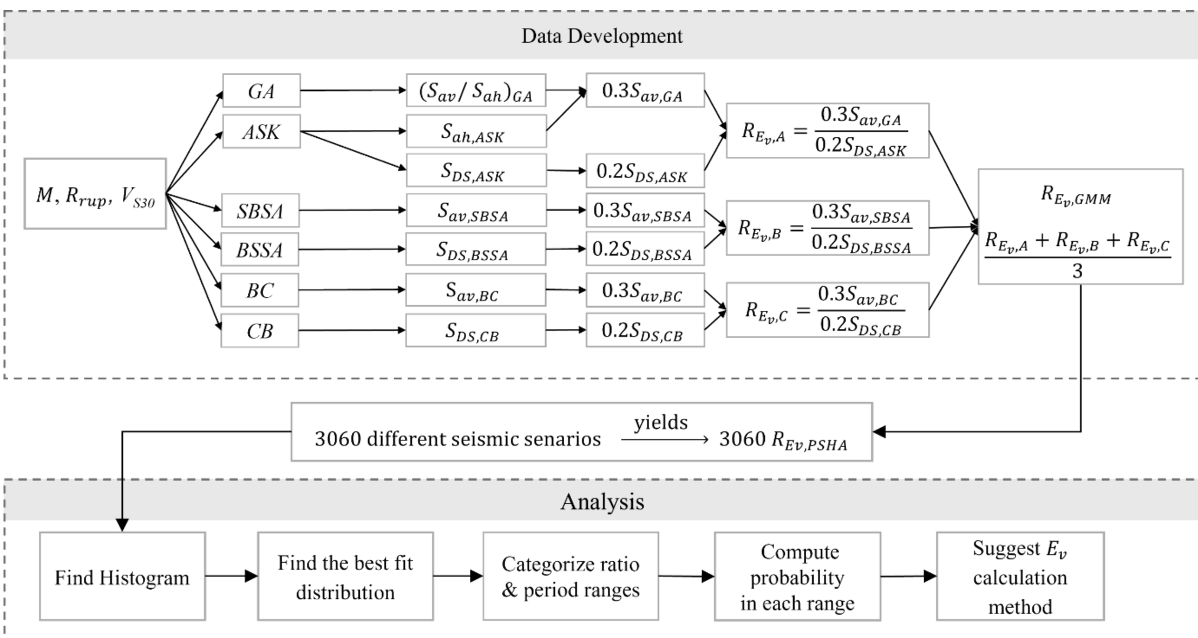

Figure 6.2. Summary of the procedure used to generate the $R_{E_v,GMM}$ dataset and evaluation method

6.2.3 Results and interpretation for GMM Scenario-Based Evaluation

6.2.3.1 Overall trends across SDC*

The results from the analysis of $R_{E_v,GMM}$ indicate that the difference between the outcomes of the two alternative approaches to quantify vertical seismic load is highly dependent on the vertical period of the structure under consideration. Figure 6.3 shows the period-dependent distribution of $R_{E_v,GMM}$ for all SDC* and discrete vertical periods. We observe that for systems with a vertical period longer than 0.55s, using $0.2S_{DS}$ to calculate E_v is always more conservative compared to $0.3S_{av}$. Conversely, for structures with a vertical period shorter than 0.55s, the approach that uses $0.2S_{DS}$ might not necessarily be conservative, underscoring the need to consider the vertical period.

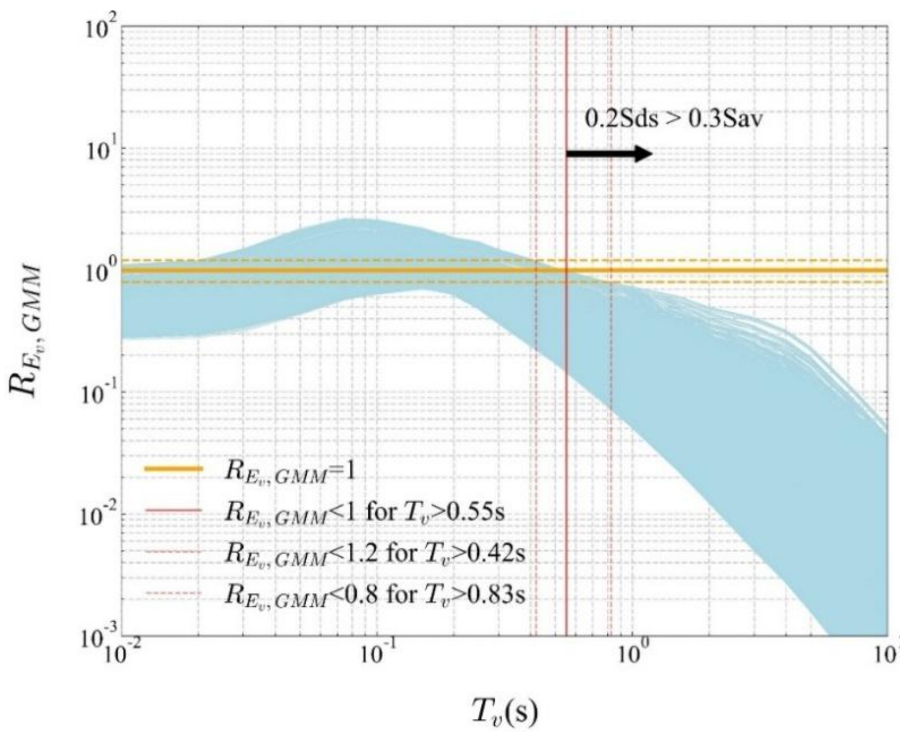

Figure 6.3. $R_{E_v,GMM}$ for all 3060 seismic scenarios as a function of T_v

6.2.3.2 Key findings for SDC* A*

SDC* of A*, encompassing 989 seismic scenarios based on GMMs, represents areas with the lowest seismic hazard. Figure 6.4 summarizes the distribution of $R_{E_v,GMM}$ values for this seismic category across the predefined vertical period ranges. The analysis reveals a consistent overestimation of E_v when using $0.2S_{DS}$ compared to using $0.3S_{av}$, especially for structure with a very short (< 0.025s) or very long (> 0.5s) vertical period, where the probability of $R_{E_v,GMM}$ being less than 0.5 exceeds 71%. In other vertical period ranges, the degree of overestimation slightly decreases, yet remains notable, suggesting that the design guidelines using $0.2S_{DS}$ are overly conservative for SDC*-A* across all vertical periods.

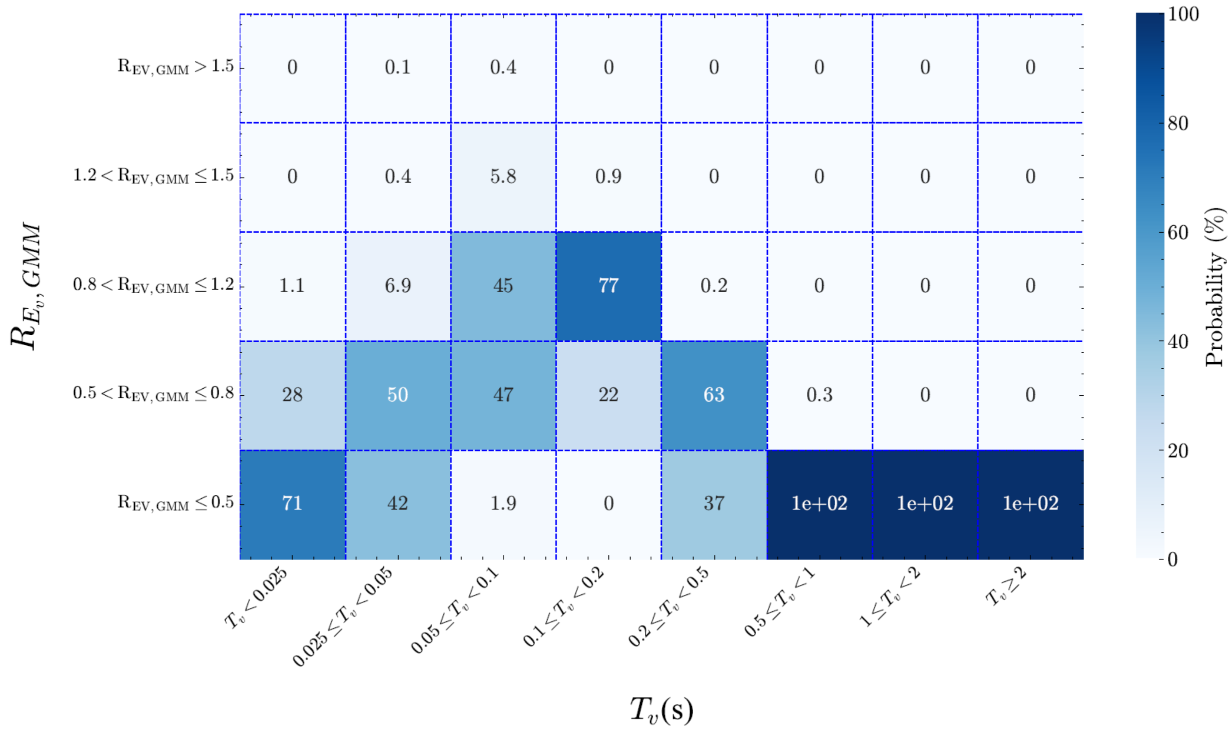

Figure 6.4. Summary of the probability distribution of $R_{E_v,GMM}$ in SDC*-A*

The following is a summary of the key observations from Figure 6.4:

- For $T_v < 0.025$ s, there is an approximately 0.99 probability that $R_{Ev,GMM}$ is less than or equal to 0.8. Most of that probability falls in the $R_{Ev,GMM} \leq 0.5$ interval (0.71 probability), while 0.28 falls in the $0.5 < R_{Ev,GMM} \leq 0.8$ interval. In other words, for structures with a vertical period less than 0.025 s in SDC* A*, computing E_v based on $0.2S_{DS}$ is generally conservative and, in most cases, highly conservative.

- For $0.025 \leq T_v < 0.05$ s, computing E_v based on $0.2S_{DS}$ remains predominantly conservative. There is a 0.42 probability that $R_{Ev,GMM} \leq 0.5$ and a 0.50 probability that $0.5 < R_{Ev,GMM} \leq 0.8$. Only a small portion of the results fall in the comparable or unconservative ranges.

- When $0.05 \leq T_v < 0.1$ s, the results become more balanced. The largest probabilities are in the slightly conservative range (0.47 probability) and the negligibly different range (0.45 probability). The probability of slight or significant underestimation is small, approximately 0.06 in total, indicating that this period range produces the one of the closest agreement between the two E_v calculation methods for SDC* A*.

- For $0.1 \leq T_v < 0.2$ s, the two approaches are even more comparable. There is a 0.77 probability that the results fall within $0.8 < R_{Ev,GMM} \leq 1.2$, and a 0.22 probability that they fall within $0.5 < R_{Ev,GMM} \leq 0.8$. Thus, using $0.2S_{DS}$ in this period range is generally either negligibly different from or slightly conservative relative to using $0.3S_{av}$.

- For $0.2 \leq T_v < 0.5$ s, computing E_v based on $0.2S_{DS}$ again becomes conservative. The probability that $0.5 < R_{Ev,GMM} \leq 0.8$ is 0.63, and the probability that $R_{Ev,GMM} \leq 0.5$ is 0.37. This indicates that the $0.2S_{DS}$ expression tends to overestimate the period-dependent vertical seismic load effect in this range.

- For vertical periods greater than 0.5 s, the results are overwhelmingly conservative. For this range the probability of $R_{Ev,GMM} \leq 0.5$ is almost 1.0.

In general, for SDC* A*, the use of $0.2S_{DS}$ does not create a meaningful concern for underestimating E_v. The results are mostly conservative across all vertical period ranges, with the closest agreement between $0.2S_{DS}$ and $0.3S_{av}$ occurring in the 0.05 to 0.2 s range. However, it should be noted that SDC* A* is not expected to govern the code-oriented recommendations because it represents the lowest seismic hazard range. In this category, both S_{DS} and S_{av} are relatively small, so the absolute difference between the two E_v expressions is limited. Thus, the SDC* A* results are included mainly for completeness, while the practical significance of the study is concentrated in the higher seismic design categories.

6.2.3.3 Key findings for SDC* B*

SDC* B* covers 639 scenarios. The heatmap (Figure 6.5) shows $R_{E_v,GMM}$ values, indicating a conservative design tendency when calculating E_v using $0.2S_{DS}$ compared to using $0.3S_{av}$ across all vertical periods.

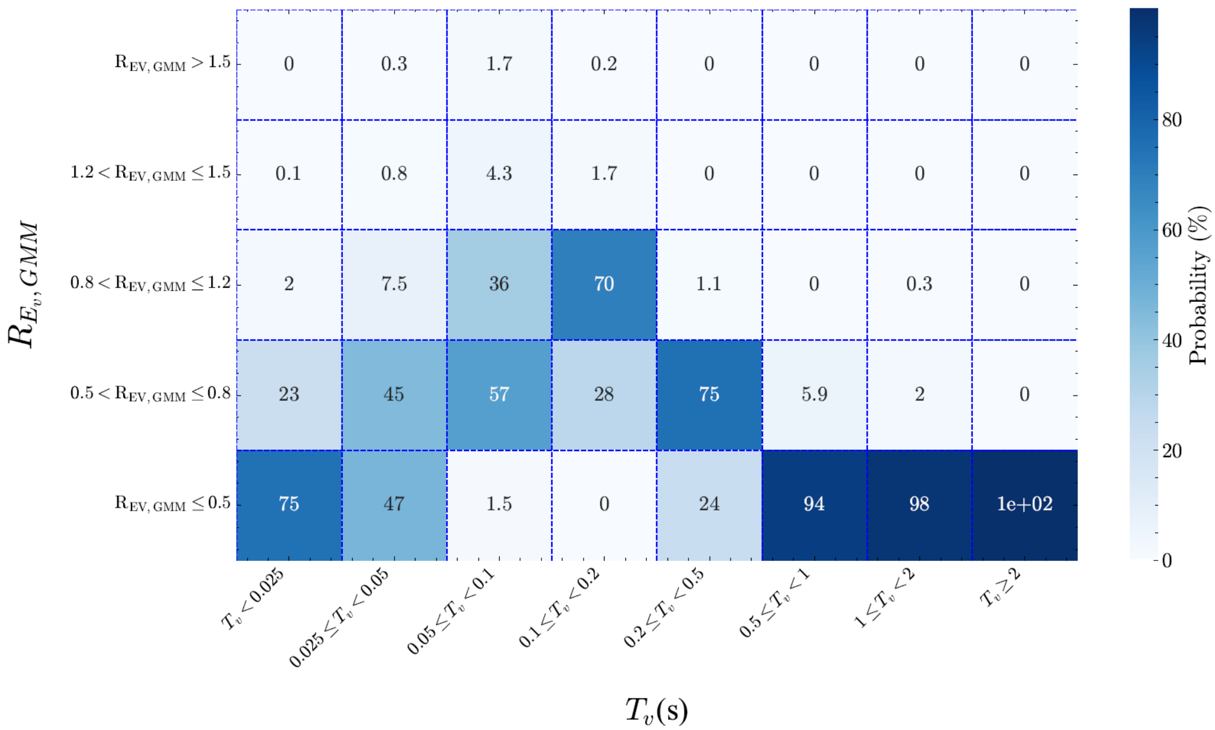

Figure 6.5. Summary of the probability distribution of $R_{E_v,GMM}$ in SDC*-B*

The following is a summary of the key observations from Figure 6.5:

- For $T_v < 0.025$ s, there is an approximately 0.98 probability that $R_{Ev,GMM}$ is less than or equal to 0.8. Most of this probability is concentrated in the $R_{Ev,GMM} \leq 0.5$ interval (0.75 probability). Therefore, for structures with very short vertical periods in SDC* B*, computing E_v based on $0.2S_{DS}$ is generally conservative and frequently highly conservative.

- For $0.025 \leq T_v < 0.05$ s, the response still remains strongly conservative. The probability that $R_{Ev,GMM} \leq 0.5$ is 0.47, and the probability that $0.5 < R_{Ev,GMM} \leq 0.8$ is 0.45. Underestimation of E_v calculated by $0.2S_{DS}$ is not a concern in this period interval.

- When $0.05 \leq T_v < 0.1$ s, the probability distribution shifts toward less conservative results. There is a 0.57 probability that $0.5 < R_{Ev,GMM} \leq 0.8$ and a 0.36 probability that $0.8 < R_{Ev,GMM} \leq 1.2$. The combined probability of slight and significant is small compared with the conservative and comparable portions of the distribution.

- For $0.1 \leq T_v < 0.2$ s, the results are primarily comparable to those obtained using $0.3S_{av}$. There is a 0.70 probability that $0.8 < R_{Ev,GMM} \leq 1.2$, and a 0.28 probability that $0.5 < R_{Ev,GMM} \leq 0.8$. Only a very small fraction (~ 0.02) of the results fall in the underestimation ranges.

- For $0.2 \leq T_v < 0.5$ s, computing E_v based on $0.2S_{DS}$ again produces conservative results. The probability that $R_{Ev,GMM} \leq 0.8$ is 0.99. Therefore, in this period range, $0.2S_{DS}$ tends to overestimate E_v relative to the period-dependent $0.3S_{av}$ expression.

- For vertical periods greater than 0.5 s, the conservative trend becomes dominant. In this range, the probability that $R_{Ev,GMM} \leq 0.8$ is almost 1.0. Thus, for long vertical periods in SDC* B*, using $0.2S_{DS}$ results in a substantial overestimation of the vertical seismic load effect.

In general, the SDC* B* results are similar to those for SDC* A*, but with a slightly reduced conservative bias in the 0.05 to 0.2 s period range. The use of $0.2S_{DS}$ is not generally unconservative for SDC* B*; rather, the primary implication is potential overestimation, especially for very short and long vertical periods. However, because SDC* B* still represents a relatively low-to-moderate seismic hazard level, these findings are not expected to control the main code-oriented recommendations of this chapter.

6.2.3.4 Key findings for SDC* C*

SDC* C* includes a set of 407 scenarios among 3060 scenarios, categorized under a higher seismic hazard relative to SDC* A* and B*. Figure 6.6 displays the distribution of $R_{E_v,GMM}$ values, showing a shift towards a less conservative but still prudent approach in the design calculations when comparing the use of $0.2S_{DS}$ to $0.3S_{av}$.

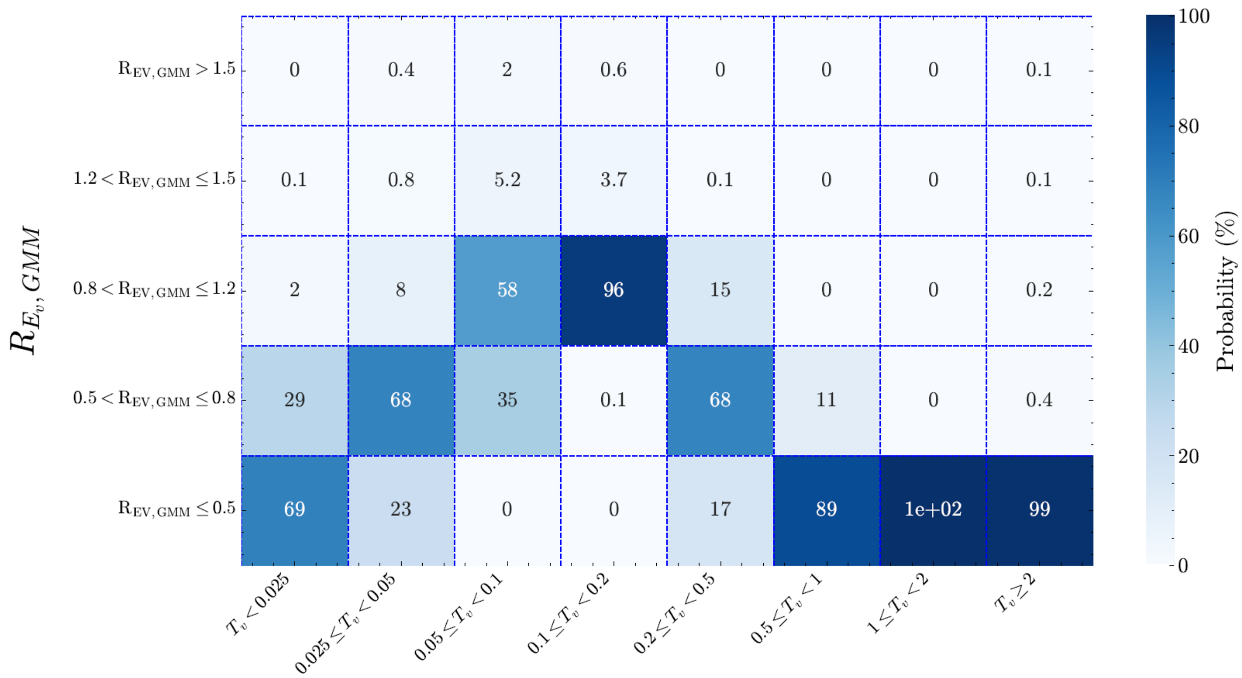

Figure 6.6. Summary of the probability distribution of $R_{E_v,GMM}$ in SDC*-C*

The following is a summary of the key observations from Figure 6.6:

- For $T_v < 0.025$ s, there is an approximately 0.98 probability that $R_{Ev,GMM}$ is less than or equal to 0.8. The probability that $R_{Ev,GMM} \leq 0.5$ is 0.69, and the probability that $0.5 < R_{Ev,GMM} \leq 0.8$ is 0.29. Therefore, for structures with very short vertical periods in SDC* C*, computing E_v based on $0.2S_{DS}$ is still highly conservative in most cases.

- For $0.025 \leq T_v < 0.05$ s, the results remain predominantly conservative, although less excessively conservative than in the shortest period interval. There is a 0.68 probability that $0.5 < R_{Ev,GMM} \leq 0.8$. The probability that the result is comparable to using $0.3S_{av}$ is 0.08, while the probability of underestimation remains small.

- When $0.05 \leq T_v < 0.1$ s, the distribution shifts toward the comparable range. The largest probability is associated with $0.8 < R_{Ev,GMM} \leq 1.2$ (0.58 probability). The combined probability of slight and significant underestimation is approximately 0.07, indicating that a modest potential for underestimating E_v begins to appear in this period range.

- For $0.1 \leq T_v < 0.2$ s, the results are largely comparable to those obtained using $0.3S_{av}$. There is a 0.96 probability that $0.8 < R_{Ev,GMM} \leq 1.2$. The probability of slight or significant underestimation is approximately 0.04 in total. Therefore, although SDC* C* shows some potential for underestimation in the moderate vertical-period range, the dominant outcome is close agreement between the two calculation methods.

- For $0.2 \leq T_v < 0.5$ s, the distribution shifts back toward conservative results. There is a 0.68 probability that $0.5 < R_{Ev,GMM} \leq 0.8$. This indicates that the $0.2S_{DS}$ expression generally overestimates E_v in this period range.

- For vertical periods greater than 0.5 s, the results derived from $0.2S_{DS}$ become highly conservative. For this range, the probability that $R_{Ev,GMM} \leq 0.8$ is almost 1.0.

In general, SDC* C* represents a transition between the strongly conservative behavior observed for SDC* A* and B* and the more critical behavior observed for SDC* D*. The use of $0.2S_{DS}$ is still mostly conservative or comparable, but the 0.05 to 0.2 s period range begins to show a small probability of underestimating E_v derived from $0.2S_{DS}$ compared to $0.3S_{av}$. This trend becomes more pronounced in SDC* D*, where the same period range is identified as the primary range of concern.

6.2.3.5 Key findings for SDC* D*

The primary focus of this section is on the SDC*-D* category, which makes up the majority of the 3,060 seismic scenarios. Figure 6.7 summarizes the probabilities that $R_{Ev,GMM}$ falls within the predefined ranges of R_{Ev} as presented in Table 6.2.

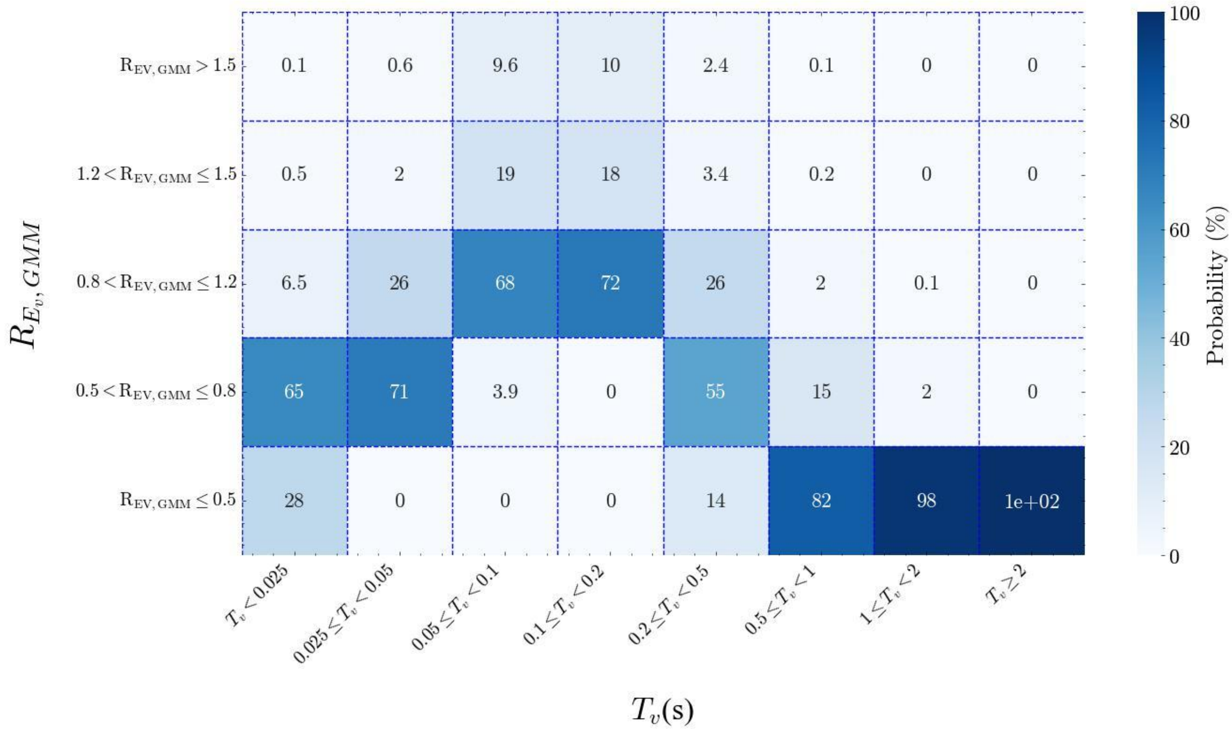

Figure 6.7. Summary of the probability distribution of $R_{E_v,GMM}$ in SDC*-D*

The following is a summary of the key observations from Figure 6.7:

- For $T_v \leq 0.025\ s$, there is a 93% probability that $R_{E_v,GMM}$ is less than 0.8 (i.e., $\mathrm{P}(R_{E_v,GMM} < 0.8) = 0.93$). However, most of that probability (0.65) falls within the

0.5 to 0.8 interval. In other words, for structures with a vertical period less than 0.025 s, computing E_v based on $0.2S_{DS}$ is generally conservative.

- For $0.025\ s < T_v \leq 0.05\ s$, computing E_v based on $0.2\mathrm{S_{DS}}$ will produce results that range from being slightly conservative (with a 0.71 probability of falling into the range $0.5 < R_{E_v,GMM} \leq 0.8$) to being negligibly different from when E_v is computed using $0.3S_{av}$ (with a 0.26 probability of falling into the range $0.8 < R_{E_v,GMM} \leq 1.2$).
- When $0.05\ s < T_v \leq 0.2\ s$, the E_v computed using $0.2S_{DS}$ ranges from being negligibly different from when $0.3S_{av}$ is used (more than 0.68 probability) to slightly and significantly underestimating the vertical seismic load effect (almost 0.3 probability). This potential underestimation is a concern.
- Computing E_v based on $0.2S_{DS}$ for the $0.2\ s < T_v \leq 0.5\ s$ period range produces results that are mostly slightly conservative (0.55 probability), but there is also significant probability (0.26) in the range where the results are negligibly different from that using $0.3S_{av}$.
- For vertical periods greater than 0.5 seconds, the E_v produced by $0.2S_{DS}$ ranges from being slightly to excessively conservative with the probability of the latter increasing with T_v. This is intuitive, as $0.2S_{DS}$ is independent of the vertical period; however, in this period range, the vertical spectrum is decreasing with the vertical period.

In general, the period range of concern when computing E_v based on $0.2\mathrm{S_{DS}}$ is between 0.05 seconds and 0.2 seconds where there is a high probability (almost 30%) of obtaining unconservative results. Whereas for vertical periods greater than 0.2 seconds, the primary concern would be producing vertical demands that are overly conservative.

6.3 Site-Specific Evaluation of E_v in California

6.3.1 Automated data generation from the ASCE 7 Hazard Tool

In this section, a dataset is developed using the PSHA results conducted by the USGS. The ASCE 7 Hazard Tool (ASCE7, 2024; ASCE, 2022), accessible online, facilitates extracting seismic design data (i.e. PSHA results) based on user-provided site coordinates and the soil class. A total of 19,316 sites across the state of California are considered. The selection is based on a uniform grid spacing of 0.05 by 0.05 degrees in latitude and longitude, ensuring a geographically diverse sample size. This grid distribution is derived from the "NHR3 Directivity-Based Probabilistic Hazard Analysis in California" project, which also provides estimated site-specific V_{S30} values (Al Atik et al., 2022; Al Atik et al., 2023). The V_{S30} value is required for defining the soil class of each site according to Table 20-2.1 of ASCE 7-22 (ASCE, 2022). To automate the data acquisition process, Python scripts are developed to extract seismic design parameters for all sites for Risk Category II from the ASCE 7 Hazard Tool. The data includes parameters such as S_{MS} (horizontal risk-targeted spectral acceleration (MCE_R) at a 0.2 second horizontal period and 5% damping ratio, adjusted for site class effects), S_{DS} (horizontal design spectral acceleration corresponding to a 0.2s horizontal period and 5% damping ratio), S_{D1} (horizontal design spectral acceleration for a 1 second horizontal period and 5% damping ratio), T_L (long-period transition period), and Seismic Design Category (SDC).

As defined earlier, $R_{E_v} = \frac{0.3S_{av}}{0.2S_{DS}}$, where S_{av} and S_{DS} are the design spectral acceleration in the vertical and horizontal directions, respectively. According to ASCE 7, the design spectral acceleration shall be taken as $\frac{2}{3}$ of the period-dependent 5%-damped MCE_R response spectrum (ASCE, 2022). Therefore, the PSHA-based ratio can also be computed as:

$$R_{E_v,PSHA} = \frac{0.3S_{aMv}}{0.2S_{MS}} \qquad \text{Eq 6.4}$$

where S_{MS} is defined as described earlier, and S_{aMv} is the period-dependent MCE_R vertical spectral acceleration. The determination of S_{aMv} follows the methodology outlined in Section 11.9.2 of ASCE 7-22. This procedure defines the vertical spectral acceleration over prescribed vertical-period ranges using S_{DS}, S_{D1}, S_{MS}, the damping modification factor F_{md}, and the vertical site coefficient C_v (according to Table 11.9-1 in ASCE 7-22). The equations used to calculate S_{aMv} for each vertical-period range are summarized in Table 6.3.

Table 6.3. Summary of S_{aMv} calculations

Period	$\boldsymbol{F_{md}}$	$\boldsymbol{S_{aMv}}$
$T_v \leq 0.025\text{s}$	1.2	$0.65C_v(S_{aM}/F_{md})$
$0.025\text{s} < T_v \leq 0.05\text{s}$	1.2	$16C_v(S_{aM}/F_{md})(T_v - 0.025) + 0.65C_v(S_{aM}/F_{md})$
$0.05\text{s} < T_v \leq 0.1\text{s}$	1.2	$1.05C_v(S_{aM}/F_{md})$
$0.1\text{s} < T_v \leq 0.2\text{s}$	1.2	$1.05C_v(S_{aM}/F_{md})$
$0.2\text{s} < T_v \leq 0.5\text{s}$	$1.2 + 0.0625(T_v - 0.2)$	$1.05C_v(S_{aM}/F_{md})$
$0.5\ s < T_v \leq 1s$	$1.2 + 0.0625(T_v - 0.2)$	$M\text{in}[1.05C_v(S_{aM}/F_{md}),\ 0.5(S_{aM}/F_{md})]$
$1s < T_v \leq 2s$	$1.25 + 0.05(T_v - 1)/9$	$M\text{in}[1.05C_v(S_{aM}/F_{md}),\ 0.5(S_{aM}/F_{md})]$
$T_v > 2\text{s}$	$1.25 + 0.05(T_v - 1)/9$	$0.5\ (S_{aM}/F_{md})$

$R_{E_v,PSHA}$ is computed for all 19,316 sites at 53 discrete T_v values. These periods are chosen to ensure enhanced accuracy in shorter period ranges where structural vertical periods are predominant, while providing larger intervals for longer vertical periods which are less common. The specific periods include 0.01 s to 0.1 s in 0.005 s increments, 0.1s to 2 s in 0.1 s increments, and 2 s to 10 s with 0.5 s increments. Consequently, a total of 1,021,748 data points (53 periods × 19,316 sites) is generated. The dataset is then categorized according to the SDC defined in ASCE 7-22, yielding the SDC distribution shown in Table 6.4.

Table 6.4. Distribution of sites in each SDC

SDC	Number of Sites
A	0
B	354
C	1,565
D	15,392
E	2,005
Total	19316

6.3.2 Probabilistic methodology

The evaluation method implemented in this section extends the probabilistic approach introduced in Section 6.2.2 with some modifications to address the nuances of the PSHA-based data. For each seismic design category, Figure 6.8 shows $R_{E_v,PSHA}$ across the various T_v ranges.

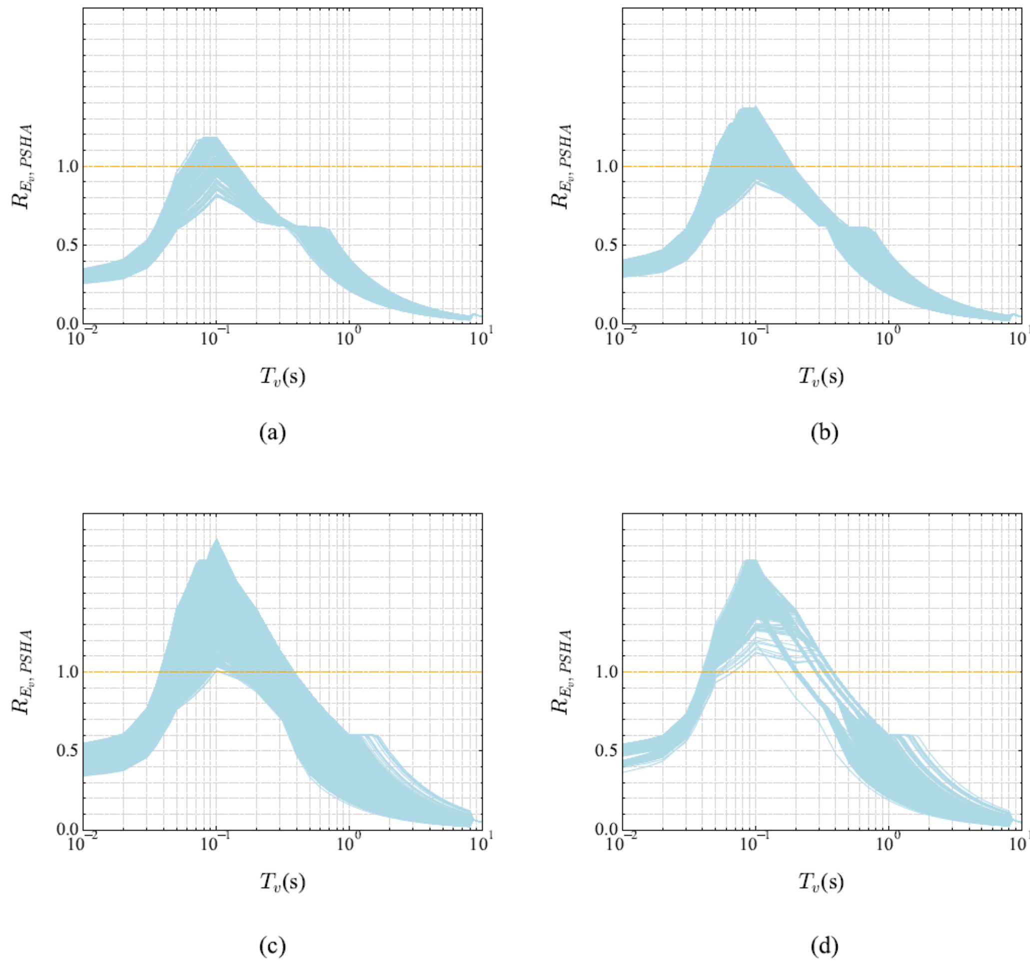

Figure 6.8. Vertical period-dependent $R_{E_v,PSHA}$ values across all sites for

SDCs (a) B, (b) C, (c) D and (d) E

For each T_v in the PSHA-based dataset, a distinct histogram is constructed. Each SDC is thus represented by 53 histograms corresponding to 53 vertical periods. Then the best-fit distribution is determined using the previously described RSS, AIC, and BIC metrics. Using the PDFs of the best-fit distributions, we compute the probability that $R_{E_v,PSHA}$ falls within the ratio categories specified in Table 6.2 based on the period ranges defined in Section 6.2.2. Figure 6.9 summarizes the data generation procedure and methodology to evaluate E_v calculations through PSHA-based data.

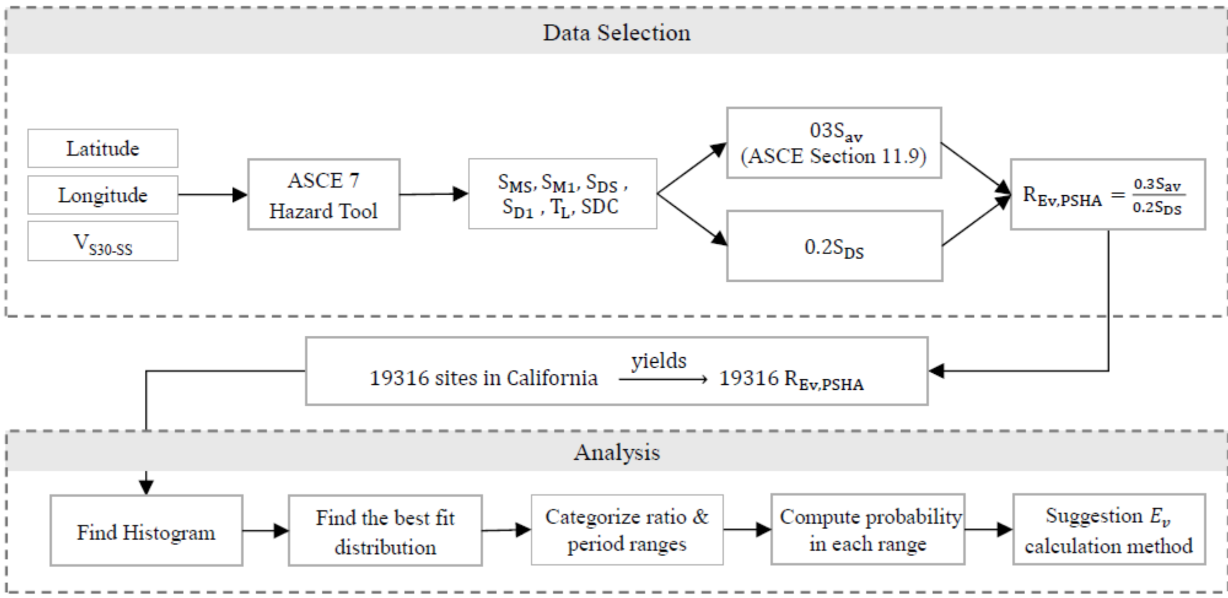

Figure 6.9. Summary of the procedure used to generate the dataset of $R_{E_v,PSHA}$ and the evaluation method

6.3.3 Results and interpretation for Site-Specific Evaluation

6.3.3.1 Overall California trends

The results from analyzing the PSHA-based dataset also highlight vertical period-dependent differences when E_v is computed using $0.2S_{DS} \times D$ compared to when $0.3S_{av}$ is used. As shown in Figure 6.10, $0.2S_{DS}$ consistently overestimates E_v compared to $0.3S_{av}$ for structures with a vertical period longer than 0.37s. Conversely, when T_v is less than 0.37s, the vertical seismic effect is both underestimated and overestimated when computed using $0.2S_{DS}$ instead of $0.3S_{av}$.

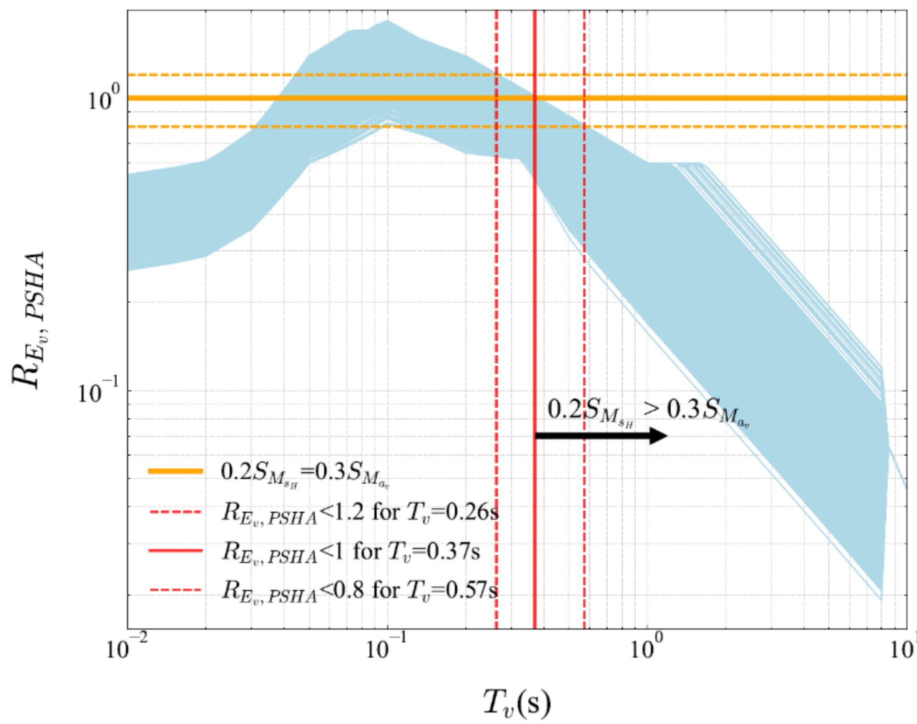

Figure 6.10. $R_{E_v,PSHA}$ for all 19316 sites in California as a function of T_v

6.3.3.2 Key findings for SDC B

SDC B includes 354 sites across California, representing areas with low to moderate seismic hazard. In Figure 6.11, the probability distribution of $R_{E_v,PSHA}$ for SDC B shows that using $0.2S_{DS}$ to compute E_v is generally conservative for very short and long vertical periods, while the two E_v expressions become more comparable in the moderate vertical-period range.

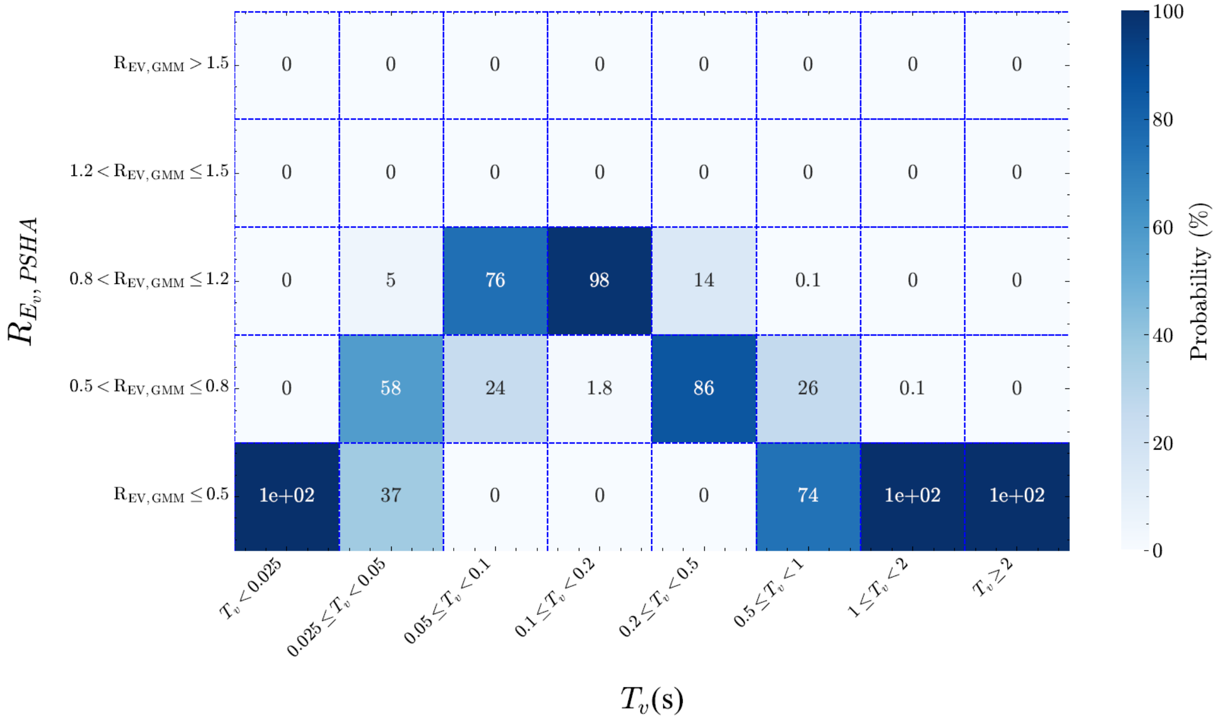

Figure 6.11. Summary of the probability distribution of $R_{E_v,PSHA}$ in SDC B

As shown in the SDC B heatmap, the key observations are as follows:

- For structures with a very short vertical period, $T_v < 0.025$ s, nearly all results fall in the $R_{Ev,PSHA} \leq 0.5$range, indicating that the vertical seismic load effect obtained from $0.2S_{DS}$is substantially larger than that obtained from $0.3S_{av}$.
- For $0.025 \leq T_v < 0.05$ s, the results remain predominantly conservative. Approximately 0.37 probability falls in the $R_{Ev,PSHA} \leq 0.5$ range, and approximately 0.58 probability falls in the $0.5 < R_{Ev,PSHA} \leq 0.8$ range. Thus, about 95% of the cases are conservative when E_v is computed using $0.2S_{DS}$.

- For $0.05 \leq T_v < 0.1$ s, the two methods become much more comparable. Approximately 0.76 probability falls within $0.8 < R_{Ev,PSHA} \leq 1.2$, indicating that $0.2S_{DS}$ and $0.3S_{av}$ provide similar estimates of E_v for most sites in this period range.
- For $0.1 \leq T_v < 0.2$ s, the results are also mostly comparable. Approximately 0.90 probability falls within $0.8 < R_{Ev,PSHA} \leq 1.2$, while approximately 0.097 probability falls within $1.2 < R_{Ev,PSHA} \leq 1.5$. This indicates that, for most SDC B sites in this period range, $0.2S_{DS}$ provides an E_v estimate that is close to that obtained from $0.3S_{av}$.
- For $0.2 \leq T_v < 0.5$ s, computing $E_v$using $0.2S_{DS}$ again becomes mostly conservative. Approximately 0.90 probability falls in the $0.5 < R_{Ev,PSHA} \leq 0.8$ range. This indicates that $0.2S_{DS}$ tends to overestimate the period-dependent E_v for SDC B sites in this period range.
- For vertical periods greater than 0.5 s, the results are strongly conservative. For $0.5 \leq T_v$, nearly all results fall in the $R_{Ev,PSHA} \leq 0.8$ range. This behavior is expected because $0.2S_{DS}$ is independent of vertical period, whereas the period-dependent vertical spectrum decreases at longer periods.

In general, the SDC B results indicate that using $0.2S_{DS}$ does not create a major concern for underestimating E_v. The method is mostly conservative for very short, intermediate-long, and long vertical periods, while it is generally comparable to $0.3S_{av}$ in the 0.05 to 0.2 s range. Therefore, SDC B is not expected to control the main code-oriented recommendations of this chapter; instead, it serves as a low-to-moderate hazard transition case between the strongly conservative behavior observed at low hazard levels and the more critical period-dependent underestimation observed in higher SDC.

6.3.3.3 Key findings for SDC C

SDC C includes 1,565 sites across California and represents areas with moderate seismic hazard. As shown in Figure 6.12, compared with SDC B, the SDC C results show a reduced conservative bias and a clearer transition toward period-dependent underestimation of E_v when $0.2S_{DS}$ is used. This trend is most evident in the $0.05 \leq T_v < 0.2$ s range, where a meaningful portion of the results shifts into the $R_{Ev,PSHA} > 1.2$ categories.

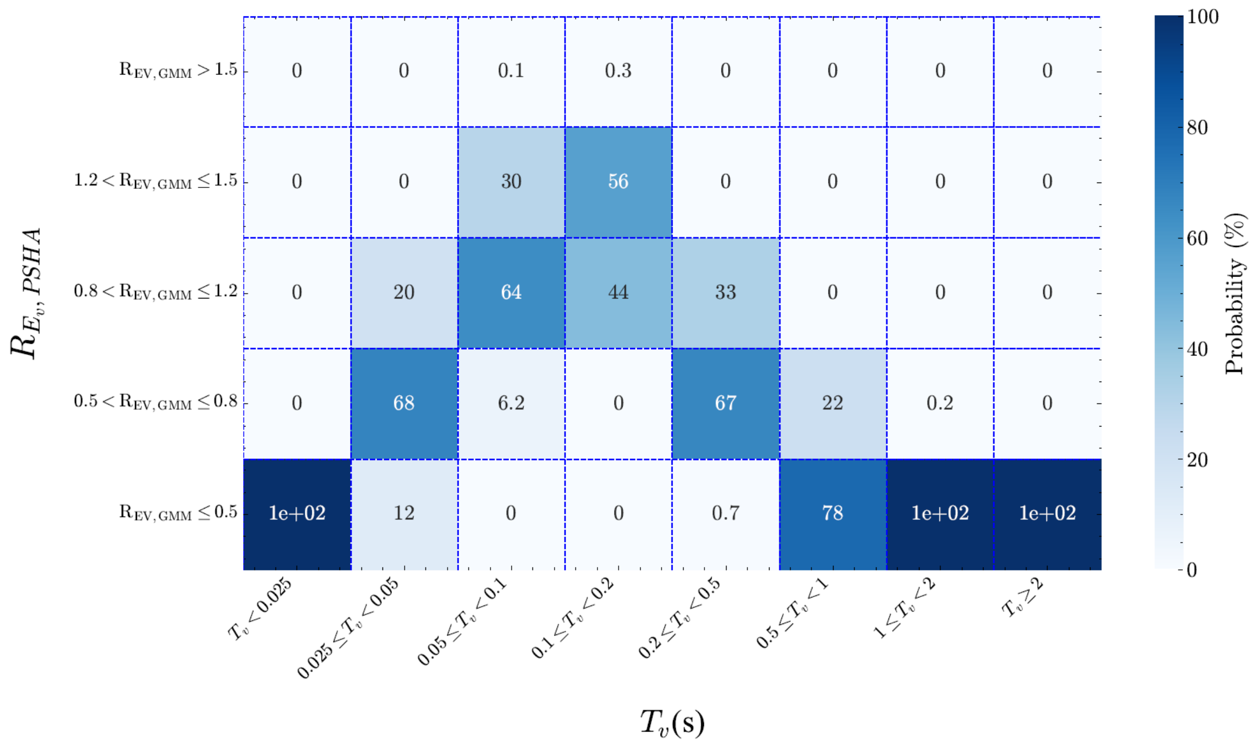

Figure 6.12. Summary of the probability distribution of $R_{E_v,PSHA}$ in SDC C

As shown in the SDC C heatmap, the key observations are as follows:

- For structures with $T_v < 0.025$ s, computing E_v using $0.2S_{DS}$ is highly conservative. Nearly all results fall in the $R_{Ev,PSHA} \leq 0.5$range. Therefore, similar to SDC B, in very short-period structures in SDC C, $0.2S_{DS}$ produces a substantially larger vertical seismic load effect than $0.3S_{av}$.

- For $0.025 \leq T_v < 0.05$ s, the results remain mostly conservative, but less strongly than in the very short-period range. Approximately 0.80 probability falls in the $R_{Ev,PSHA} \leq 0.8$ range. In addition, approximately 0.20 probability falls in the comparable range of $0.8 < R_{Ev,PSHA} \leq 1.2$. Thus, the use of $0.2S_{DS}$ is still predominantly conservative, although a notable fraction of cases begins to show comparable results between the two E_v expressions.
- For $0.05 \leq T_v < 0.1$ s, the distribution becomes more mixed. Approximately 0.64 probability falls within $0.8 < R_{Ev,PSHA} \leq 1.2$, indicating comparable estimates of E_v for most sites. However, approximately 0.30 probability falls in the $1.2 < R_{Ev,PSHA} \leq 1.5$ range, and a very small additional portion falls in the $R_{Ev,PSHA} > 1.5$ range. This indicates that, although the two methods are often comparable in this period range, there is a meaningful probability that $0.2S_{DS}$ underestimates E_v relative to $0.3S_{av}$.
- For $0.1 \leq T_v < 0.2$ s, the potential for underestimation becomes more significant. Approximately 0.44 probability falls in the comparable range, while approximately 0.56 probability falls in the $1.2 < R_{Ev,PSHA} \leq 1.5$ range. A small fraction also falls in the $R_{Ev,PSHA} > 1.5$ range. Therefore, for SDC C sites in this period range, $0.2S_{DS}$ is more likely to underestimate E_v than to overestimate it. This period range marks the beginning of the more critical behavior observed later in SDC D and SDC E.
- For $0.2 \leq T_v < 0.5$ s, the results shift back toward conservative or comparable behavior. Approximately 0.67 probability falls in the $0.5 < R_{Ev,PSHA} \leq 0.8$ range, and

approximately 0.33 probability falls in the $0.8 < R_{Ev,PSHA} \leq 1.2$ range. This indicates that $0.2S_{DS}$ generally overestimates E_v in this period range, although the overestimation is usually moderate rather than extreme.

- For vertical periods greater than 0.5 s, $0.2S_{DS}$ again becomes strongly conservative. For $0.5 \leq T_v < 1$ s, approximately 0.80 probability falls in the $R_{Ev,PSHA} \leq 0.5$ range, and approximately 0.19 probability falls in the $0.5 < R_{Ev,PSHA} \leq 0.8$ range. For $1 \leq T_v < 2$ s and $T_v \geq 2$ s, nearly all results fall in the $R_{Ev,PSHA} \leq 0.5$ range, indicating substantial overestimation of E_v when $0.2S_{DS}$ is used.

Overall, SDC C represents a transition between the mostly conservative behavior observed in SDC B and the more critical underestimation observed in SDC D and SDC E. The main period range of concern is $0.05 \leq T_v < 0.2$ s, especially $0.1 \leq T_v < 0.2$ s, where the probability of $R_{Ev,PSHA} > 1.2$ becomes significant. For very short and long vertical periods, however, $0.2S_{DS}$ remains conservative and can lead to unnecessary overestimation of the vertical seismic load effect.

6.3.3.4 Key findings for SDC D

According to Table 6.4, out of the 19,316 sites in California evaluated in this study, approximately 80% of the dataset (15,392) are classified as SDC D. Figure 6.13 shows the probability that $R_{E_v,PSHA}$ falls within the categories specified in Table 6.2 for predefined Tv intervals.

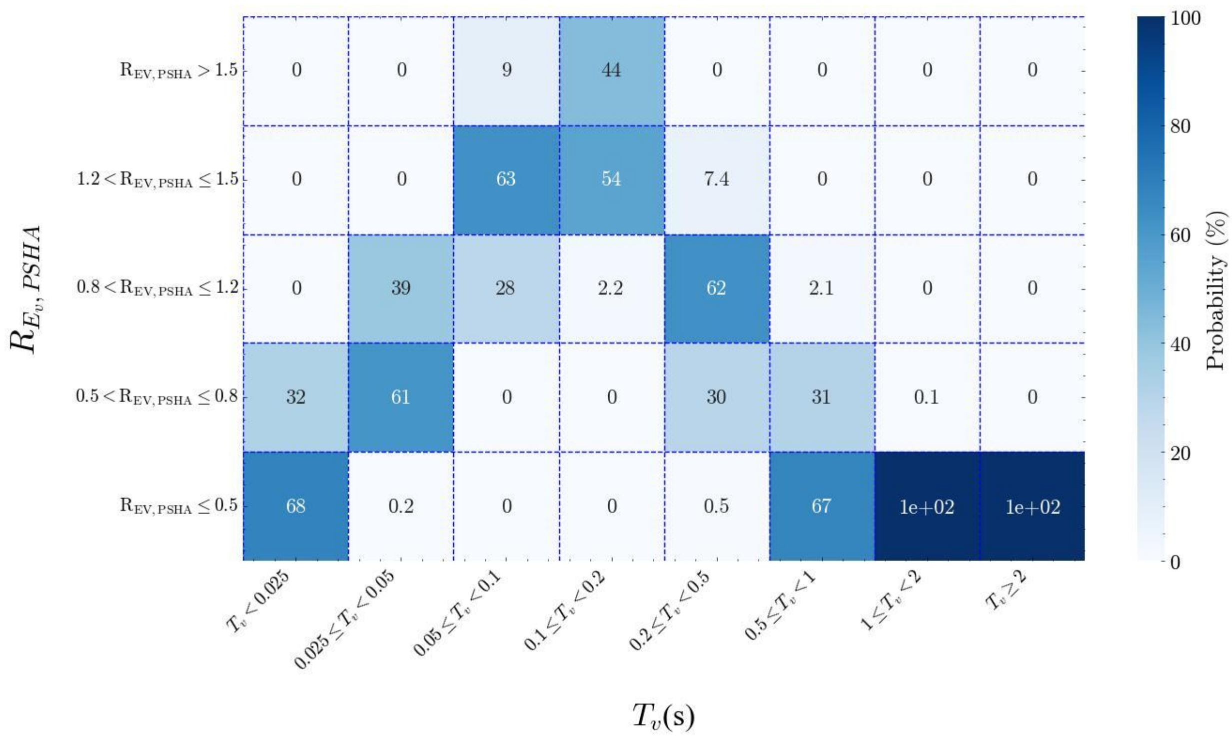

Figure 6.13. Summary of the probability distribution of $R_{E_v,PSHA}$ in SDC D

The key observations are as follows:

- For structures with a very short vertical period (i.e., $T_v \leq 0.025$ s), using $0.2S_{DS}$ to calculate E_v is highly likely to be very conservative with a 0.68 probability that $R_{E_v,PSHA}$ is less than or equal to 0.5. In other words, computing E_v using $0.2S_{DS}$ for structures in this period range will result in significant overestimation of the vertical demand. The remaining 0.32 probability corresponds to $0.5 < R_{E_v,PSHA} \leq 0.8$.
- Computing E_v based on $0.2S_{DS}$ for structures with $0.025\ s < T_v \leq 0.05\ s$ will most likely (i.e., 0.61 probability) produce designs that are slightly conservative relative to that using $0.3S_{av}$. However, the probability that the resulting vertical seismic load effect is comparable to using $0.3S_{av}$ is also significant (0.39).

- When applied to structures within the period range of $0.05\ s < T_v \leq 0.2\ s$, vertical seismic effects based on $0.2\mathrm{S_{DS}}$ will either be slightly unconservative $\left(1.2 < R_{E_v,PSHA} \leq 1.5\right)$ with 0.54 to 0.63 probability or very unconservative $\left(R_{E_v,PSHA} > 1.5\right)$ with 0.09 to 0.44 probability. The period range of $0.1\ \mathrm{s} < \mathrm{T_v} \leq 0.2\ \mathrm{s}$ is especially concerning because there is a 44% probability that E_v values computed using $0.2S_{DS}$ are less than those computed using $0.3S_{av}$.
- Using $0.2S_{DS}$ to compute E_v for structures with $0.2\ s < T_v \leq 0.5\ s$ will most likely (0.62 probability) produce designs that are comparable to when $0.3S_{av}$ is used. However, there is also a 30% probability of producing slightly conservative designs.
- The vertical seismic effect for structures with a vertical period greater than 0.5 seconds will always be overestimated (to different degrees, but mostly significantly) when computed using $0.2S_{DS}$.

In general, the results in Figure 6.13 show that using $0.2S_{DS}$ to compute E_v has a high probability (> 0.67) of producing highly conservative designs for structures with very short $(< 0.025\mathrm{s})$ or long $(> 0.5\mathrm{s})$ vertical periods. However, the vertical period range of primary concern is $0.05\ s < T_v \leq 0.2s$ where E_v values estimated based on $0.2S_{DS}$ will be underestimated to varying degrees including by as much as more than 50%.

6.3.3.5 Key findings for SDC E

SDC E includes 2,005 sites in California and represents the highest seismic hazard category in the PSHA-based dataset. As shown in Figure 6.14, the SDC E results also show the strongest period-dependent contrast among the California SDCs.

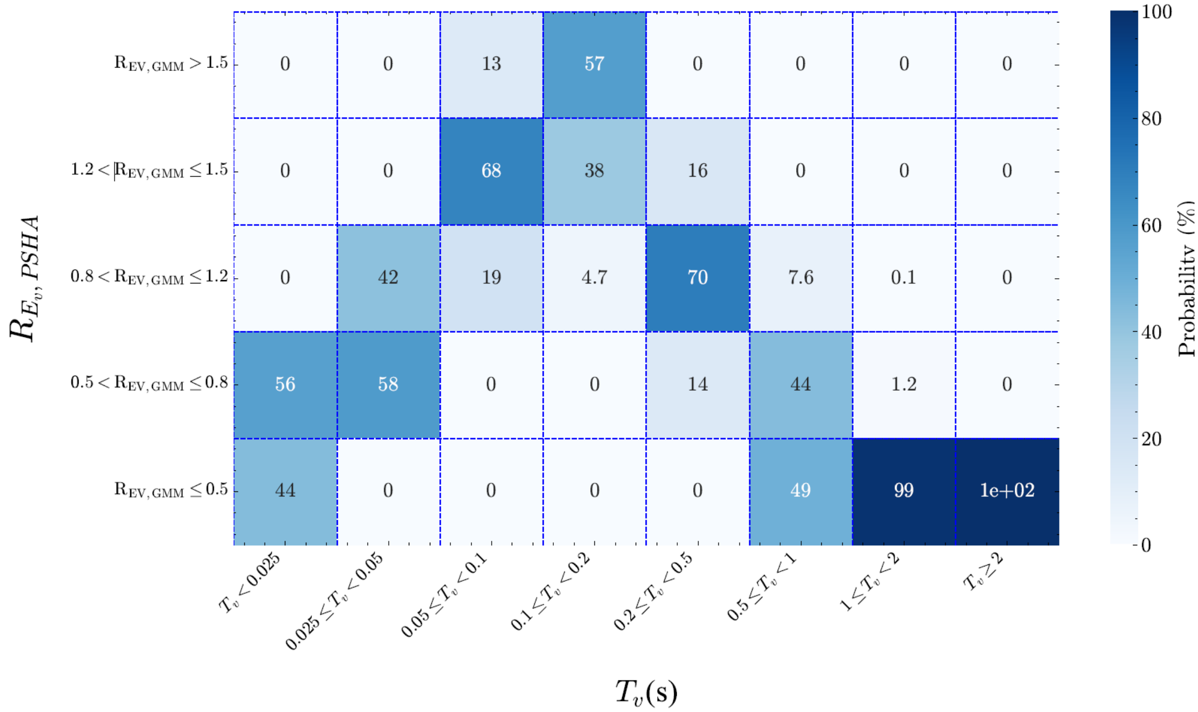

Figure 6.14. Summary of the probability distribution of $R_{E_v,PSHA}$ in SDC E

As shown in the SDC E heatmap, the key observations are as follows:

- For structures with $T_v < 0.025$ s, using $0.2S_{DS}$ to compute E_v is conservative rather than $0.3S_{av}$. Approximately 0.44 probability falls in the $R_{Ev,PSHA} \leq 0.5$ range, while approximately 0.56 probability falls in the $0.5 < R_{Ev,PSHA} \leq 0.8$ range. Therefore, all or nearly all cases in this period range are conservative, although the conservatism is less extreme than that observed in SDC B, C, and D.
- For $0.025 \leq T_v < 0.05$ s, the results are split between slightly conservative and comparable outcomes. Approximately 0.58 probability falls in the $0.5 < R_{Ev,PSHA} \leq 0.8$ range, while approximately 0.42 probability falls in the $0.8 < R_{Ev,PSHA} \leq 1.2$ range. This indicates that $0.2S_{DS}$ is generally conservative or comparable to $0.3S_{av}$ for short-period structures in SDC E, with no meaningful probability of underestimation.

- For $0.05 \leq T_v < 0.1$ s, the results shift strongly toward underestimation categories. Approximately 0.19 probability falls in the comparable range, while approximately 0.68 probability falls in the $1.2 < R_{Ev,PSHA} \leq 1.5$ range and approximately 0.13 probability falls in the $R_{Ev,PSHA} > 1.5$ range. Therefore, about 80% of the cases indicate that $0.2S_{DS}$ underestimates E_v relative to $0.3S_{av}$. This period range is therefore a major concern for SDC E.
- For $0.1 \leq T_v < 0.2$ s, the underestimation becomes even more pronounced. Only a small portion of data falls in the comparable range, while approximately 0.38 probability falls in the $1.2 < R_{Ev,PSHA} \leq 1.5$ range and most sites (with probability of 0.57) falls in the $R_{Ev,PSHA} > 1.5$ range. Thus, 95% of the cases indicate underestimation of E_v when $0.2S_{DS}$ is used instead of $0.3S_{av}$, and more than half of the cases indicate underestimation by more than 50%. This is the most critical period range for SDC E.
- For $0.2 \leq T_v < 0.5$ s, the results become more balanced. Near 0.14 probability falls in the slightly conservative range, most sites (with probability 0.70) falls in the comparable range, and approximately 0.16 probability falls in the $1.2 < R_{Ev,PSHA} \leq 1.5$ range. Therefore, for this period range, $0.2S_{DS}$ and $0.3S_{av}$generally produce comparable estimates of E_v, although a small probability of underestimation remains.
- For vertical periods greater than 0.5 s, the $0.2S_{DS}$-based expression again produces larger values of E_v. For $0.5 \leq T_v < 1$ s, approximately 0.93 probability falls in the $R_{Ev,PSHA} \leq 0.8$ range, and only the smaller portion falls in the comparable range. For $1 \leq T_v\ s$, nearly all results fall in the $R_{Ev,PSA} \leq 0.5$ range.

In general, SDC E exhibits the strongest period-dependent behavior among the California seismic design categories. The $0.2S_{DS}$-based expression gives larger $E_v$values for very short and long vertical periods compared to $0.3S_{av}$, but it gives smaller values for $0.05 \leq T_v < 0.2$ s. This finding is especially important because SDC E represents the highest seismic hazard category, where the absolute magnitude of E_v is larger and differences between the two expressions have greater design significance. Therefore, for SDC E structures with vertical periods in the moderate range, the period-dependent $0.3S_{av}$ expression provides a more representative estimate of the vertical seismic load effect.

6.4 Code-Oriented Recommendations & Proposed S_{av} Refinement

The scenario-based and site-specific evaluations show that the adequacy of the current $0.2S_{DS}$-based expression for vertical seismic load effect is strongly dependent on vertical period. The results from both the NGA-West2 GMM scenario dataset and the California PSHA dataset indicate that a single period-independent expression cannot represent the full range of vertical seismic demand with the same level of accuracy. In some vertical-period ranges, $0.2S_{DS} \times D$ produces values of E_v that are substantially larger than those obtained from the period-dependent $0.3S_{av} \times D$ expression. In other ranges, particularly for moderate vertical periods in higher seismic design categories, $0.2S_{DS} \times D$ can produce smaller values than $0.3S_{av} \times D$.

This section translates the findings of the chapter into code-oriented recommendations. The recommendations are organized by vertical period and seismic design category, with the objective of avoiding both underestimation and unnecessary overestimation of vertical seismic load effects. The section also presents a proposed refinement to the long-period calculation of S_{av}.

6.4.1 Recommended E_v expression by period range and SDC

For interpreting the recommendations, the ratio $R_{Ev} = \frac{0.3S_{av}}{0.2S_{DS}}$ is used as the primary comparison metric. When $R_{Ev} < 1.0$, the $0.2S_{DS}$-based expression produces a larger estimate of E_v than the $0.3S_{av}$-based expression. When $R_{Ev} > 1.0$, the period-dependent $0.3S_{av}$-based expression produces a larger estimate of E_v. Therefore, the recommendations are based not only on whether $0.2S_{DS}$ is larger or smaller than $0.3S_{av}$, but also on the degree of difference between the two approaches.

The results for SDC D are especially important because SDC D represents the dominant portion of the California PSHA dataset and is also one of the most relevant seismic design categories for practical building design in high-seismic regions. Table 6.5 summarizes the results for SDC D and identifies the preferred calculation approach for each vertical-period range.

Table 6.5. Summary of results for SDC D

Vertical period	**E_v Based on S_{DS}**	**Suggestion Method for Calculating E_v**
$T_v \leq 0.025s$	Very Conservative	$0.3S_{av} \times D$
$0.025s < T_v \leq 0.05s$	Comparable to Conservative	$0.2S_{DS} \times D$ *or* $0.3S_{av} \times D$
$0.05s < T_v \leq 0.1s$	Unconservative	$0.3S_{av} \times D$
$0.1s < T_v \leq 0.2s$	Unconservative	$0.3S_{av} \times D$
$0.2s < T_v \leq 0.5s$	Comparable to Conservative	$0.2S_{DS} \times D$ *or* $0.3S_{av} \times D$
$T_v > 0.5s$	Very Conservative	$0.3S_{av} \times D$

For SDC D, the period range $0.05 < T_v \leq 0.2$ s is the main range of concern. In this range, both the GMM-based and PSHA-based evaluations show that $0.2S_{DS} \times D$ can underestimate the vertical seismic load effect relative to $0.3S_{av} \times D$. Therefore, the period-dependent expression is recommended for this range. For very short vertical periods and for periods greater than 0.5 s, the opposite behavior is observed: $0.2S_{DS} \times D$ tends to produce values that are much larger than the period-dependent estimate. In those ranges, using $0.3S_{av} \times D$ provides a more rational estimate of E_v and avoids unnecessary amplification of the vertical demand. The same interpretation was extended to the other seismic design categories. The overall behavior of $0.2S_{DS} \times D$ across the seismic design categories is summarized in Table 6.6.

Table 6.6. Summary of key findings for all seismic design categories

Period	**SDC: B**	**SDC: C**	**SDC: D**	**SDC: E**
$T_v \leq 0.025$s	Very Conservative	Very Conservative	Very Conservative	Very Conservative
$0.025\text{s} < T_v \leq 0.05$s	Conservative	Comparable to Conservative	Comparable to Conservative	Comparable to Conservative
$0.05\text{s} < T_v \leq 0.1$s	Comparable to Conservative	Unconservative	Unconservative	Unconservative
$0.1\text{s} < T_v \leq 0.2$s	Comparable to Conservative	Unconservative	Unconservative	Unconservative
$0.2\text{s} < T_v \leq 0.5$s	Conservative	Comparable to Conservative	Comparable to Conservative	Comparable to Conservative
$T_v > 0.5$s	Very Conservative	Very Conservative	Very Conservative	Very Conservative

The site-specific PSHA dataset in California did not include SDC A sites; therefore, the code-oriented recommendations are focused on SDC B, C, D, and E. The scenario-based SDC* A* results are still useful as a low-hazard reference case, but they are not expected to control the main design recommendations because the absolute values of S_{DS}, S_{av}, and subsequently E_v are relatively small in that category. Moreover, the results indicate that SDC B generally does not control the main recommendations of this chapter. Although differences between two approaches are present, the absolute values of E_v are smaller than in the higher seismic design categories, and the probability of significant underestimation is limited. SDC C represents a transition category, where the moderate vertical-period range begins to show a clear need for the period-dependent approach. SDC D and SDC E provide the strongest evidence that T_v should be considered explicitly when evaluating vertical seismic load effects. In these categories, especially for $0.05 < T_v \leq 0.2$ s, the $0.3S_{av} \times D$ provides a more appropriate basis for design. Table 6.7 provides the suggested approach for calculating E_v by vertical-period range and seismic design category.

Table 6.7. Suggested approaches for calculating E_v based on the vertical period of the structure

Period	SDC: B	SDC: C	SDC: D	SDC: E
Very short vertical period $T_v \leq 0.025s$	$0.3S_{av} \times D$	$0.3S_{av} \times D$	$0.3S_{av} \times D$	$0.3S_{av} \times D$
Short vertical period $0.025s < T_v \leq 0.05s$	$0.3S_{av} \times D$	$0.2S_{DS} \times D$ or $0.3S_{av} \times D$	$0.2S_{DS} \times D$ or $0.3S_{av} \times D$	$0.2S_{DS} \times D$ or $0.3S_{av} \times D$
Moderate vertical period $0.05s < T_v \leq 0.2s$	$0.2S_{DS} \times D$ or $0.3S_{av} \times D$	$0.3S_{av} \times D$	$0.3S_{av} \times D$	$0.3S_{av} \times D$
Long vertical period $0.2s < T_v \leq 0.5s$	$0.2S_{DS} \times D$ or $0.3S_{av} \times D$	$0.2S_{DS} \times D$ or $0.3S_{av} \times D$	$0.2S_{DS} \times D$ or $0.3S_{av} \times D$	$0.2S_{DS} \times D$ or $0.3S_{av} \times D$
Very long vertical period $0.5s < T_v$	$0.3S_{av} \times D$	$0.3S_{av} \times D$	$0.3S_{av} \times D$	$0.3S_{av} \times D$

6.4.2 Summary of Evaluation of Vertical Load Effects in ASCE7-22

In Summary the period-dependent $0.3S_{av} \times D$ is most important in two cases. The first is the moderate vertical-period range, especially $0.05 < T_v \leq 0.2$ s, for SDC C, D, and E. In this range, $0.2S_{DS} \times D$ can produce smaller values of E_v than the period-dependent approach. The second is the very short and very long vertical-period ranges, where $0.2S_{DS} \times D$ often produces values that are substantially larger than necessary. In those cases, $0.3S_{av} \times D$ is recommended for design because it better reflects the period-dependent shape of the vertical design spectrum.

6.4.3 Proposed long-period refinement to S_{av}

The recommendations above rely on the period-dependent vertical design spectral acceleration, S_{av}. Therefore, the calculation of S_{av} itself must provide a stable and consistent representation of the vertical spectrum over the full range of vertical periods. In this study, S_{av} was determined following the methodology in Section 11.9.2 of ASCE 7-22 (ASCE, 2022). This procedure uses parameters such as S_{MS}, C_v, and F_{md} to compute the period-dependent vertical spectral acceleration.

The evaluation of the 19,316 California sites showed that the current ASCE 7-22 calculation procedure can lead to less consistent behavior of $R_{Ev,PSHA}$ for long vertical periods, particularly in the range between approximately 0.5 s and 2 s. This behavior is visible in Figure 6.15(a), where the current calculation method produces an irregular transition in the long-period range. To improve the long-period behavior of S_{av}, a refinement is proposed for vertical periods greater than 0.5 s. Specifically, the lower-limit term used in the long-period calculation is modified from $0.5\left(\frac{S_{aM}}{F_{md}}\right)$ to $0.4\left(\frac{S_{aM}}{F_{md}}\right)$ for $T_v > 0.5$ s.

This adjustment produces a smoother and more consistent variation of $R_{Ev,PSHA}$ in the long-period range, as shown in Figure 6.15(b). The proposed modification does not change the main conclusions of the chapter. The period range $0.05 < T_v \leq 0.2$ s remains the primary range where $0.3S_{av} \times D$ is needed to avoid underestimating E_v in higher seismic design categories. Similarly, very long vertical periods still show that the period-dependent approach is more appropriate than the period-independent $0.2S_{DS} \times D$. The purpose of the proposed refinement is therefore not to change the overall recommendation framework, but to improve the consistency of the S_{av} calculation for long periods.

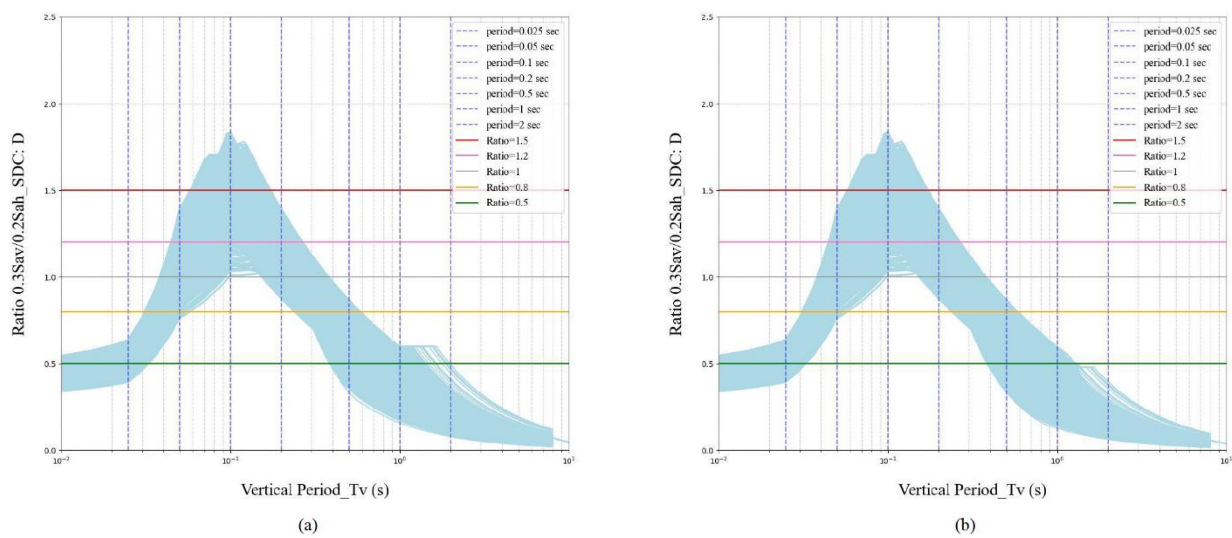

Figure 6.15. (a) $R_{E_v,PSHA}$ for SDC-D based on the current calculation method ASCE 7-22, (b) $R_{E_v,PSHA}$ for SDC-D based on suggested calculation method

CHAPTER 7. Summary, Conclusions, Limitations & Future Work

7.1 Overview of Research

This dissertation investigated the response of building systems to the vertical component of earthquake ground motions using dense measured data from a prototype smart-city environment, numerical simulation, and statistical evaluation. The research was motivated by a gap in current earthquake engineering practice: while vertical ground motions are acknowledged in modern seismic design provisions, several important features of vertical structural seismic response remain simplified or incompletely represented. In particular, the vertical dynamic characteristics of buildings are less commonly identified than horizontal modal properties, vertical floor response spectra are not explicitly represented in nonstructural component design provisions, and the current alternatives for calculating vertical seismic load effects are not consistent across vertical period ranges.

The work developed an integrated framework that connects measured structural response, physical interpretation, and design implications. First, dense Community Seismic Network (CSN) recordings from selected buildings located at the NASA Jet Propulsion Laboratory (JPL) campus were used to establish a multi-building, floor-by-floor dataset of triaxial seismic response. Second, data-driven signal-processing methods were used to identify vertical and horizontal frequency ranges from measured floor accelerations. Third, a detailed building finite-element model was used to interpret the physical origin of measured vertical frequency bands and distinguish global vertical modes from slab-dominated response. Fourth, measured vertical and horizontal floor response spectra were computed and transformed into height amplification factors to evaluate how floor acceleration demands vary with component period and floor elevation. Finally, a probabilistic code evaluation was conducted considering alternative expressions used to calculate the vertical seismic load effect, E_v.

The central finding of the dissertation is that vertical structural response should not be treated as a height-independent or period-independent effect. The measured data show that vertical response can amplify substantially over the height of a building. However, this amplification is concentrated in short-period ranges associated with the building's vertical dynamic characteristics. The simulation results further show that these measured frequency bands are not controlled by a single mechanism. They include global vertical modes of the primary vertical load-resisting system, coupled with slab-dominated vibration. The floor response spectra demonstrate that this dynamic filtering is directly relevant to acceleration-sensitive nonstructural components. The seismic design code-oriented evaluation of $E_v$shows that the adequacy of current vertical seismic load expressions depends strongly on the vertical period of the structure.

Taken together, the dissertation advances three related contributions. It provides a measured data framework for identifying vertical structural frequencies in densely instrumented buildings. It develops empirical evidence that vertical and horizontal floor response spectra require period-dependent and height-dependent interpretation. It also provides a probabilistic seismic design code-oriented evaluation of vertical seismic load effects and identifies period ranges where current simplified expressions can either underestimate or overestimate the period-dependent vertical demand. These contributions support a more explicit treatment of vertical response in structural analysis, nonstructural seismic design, and future seismic design provisions.

7.2 Summary of the Research

The dissertation progresses from data foundation to frequency identification, physical interpretation, floor and component response characterization, and seismic design code evaluation. Chapters 2 through 6 each address a specific part of this progression. The following sections summarize the main contributions and findings of each chapter.

7.2.1 Chapter 2: Instrumented Building and Data Pipeline

Chapter 2 established the data foundation for the dissertation by describing CSN and the JPL campus instrumentation. The CSN dataset is especially well-suited for this research because it provides dense triaxial measurements at relatively low cost, including sensors distributed along the heights of buildings. This floor-by-floor instrumentation is especially critical for studying vertical structural response and can reveal how vertical acceleration demand develops across the building height or how different floors respond within different frequency bands.

The chapter considered the JPL campus as a prototype smart-city testbed for seismic response studies. The campus contains a dense array of approximately 220 triaxial accelerometers, including roughly 100 ground-level stations and many sensors installed inside buildings.

Six instrumented JPL mid-rise buildings were selected for the main data-driven analyses: JPL 180, JPL 183, JPL 238, JPL 264, JPL 321, and JPL 303. These buildings range from four to nine stories and include at least one triaxial sensor per floor, with some buildings containing multiple sensor lines. The event set used for between-building comparison included the El Monte, Pacoima, Searle Valley, and Ridgecrest earthquakes. This combination of multiple buildings and multiple earthquakes allowed the dissertation to separate repeatable structural response features from event-specific or noise-related effects.

A major contribution of the chapter was the Python-based data preparation pipeline. The pipeline was developed to make the CSN records usable for systematic building-response analysis without relying on manual downloading or case-by-case file handling. It accesses the CSN web data source, applies event-selection criteria such as earthquake name, magnitude range, and source-to-site distance, downloads the selected records, extracts the compressed files, checks whether the target building sensors recorded the selected events, and generates a record-availability summary. This check was especially important because not every building or floor recorded every earthquake with acceptable quality.

The Python workflow also converted CSN records from SAC format into the text-based format required by the project processing tools. By standardizing file naming, event labels, building identifiers, sensor locations, and component directions, the pipeline created a consistent dataset that could be passed directly to later frequency-domain analyses and floor-response calculations. The same workflow supported NGA-consistent signal processing, including high-pass and low-pass filtering and zero-padding to align all channels within each earthquake. In this way, the introduced data preparation pipeline served as the reproducible bridge between raw dense-network recordings and the engineering results developed in later chapters.

7.2.2 Chapter 3: Identification of Structural Frequencies via Data-Driven Methods

Chapter 3 developed and applied a data-driven framework for identifying structural frequency ranges from earthquake recordings. The framework combined Fourier amplitude spectra (FAS), Welch power spectral density (PSD) estimates, floor-to-reference transfer functions, and magnitude-squared coherence. Each tool played a specific role: FAS and PSD identified energetic frequency content, transfer functions isolated building amplification relative to the reference level, and coherence was used to verify that floor and reference motions were linearly related at the candidate frequencies. A candidate structural response frequency is considered only when it was repeatable across floors and events, appeared as an amplified peak, and was supported by coherence.

The framework was applied to both vertical and horizontal components for all six JPL buildings. In the vertical direction, each building exhibited repeatable frequency ranges within the usable bandwidth of the recordings. The dominant vertical frequency was generally located in the higher-frequency portion of the identified vertical response bands. Representative dominant vertical frequencies were approximately 7.2 Hz for JPL 183, 5.4 Hz for JPL 180, 8.8 Hz for JPL 238, 5.1 Hz for JPL 264, 9.4 Hz for JPL 321, and 8.5 Hz for JPL 303. These values show that the strongest vertical amplification in the measured transfer functions often occurs at short periods.

The horizontal motions showed a different pattern. The dominant (fundamental) horizontal frequency has representative values ranging from approximately 0.7 Hz to 1.8 Hz across the buildings. This contrast between vertical and horizontal behavior is one of the most important findings of Chapter 3. In the horizontal direction, the dominant response is typically governed by the first global lateral mode. In the vertical direction, however, the frequency bands with the strongest PSD and transfer-function peaks often occur at higher vertical frequency ranges.

Chapter 3, therefore, demonstrated that vertical frequency identification cannot simply be treated as an analog of horizontal fundamental-period identification. Vertical response is influenced by several mechanisms, including axial deformation of columns and walls, local floor-system bending, slab participation, and higher-order vertical modes. The chapter also showed that transfer-function amplitudes generally increase with elevation at dominant response bands, indicating that the power of vertical acceleration signals can develop systematic height-dependent amplification even when the absolute frequencies differ from building to building.

The main contribution of Chapter 3 is the establishment of a repeatable measured-data methodology for extracting vertical response frequencies from real building recordings. The chapter also provides the frequency basis used in Chapter 4 to interpret vertical modal mechanisms and in Chapter 5 to evaluate floor response spectra at structural response periods.

7.2.3 Chapter 4: Identification of Structural Vertical Frequencies via Simulation

Chapter 4 used numerical simulations to investigate the physical origins of the vertical frequency bands identified in the recordings. The JPL 183, a nine-story instrumented building with two vertical sensor lines, was considered. A detailed three-dimensional ETABS model was refined for vertical response analysis by assigning vertical mass, refining the slab mesh, completing missing structural elements, representing floor slabs with shell elements, and mapping CSN sensor locations to model nodes.

A key finding of Chapter 4 is that vertical modal analysis requires a much larger number of modes than typical horizontal modal analysis. For the JPL 183 model, 50 modes captured only about 0.1% cumulative vertical modal mass participation, 400 modes captured about 12%, 2,000 modes captured about 44%, 4,000 modes captured about 75%, and nearly 10,000 modes were required to exceed 90% cumulative vertical modal mass participation. This slow accumulation of vertical modal mass participation is also strongly affected by the finite-element discretization of the floor slabs. Since the vertical direction includes both global building modes and slab-dominated local modes, a refined slab mesh is needed to capture the short-period vertical frequencies observed in the field recordings, which substantially increases the number of nodes, degrees of freedom, and extracted modes required compared with a typical horizontal modal analysis. Therefore, the results suggest that the conventional 90% modal mass participation target used in horizontal modal analysis may not be an efficient or meaningful criterion for vertical modal analysis.

The chapter then introduced stiffness-perturbation studies to distinguish global vertical modes from slab-dominated modes. In one model variant, slab stiffness was increased to suppress slab deformation and reveal modes associated primarily with the vertical load-resisting system. In another variant, the stiffness of the vertical elements was increased so that slab-related mechanisms became more apparent.

The stiffness-perturbation results showed that frequency bands near 3-4 Hz and 7-8 Hz are associated primarily with the global vertical response of the building, involving the columns, walls, and frame system. The 5-6 Hz band is more strongly associated with slab-dominated response, while the approximately 4 Hz band can involve coupled behavior between the slab and vertical load-resisting system. A low-frequency mode near 1 Hz appeared in the model, but it was not treated as a primary measured vertical response band because it was sensitive to modeling and bandwidth considerations.

The simulation results agreed closely with the measured JPL 183 frequency families from Chapter 3. The measured response contained repeatable bands near 1.6-1.9 Hz, 3.1-3.4 Hz, 4.0-4.4 Hz, 5.4-5.6 Hz, and 7.2-7.6 Hz. This agreement between recorded data and numerical simulation is one of the strongest validation points in the dissertation. It demonstrates that measured vertical response peaks can be physically interpreted when dense data are combined with targeted model perturbation.

The main conclusion of Chapter 4 is that vertical building response is governed by multiple mechanisms. A single vertical frequency is not sufficient to describe the response of an instrumented mid-rise building. Instead, global vertical modes, slab-dominated modes, and coupled modes can all appear within the frequency range of engineering interest. The results of this chapter also showed that the dominant vertical frequency bands identified from the data-driven analyses in Chapter 3, those associated with the largest PSD peaks and transfer-function magnitudes, are primarily linked to the building's global vertical modes and the vertical load-resisting system vibration, rather than slab vibration.

7.2.4 Chapter 5: Floor Response Spectra

Chapter 5 evaluated vertical floor response spectra (VFRS) and horizontal floor response spectra (HFRS) for the six instrumented JPL buildings subjected to the four common earthquake events. For each building, event, floor, and sensor line, 5%-damped pseudo-spectral acceleration (PSA) was computed from processed absolute floor acceleration records. Height amplification factors were then calculated to quantify how floor-level spectral demand changes with elevation relative to a reference level.

A short-period validation step confirmed the reliability of the spectral calculations. In both vertical and horizontal directions, the 0.01 s PSA closely reproduced the corresponding peak floor acceleration (PFA). The mean ratio between PSA at 0.01 s and PFA was approximately 0.998 in both directions. This result verified that the computed spectra satisfy the expected rigid-component limit and supported the use of the short-period spectral ordinate as a meaningful measure of near-rigid nonstructural component demand.

The VFRS showed a clear short-period character. Across the six buildings, the strongest vertical spectral demands were generally concentrated between about 0.08 s and 0.25 s, with building-specific peaks most often near 0.10 s to 0.20 s. These periods overlap with the dominant vertical response ranges identified in Chapter 3. The measured vertical spectra also showed systematic amplification with height, although the largest of these amplifications did not always occur at the highest level. In some buildings, upper-middle floors produced the controlling spectral ordinates, indicating that the vertical response is better described as upper-floor dominated rather than strictly roof dominated.

The vertical height-amplification results provided several important quantitative findings. At the short-period limit of 0.01 s, mean top-floor vertical HAF values reached approximately 2.0 in several buildings. When evaluated at the period corresponding to the maximum mean vertical amplification, the strongest top-floor mean HAF reached approximately 5.7 in JPL 264 at 0.20 s. Event-wise pooled results also showed that all four earthquakes produced upper-floor amplification above unity at 0.20 s, with an average pooled top-level amplification of approximately 2.5. These results show that vertical in-structure demand can be much larger than the reference-floor demand, especially when the oscillator period aligns with the dominant vertical period range of the supporting structure.

This finding is especially important for nonstructural component anchorage because it shows that vertical component demand is controlled by both the component period and building dominant vertical response bands, not only by peak floor acceleration or the first vertical mode.

The horizontal floor response spectra showed a different behavior. Short-period horizontal amplification was generally more modest and less consistently monotonic with height. Stronger horizontal amplification occurred at intermediate-to-longer periods, especially near approximately 0.5 s to 1.5 s, where the response aligned more closely with dominant/fundamental horizontal modal behavior. The mean of the fitted horizontal highest-level HAF reached its maximum near 1.5 s, while individual building-line cases showed larger event-specific amplification. Thus, the horizontal response is also period dependent, but its strongest height effect occurs at longer periods than the vertical response.

The comparison with ASCE/SEI 7-22 Chapter 13 (section 13.3.1.1) showed that current simplified height-amplification concepts in the horizontal direction capture the general idea that acceleration demand can increase with height, but they do not fully represent the measured period dependence. For vertical response, ASCE/SEI 7-22 does not provide an explicit vertical floor-response-spectrum or height-amplification model. The transferred horizontal ASCE height-amplification shape was generally conservative for the pooled vertical central trend, but it was too period-insensitive and did not reflect the short-period concentration of measured vertical amplification. Conversely, treating vertical response as having no explicit height amplification was too low relative to the measured empirical factors.

The main design-oriented contribution of Chapter 5 is the development of preliminary empirical height-amplification recommendations for both vertical and horizontal floor response spectra. For the vertical direction, the chapter proposed a separate vertical height-amplification factor with central-trend and upper-bound coefficients that vary with component period. This proposed factor is intended to complement, not replace, the code-level vertical seismic load effect. For the horizontal direction, the chapter showed that a component-period-dependent refinement would better represent measured HFRS behavior than a height-only or support-period-only expression. Overall, Chapter 5 demonstrated that the floor and component acceleration demand is both height dependent and period dependent of both the supporting structure and nonstructural component, and that the vertical and horizontal directions require distinct interpretations.

7.2.5 Chapter 6: Vertical Seismic Load Effects

Chapter 6 shifted from measured floor acceleration amplification to the seismic design code-level vertical seismic load effect, E_v. The chapter evaluated two alternative expressions currently used in design practice: the vertical period-independent expression based on $0.2S_{DS}D$, and the vertical period-dependent expression based on $0.3S_{av}D$. The comparison was expressed through the ratio $R_{E_v} = \frac{0.3S_{av}}{0.2S_{DS}}$. Values greater than 1.0 indicate that the period-dependent vertical spectral expression produces a larger vertical seismic load effect than the $0.2S_{DS}$ expression, while values less than 1.0 indicate that $0.2S_{DS}$ is more conservative than $0.3S_{av}$.

The chapter used two complementary datasets. The first was a scenario-based dataset developed from NGA-West2 ground motion models. Three horizontal-vertical ground motion model (GMM) pairings were used: ASK with GA, BSSA with SBSA, and CB with BC. The resulting scenario dataset covered combinations of earthquake magnitude, rupture distance, site condition, and vertical period, producing 3,060 seismic scenarios at 21 discrete periods and 64,260 R_{E_v} data points. The second California site-specific dataset was based on ASCE 7 Hazard Tool parameters for 19,316 sites and 53 discrete vertical periods, producing 1,023,748 R_{E_v} values. These two datasets provided independent ways to evaluate whether the current E_v expressions behave consistently across vertical period and seismic design category.

The results from both datasets showed that the adequacy of $0.2S_{DS}$ is strongly dependent on the vertical period. For very short vertical periods, especially $T_v \leq 0.025$ s, the $0.2S_{DS}$ expression is generally conservative and can substantially overestimate the E_v value compared to $0.3S_{av}$. A similar trend occurs for long vertical periods, especially $T_v > 0.5$s, because $0.2S_{DS}D$ remains constant while the vertical spectral acceleration decreases with period. The primary range of concern is the moderate vertical-period range, especially $0.05\ s < T_v \leq 0.2\ s$, where $0.2S_{DS}D$ can underestimate the E_v compared to the $0.3S_{av}$, particullary in higher seismic design categories.

The site-specific California results made this period dependence especially clear. In SDC D, which represented the largest portion of the California dataset, the 0.05 s to 0.2 s range showed substantial probability of underestimation when E_v was computed using $0.2S_{DS}D$. The range $0.1\ s < T_v \leq 0.2\ s$ was particularly critical because a significant portion of the results indicated underestimation by more than 50% relative to the period-dependent expression. SDC E showed even stronger period-dependent contrast, with the moderate vertical-period range producing the largest concern for underestimation.

Based on these findings, Chapter 6 recommended a period-dependent approach for calculating E_v. For SDC C, D, and E structures with moderate vertical periods, the use of $0.3S_{av}D$ is recommended because $0.2S_{DS}D$ can be unconservative for seismic design. For very short and very long vertical periods, $0.3S_{av}D$ is also preferred because $0.2S_{DS}D$ can be excessively conservative and therefore may produce unnecessary vertical demand and cost. For transition ranges where the two methods are generally comparable or slightly conservative, either method may be acceptable depending on the seismic design category and design context. The chapter also proposed a long-period refinement to the calculation of the vertical spectral acceleration to improve the smoothness and consistency of the vertical spectrum for longer periods.

The main conclusion of Chapter 6 is that a vertical period-independent expression cannot consistently represent vertical seismic demand across the full range of vertical periods. This conclusion reinforces the measured-building findings from Chapters 3 through 5. The vertical period matters for identifying structural frequencies, for determining vertical floor response spectra, and for calculating code-level vertical seismic load effects. Chapter 6, therefore, extends the dissertation's central theme from building response measurement to design provisions: vertical response should be represented with explicit period dependence whenever possible.

7.3 Limitations & Future Work

The dissertation provides measured data, simulation-based, and code-oriented evidence that vertical structural response deserves more explicit treatment in earthquake engineering. This study also offers several recommendations to inform future seismic design practice and potential refinements to code provisions. At the same time, the findings should be interpreted within the scope of the available data, the modeling assumptions, and the design context. The following summarizes the principal limitations of the work and identifies future research directions that would strengthen and extend the conclusions.

The first limitation is the size and scope of the measured building dataset. The data-driven frequency identification and floor response spectra were based on six mid-rise buildings located on the JPL campus. Although these buildings provide valuable variation in height, sensor layout, and structural characteristics, they are all located within the same campus and regional seismic setting. This limitation reflects a broader challenge in current structural monitoring practice: few networks provide dense, floor-by-floor triaxial instrumentation across many buildings and geographic locations. Therefore, the results cannot by themselves represent the full range of building types, heights, structural systems, and site conditions. However, as the Community Seismic Network continues to expand, the framework developed in this dissertation can be applied to a larger and more diverse set of buildings. Future applications of this framework will be important for confirming, refining, or extending the findings of this study across different structural systems, regions, and earthquake conditions.

The second limitation is the number and intensity of the earthquake records. The dataset used for inter-building comparison consisted of four earthquakes. This was necessary to support consistent building-to-building comparisons, but it limits the statistical validity of the ground-motion inputs. The events produced useful elastic response, but they did not represent a broad suite of strong shaking levels, near-fault motions, or nonlinear structural response conditions. Future research should incorporate additional earthquake records, especially stronger events, to evaluate whether the vertical frequency ranges, height-amplification trends, and floor response spectra identified here remain stable at larger response amplitudes. Such data would also make it possible to examine stiffness degradation, damage-sensitive frequency shifts, and the interaction between vertical and horizontal response under more demanding seismic conditions.

The third limitation is related to instrumentation and record quality. The CSN sensors provide very dense floor-by-floor measurements, but they are low-cost MEMS accelerometers with a nominal sampling rate of approximately 50 Hz. This sampling rate is suitable for many engineering frequency ranges, but it limits the resolution of very high-frequency responses and requires careful filtering. Some buildings and events also had missing or unusable sensor records, requiring changes in reference floor or exclusion of specific floors. Future deployments can strengthen this type of analysis by increasing sensor redundancy, improving synchronization and quality-control procedures, adding higher-sampling-rate sensors in selected buildings, and placing multiple sensors at different plan locations on the same floor. Future work should also examine how sensor location within the floor plan affects the identified dominant vertical frequency. Because sensors near columns, walls, or perimeter framing may emphasize global vertical response, while sensors near mid-panel slab regions may emphasize slab-flexural vibration, additional measurements at multiple plan locations on the same floor are needed to distinguish global and slab-dominated vertical response more directly. These improvements would help distinguish global vertical response from local slab behavior, diaphragm effects, and nonstructural disturbances.

The fourth limitation involves signal processing and frequency identification. The identified frequency ranges depend on usable bandwidth, filtering choices, signal-to-noise ratio, peak selection, and coherence interpretation. Frequencies near the lower usable-bandwidth boundary are especially sensitive to record-specific excitation and processing decisions. Similarly, high-frequency features may be difficult to distinguish from noise or local nonstructural disturbances. The use of transfer functions and coherence provides a strong validation framework, but it does not eliminate all uncertainty in peak classification. For this reason, this study reports vertical response frequencies as ranges rather than as a single deterministic value for each building. Future work should build on this approach by incorporating additional automated system-identification and signal-processing tools to improve the separation of closely spaced modes and allow measured vertical mode shapes to be estimated more directly.

The fifth limitation concerns the simulation component. The detailed finite-element investigation was conducted for a well-instrumented building. This model provided an important physical interpretation of the measured vertical frequency bands, especially the distinction between global vertical modes, slab-dominated modes, and coupled response, but the same simulation-based classification can be repeated for other buildings. Future work should expand the simulation to multiple instrumented buildings. Future simulations should also evaluate soil-structure interaction, boundary flexibility, cracked concrete stiffness, and nonlinear response-history behavior under combined horizontal and vertical ground motions.

The sixth limitation is associated with the empirical FRS and HAF recommendations. The final proposed vertical and horizontal height-amplification models were calibrated using the JPL-CSN dataset and the selected set of earthquake records. They are very useful as preliminary design-oriented models, but they are not yet broad code provisions, and they should not be generalized to all buildings. Future research should therefore evaluate additional component damping ratios, a broader range of earthquake characteristics, such as magnitude, source-to-site distance, duration, frequency content, and near-fault effects, as well as within-floor sensor location. A larger measured and simulated dataset would allow the proposed height-amplification models to be recalibrated with uncertainty bounds.

The seventh limitation concerns the Chapter 6 code evaluation. The E_v analysis used NGA-West2 scenario-based ground motion models and PSHA-derived ASCE 7 Hazard Tool parameters for California sites. Although the dataset is large and code-relevant, the site-specific analysis is geographically focused on California (the western United States). Future work should extend this analysis to other high-seismic regions.

A particularly promising future direction is the integration of the measured-response framework with real-time smart-city monitoring. The JPL-CSN deployment demonstrates that dense instrumentation can also support rapid situational awareness. The Python-based data preparation and processing workflow developed in this dissertation already provides a reproducible path from raw CSN records to usable structural-response data. With further development, this workflow could be adapted for near-real-time applications that estimate building-specific frequency shifts, floor response spectra, vertical amplification, and potential nonstructural component demand immediately after an earthquake. Such tools could support targeted inspection, rapid damage screening, and resilience-based decision making for campuses, cities, and infrastructure owners.

Finally, the dissertation focused on the vertical component of response as measured and modeled within the available data and code frameworks. Real earthquake performance depends on combined horizontal and vertical excitation, structural irregularity, nonlinear behavior, nonstructural component details, and post-earthquake functional requirements. These interactions remain beyond the full scope of the present work and motivate the future research directions described below.

In conclusion, this dissertation demonstrates that dense measured data, targeted simulation, and statistical analysis can substantially improve the understanding of vertical structural response. The results show that vertical response is measurable, repeatable, height-dependent, period-dependent, and strongly connected to both global structural modes and floor-system behavior. These findings provide a foundation for future research and for the eventual development of more explicit vertical-response provisions in seismic design practice.

Appendix A. Overview of SAC files

The Seismic Analysis Code (SAC) is a versatile interactive tool created for the examination of sequential data, with a special emphasis on time-series data. Originating to cater to the nuanced requirements of research seismologists, SAC facilitates a myriad of operations, ranging from quick preliminary analyses and routine processing to in-depth research and crafting publication-ready graphics.

At its core, each signal in SAC is stored within an individual data file. These files not only house the data but also encompass a descriptive header that offers insights into the content of that specific file. Typically, signals are loaded from the disk to the memory via the READ command. Impressively, SAC can concurrently process up to 200 signals of varying sizes. Post this, users can then execute a range of commands to manipulate and analyze these signals.

SAC prides itself on its user-friendly interface, with most operational parameters being equipped with well-thought-out default values. However, for those seeking customization, almost all these parameters can be adjusted according to the user's preferences.

A unique feature of SAC is its mode of operation. Rather than proactively prompting users for input, SAC operates in an interactive, command-driven manner. This means the user must input specific commands to drive actions in SAC. These commands can either be inputted directly or sourced from a macro file. SAC segregates its commands into three primary categories:

1. Parameter-setting Commands: Alter the values of internal SAC parameters.
2. Action-producing Commands: Perform operations based on these parameter values.

3. Data-set Manipulation Commands: Determine which files are actively in memory and hence can be acted upon.

SAC provides abbreviations for its frequently used commands, enhancing user convenience. For more information, refer to SAC Manual. (Goldstein et al., 2003; *Manuals: SAC*; Peng, 2013)

Appendix B. FFT vs DFT

The Discrete Fourier Transform (DFT) and the Fast Fourier Transform (FFT) are both mathematical algorithms used to analyze and transform signals from the time domain to the frequency domain. The primary difference between them lies in their computational complexity.

Discrete Fourier Transform (DFT):

The DFT is a mathematical transformation that converts a discrete sequence of N complex numbers (sampled from a continuous signal) into another sequence of N complex numbers. This new sequence represents the same signal in the frequency domain. The DFT formula for a given frequency component k is (Duhamel & Vetterli, 1990):

$$X[k] = \sum_{n=0}^{N-1} x[n] \,.\, e^{-i2\pi kn/N} \qquad \text{(Eq B. 1.)}$$

where X[k] is the complex amplitude of the frequency component at index k in the frequency domain. x[n] is the complex input signal at index n in the time domain. N is the number of samples in the signal, and i is the imaginary unit. Computing the DFT using this formula has a time complexity of $O(N^2)$, which becomes inefficient for large input sizes.

Fast Fourier Transform (FFT):

The FFT is an optimized method to compute the DFT in a more efficient manner. The Cooley-Tukey FFT algorithm is one of the most renowned methods for this purpose. It leverages the symmetry properties of the DFT, breaking the computation into smaller subproblems. This method reduces the time complexity of the DFT to $O(N \log N)$, which is a substantial improvement, especially for large input sizes (Duhamel & Vetterli, 1990).

Comparison:

- Computational Complexity: The pivotal difference lies in computational complexity. While the DFT operates at a time complexity of $O(N^2)$, the FFT offers a much more efficient time complexity of $O(N \log N)$. This efficiency renders the FFT as a faster option, especially for large input sizes (such as recorded motions).
- Efficiency: Because of its swifter computation time, the FFT is the preferred choice in practical applications where real-time or rapid processing is essential. On the other hand, the DFT is typically utilized when the input size is manageable or when computational efficiency isn't a top priority.

In conclusion, both the DFT and FFT serve to transform signals from the time domain to the frequency domain. However, in the realm of research, the FFT stands out since it makes signal processing and real-time analysis faster. For more information regarding DFT and FFT refer to "Fast Fourier Transforms: a tutorial review and a state of the art" by P. Duhamel & M. Vetterli. (Duhamel & Vetterli, 1990)

Appendix C. Welch's Method for PSD Estimation

The power spectral density (PSD) is a fundamental tool in the analysis of signals. It provides insights into the distribution of power over frequency for a specific signal. Due to noise and other imperfections in real-world signals, direct computation of the PSD from a finite-length signal can often be challenging. The periodogram is a classic method for estimating the PSD. It is the magnitude squared of the Fourier transform of a signal, effectively highlighting its frequency components. However, the periodogram is known for its high variability or lack of consistency. To address this, various methods have been introduced to improve the periodogram's reliability. One such method is Welch's averaged periodogram method, detailed in the following steps (Welch, 1967):

1. **Signal Segmentation:**

   The initial step in Welch's method is to divide the time signal into overlapping segments. The length of each segment and the degree of overlap are parameters that can be fine-tuned based on the nature of the signal. For a signal of length N, if L is the selected segment length and D is the overlap, then each segment will have L samples, with consecutive segments $L - D$ samples apart.

2. **Windowing:**

   Each of these segments undergoes windowing using a specific window function. Windowing in signal processing involves applying a specific window function to a segment of a continuous signal to mitigate spectral leakage. Spectral leakage occurs when a segment is truncated, which can distort its true frequency content. By applying a window function, the signal's amplitude is gradually reduced towards the edges of the segment, reducing this distortion. There are various window functions, such as Hamming, Hann, and Blackman, each with unique characteristics. Mathematically, windowing is represented as:

$$x_{windowed} = x(n) \times w(n) \qquad \text{(Eq C.1)}$$

where x(n) is the nth sample in the segment, and w(n) is the nth sample of the window function.

3. **Computation of Periodograms:**

   For each windowed segment, the periodogram is calculated, which, as previously mentioned, is essentially the magnitude squared of the discrete Fourier transform of the signal segment. This process results in multiple periodograms derived from the different segments.

$$P_{xx}(f) = \frac{1}{L}|X(f)|^2 \qquad \text{(Eq C.2)}$$

   where $X(f)$ is the Fourier transform of the windowed segment, and $P_{xx}(f)$ is the periodogram of the segment at frequency f.

4. **Averaging Periodograms:**

   The core of the process is the averaging of the computed periodograms from all segments. This step smoothens out the inconsistencies present in individual periodograms, thus producing a more stable and accurate PSD estimation.

$$P_{avg}(f) = \frac{1}{M}\sum_{m=1}^{M} P_{xx,m}(f) \qquad \text{(Eq C.3)}$$

where M is the total number of segments, $P_{xx,m}(f)$ is the periodogram of the m$^{\text{th}}$ segment at frequency f.

Benefits and Considerations:

Using Welch's method minimizes the periodogram's variability, effectively reducing the influence of noise. This leads to a more consistent PSD estimate, especially crucial for noisy signals. However, it's essential to note that the resolution of the PSD estimate is influenced by the segment length, overlap, and windowing. For more information, refer to “PSD Computations Using Welch’s Method” by O tis M. Solom on (Solomon Jr, 1991).

In our research, the goal of employing Welch’s method is to ensure robust and consistent PSD estimations, thereby enhancing the quality of the analytical results.

Appendix D. Transfer and Coherency Functions

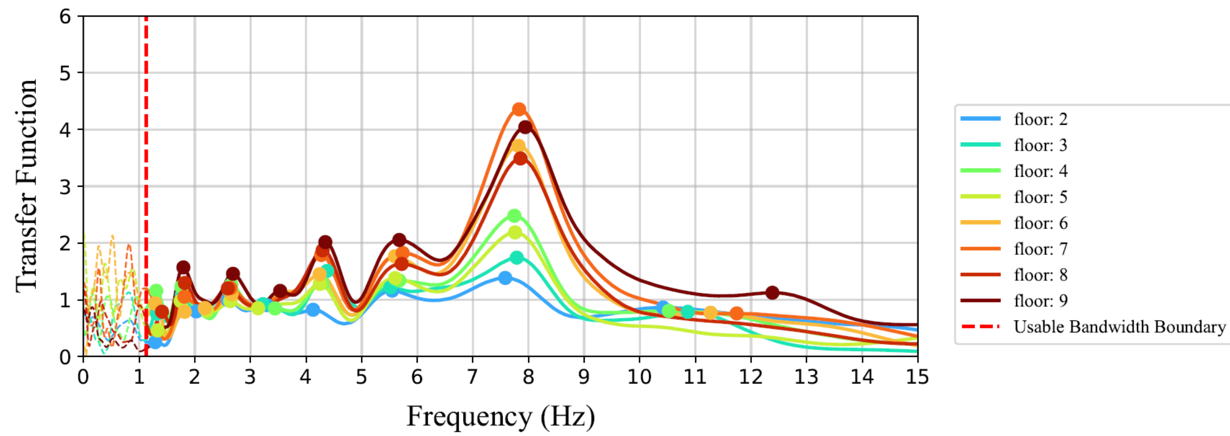

(a)

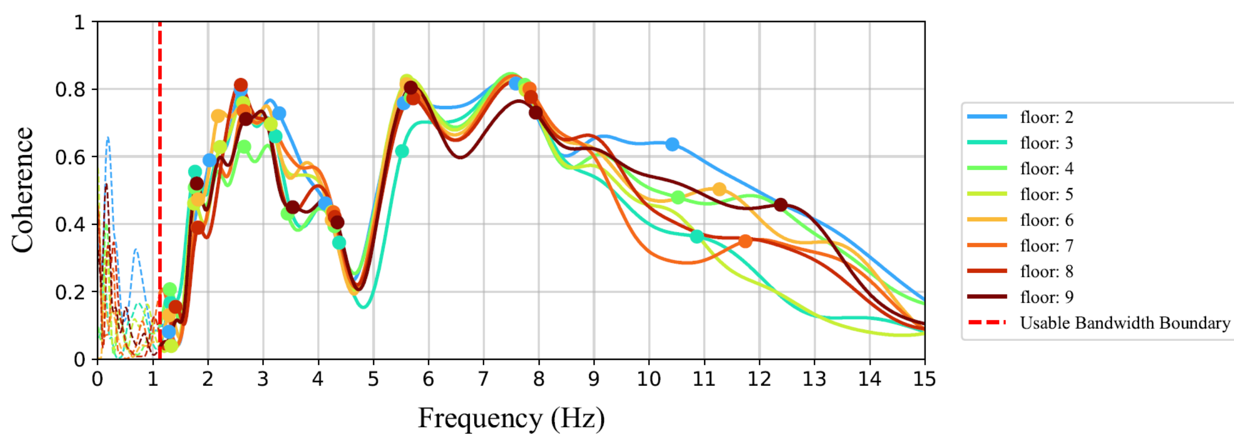

(b)

Figure D.1. a) Vertical floor-to-base transfer function and b) magnitude-squared coherence for JPL 183 during the Pacoima earthquake. The dashed red line marks the lower usable bandwidth

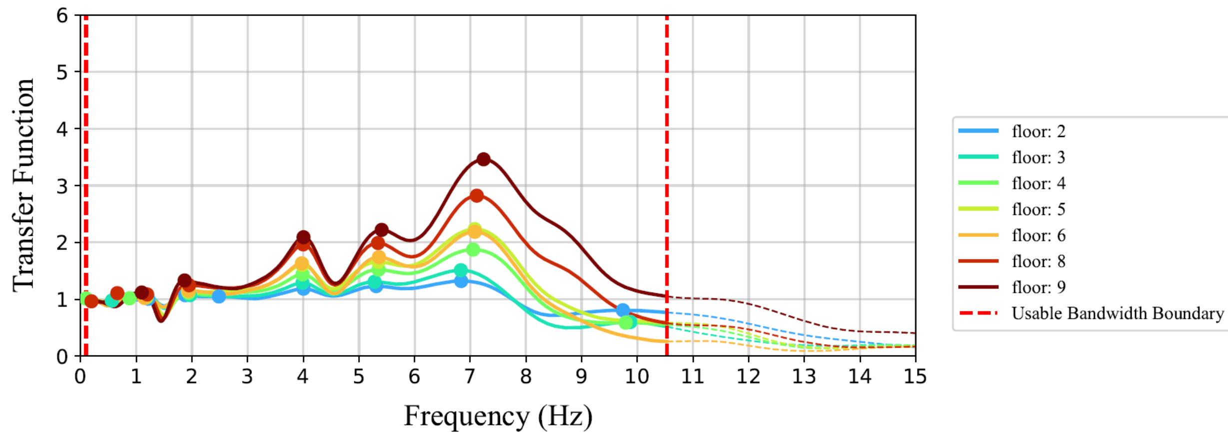

(a)

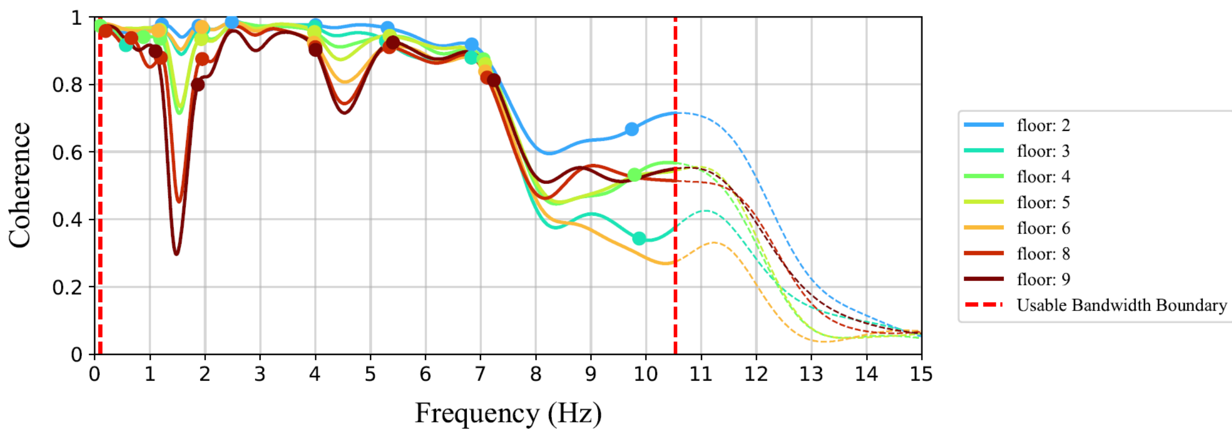

(b)

Figure D.2. a) Vertical floor-to-base transfer function and b) magnitude-squared coherence for JPL 183 during the Ridgecrest earthquake. The dashed red line marks the lower usable bandwidth

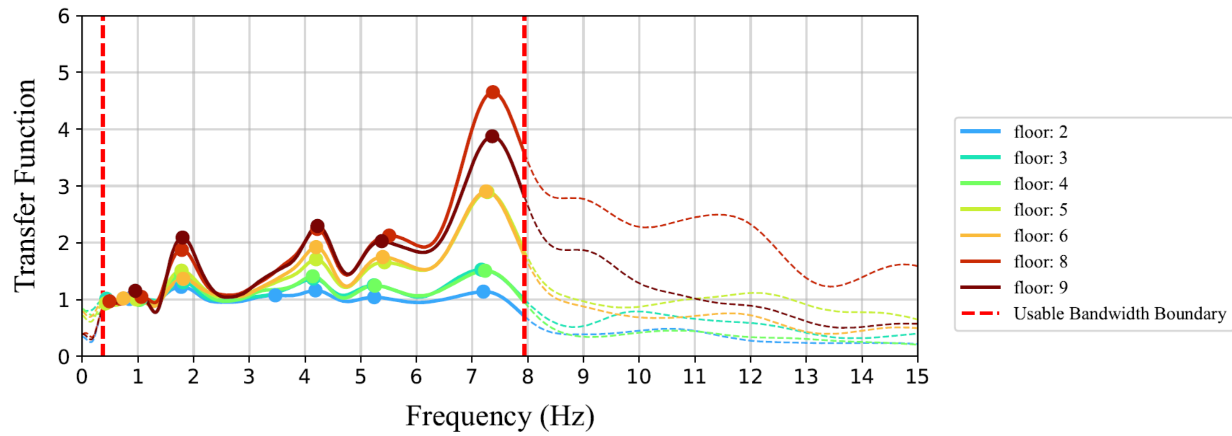

(a)

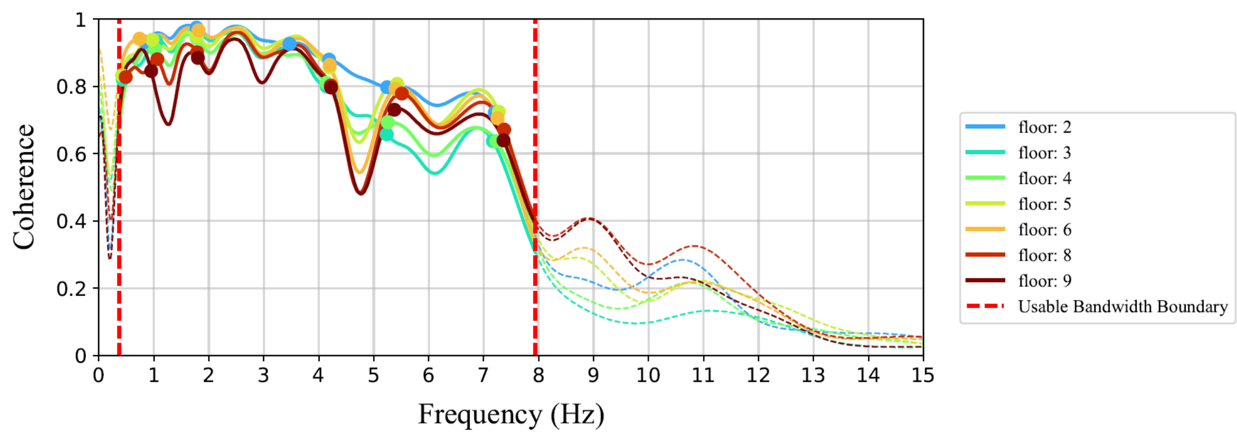

(b)

Figure D.3. a) Vertical floor-to-base transfer function and b) magnitude-squared coherence for JPL 183 during the Searle Valley earthquake. The dashed red line marks the lower usable bandwidth

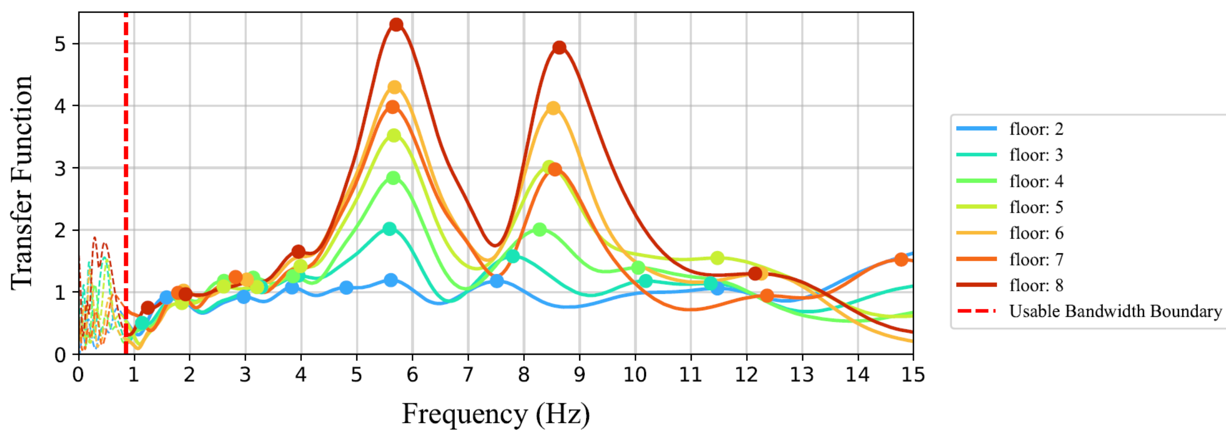

(a)

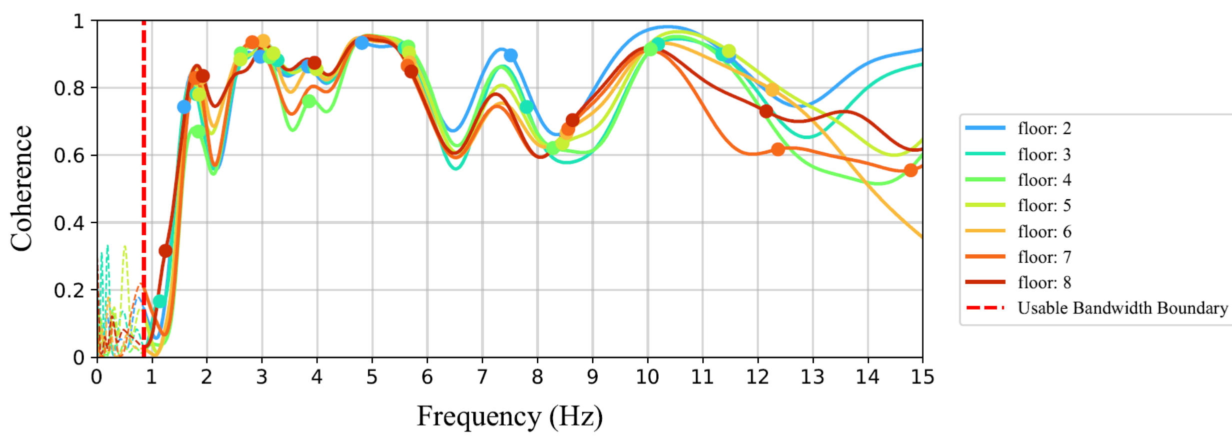

(b)

Figure D.4. a) Vertical floor-to-base transfer function and b) magnitude-squared coherence for JPL 180 during the Pacoima earthquake. The dashed red line marks the lower usable bandwidth

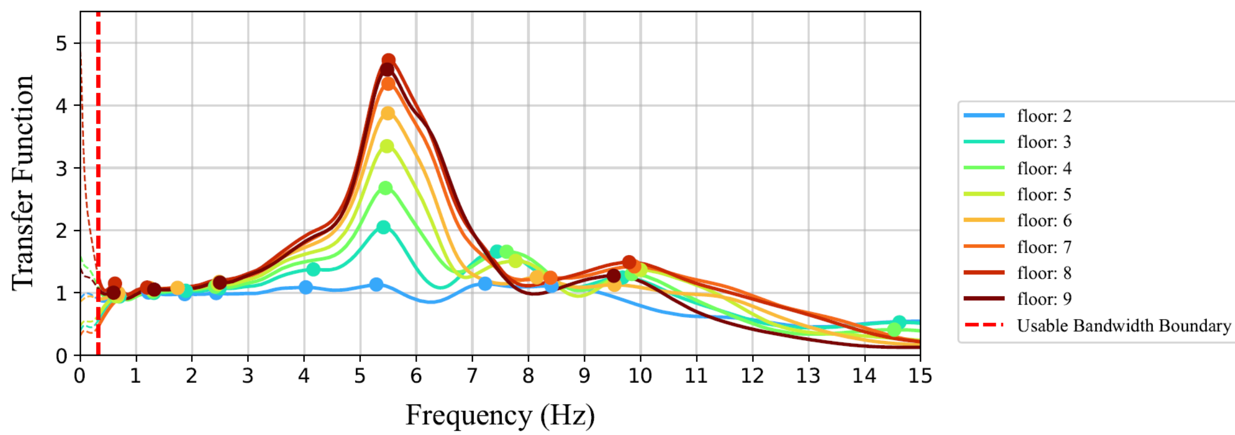

(a)

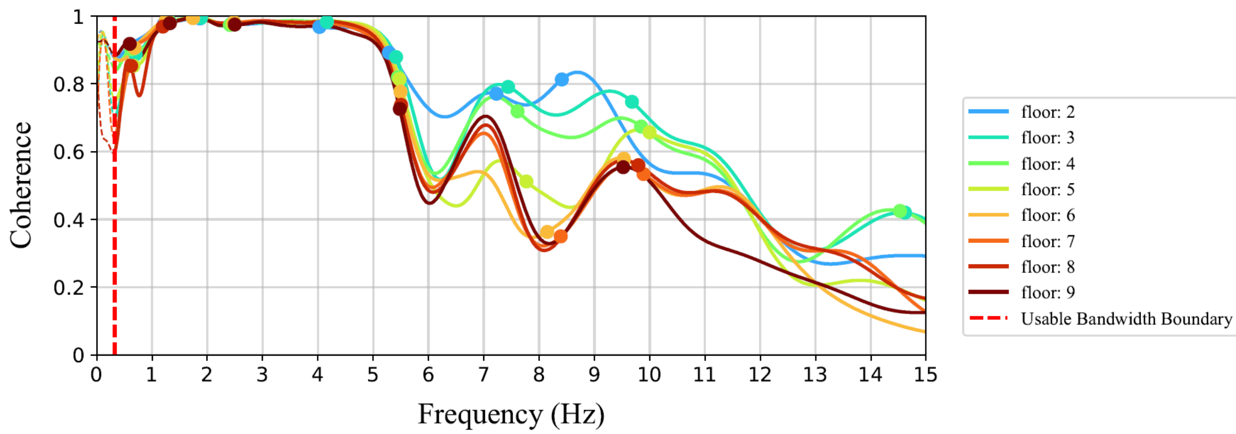

(b)

Figure D.5. a) Vertical floor-to-base transfer function and b) magnitude-squared coherence for JPL 180 during the Ridgecrest earthquake. The dashed red line marks the lower usable bandwidth

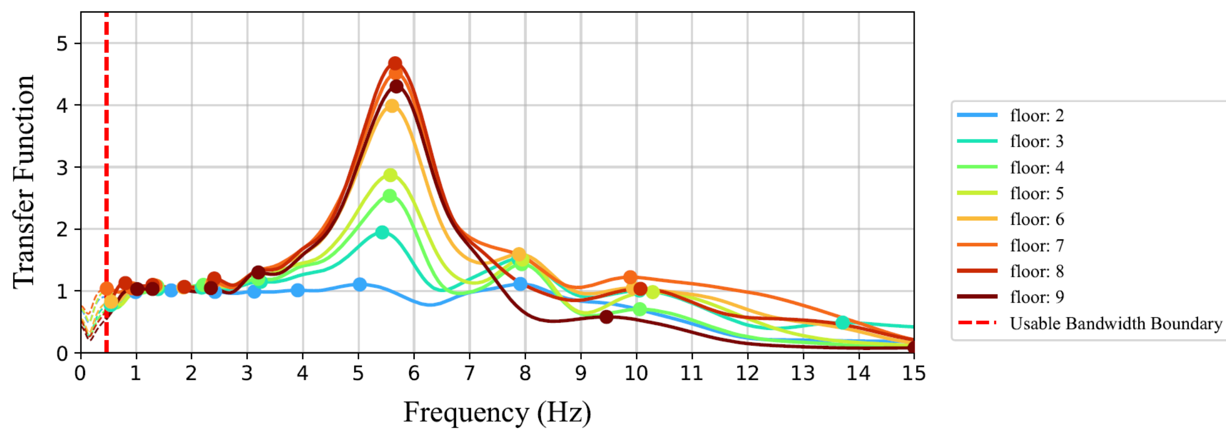

(a)

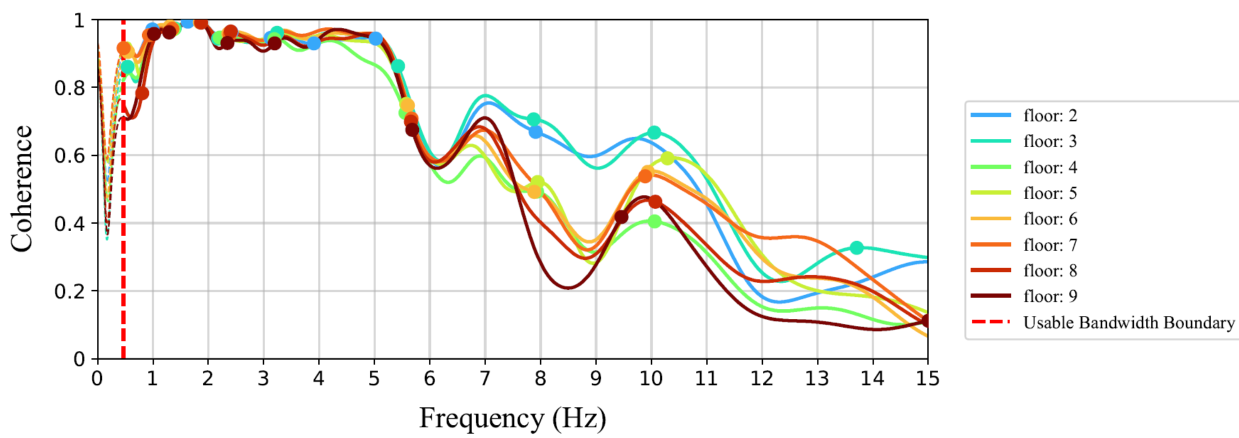

(b)

Figure D.6. a) Vertical floor-to-base transfer function and b) magnitude-squared coherence for JPL 180 during the Searle Valley earthquake. The dashed red line marks the lower usable bandwidth

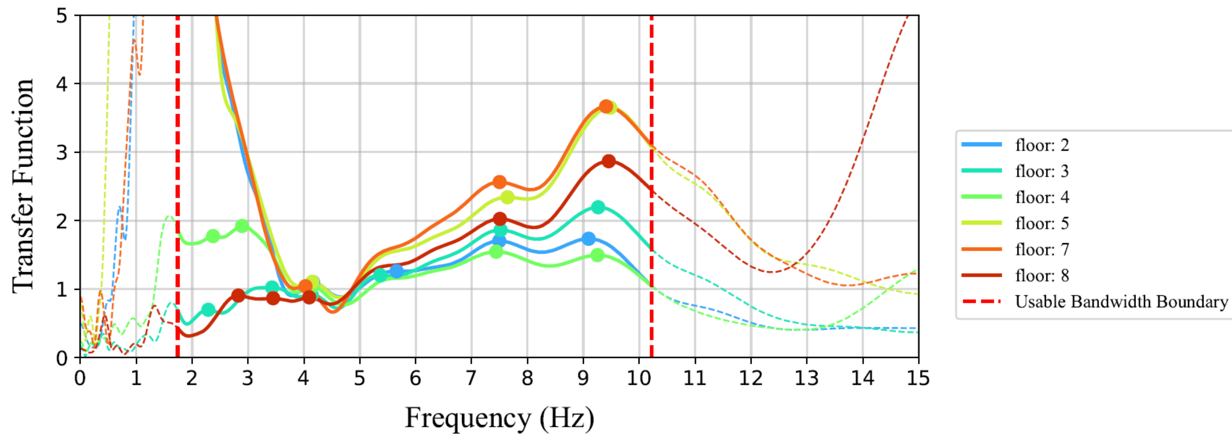

(a)

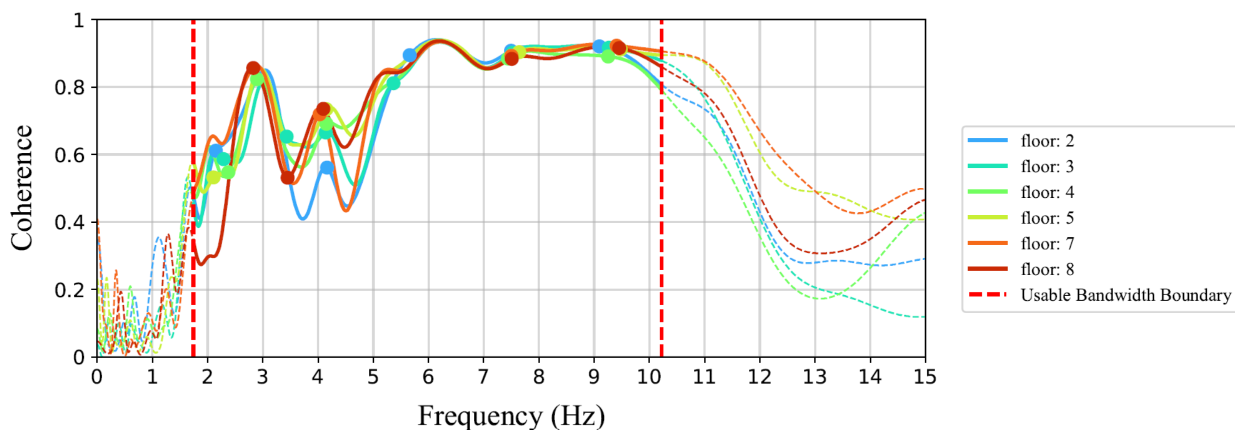

(b)

Figure D.7. a) Vertical floor-to-base transfer function and b) magnitude-squared coherence for JPL 238 during the Pacoima earthquake. The dashed red line marks the lower usable bandwidth

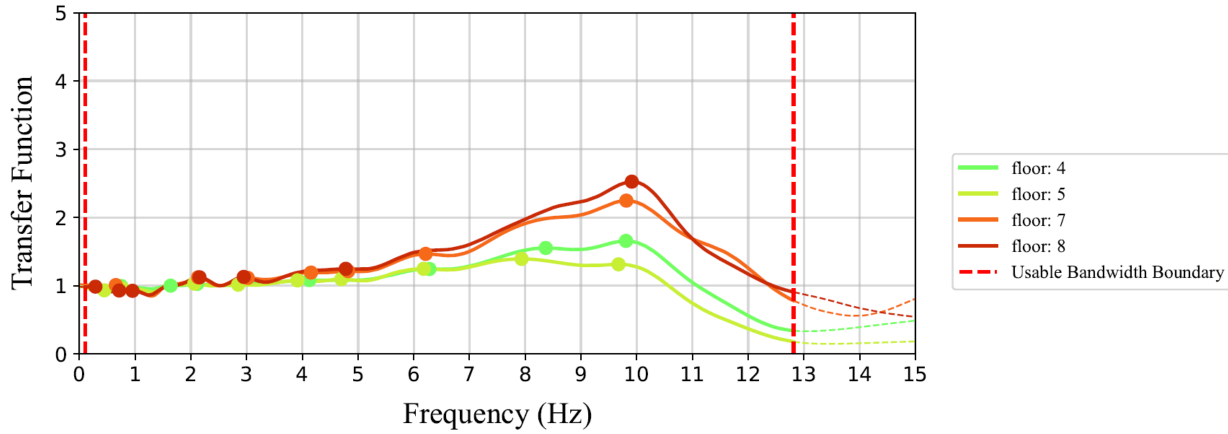

(a)

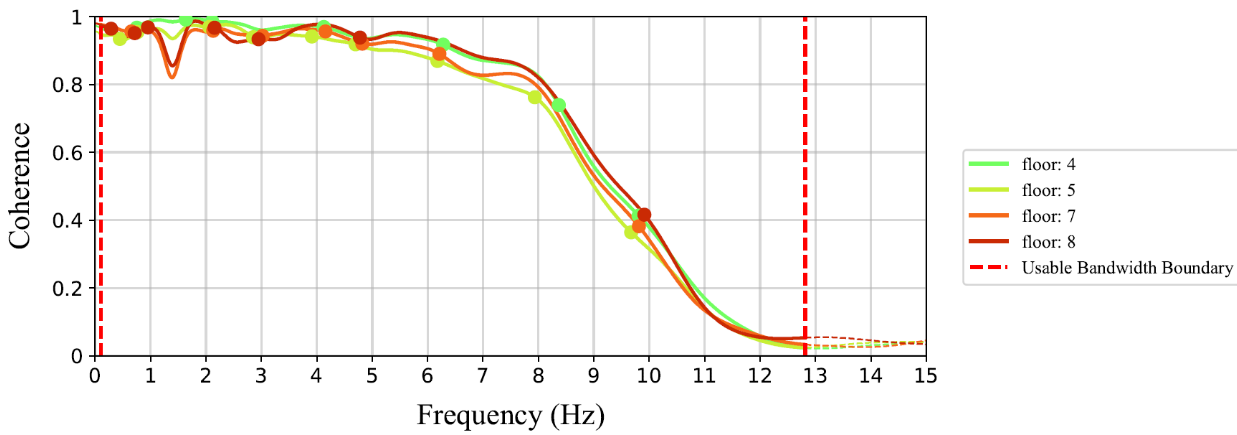

(b)

Figure D.8. a) Vertical floor-to-base transfer function and b) magnitude-squared coherence for JPL 238 during the Ridgecrest earthquake. The dashed red line marks the lower usable bandwidth

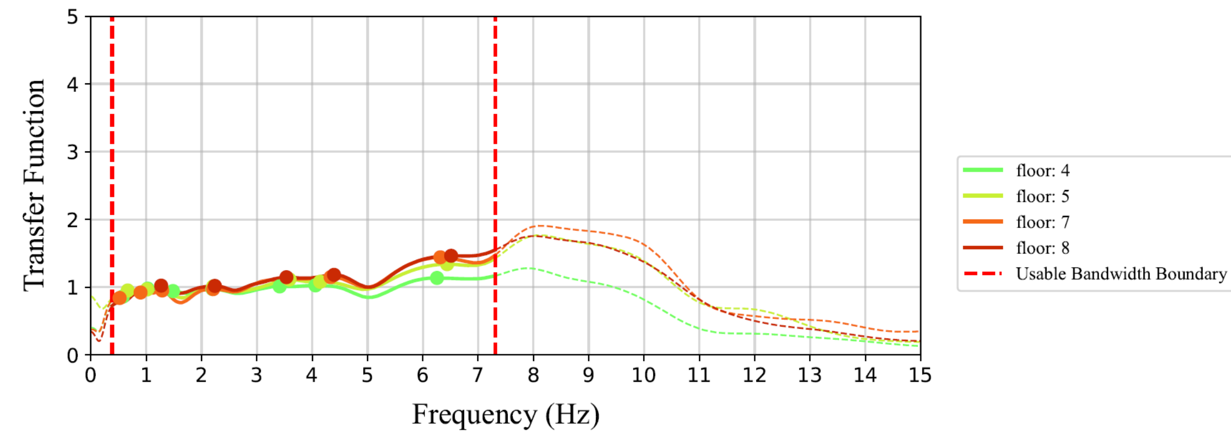

(a)

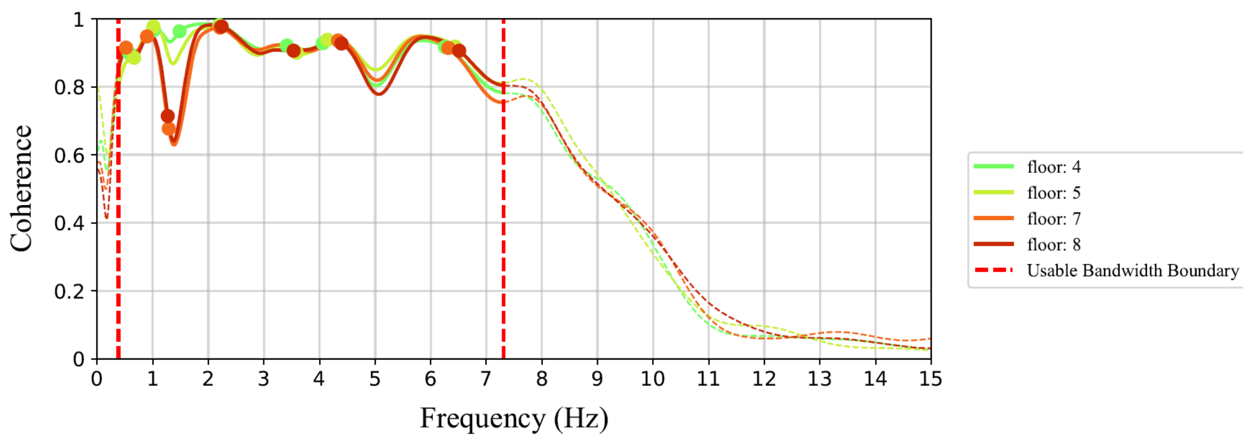

(b)

Figure D.9. a) Vertical floor-to-base transfer function and b) magnitude-squared coherence for JPL 238 during the Searle Valley earthquake. The dashed red line marks the lower usable bandwidth

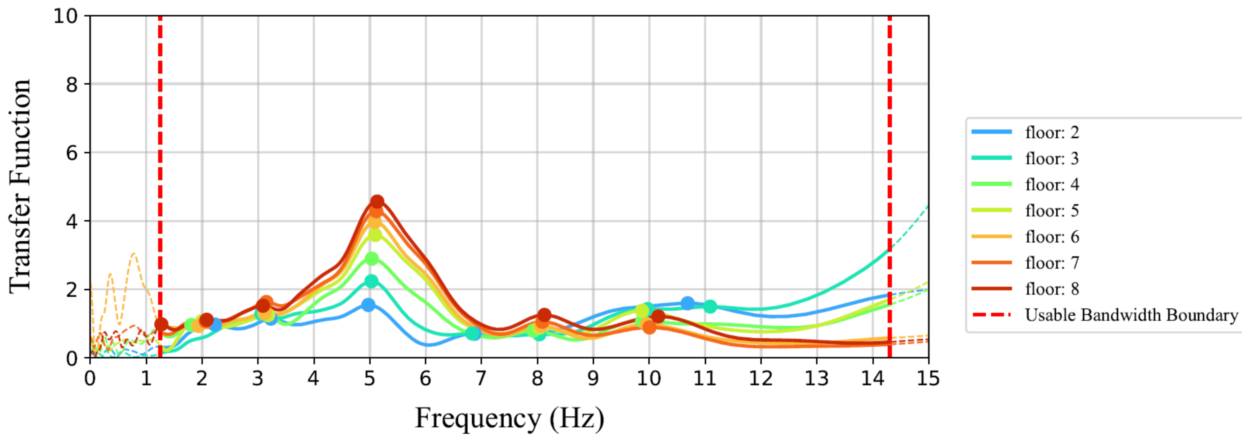

(a)

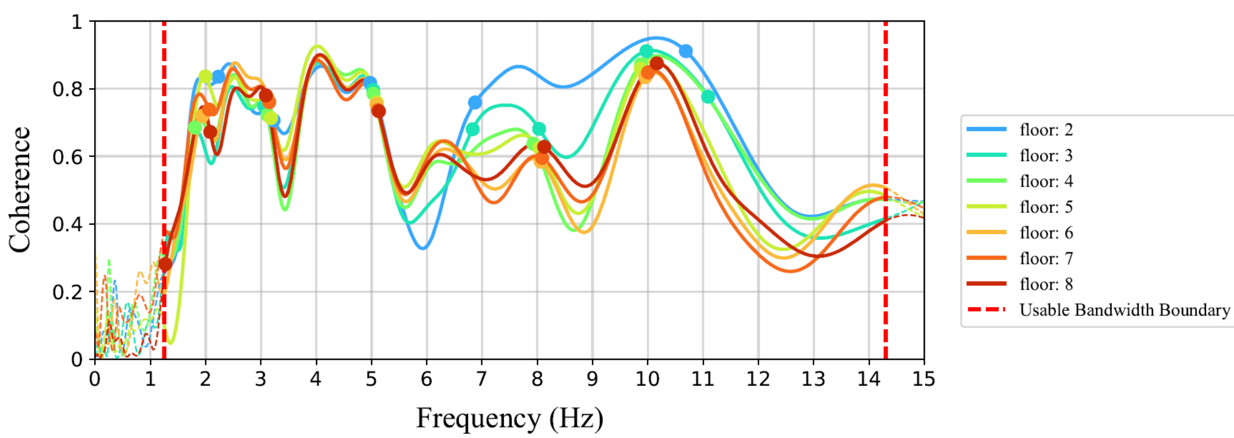

(b)

Figure D.10. a) Vertical floor-to-base transfer function and b) magnitude-squared coherence for JPL 264 during the Pacoima earthquake. The dashed red line marks the lower usable bandwidth

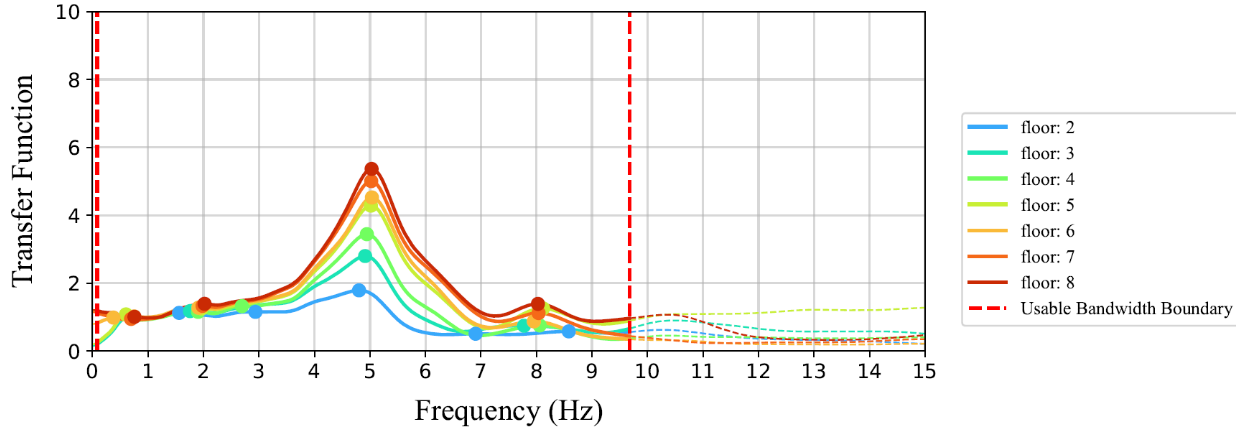

(a)

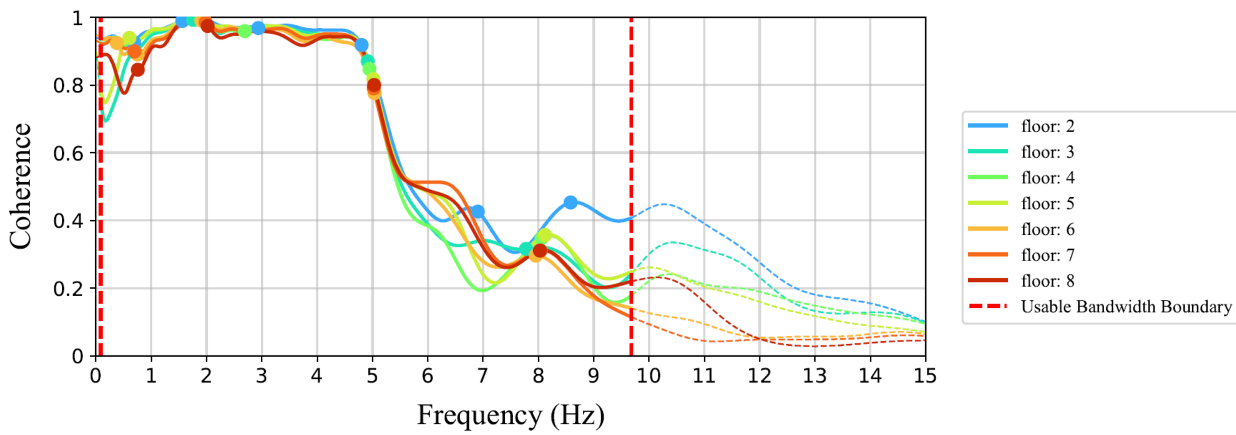

(b)

Figure D.11. a) Vertical floor-to-base transfer function and b) magnitude-squared coherence for JPL 264 during the Ridgecrest earthquake. The dashed red line marks the lower usable bandwidth

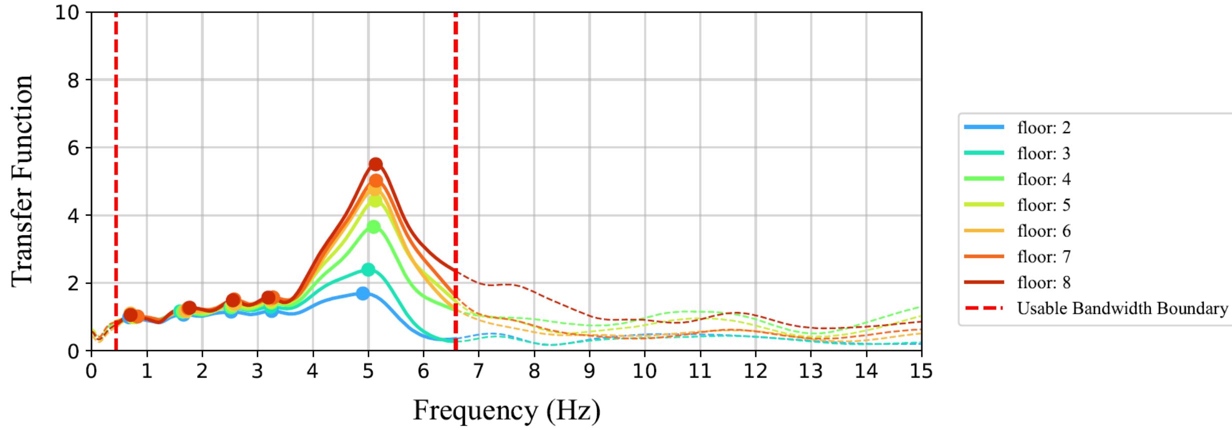

(a)

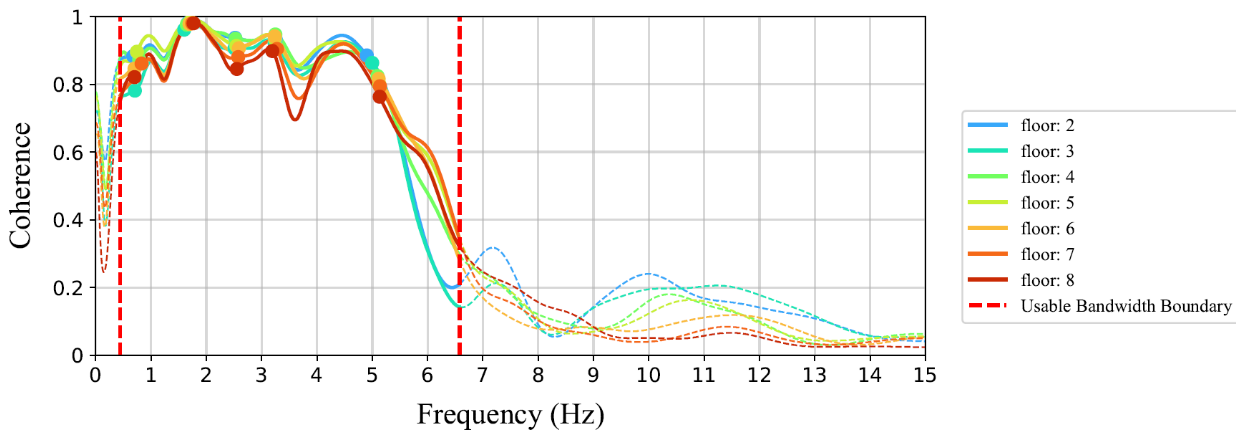

(b)

Figure D.12. a) Vertical floor-to-base transfer function and b) magnitude-squared coherence for JPL 264 during the Searle Valley earthquake. The dashed red line marks the lower usable bandwidth

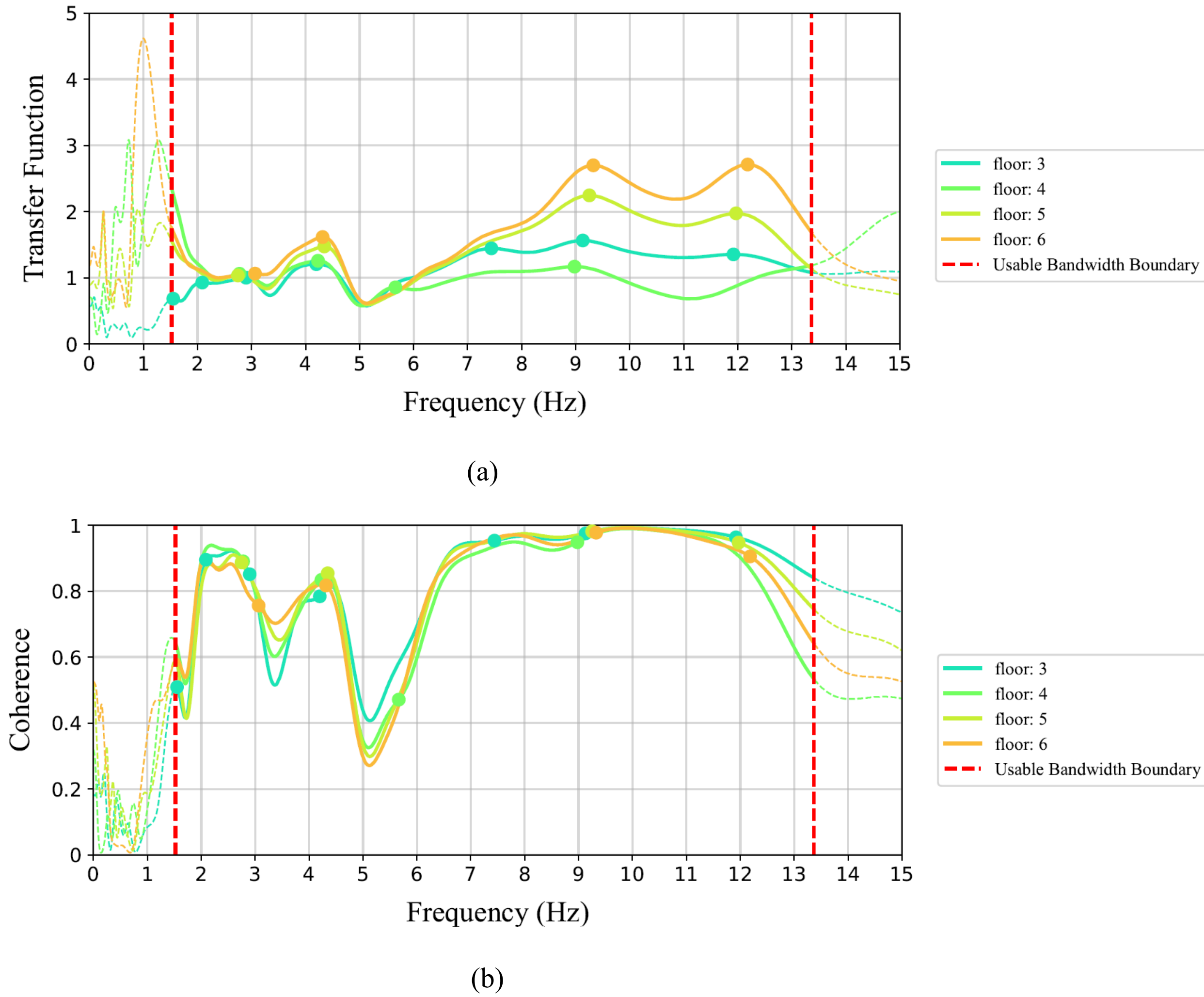

Figure D.13. a) Vertical floor-to-base transfer function and b) magnitude-squared coherence for JPL 321 during the Pacoima earthquake. The dashed red line marks the lower usable bandwidth

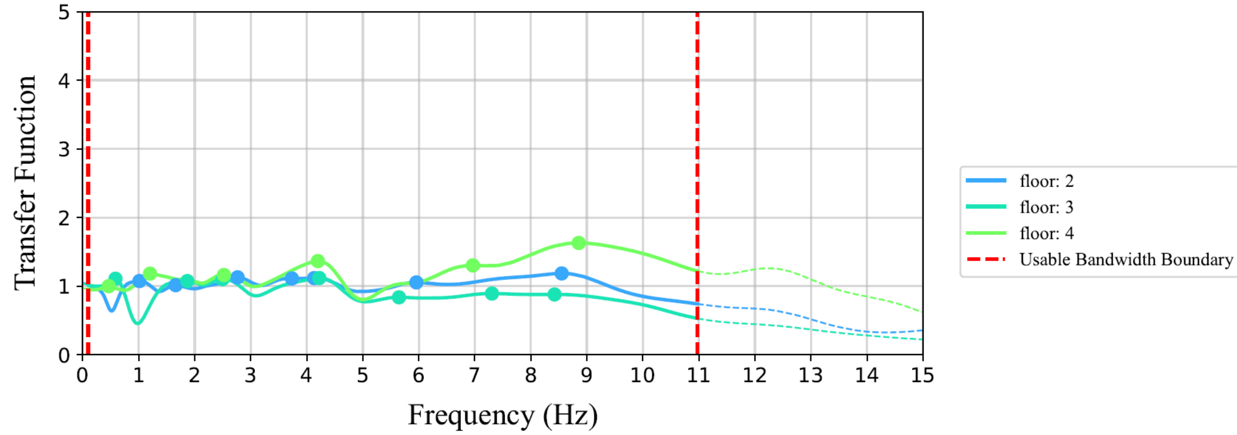

(a)

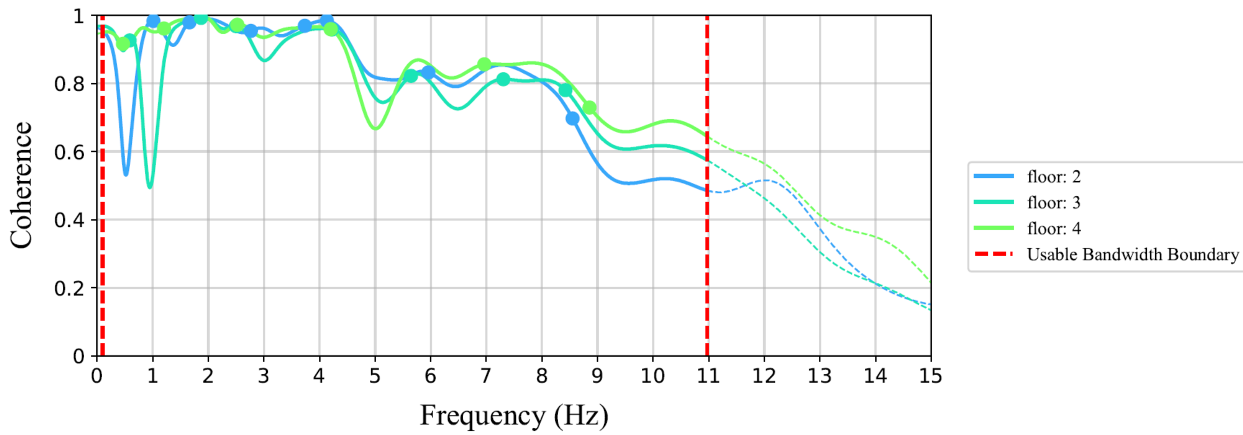

(b)

Figure D.14. a) Vertical floor-to-base transfer function and b) magnitude-squared coherence for JPL 321 during the Ridgecrest earthquake. The dashed red line marks the lower usable bandwidth

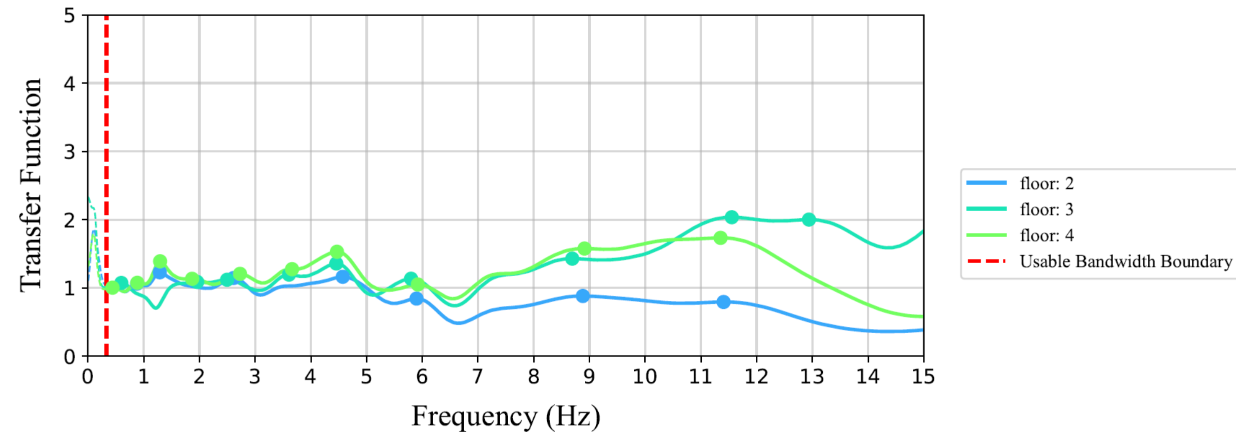

(a)

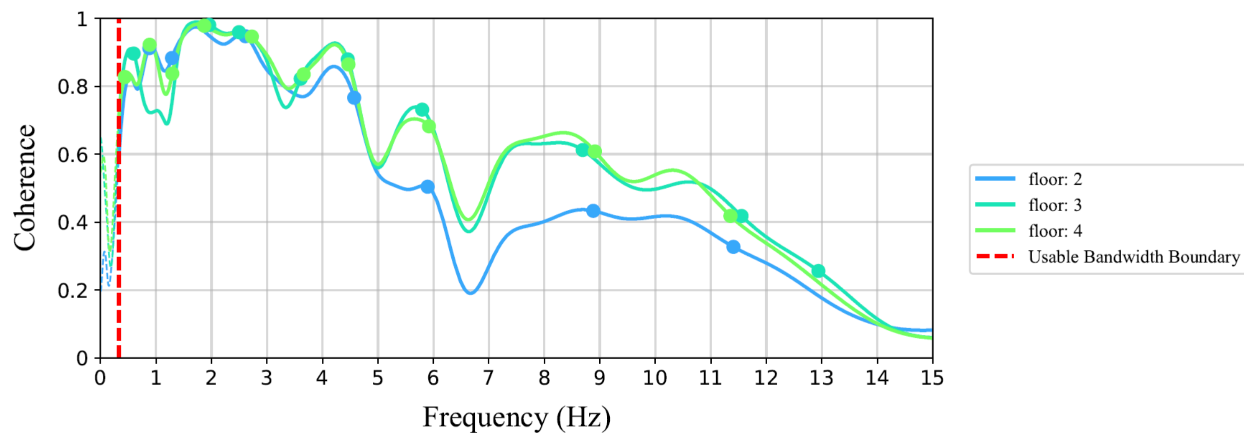

(b)

Figure D.15. a) Vertical floor-to-base transfer function and b) magnitude-squared coherence for JPL 321 during the Searle Valley earthquake. The dashed red line marks the lower usable bandwidth

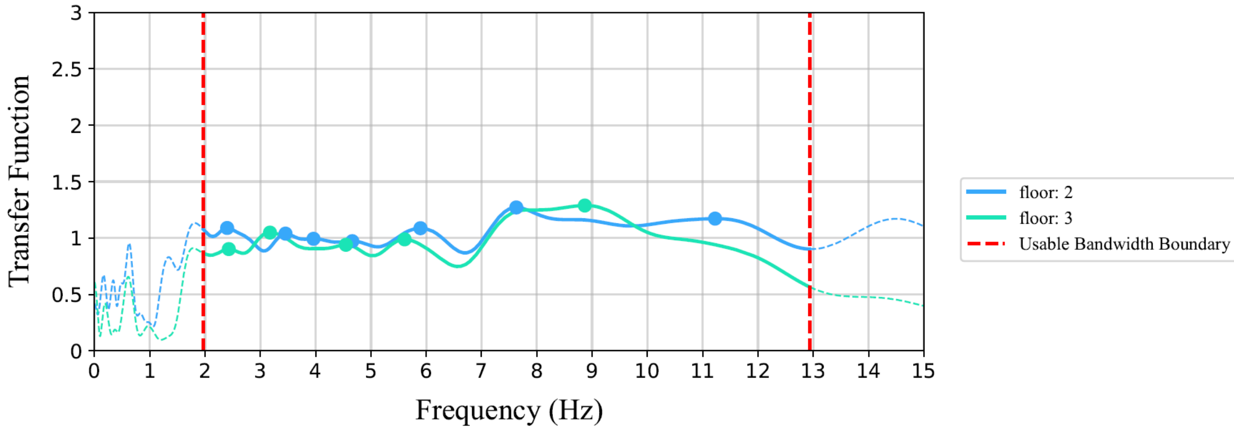

(a)

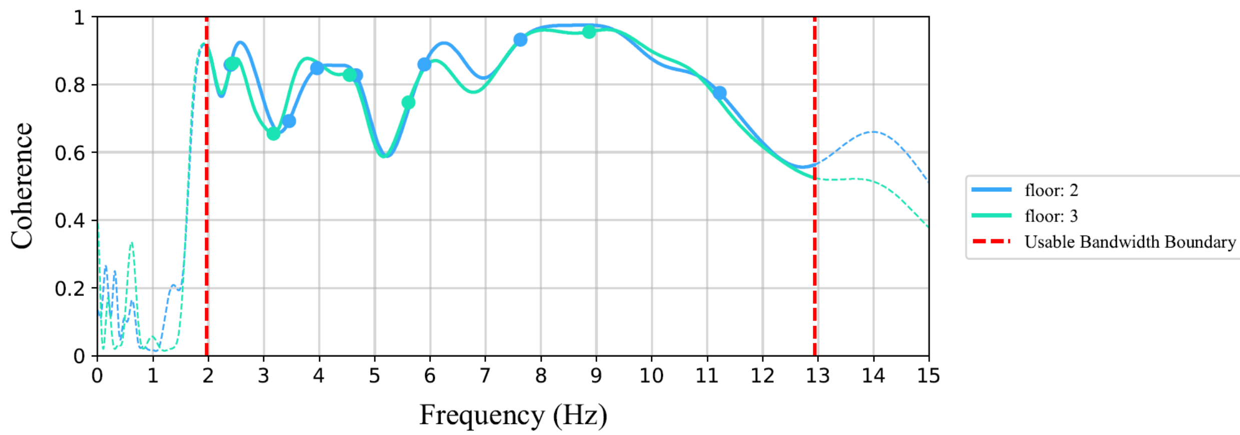

(b)

Figure D.16. a) Vertical floor-to-base transfer function and b) magnitude-squared coherence for JPL 303 during the Pacoima earthquake. The dashed red line marks the lower usable bandwidth

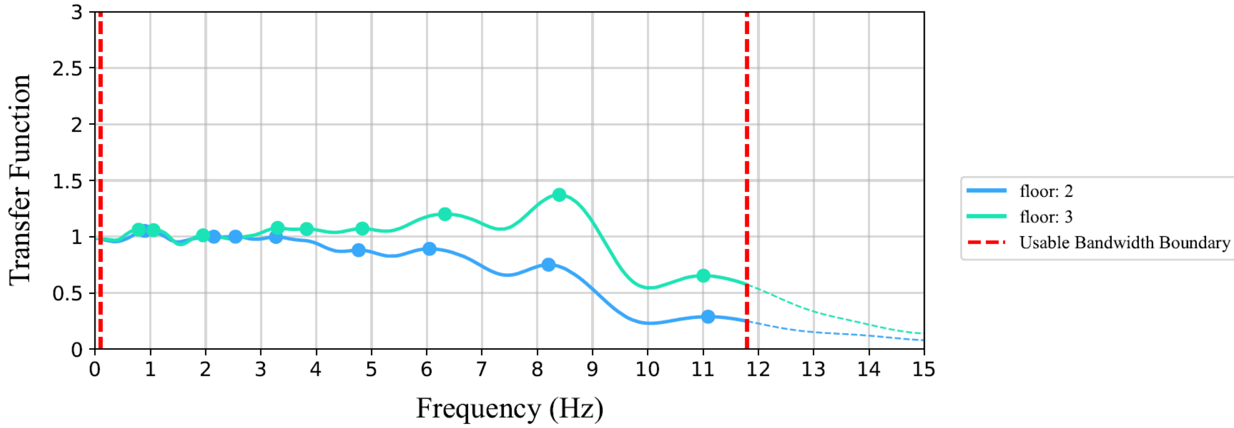

(a)

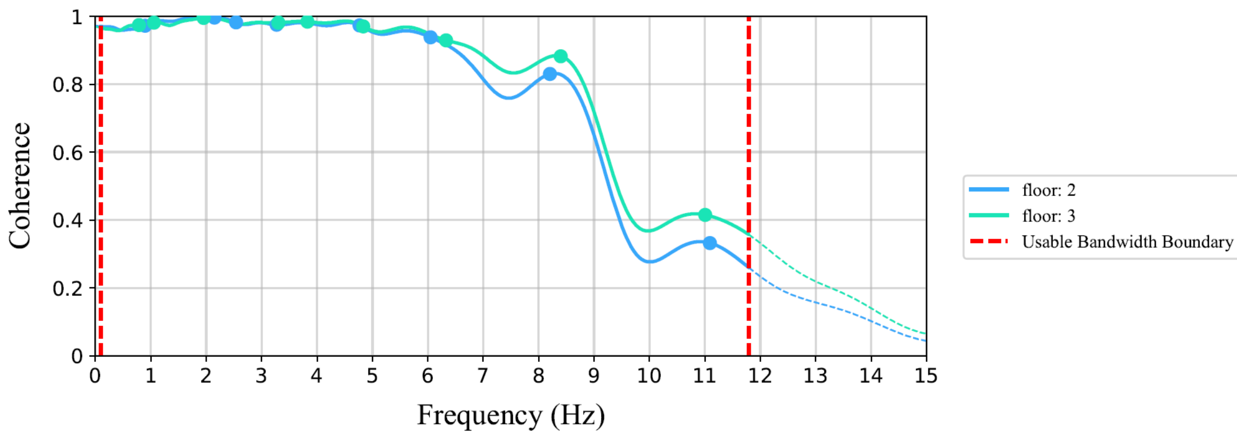

(b)

Figure D.17. a) Vertical floor-to-base transfer function and b) magnitude-squared coherence for JPL 303 during the Ridgecrest earthquake. The dashed red line marks the lower usable bandwidth

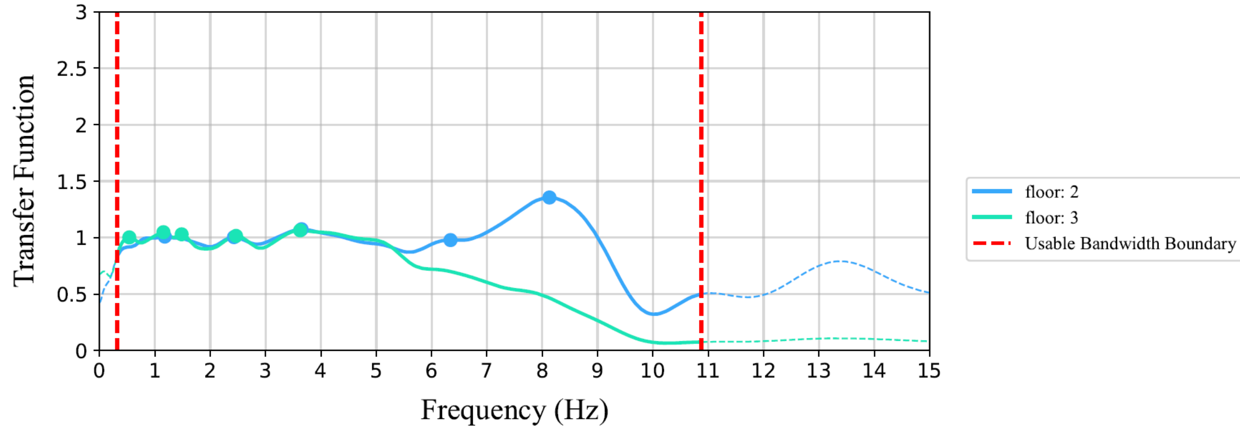

(a)

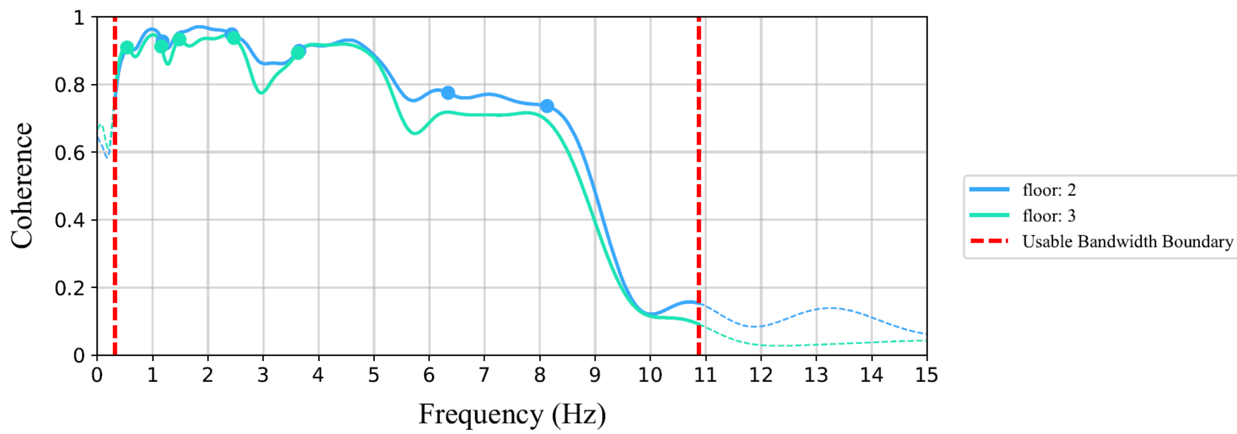

(b)

Figure D.18. a) Vertical floor-to-base transfer function and b) magnitude-squared coherence for JPL 303 during the Searle Valley earthquake. The dashed red line marks the lower usable bandwidth

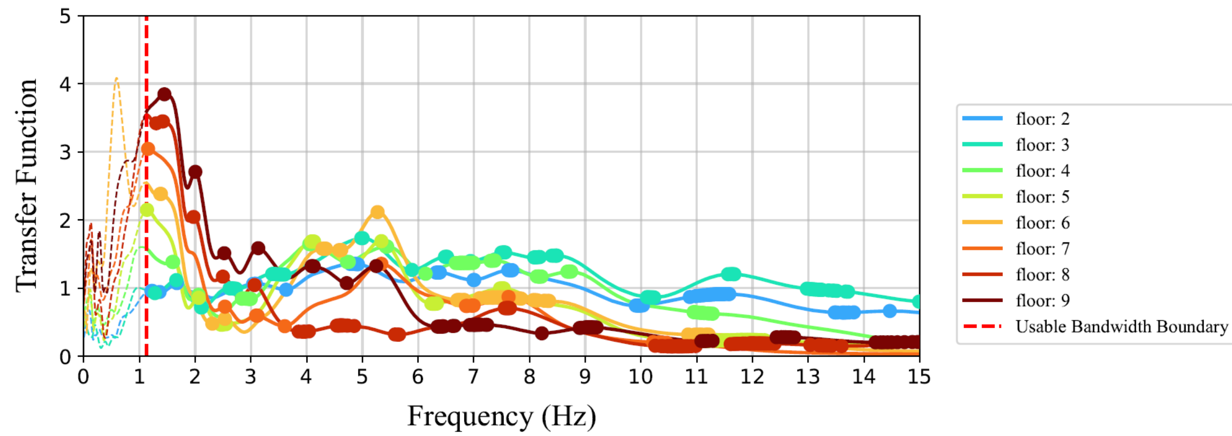

(a)

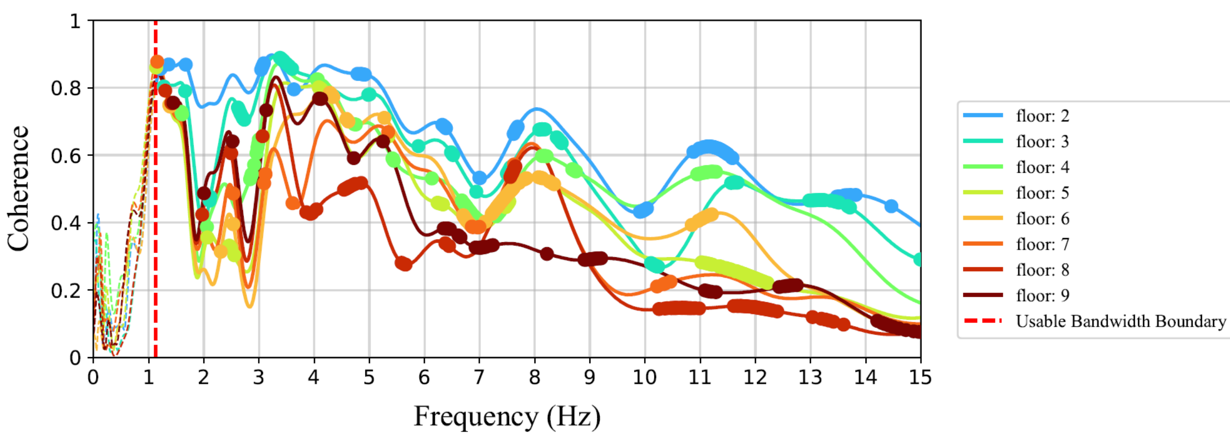

(b)

Figure D.19. a) Horizontal floor-to-base transfer function and b) magnitude-squared coherence for JPL 183 during the Pacoima earthquake. The dashed red line marks the lower usable bandwidth

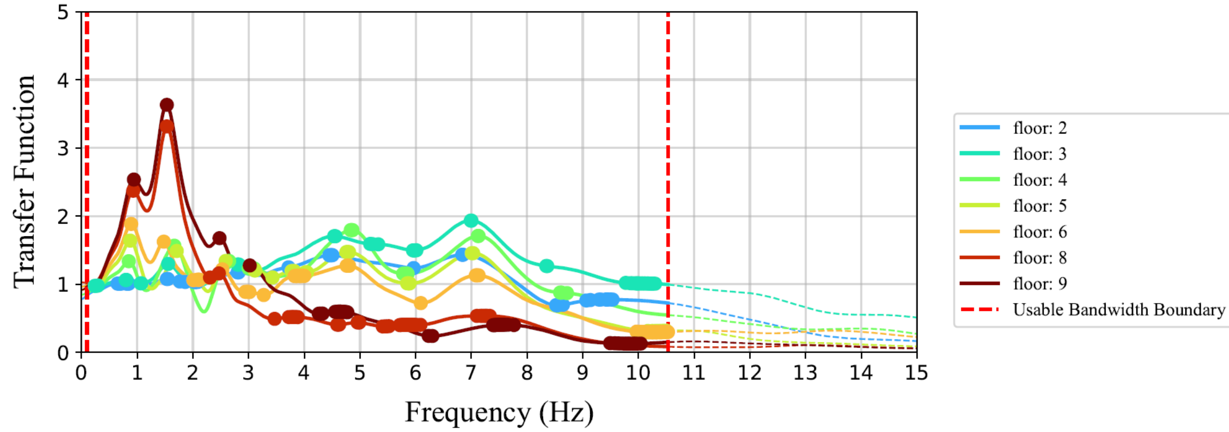

(a)

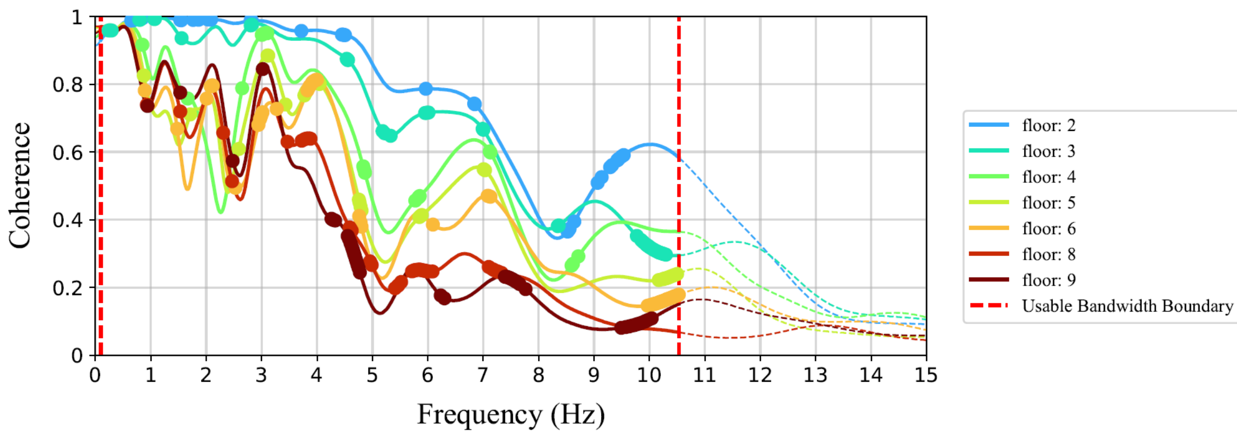

(b)

Figure D.20. a) Horizontal floor-to-base transfer function and b) magnitude-squared coherence for JPL 183 during the Ridgecrest earthquake. The dashed red line marks the lower usable bandwidth

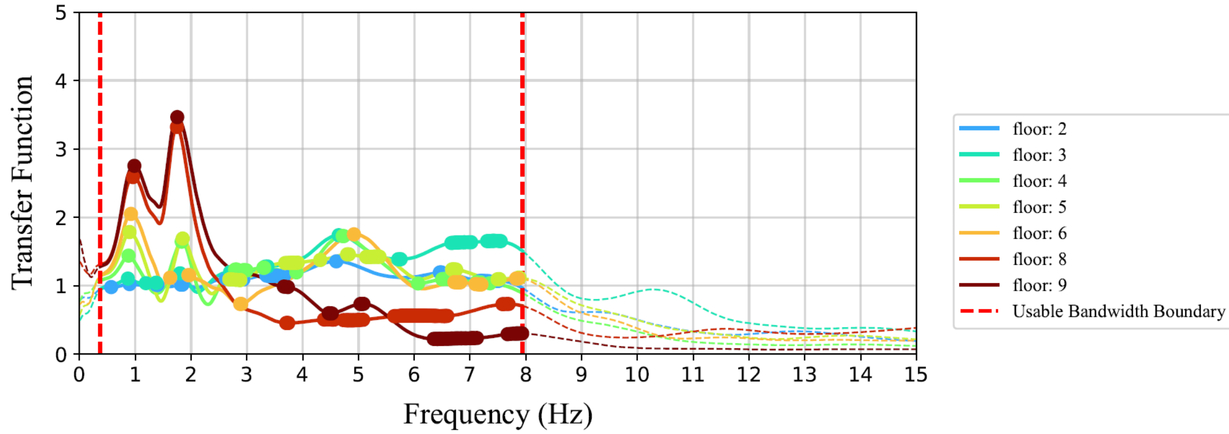

(a)

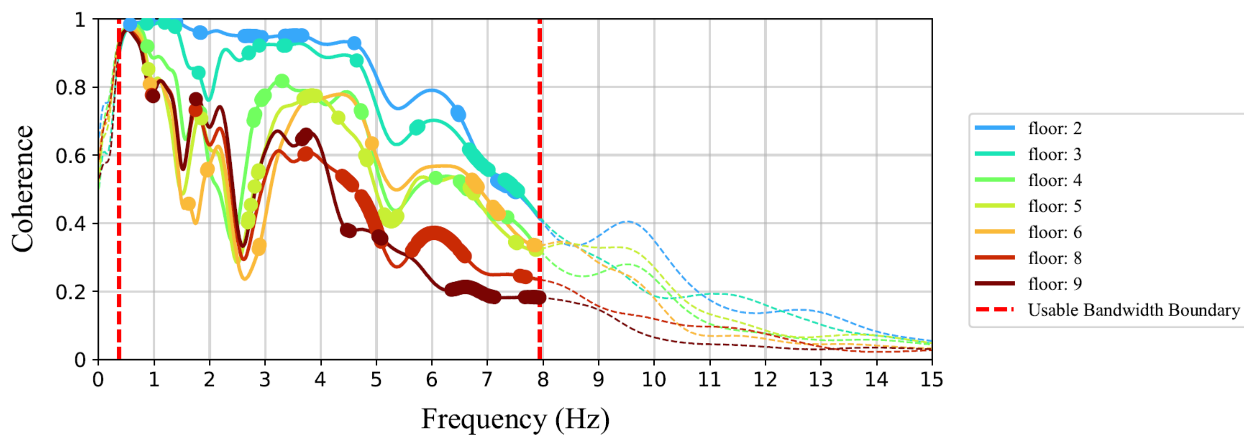

(b)

Figure D.21. a) Horizontal floor-to-base transfer function and b) magnitude-squared coherence for JPL 183 during the Searle Valley earthquake. The dashed red line marks the lower usable bandwidth

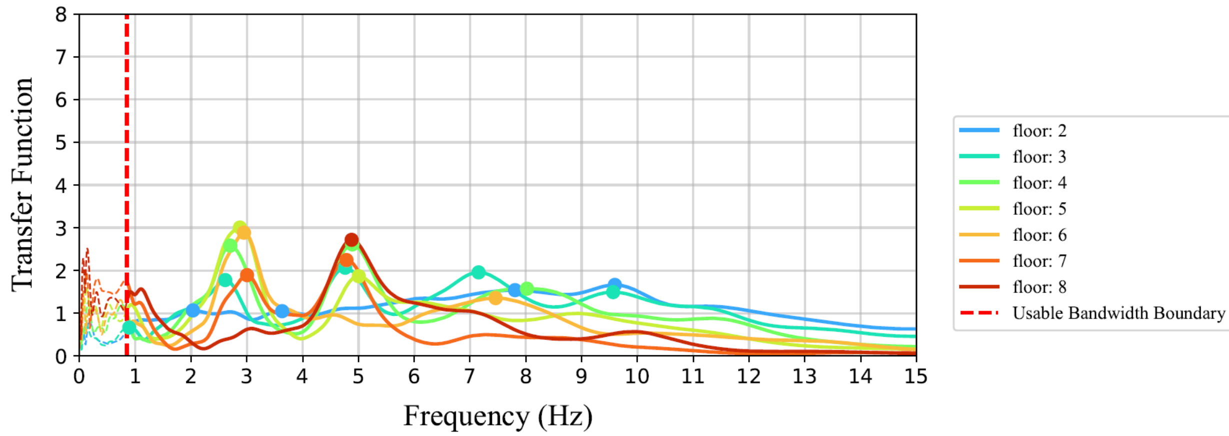

(a)

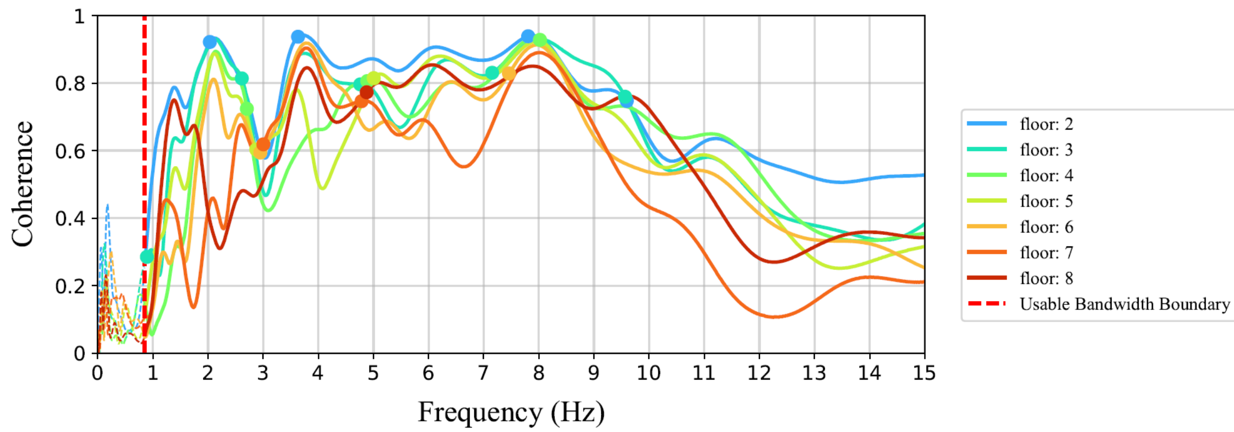

(b)

Figure D.22. a) Horizontal floor-to-base transfer function and b) magnitude-squared coherence for JPL 180 during the Pacoima earthquake. The dashed red line marks the lower usable bandwidth

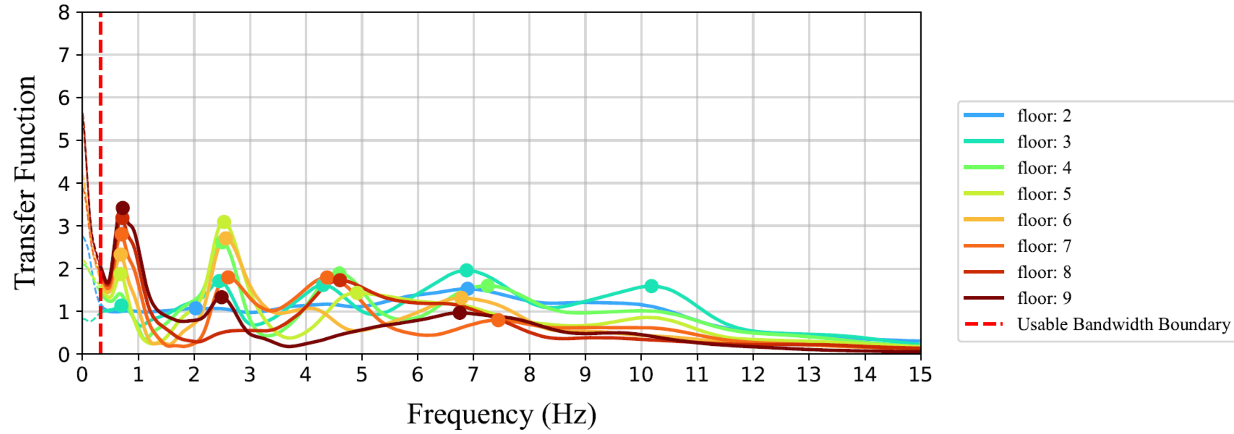

(a)

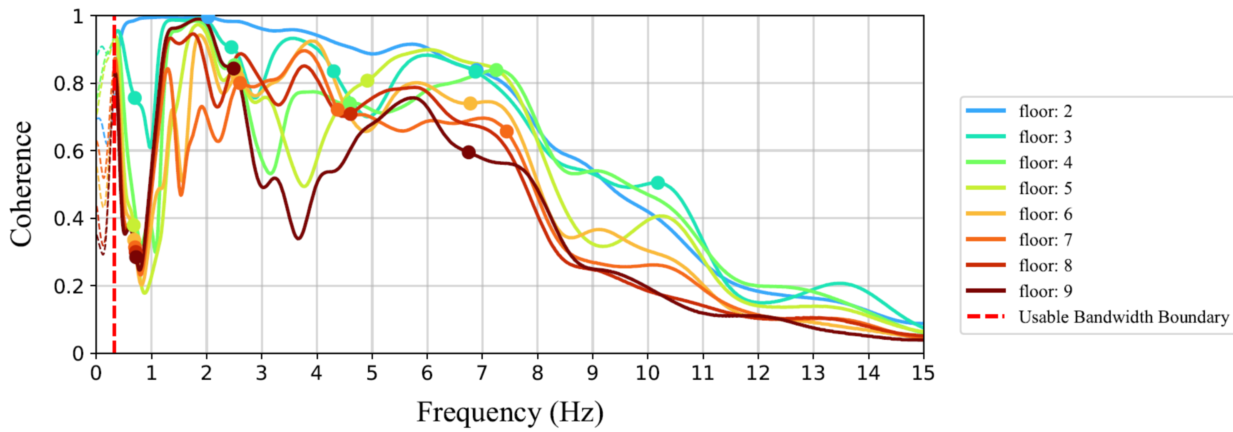

(b)

Figure D.23. a) Horizontal floor-to-base transfer function and b) magnitude-squared coherence for JPL 180 during the Ridgecrest earthquake. The dashed red line marks the lower usable bandwidth

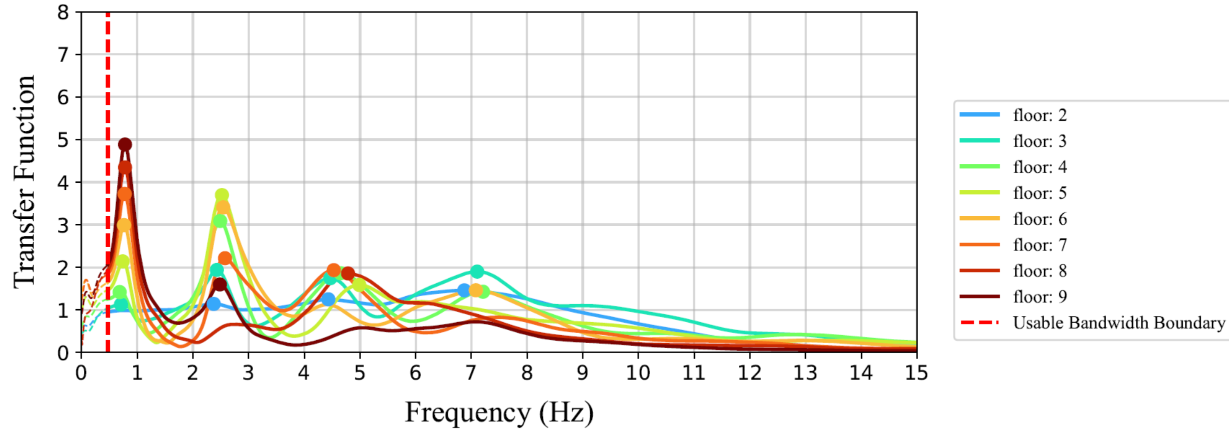

(a)

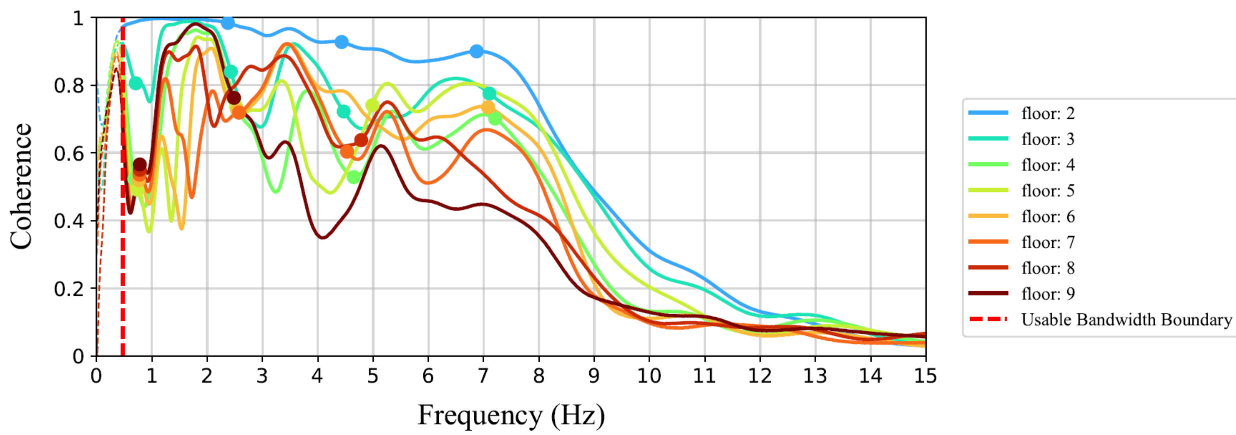

(b)

Figure D.24. a) Horizontal floor-to-base transfer function and b) magnitude-squared coherence for JPL 180 during the Searle Valley earthquake. The dashed red line marks the lower usable bandwidth

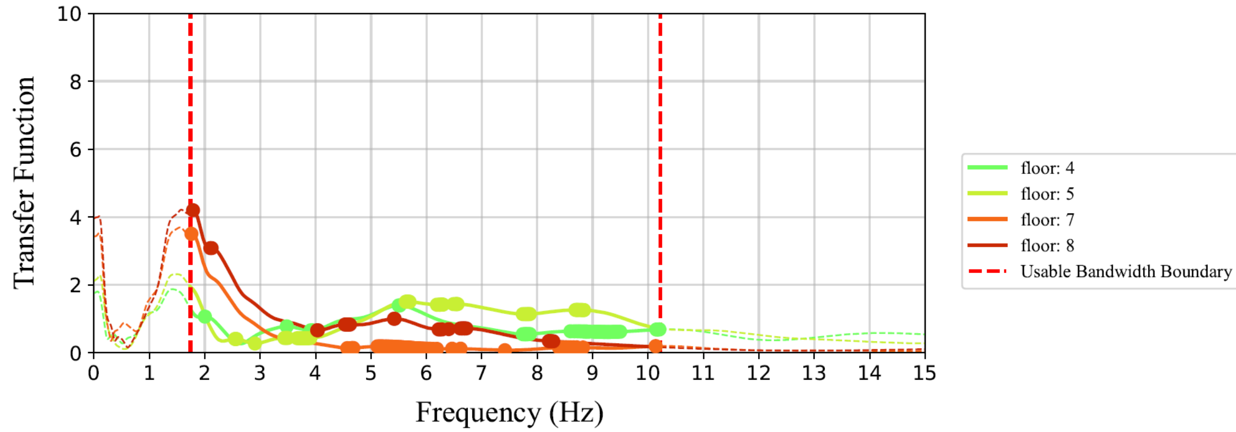

(a)

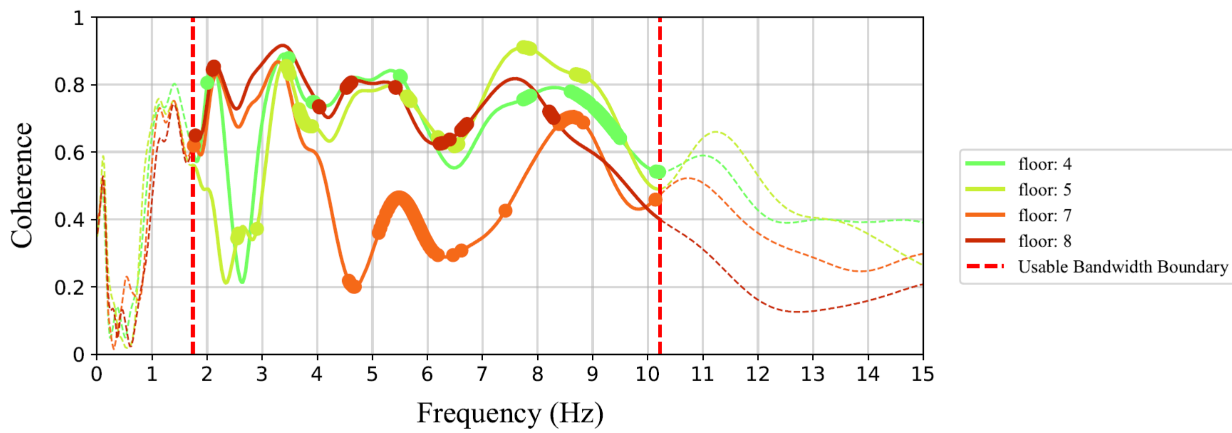

(b)

Figure D.25. a) Horizontal floor-to-base transfer function and b) magnitude-squared coherence for JPL 238 during the Pacoima earthquake. The dashed red line marks the lower usable bandwidth

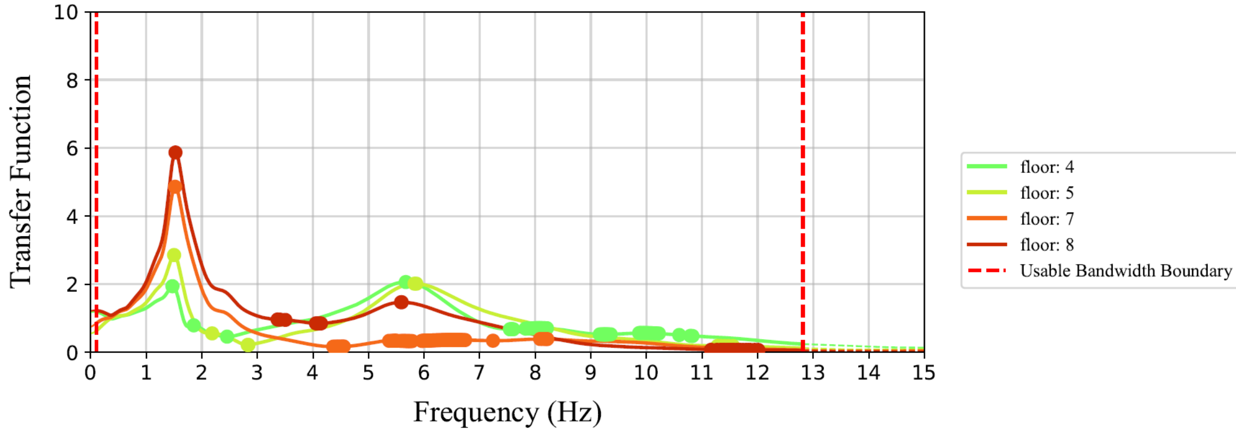

(a)

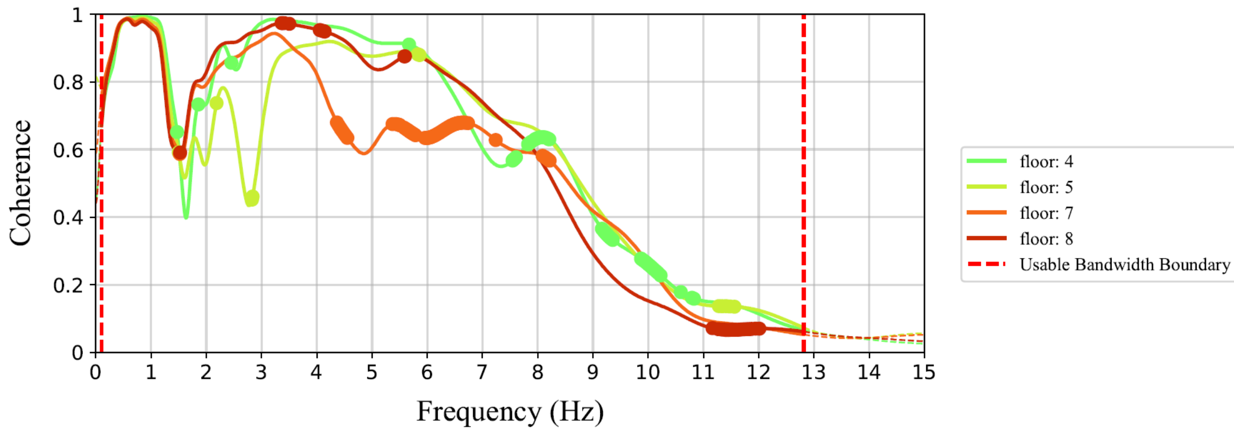

(b)

Figure D.26. a) Horizontal floor-to-base transfer function and b) magnitude-squared coherence for JPL 238 during the Ridgecrest earthquake. The dashed red line marks the lower usable bandwidth

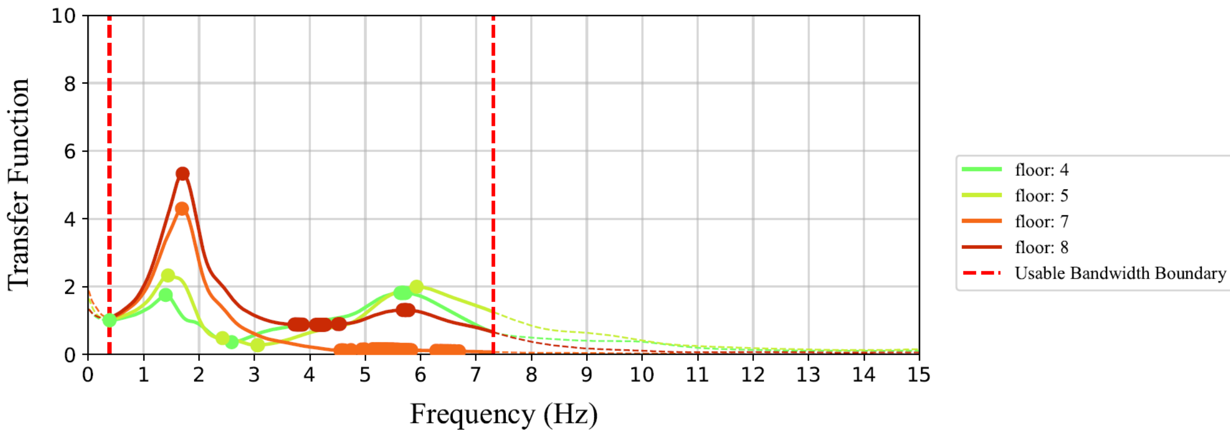

(a)

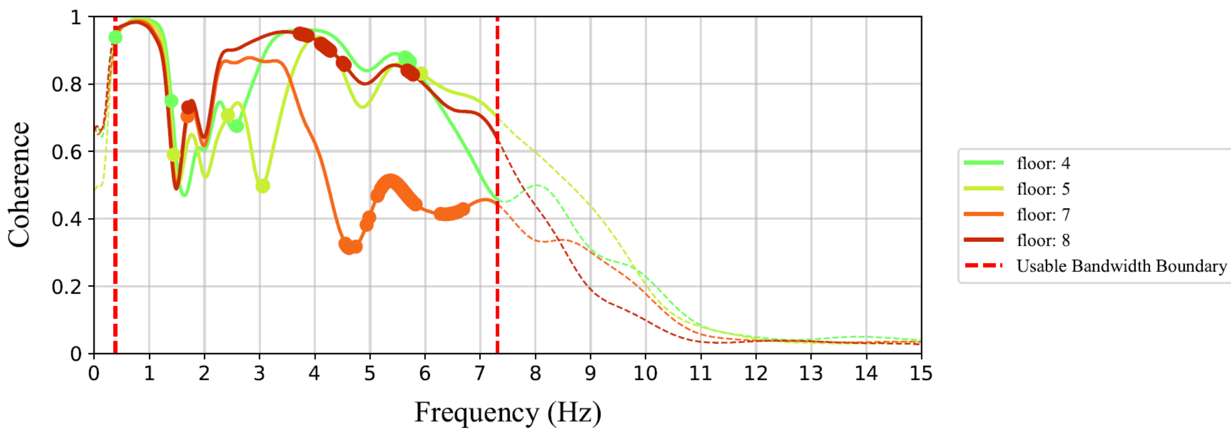

(b)

Figure D.27. a) Horizontal floor-to-base transfer function and b) magnitude-squared coherence for JPL 238 during the Searle Valley earthquake. The dashed red line marks the lower usable bandwidth

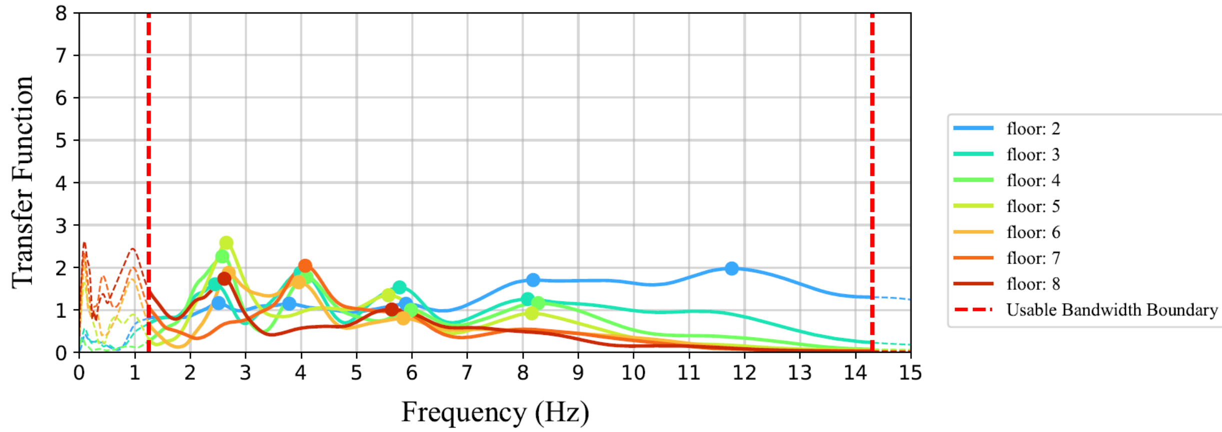

(a)

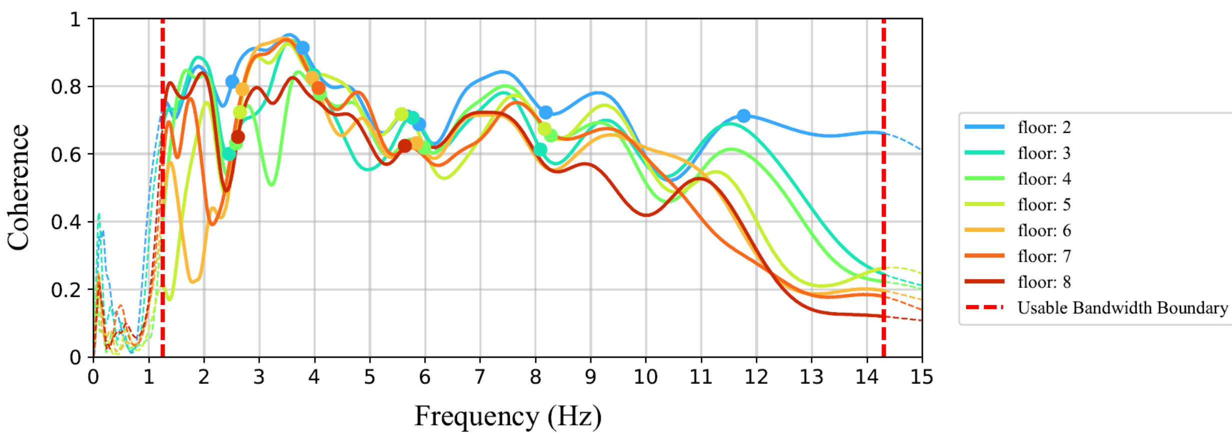

(b)

Figure D.28. a) Horizontal floor-to-base transfer function and b) magnitude-squared coherence for JPL 264 during the Pacoima earthquake. The dashed red line marks the lower usable bandwidth

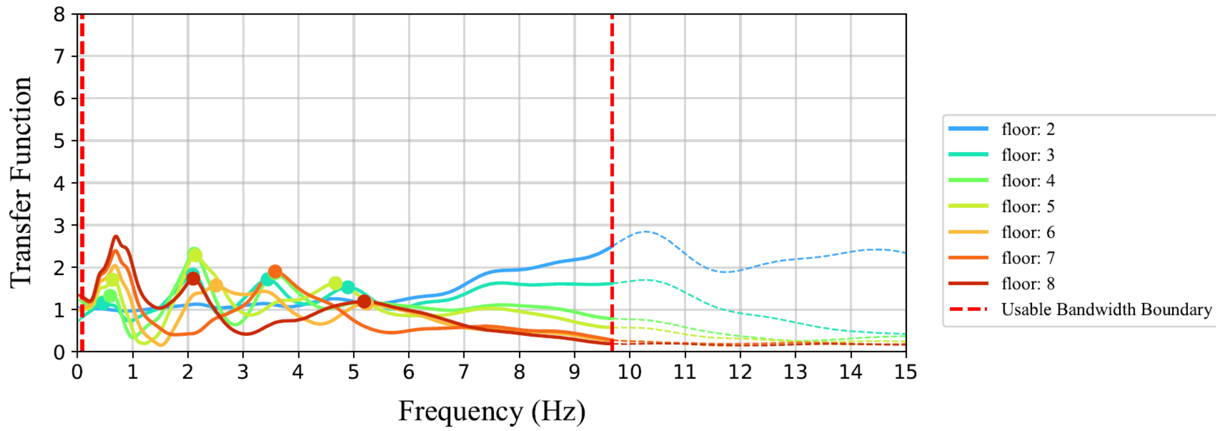

(a)

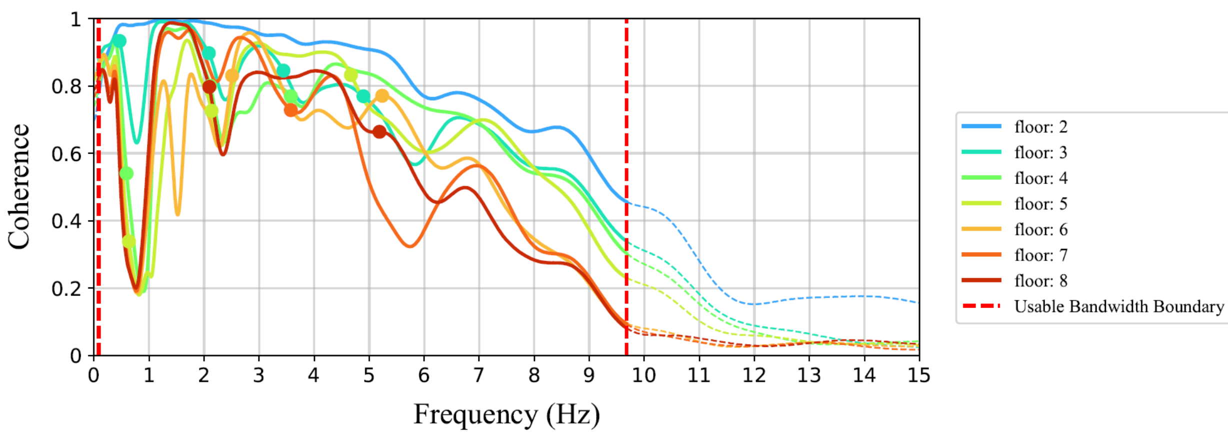

(b)

Figure D.29. a) Horizontal floor-to-base transfer function and b) magnitude-squared coherence for JPL 264 during the Ridgecrest earthquake. The dashed red line marks the lower usable bandwidth

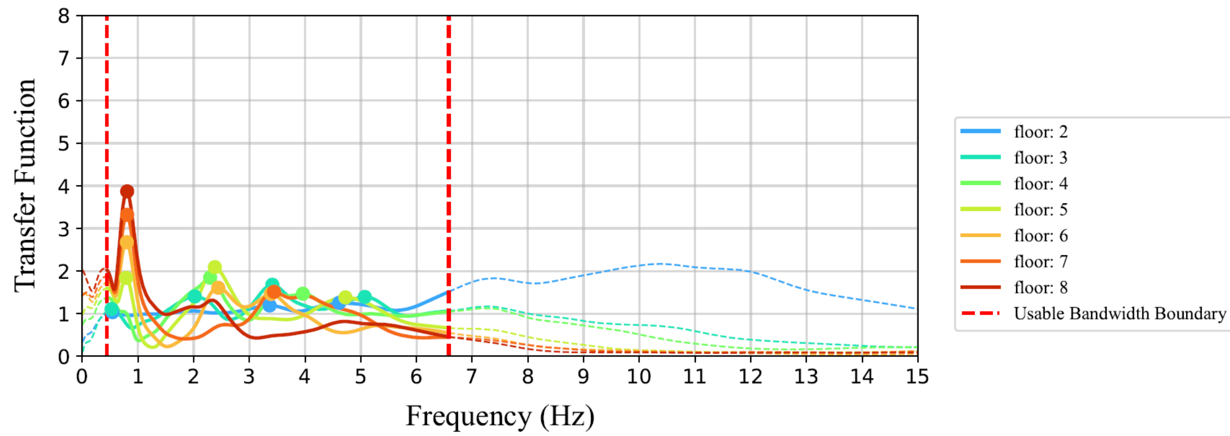

(a)

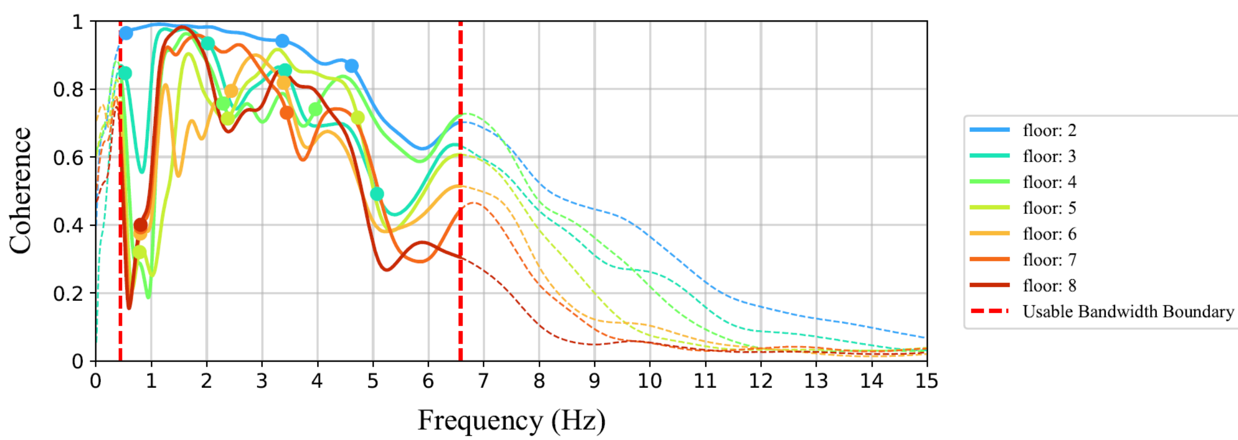

(b)

Figure D.30. a) Horizontal floor-to-base transfer function and b) magnitude-squared coherence for JPL 264 during the Searle Valley earthquake. The dashed red line marks the lower usable bandwidth

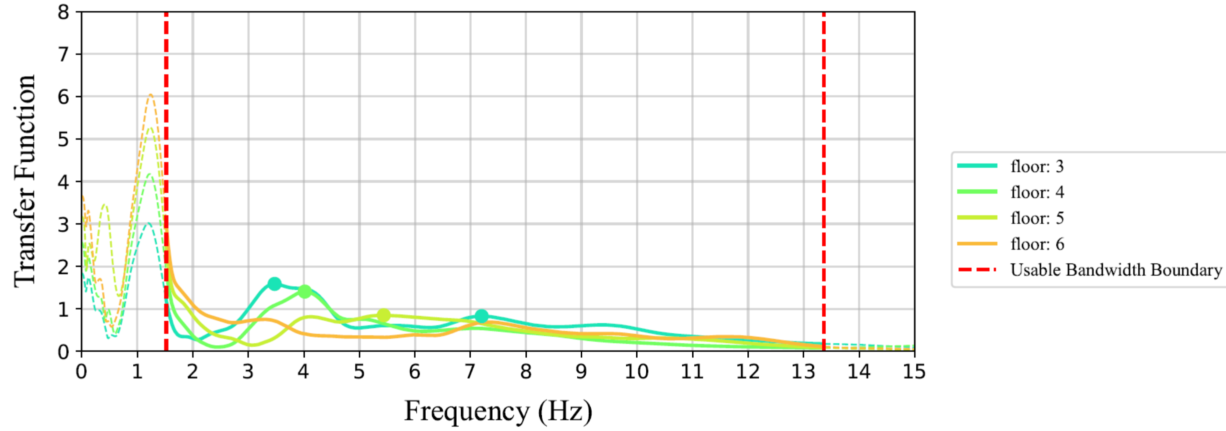

(a)

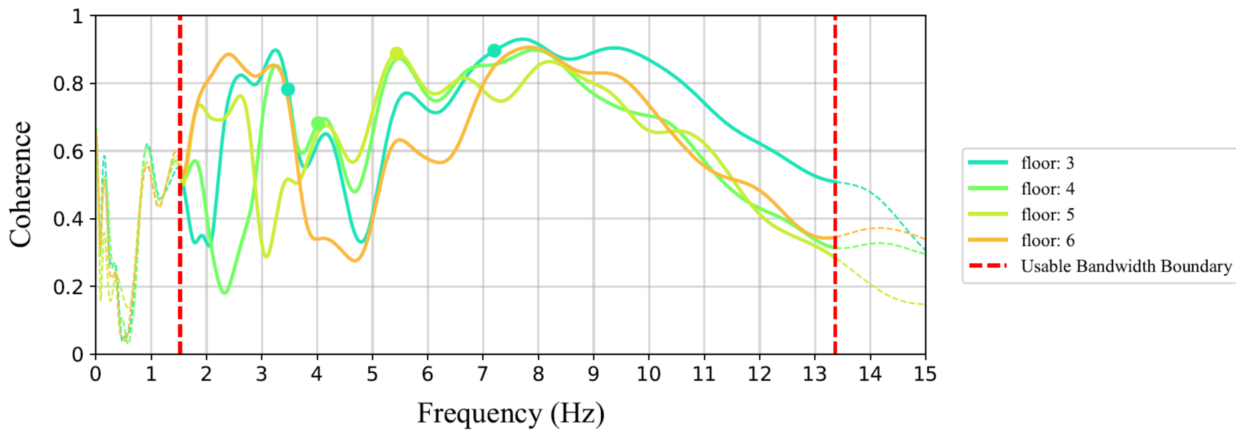

(b)

Figure D.31. a) Horizontal floor-to-base transfer function and b) magnitude-squared coherence for JPL 321 during the Pacoima earthquake. The dashed red line marks the lower usable bandwidth

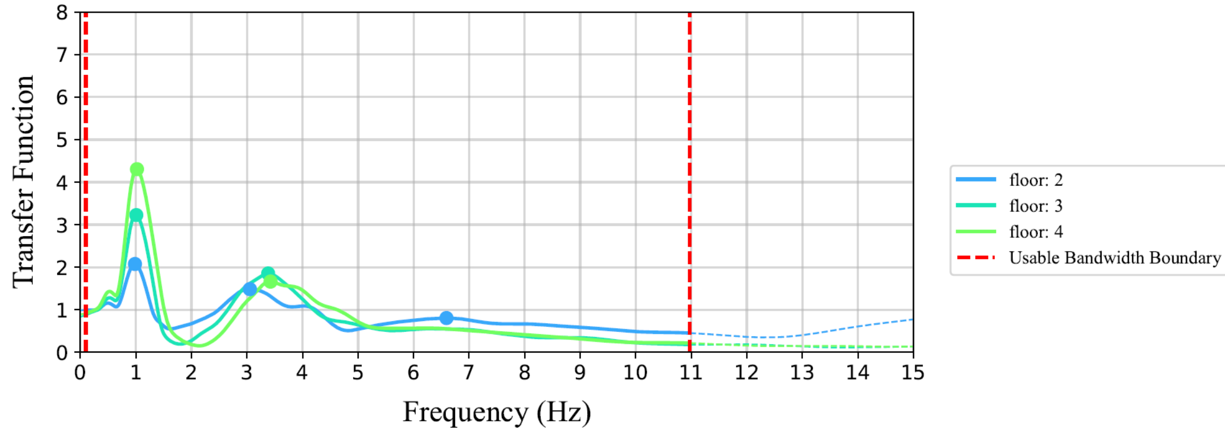

(a)

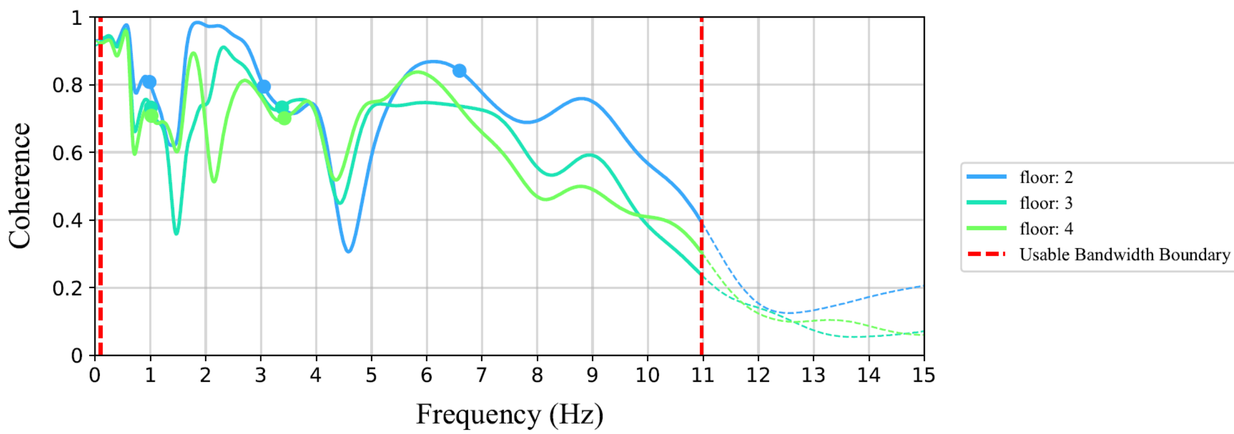

(b)

Figure D.32. a) Horizontal floor-to-base transfer function and b) magnitude-squared coherence for JPL 321 during the Ridgecrest earthquake. The dashed red line marks the lower usable bandwidth

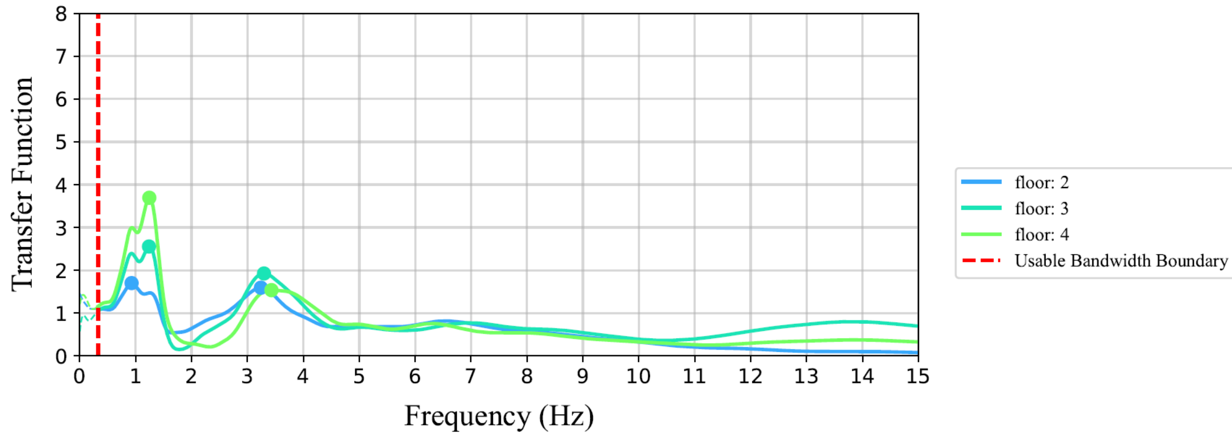

(a)

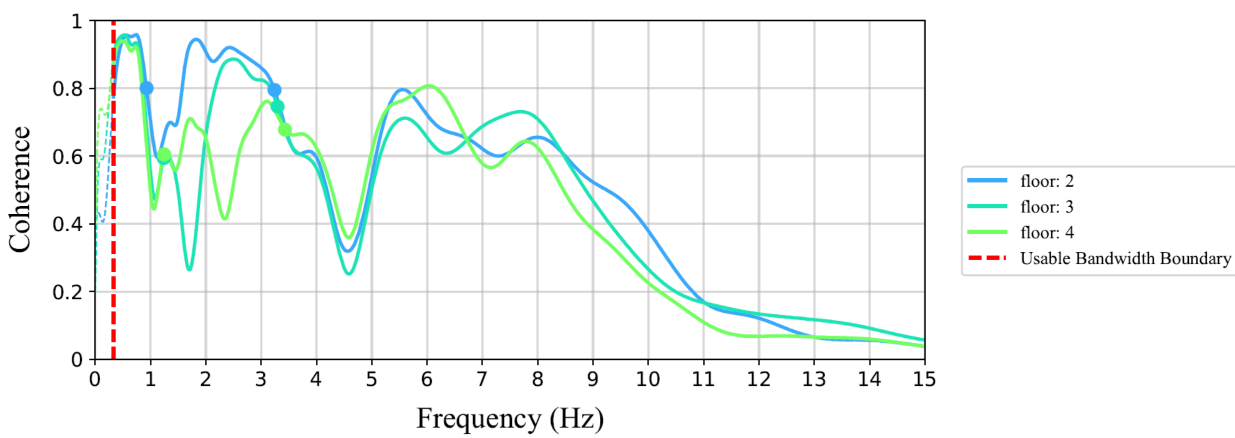

(b)

Figure D.33. a) Horizontal floor-to-base transfer function and b) magnitude-squared coherence for JPL 321 during the Searle Valley earthquake. The dashed red line marks the lower usable bandwidth

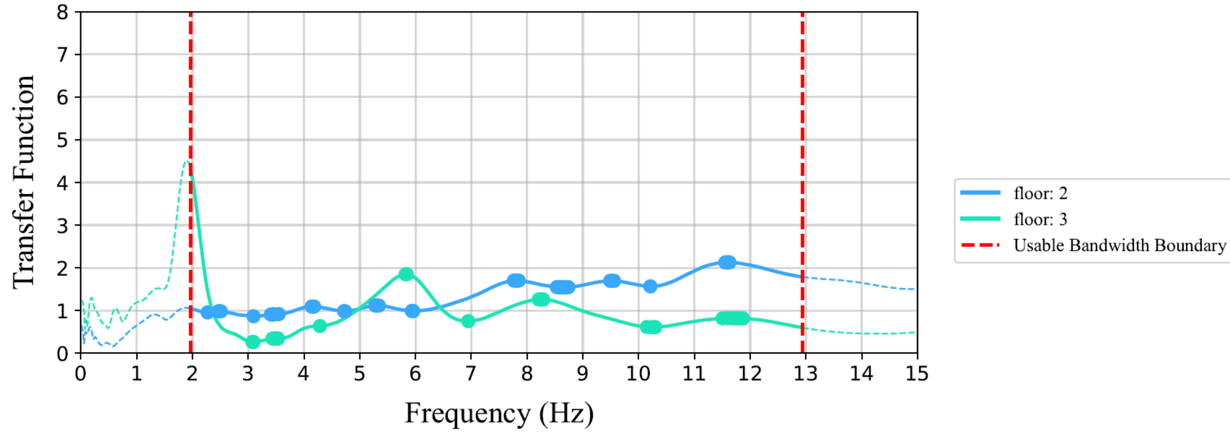

(a)

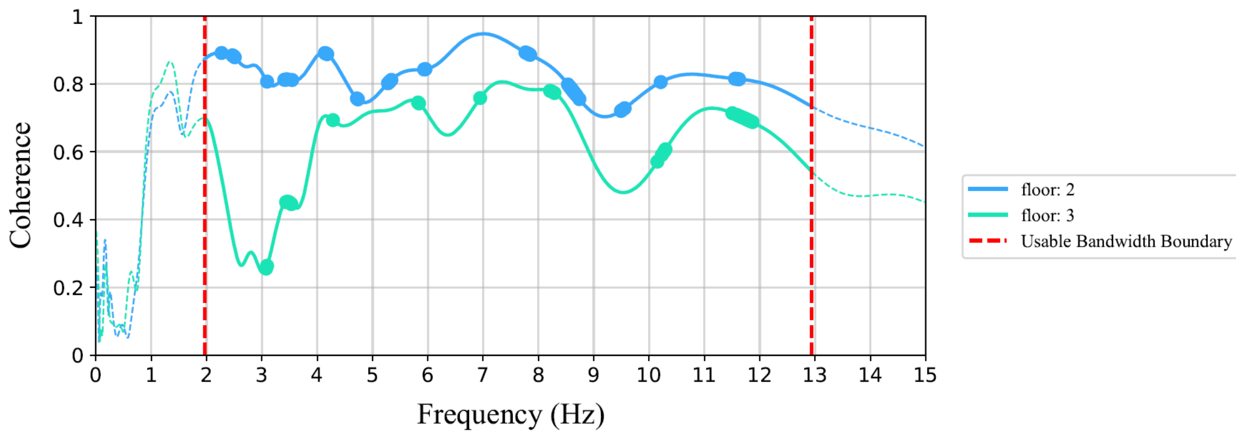

(b)

Figure D.34. a) Horizontal floor-to-base transfer function and b) magnitude-squared coherence for JPL 303 during the Pacoima earthquake. The dashed red line marks the lower usable bandwidth

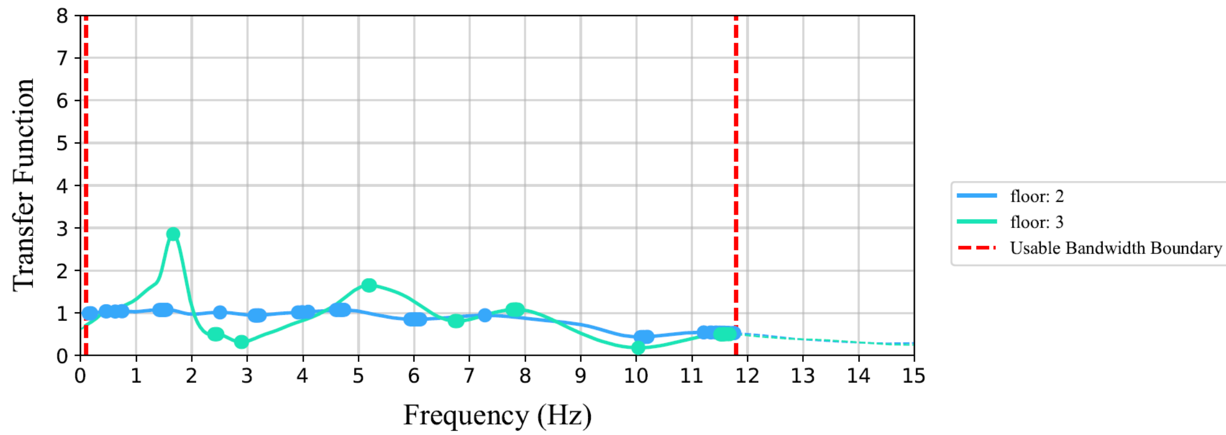

(a)

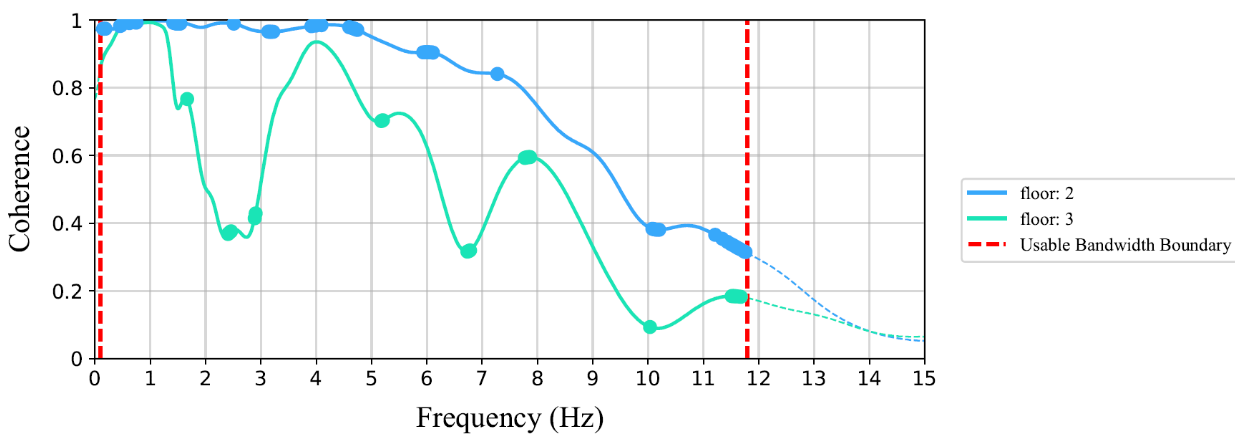

(b)

Figure D.35. a) Horizontal floor-to-base transfer function and b) magnitude-squared coherence for JPL 303 during the Ridgecrest earthquake. The dashed red line marks the lower usable bandwidth

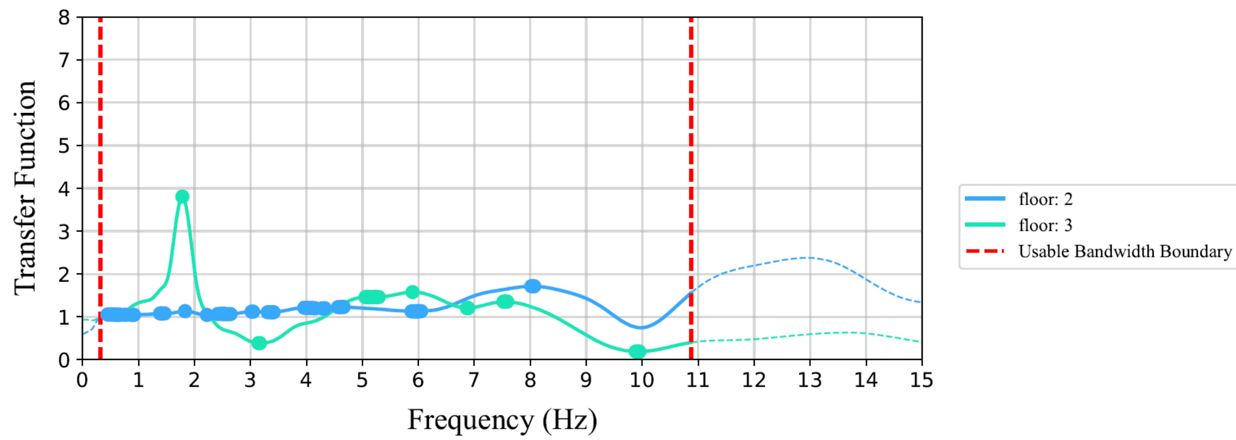

(a)

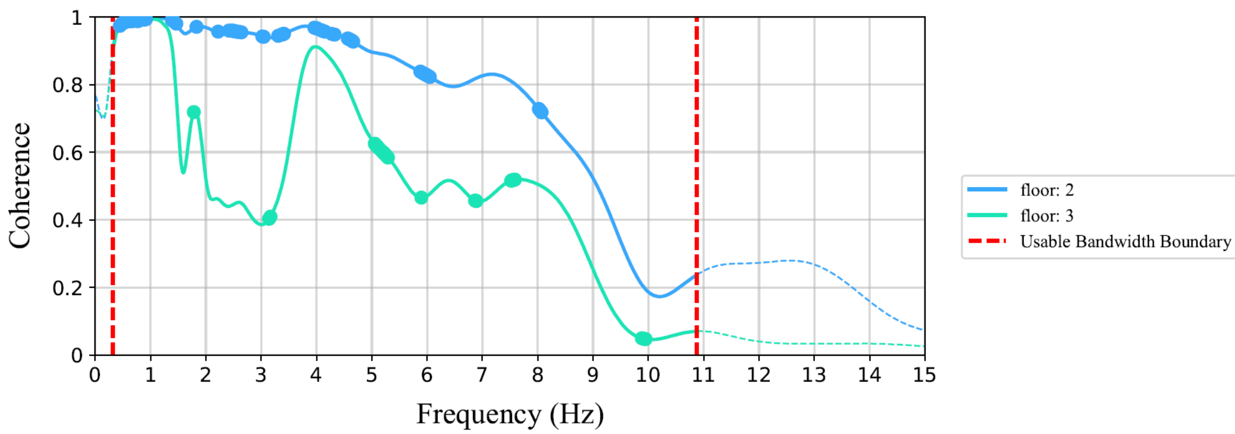

(b)

Figure D.36. a) Horizontal floor-to-base transfer function and b) magnitude-squared coherence for JPL 303 during the Searle Valley earthquake. The dashed red line marks the lower usable bandwidth

Appendix E. PFA vs. PSA(T=0.01s)

Table E.1. Summary of short-period validation statistics for each building in the horizontal direction

Statistic	JPL 180	JPL 183	JPL 238	JPL 264	JPL 303	JPL 321
Number of datapoints (n)	93	61	23	32	13	19
Pearson (r)	~ 1	~ 1	~ 1	~ 1	~ 1	~ 1
Spearman (ρ)	~ 1	~ 1	~ 1	~ 1	~ 1	~ 1
Slope of (PSA) on (PFA)	0.9992	0.9994	0.9990	0.9991	0.9982	0.9995
Intercept (g)	-1.4E-05	-1.6E-05	-1.3E-05	-1.0E-05	-2.5E-07	-1.7E-05
R^2	~ 1	~ 1	~ 1	~ 1	~ 1	~ 1
Mean ratio (PSA/PFA)	0.9981	0.9982	0.9983	0.9983	0.9982	0.9981
Median ratio (PSA/PFA)	0.9979	0.9984	0.9986	0.9985	0.9978	0.9981
frac_within_5pct	1	1	1	1	1	1

Table E.2. Summary of short-period validation statistics for each building in the vertical direction

Statistic	JPL 180	JPL 183	JPL 238	JPL 264	JPL 303	JPL 321
Number of datapoints (n)	93	61	25	32	13	19
Pearson (r)	~ 1	~ 1	~ 1	~ 1	~ 1	~ 1
Spearman (ρ)	~ 1	0.9999	~ 1	~ 1	0.9945	~ 1
Slope of (PSA) on (PFA)	0.9961	0.9970	0.9968	0.9976	0.9975	0.9958
Intercept (g)	2.5E-05	8.3E-06	8.2E-06	2.2E-06	2.7E-06	2.9E-05
R^2	~ 1	~ 1	~ 1	~ 1	~ 1	~ 1
Mean ratio (PSA/PFA)	0.9977	0.9977	0.9974	0.9977	0.9978	0.9972
Median ratio (PSA/PFA)	0.9975	0.9977	0.9974	0.9976	0.9969	0.9967
frac_within_5pct	1	1	1	1	1	1

Appendix F. Floor-by-floor Floor Response Spectra

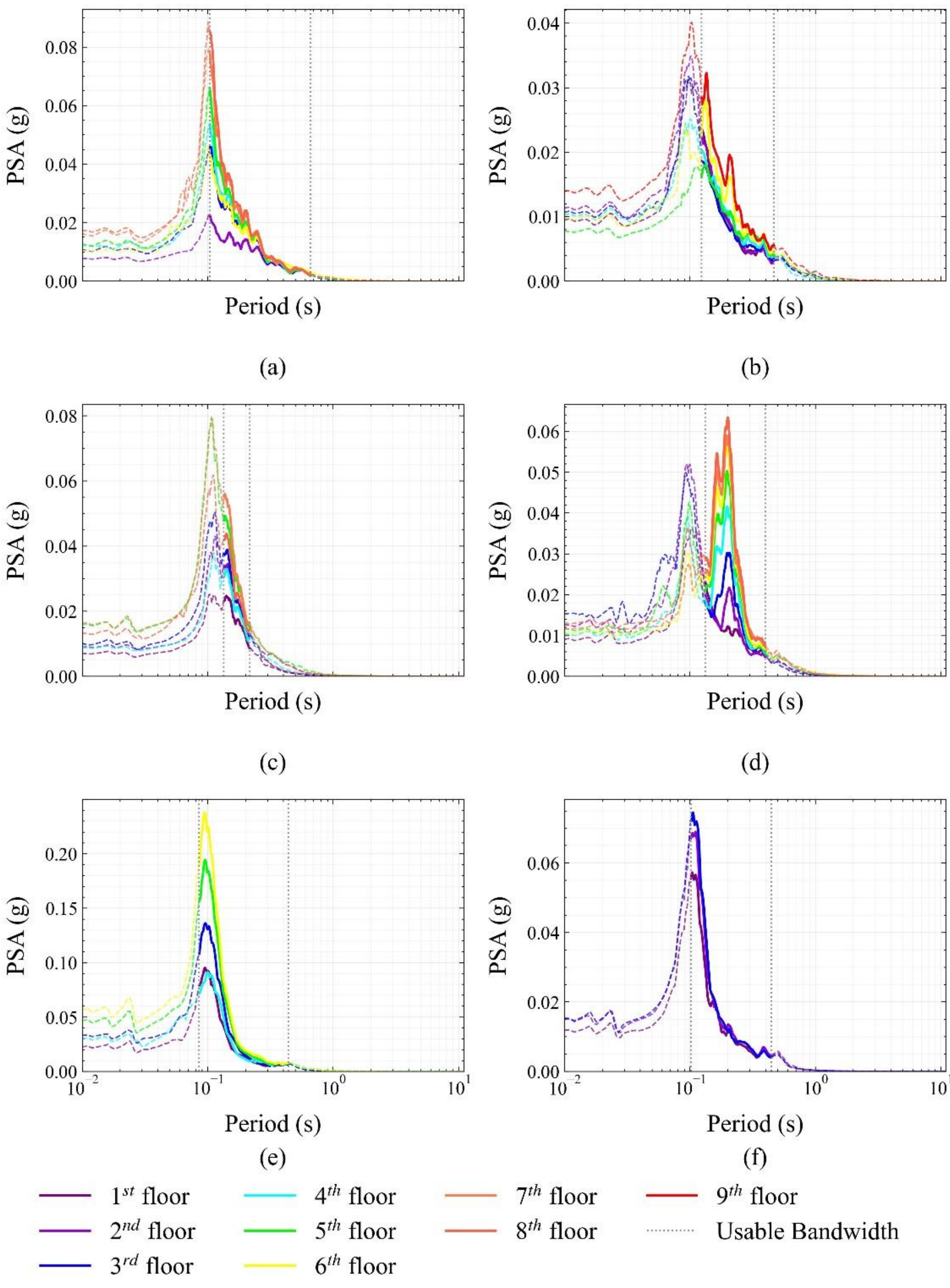

Figure F.1. Floor-by-floor VFRS plots for the Pacoima earthquake for a) JPL 180, b) JPL 183, c) JPL 238, d) JPL 264, e) JPL 321, and f) JPL 303

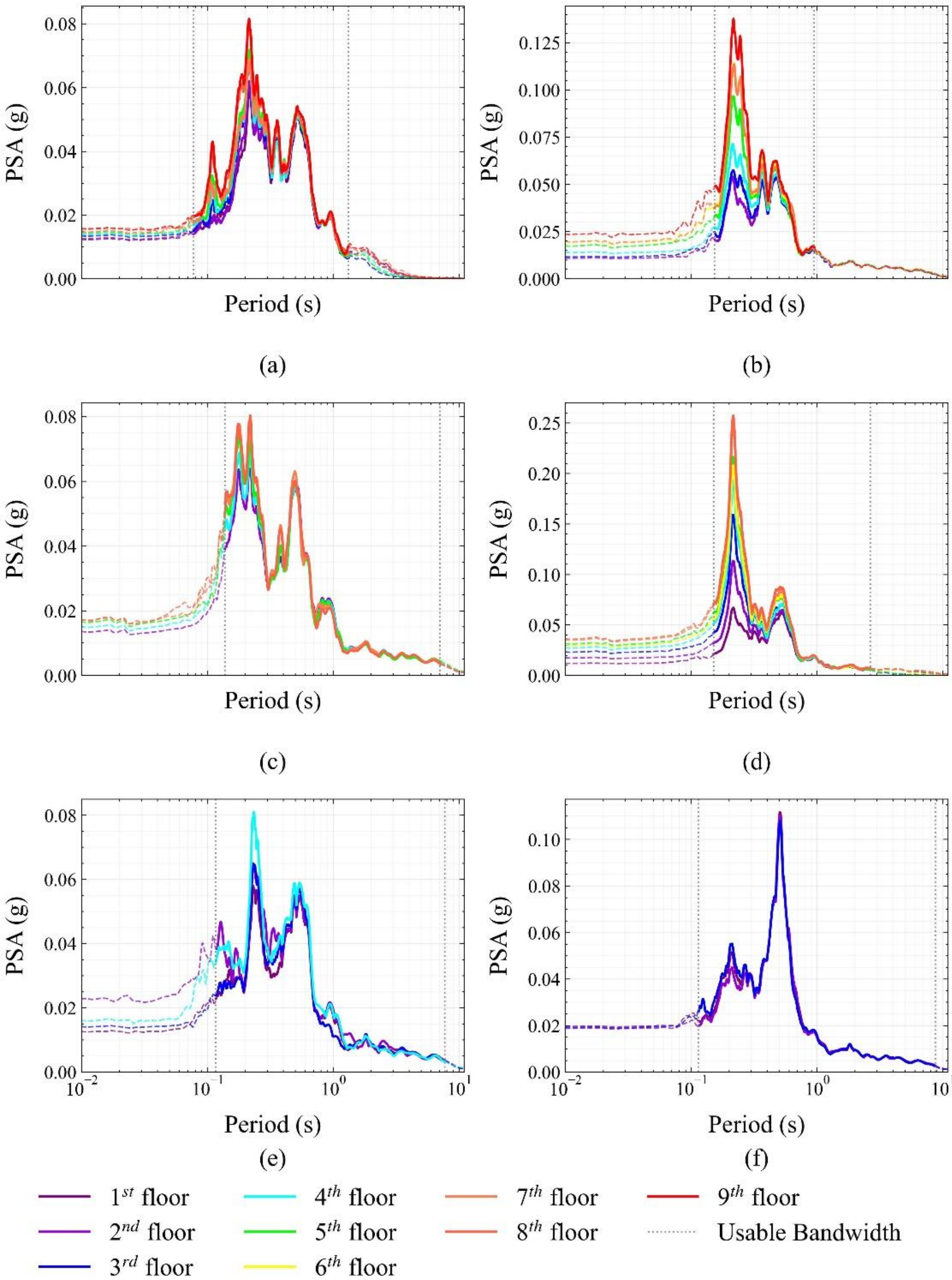

Figure F.2. Floor-by-floor VFRS plots for the Ridgecrest earthquake for a) JPL 180, b) JPL 183, c) JPL 238, d) JPL 264, e) JPL 321, and f) JPL 303

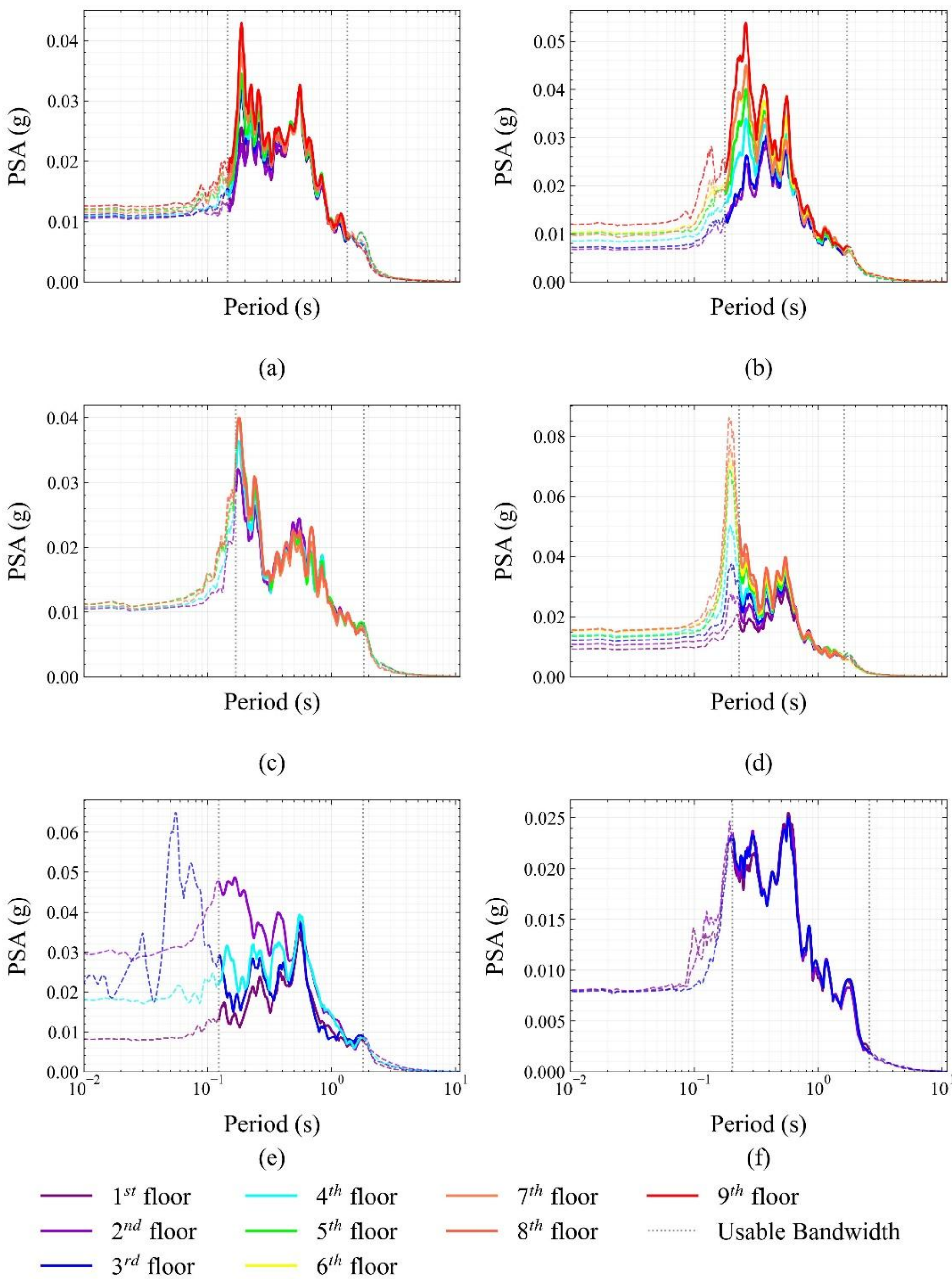

Figure F.3. Floor-by-floor VFRS plots for the Searle Valley earthquake for a) JPL 180, b) JPL 183, c) JPL 238, d) JPL 264, e) JPL 321, and f) JPL 303

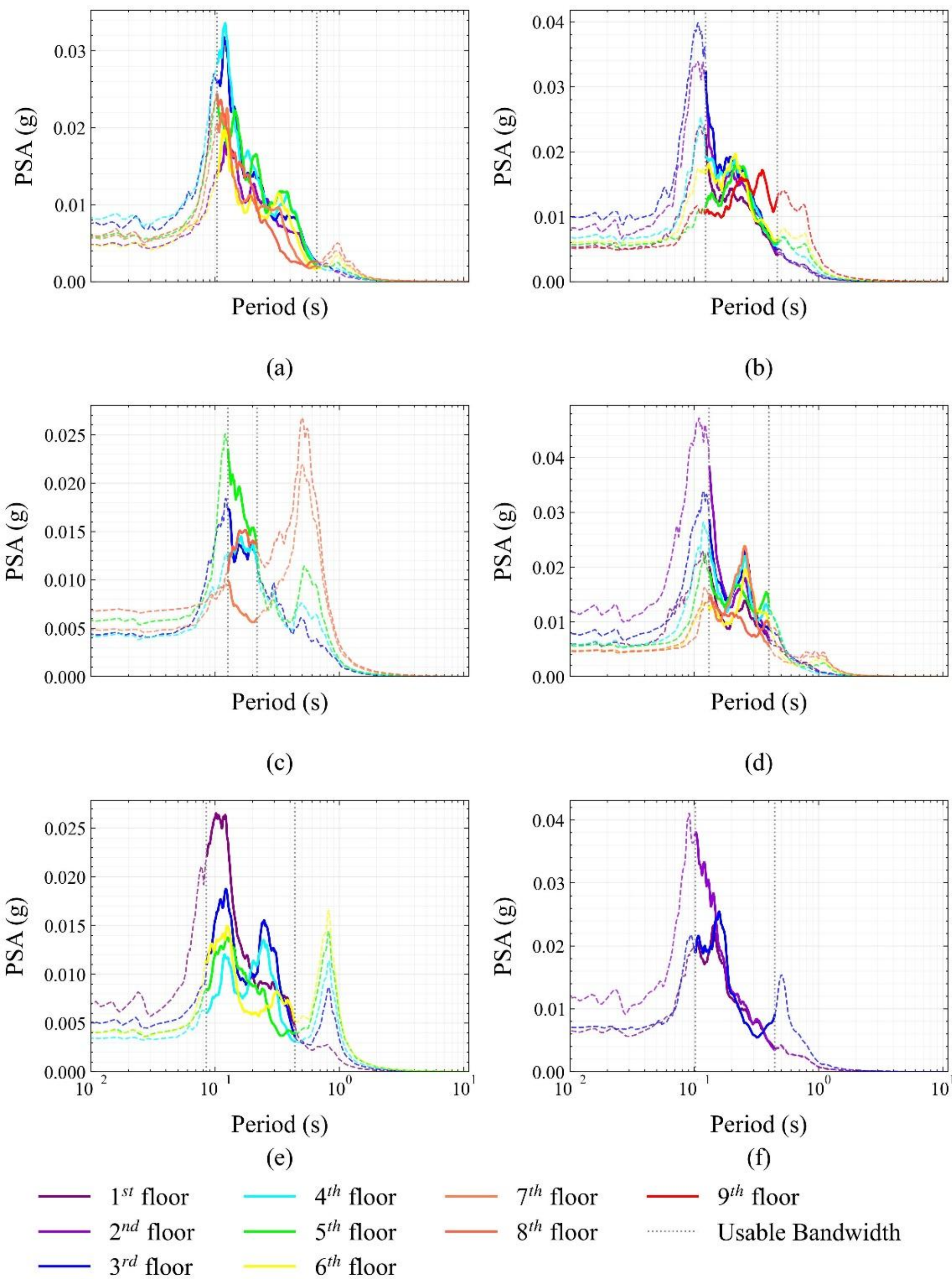

Figure F.4. Floor-by-floor HFRS plots for the Pacoima earthquake for a) JPL 180, b) JPL 183, c) JPL 238, d) JPL 264, e) JPL 321, and f) JPL 303

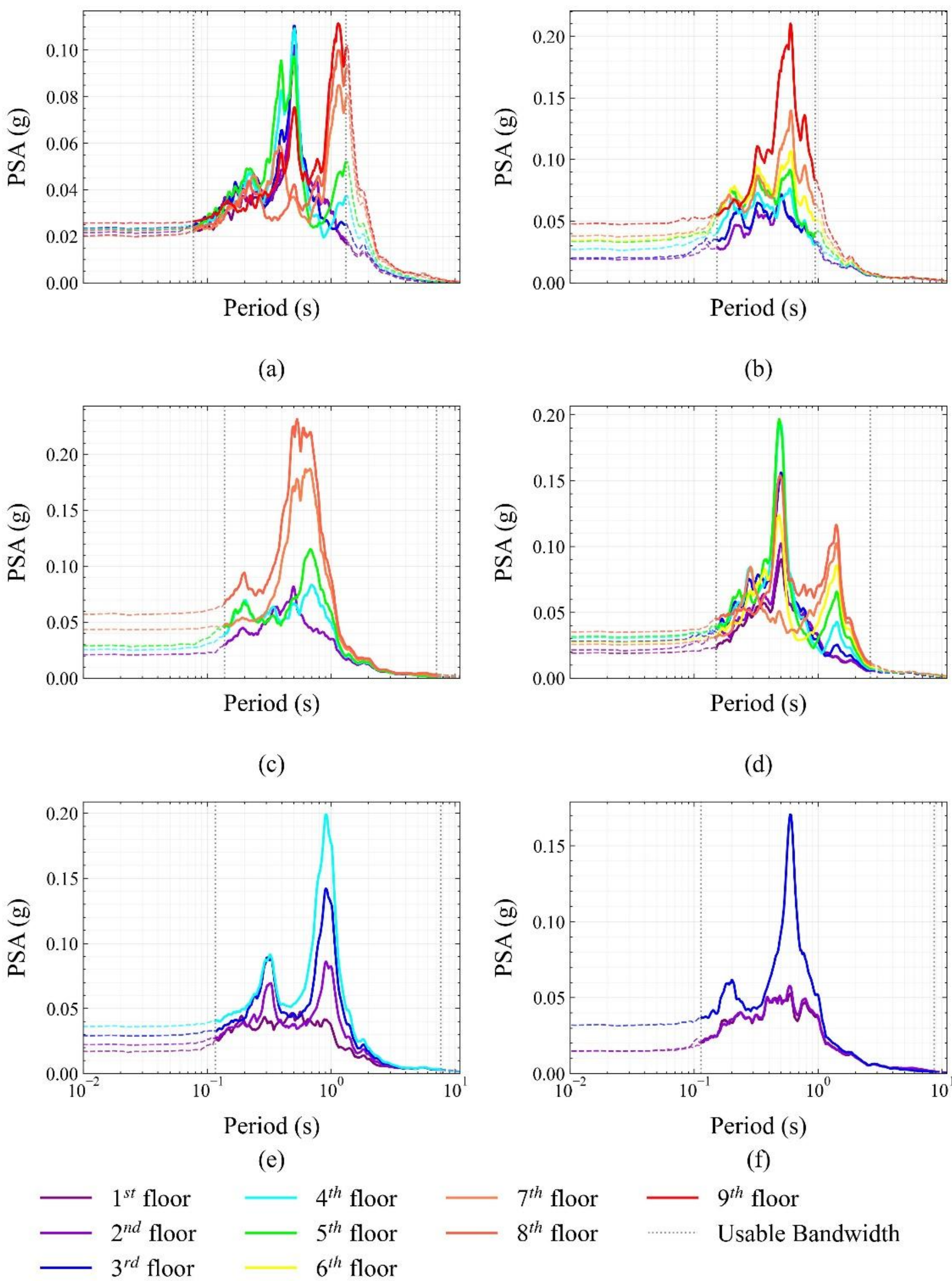

Figure F.5. Floor-by-floor HFRS plots for the Ridgecrest earthquake for a) JPL 180, b) JPL 183, c) JPL 238, d) JPL 264, e) JPL 321, and f) JPL 303

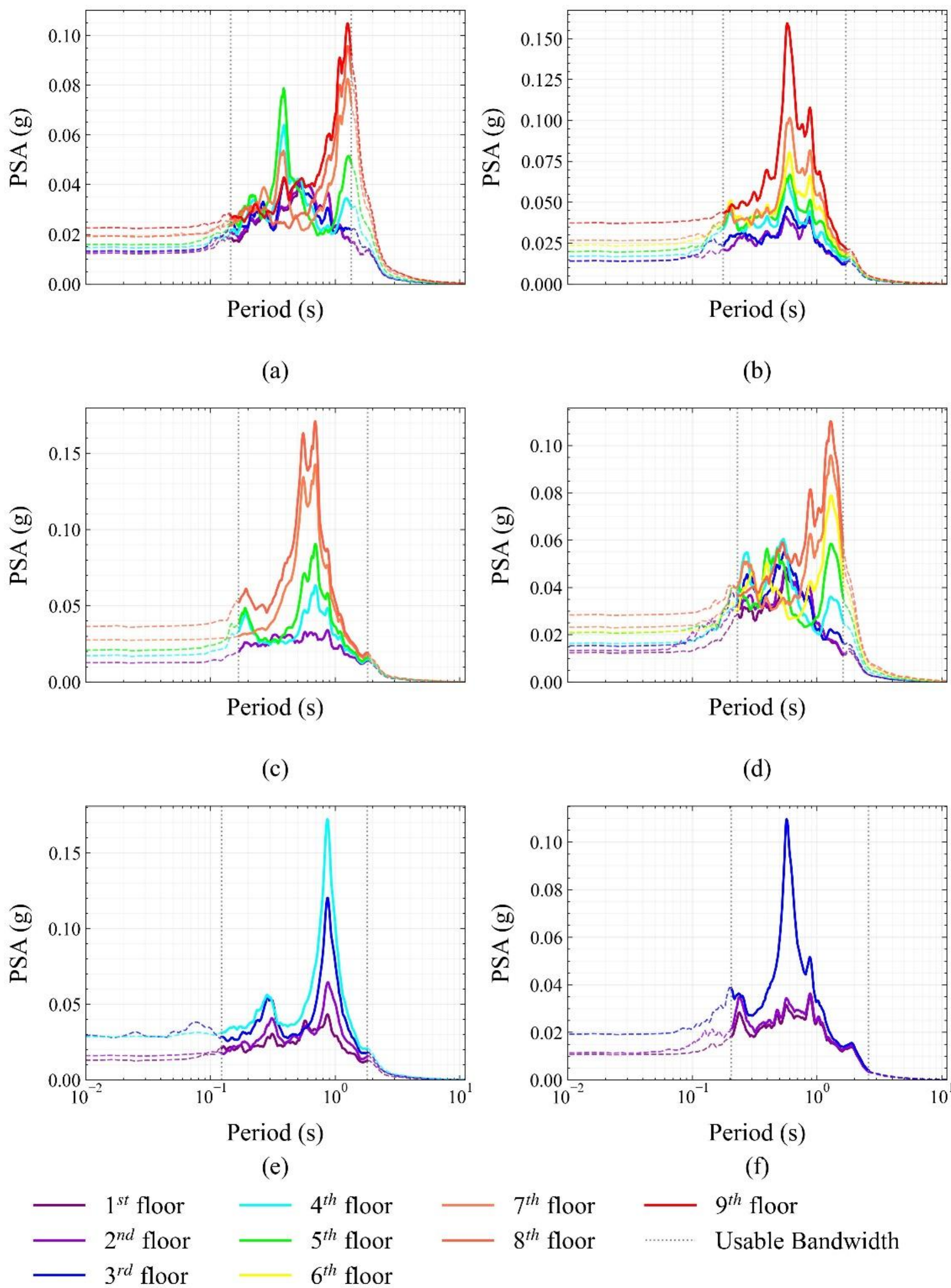

Figure F.6. Floor-by-floor HFRS plots for the Searle Valley earthquake for a) JPL 180, b) JPL 183, c) JPL 238, d) JPL 264, e) JPL 321, and f) JPL 303

References

Abdelbarr, M. H., Kohler, M. D., & Masri, S. F. (2023). Structural identification of a 52-story high-rise in downtown Los Angeles based on short-term wind vibration measurements. Journal of Structural Engineering, 149(1), 05022002.

Abrahamson, N., & Litehiser, J. (1989). Attenuation of vertical peak acceleration. Bulletin of the Seismological Society of America, 79(3), 549-580.

Abrahamson, N. A., Silva, W. J., & Kamai, R. (2014). Summary of the ASK14 ground motion relation for active crustal regions. Earthquake Spectra, 30(3), 1025-1055.

Acosta, A. A., Miranda, E., & Deierlein, G. G. (2023). Response spectrum method for structures subjected to vertical ground motions: Absolute acceleration method. Earthquake Engineering & Structural Dynamics, 52(15), 4820-4841.

Akaike, H. (1974). A new look at the statistical model identification. IEEE Transactions on Automatic Control, 19(6), 716-723.

Al Atik, L., Gregor, N., Bozorgnia, Y., & Mazzoni, S. (2022). GIRS 2022-12: Directivity-Based Probabilistic Seismic Hazard Analysis for the State of California: Report 1, No-Directivity Baseline Case. Natural Hazards Risk and Resiliency Research Center (NHR3), Issue. https://doi.org/10.34948/N32010

Al Atik, L., Gregor, N., Mazzoni, S., & Bozorgnia, Y. (2023). GIRS 2023-05: Directivity-Based Probabilistic Seismic Hazard Analysis For The State Of California: Report 2, Directivity Implementation. Natural Hazards Risk and Resiliency Research Center (NHR3), Issue. https://doi.org/10.34948/N3KS3B

Alonso-Rodríguez, A., & Miranda, E. (2016). Dynamic behavior of buildings with non-uniform stiffness along their height assessed through coupled flexural and shear beams. Bulletin of Earthquake Engineering, 14(12), 3463-3483.

Anajafi, H., & Medina, R. A. (2018). Evaluation of ASCE 7 equations for designing acceleration-sensitive nonstructural components using data from instrumented buildings. Earthquake Engineering & Structural Dynamics, 47(4), 1075-1094.

Anajafi, H., & Medina, R. A. (2019). Lessons learned from evaluating the responses of instrumented buildings in the United States: the effects of supporting building characteristics on floor response spectra. Earthquake Spectra, 35(1), 159-191.

Ancheta, T. D., Darragh, R. B., Stewart, J. P., Seyhan, E., Silva, W. J., Chiou, B. S.-J., Wooddell, K. E., Graves, R. W., Kottke, A. R., Boore, D. M., Kishida, T., & Donahue, J. L. (2014). NGA-West2 database. Earthquake Spectra, 30(3), 989-1005.

Anderson, J. C., & Bertero, V. V. (1973). Effects of gravity loads and vertical ground acceleration on the seismic response of multistory frames. Memorias, V World Conference on Earthquake Engineering,

Applied Technology Council. (1978). Tentative provisions for the development of seismic regulations for buildings: A cooperative effort with the design professions, building code interests, and the research community (ATC 3-06). US Department of Commerce, National Bureau of Standards.

ASCE7. (2024). ASCE 7 Hazard Tool. https://asce7hazardtool.online

ASCE. (2016). Minimum Design Loads for Buildings and Other Structures (ASCE/SEI 7-16), American Society of Civil Engineers, Reston, VA. In American Society of Civil Engineers (pp. 6-15).

ASCE. (2022). Minimum Design Loads and Associated Criteria for Buildings and Other Structures, ASCE/SEI 7-22. American Society of Civil Engineers.

Banerji, S. K. (1925). VI. On the depth of earthquake focus. The London, Edinburgh, and Dublin Philosophical Magazine and Journal of Science, 49(289), 65-80.

Bendat, J. S., & Piersol, A. G. (1993). Engineering applications of correlation and spectral analysis (2nd ed.). New York: Wiley.

Bendat, J. S., & Piersol, A. G. (2011). Random data: Analysis and Measurement Procedures. John Wiley & Sons.

Biot, M. A. (1943). Analytical and experimental methods in engineering seismology. Transactions of the American Society of Civil Engineers, 108(1), 365-385.

Blake, A. (1933). The recording of strong seismic motion. Bulletin of the Seismological Society of America, 23(3), 111-127.

Bolourani, A., Burton, H. V., & Bozorgnia, Y. (2025). Evaluation of Vertical Seismic Load Effects Specified in the United States Building Code. Journal of Structural Engineering, 151(12), 04025224. https://doi.org/10.1061/JSENDH.STENG-14498

Boore, D. M. (2005). On pads and filters: Processing strong-motion data. Bulletin of the Seismological Society of America, 95(2), 745-750.

Boore, D. M., Stewart, J. P., Seyhan, E., & Atkinson, G. M. (2014). NGA-West2 equations for predicting PGA, PGV, and 5% damped PSA for shallow crustal earthquakes. Earthquake Spectra, 30(3), 1057-1085.

Bozorgnia, Y., & Bertero, V. V. (2004). Earthquake engineering: from engineering seismology to performance-based engineering. CRC Press.

Bozorgnia, Y., & Campbell, K. W. (2004). The vertical-to-horizontal response spectral ratio and tentative procedures for developing simplified V/H and vertical design spectra. Journal of Earthquake Engineering, 8(02), 175-207.

Bozorgnia, Y., & Campbell, K. W. (2016). Ground motion model for the vertical-to-horizontal (V/H) ratios of PGA, PGV, and response spectra. Earthquake Spectra, 32(2), 951-978.

Bozorgnia, Y., Mahin, S. A., & Brady, A. G. (1998). Vertical response of twelve structures recorded during the Northridge earthquake. Earthquake Spectra, 14(3), 411-432.

Bozorgnia, Y., Niazi, M., & Campbell, K. W. (1995). Characteristics of free-field vertical ground motion during the Northridge earthquake. Earthquake Spectra, 11(4), 515-525.

Bracewell, R. N. (1986). The Fourier transform and its applications (Vol. 31999). McGraw-hill New York.

Brigham, E. O. (1988). The fast Fourier transform and its applications. Prentice-Hall, Inc.

Bruneau, M., Chang, S. E., Eguchi, R. T., Lee, G. C., O'Rourke, T. D., Reinhorn, A. M., Shinozuka, M., Tierney, K., Wallace, W. A. and Von Winterfeldt, D. (2003). A framework to quantitatively assess and enhance the seismic resilience of communities. Earthquake Spectra, 19(4), 733-752.

Campbell, K. W., & Bozorgnia, Y. (2014). NGA-West2 ground motion model for the average horizontal components of PGA, PGV, and 5% damped linear acceleration response spectra. Earthquake Spectra, 30(3), 1087-1115.

Chaudhuri, S. R., & Hutchinson, T. C. (2004). Distribution of peak horizontal floor acceleration for estimating nonstructural element vulnerability. 13th World Conference on Earthquake Engineering.

Chen, C. I. (2023). A Study of the Effect of Vertical Ground Motions on Tall Reinforced Concrete Buildings [Doctoral dissertation, University of California, Berkeley]. eScholarship. https://escholarship.org/uc/item/5p26s932

Chopra, A. K. (2000). Dynamics of Structures: Theory and Applications to Earthquake Engineering. Prentice Hall / Pearson.

Clayton, J. S., & Medina, R. A. (2012). Proposed method for probabilistic estimation of peak component acceleration demands. Earthquake Spectra, 28(1), 55-75.

Clayton, R.W., Heaton, T.H., Chandy, M., Krause, A., Kohler, M.D., Bunn, J., Guy, R., Olson, M., Faulkner, M., Cheng, M.H., Strand, L., Chandy, R., Obenshain, D., Liu, A.H., & Aivazis, M.A. (2011). Community seismic network. Annals of Geophysics, 54(6), 738-747.

Clayton, R. W., Heaton, T., Kohler, M., Chandy, M., Guy, R., & Bunn, J. (2015). Community seismic network: A dense array to sense earthquake strong motion. Seismological Research Letters, 86(5), 1354-1363.

Clayton, R. W., Kohler, M., Guy, R., Bunn, J., Heaton, T., & Chandy, M. (2020). CSN-LAUSD network: A dense accelerometer network in Los Angeles Schools. Seismological Research Letters, 91(2A), 622-630.

Clough, R. W., & Penzien, J. (1993). Dynamics of Structures. McGraw-Hill.

Community Seismic Network. http://csn.caltech.edu/

Computers and Structures, I. (2023). ETABS (Version 21) [Computer software]. Computers and Structures, Inc. https://www.csiamerica.com/products/etabs

Cooley, J. W., & Tukey, J. W. (1965). An algorithm for the machine calculation of complex Fourier series. Mathematics of Computation, 19(90), 297-301.

Departments of the Army (1986). Seismic design guidelines for essential buildings (Departments of the Army (TM 5-809-10-1), Navy (NAVFAC P355. 1), and the Air Force (AFM 88-3, Chapter 13, Section A), Issue.

Di Sarno, L., Elnashai, A., & Manfredi, G. (2011). Assessment of RC columns subjected to horizontal and vertical ground motions recorded during the 2009 L'Aquila (Italy) earthquake. Engineering structures, 33(5), 1514-1535.

Douglas, J., & Boore, D. M. (2011). High-frequency filtering of strong-motion records. Bulletin of Earthquake Engineering, 9(2), 395-409.

Duhamel, P., & Vetterli, M. (1990). Fast Fourier transforms: a tutorial review and a state of the art. Signal Processing, 19(4), 259-299.

Evans, J. R., Hamstra, R. H. Jr., Kündig, C., Camina, P., & Rogers, J. A. (2005). TREMOR: A wireless MEMS accelerograph for dense arrays. Earthquake Spectra, 21(1), 91-124.

Fathali, S., & Lizundia, B. (2011). Evaluation of current seismic design equations for nonstructural components in tall buildings using strong motion records. The Structural Design of Tall and Special Buildings, 20, 30-46.

Federal Emergency Management Agency. (2009). NEHRP Recommended Seismic Provisions for New Buildings and Other Structures . Federal Emergency Management Agency (FEMA P-750).

Field, C. A., & Welsh, A. H. (2007). Bootstrapping clustered data. Journal of the Royal Statistical Society Series B: Statistical Methodology, 69(3), 369-390.

Filiatrault, A., Perrone, D., Merino, R. J., & Calvi, G. M. (2021). Performance-based seismic design of nonstructural building elements. Journal of Earthquake Engineering, 25(2), 237-269.

Francis, T., Hendry, B., & Sullivan, T. (2017). Vertical spectral demands on building elements induced by earthquake excitation. New Zealand Society for Earthquake Engineering Annual Conference, Wellington, New Zealand,

Ghahari, S. F., Jahankhah, H., & Ghannad, M. A. (2010). Study on elastic response of structures to near-fault ground motions through record decomposition. Soil Dynamics and Earthquake Engineering, 30(7), 536-546.

Goldstein, P., Dodge, D., Firpo, M., & Minner, L. (2003). SAC2000: Signal processing and analysis tools for seismologists and engineers. The IASPEI international handbook of earthquake and engineering seismology, 81, 1613-1620.

Goulet, C. A., Kishida, T., Ancheta, T. D., Cramer, C. H., Darragh, R. B., Silva, W. J., Hashash, Y. M. A., Harmon, J., Parker, G. A., Stewart, J. P., & Youngs, R. R. (2021). PEER NGA-East database. Earthquake Spectra, 37(1_suppl), 1331-1353. https://doi.org/10.1177/87552930211015695

Gremer, N., Adam, C., Medina, R. A., & Moschen, L. (2019). Vertical peak floor accelerations of elastic moment-resisting steel frames. Bulletin of Earthquake Engineering, 17(6), 3233-3254.

Gutenberg, B. (1931). Microseisms in north America. Bulletin of the Seismological Society of America, 21(1), 1-24.

Gülerce, Z., & Abrahamson, N. A. (2011). Site-specific design spectra for vertical ground motion. Earthquake Spectra, 27(4), 1023-1047.

Haddadi, H., Shakal, A., Huang, M., Parrish, J., Stephens, C., Savage, W., & Leith, W. (2012). Report on progress at the center for engineering strong motion data (CESMD). The 15th world conference on earthquake engineering. Lisbon, Portugal, Hamidia, M., Shokrollahi, N., & Ardakani, R. R. (2022). The collapse margin ratio of steel frames considering the vertical component of earthquake ground motions. Journal of Constructional Steel Research, 188, 107054.

Harrington, C. C., & Liel, A. B. (2016). Collapse assessment of moment frame buildings, considering vertical ground shaking. Earthquake Engineering & Structural Dynamics, 45(15), 2475-2493.

Harris, C. R., Millman, K. J., van der Walt, S. J., Gommers, R., Virtanen, P., Cournapeau, D., Wieser, E., Taylor, J., Berg, S., Smith, N. J., Kern, R., Picus, M., Hoyer, S., van Kerkwijk, M. H., Brett, M., Haldane, A., del Río, J. F., Wiebe, M., Peterson, P., Oliphant, T. E. (2020). Array programming with NumPy. nature, 585(7825), 357-362.

Hunter, J. D. (2007). Matplotlib: A 2D graphics environment. Computing in science & engineering, 9(03), 90-95.

James, G., Witten, D., Hastie, T., & Tibshirani, R. (2013). An introduction to statistical learning (Vol. 112). Springer.

Kehoe, B., & Hachem, M. (2003). Procedures for estimating floor accelerations. Proc., ATC-29-2 Seminar on Seismic Design, Performance, and Retrofit of Nonstructural Components in Critical Facilities, Applied Technology Council, Redwood City, Calif,

Keskin, E. (2020). Effect of vertical ground motion on the performance of high-rise buildings [Master's thesis, Middle East Technical University].

Klotz, O. (1915). The earthquake of February 18, 1911. Journal of the Royal Astronomical Society of Canada, Vol. 9, p. 428, 9, 428.

Kohler, M. D., Guy, R., Bunn, J., Massari, A., Clayton, R., Heaton, T., Chandy, K. M., Ebrahimian, H., & Dorn, C. (2018). Community seismic network and localized earthquake situational awareness. Proceedings of the 11th US National Conference on Earthquake Engineering (11NCEE), Los Angeles, CA, USA,

Kohler, M. D., Clayton, R. W., Bozorgnia, Y., Taciroglu, E., & Guy, R. (2022). The community seismic network: Applications and expansion to 1200 stations. AGU Fall Meeting Abstracts,

Kohler, M. D., Massari, A., Heaton, T. H., Kanamori, H., Hauksson, E., Guy, R., Clayton, R. W., Bunn, J., & Chandy, K. M. (2016). Downtown Los Angeles 52-story high-rise and free-field response to an oil refinery explosion. Earthquake Spectra, 32(3), 1793-1820.

Konno, K., & Ohmachi, T. (1998). Ground-motion characteristics estimated from spectral ratio between horizontal and vertical components of microtremor. Bulletin of the Seismological Society of America, 88(1), 228-241.

LATBSDC. (2023). An alternative procedure for seismic analysis and design of tall buildings located in the Los Angeles region. 2023 Edition. In Los Angeles Tall Buildings Structural Design Council.

Lawrence Livermore National Laboratory. (2019). Updating On-Site Ground Motion Reporting and Simulation of Ground Motions from Nearby Earthquakes at LLNL.

Lee, H., & Mosalam, K. (2014). Effect of vertical acceleration on shear strength of reinforced concrete columns. PEER Report 2014-04). Pacific Earthquake Engineering Research Center.

Liberatore, D., Doglioni, C., AlShawa, O., Atzori, S., & Sorrentino, L. (2019). Effects of coseismic ground vertical motion on masonry constructions damage during the 2016 Amatrice-Norcia (Central Italy) earthquakes. Soil Dynamics and Earthquake Engineering, 120, 423-435.

Lu, W., Huang, B., Chen, S., & Mosalam, K. M. (2017). Acceleration demand of the outer-skin curtain wall system of the Shanghai Tower. The Structural Design of Tall and Special Buildings, 26(5), e1341.

Manuals: SAC. (10/27/2014). Seismological Facility for the Advancement of Geoscience (SAGE). http://ds.iris.edu/ds/nodes/dmc/manuals/sac/

Massari, A., Clayton, R. W., & Kohler, M. (2018). Damage detection by template matching of scattered waves. Bulletin of the Seismological Society of America, 108(5A), 2556-2564.

Massari, A., Kohler, M., Clayton, R., Guy, R., Heaton, T., Bunn, J., Chandy, K. M., & Demetri, D. (2017). Dense building instrumentation application for city-wide structural health monitoring and resilience. Proceedings of the 16th World Conference on Earthquake Engineering (16WCEE), Santiago, Chile,

Mazloom, S., & Assi, R. (2023). Vertical floor spectra in low-and mid-rise elastic RC moment resisting frame buildings. Engineering Structures, 290, 116352.

Merino, R. J., Perrone, D., & Filiatrault, A. (2020). Consistent floor response spectra for performance-based seismic design of nonstructural elements. Earthquake Engineering & Structural Dynamics, 49(3), 261-284.

Mikami, A., Stewart, J., & Kamiyama, M. (2008). Effects of time series analysis protocols on transfer functions calculated from earthquake accelerograms. Soil Dynamics and Earthquake Engineering, 28(9), 695-706.

Miranda, E., & Taghavi, S. (2005). Approximate floor acceleration demands in multistory buildings. I: Formulation. Journal of Structural Engineering, 131(2), 203-211.

Mohammed, S., Shams, R., Nweke, C. C., Buckreis, T. E., Kohler, M. D., Bozorgnia, Y., & Stewart, J. P. (2024). Usability of Community Seismic Network recordings for ground-motion modeling. Earthquake Spectra, 40(4), 2598-2622.

Moschen, L., Medina, R. A., & Adam, C. (2015). Vertical acceleration demands on nonstructural components in buildings. 5th International Conference on Computational Methods in Structural Dynamics and Earthquake Engineering (COMPDYN 2015),

Niazi, M., & Bozorgnia, Y. (1991). Behavior of near-source peak horizontal and vertical ground motions over SMART-1 array, Taiwan. Bulletin of the Seismological Society of America, 81(3), 715-732.

Nielsen, G., Rees, S., Zekioglu, A., Sarebanha, A., Biscombe, L., Shao, B., & Dong, B. (2020). A 3-D seismic isolation system to protect the Loma Linda University Hospital from near-fault earthquakes. 17th World Conference on Earthquake Engineering, 17WCEE, Sendai, Japan,

Nyquist, H. (1924). Certain factors affecting telegraph speed. Transactions of the American Institute of Electrical Engineers, 43, 412-422.

Oppenheim, A. V., Schafer, R. W., & Buck, J. R. (1999). Discrete-time signal processing. Pearson Education India.

Papazoglou, A., & Elnashai, A. (1996). Analytical and field evidence of the damaging effect of vertical earthquake ground motion. Earthquake Engineering & Structural Dynamics, 25(10), 1109-1137.

Peng, Z. (2013). Introduction to Seismic Analysis Code (SAC), 2013 beta version. Georgia Tech. http://geophysics.eas.gatech.edu/classes/SAC/

Press, W. H., Teukolsky, S. A., Vetterling, W. T., & Flannery, B. P. (1992). Numerical recipes in C: The art of scientific computing. Press Syndicate of the University of Cambridge, New York, 24(78), 36.

Reinoso, E., & Miranda, E. (2005). Estimation of floor acceleration demands in high-rise buildings during earthquakes. The structural design of tall and special buildings, 14(2), 107-130.

Schwarz, G. (1978). Estimating the dimension of a model. The Annals of Statistics, 461-464.

Solomon, O. M. Jr. (1991). PSD computations using Welch's method. (NASA STI/Recon Technical Report N, 92, 23584.)

Stewart, J. P., Boore, D. M., Seyhan, E., & Atkinson, G. M. (2016). NGA-West2 equations for predicting vertical-component PGA, PGV, and 5%-damped PSA from shallow crustal earthquakes. Earthquake Spectra, 32(2), 1005-1031.

Stewart, J. P., & Fenves, G. L. (1998). System identification for evaluating soil–structure interaction effects in buildings from strong motion recordings. Earthquake engineering & structural dynamics, 27(8), 869-885.

Sullivan, T. J., Calvi, P. M., & Nascimbene, R. (2013). Towards improved floor spectra estimates for seismic design. Earthquakes and Structures, 4(1), 109-132.

Tamhidi, A. (2022). Earthquake Resilient Smart Cities: A Framework for Collection and Utilization of Highly Granular Field Data for Seismic Performance Characterization of Soft-Story Buildings [Doctoral dissertation, University of California, Los Angeles].

Tamhidi, A., Kuehn, N. M., & Bozorgnia, Y. (2023). Uncertainty quantification of ground motion time series generated at uninstrumented sites. Earthquake Spectra, 39(1), 551-576.

Trifunac, M., & Todorovska, M. (2001). Evolution of accelerographs, data processing, strong motion arrays and amplitude and spatial resolution in recording strong earthquake motion. Soil Dynamics and Earthquake Engineering, 21(6), 537-555.

Trifunac, M. D., & Lee, V. W. (1990). Frequency dependent attenuation of strong earthquake ground motion. Soil Dynamics and Earthquake Engineering, 9(1), 3-15.

Varevac, D., Draganić, H., & Gazić, G. (2010). Influence of the vertical component of earthquake on large span RC beams. Tehnički vjesnik, 17(3), 357-366.

Vera, A. A. A. (2022). Dynamic Behavior of Buildings Subjected to Vertical Ground Motions [Doctoral dissertation, Stanford University].

Wang, P., Stewart, J. P., Bozorgnia, Y., Boore, D. M., & Kishida, T. (2017). R package for computation of earthquake ground motion response spectra. Pacific Earthquake Engineering Center, Report, 9.

Wang, T., Shang, Q., & Li, J. (2021). Seismic force demands on acceleration-sensitive nonstructural components: a state-of-the-art review. Earthquake engineering and engineering vibration, 20(1), 39-62.

Welch, D. P., & Sullivan, T. J. (2017). Illustrating a new possibility for the estimation of floor spectra in nonlinear multi-degree of freedom systems. 16th world conference on earthquake engineering,

Welch, P. (1967). The use of fast Fourier transform for the estimation of power spectra: a method based on time averaging over short, modified periodograms. IEEE Transactions on Audio and Electroacoustics, 15(2), 70-73.

Wood, H. O. (1911). The observation of earthquakes: A guide for the general observer. Bulletin of the Seismological Society of America, 1(2), 48-82. https://doi.org/10.1785/bssa0010020048